INTERNATIONAL DOCTORAL
SCHOOL OF THE USC

Irma
Riádigos Sánchez

PhD Thesis

INTERACTIONS BETWEEN COSMIC RAYS AND THE ATMOSPHERE: MODELING AND PRACTICAL APPLICATIONS

Santiago de Compostela, 2021

Doctoral Programme in Nuclear and Particles Physics

TESE DE DOUTORAMENTO

INTERACTIONS BETWEEN COSMIC RAYS AND THE ATMOSPHERE: MODELING AND PRACTICAL APPLICATIONS

Irma Riádigos Sánchez

ESCOLA DE DOUTORAMENTO INTERNACIONAL DA UNIVERSIDADE DE SANTIAGO DE COMPOSTELA

PROGRAMA DE DOUTORAMENTO EN FÍSICA NUCLEAR E DE PARTÍCULAS

SANTIAGO DE COMPOSTELA

AÑO 2021

DECLARACIÓN DO AUTOR/A DA TESE

D./Dna. **Irma Riádigos Sánchez**

Título da tese: **Interactions between Cosmic Rays and the Atmosphere: Modeling and Practical Applications**

Presento a miña tese, seguindo o procedemento axeitado ao Regulamento, e declaro que:

1) A tese abarca os resultados da elaboración do meu traballo.
2) De ser o caso, na tese faise referencia ás colaboracións que tivo este traballo.
3) Confirmo que a tese non incorre en ningún tipo de plaxio doutros autores nin de traballos presentados por min para a obtención doutros títulos.
4) A tese é a versión definitiva presentada para a súa defensa e coincide a versión impresa coa presentada en formato electrónico

E comprométome a presentar o Compromiso Documental de Supervisión no caso de que o orixinal non estea na Escola.

En **Santiago de Compostela**, **22 de Decembro de 2021**.

Sinatura electrónica

AUTORIZACIÓN DO DIRECTOR / TITOR DA TESE

INTERACTIONS BETWEEN COSMIC RAYS AND THE ATMOSPHERE: MODELING AND PRACTICAL APPLICATIONS

D. Vicente Pérez Muñuzuri
D. Diego González Díaz

INFORMA/N:

Que a presente tese, correspóndese co traballo realizado por Dna. **Irma Riádigos Sánchez**, baixo a miña dirección/titorización, e autorizo a súa presentación, considerando que reúne os requisitos esixidos no Regulamento de Estudos de Doutoramento da USC, e que como director desta non incorre nas causas de abstención establecidas na Lei 40/2015.

De acordo co indicado no Regulamento de Estudos de Doutoramento, declara tamén que a presente tese de doutoramento é idónea para ser defendida en base á modalidade de Monográfica con reprodución de publicacións, nos que a participación da doutoranda foi decisiva para a súa elaboración e as publicacións se axustan ao Plan de Investigación.

En Santiago de Compostela, 22 de decembro de 2021

Fdo. Vicente Pérez Muñuzuri

Fdo. Diego González Díaz

Las cosas podrían haber sucedido de cualquier otra manera y, sin embargo, sucedieron así.

- Miguel Delibes, en su novela "El Camino"

Agradecimientos

Tomo prestada la frase con la que Miguel Delibes comienza su obra “El Camino”, y que sirve de apertura para esta tesis, puesto que resume con perfecta precisión lo que supone peregrinar por el enrevesado mundo de la etapa doctoral. La teoría del caos de la Física No Lineal insinúa que pequeñas variaciones en las condiciones iniciales dan lugar a grandes cambios en el resultado final. Yo no sabría identificar qué circunstancias o sucesos dieron lugar para que me encuentre en este momento escribiendo estas palabras para dar término a esta tesis, simplemente sé que sucedieron así. Al igual que he descubierto durante estos años de doctorado que la ciencia es un ente escurridizo y sibilino, que sin embargo, sucede de una manera determinada y no otra, y que nuestro papel consiste en desvelar sus misterios, que aunque nos gusten más o menos, son como son. Dicho esto, me gustaría agradecer todo el apoyo recibido durante el camino y que ha hecho posible esta tesis.

En primer lugar, dar las gracias a mi director de tesis, Prof. Vicente Pérez Muñuzuri, por la confianza depositada desde el primer momento y concederme la oportunidad de abrirme camino en el mundo de la investigación. Gracias por no perder la fe en mí, por aconsejarme y por empujarme cuando más lo necesitaba. Me gustaría agradecer en especial al Prof. Diego González Díaz, por su ayuda infinita y dedicación desde el principio, y por la generosidad de brindarme su capacidad y experiencia científica, fundamentales para la realización de esta tesis. Agradecer también al Prof. J.A. Garzón Heydt su codirección en los primeros momentos de este trabajo y por coordinar la colaboración Tragaldabas, en la cual he sido incluida e hizo posible parte del trabajo de esta tesis.

I want to thank Dr. Eloïse Marais for hosting me and giving me the opportunity to do my research stay at the University of Leicester (UK) which has been so enriching both professionally and personally. I also thank Dr. Jeffrey Pierce for his guidance and advice on the analyses derived from the research stay.

Un especial agradecimiento a Damián García Castro, compañero de batallas, y que al igual que yo, comenzó esta aventura doctoral en paralelo. Gracias por la disposición y contribución a esta tesis, sin la cual nunca podría haber llegado a su concreción.

Mi más profundo agradecimiento a mis compañeros de laboratorio por haber creado el mejor y más estimulante de los ambientes de trabajo, por su ayuda, su consejo y su conocimiento, y por compartir congresos, tertulias, celebraciones, Conchi-cafés y gracias por no decir nunca que no a un churrasco. Especial agradecimiento a Carlos, orquestador de las churrascadas y los descansos productivos; a Dani, por los python-consejos y las largas charlas de despacho; y especial mención a Mariamo, Damián y Martín, compañeros de viaje desde el primer día de carrera hasta el GFNL. Gracias a Alberto, David, Miguel, Sara, Ana, Alejandro, Breo, Sabela, Jorge, e Ismael. También agradecer a los otros profesores del grupo, Gonzalo Míguez y Alberto P. Muñuzuri.

Gracias a la profesora Ana Ulla (UVigo) por su interés y darme la oportunidad de participar

en sus pequeños proyectos.

A mis amigos y compañeros de viaje, por el apoyo moral prestado en tantos momentos y horas pasados juntos, que tanto me han ayudado a equilibrarme y distraerme en los momentos más intrincados de la tesis. A Janet por todas la aventuras compartidas, y aunque en los últimos años la distancia lo pone más complicado, siempre encontramos la forma de volver a reunirnos. A María y Dani, por los buenos momentos compartidos y por los que quedan. Por supuesto, agradecer a Silvia, Jacobo, Ruth y Carme, por ser tan geniales y estar siempre ahí. Y gracias Iria por tu energía contagiosa y positividad.

Gracias de todo corazón a Darío, por habernos encontrado en el camino, por tu apoyo incondicional, y por estar siempre ahí inclusive en los momentos más tormentosos.

Gracias a mi familia; a mis padres por animarme siempre a salir a por todas, sin importar las circunstancias, y en especial, a mi hermana Carla, por aguantar siempre “esas cosas raras tuyas”.

Y por último, me gustaría recordar con especial cariño al profesor Luis Gustavo Rodríguez Taboada, que aunque tristemente nunca llegará a leer estas palabras, siempre recordaré el día en el que el runrún de la física empezó a detonar en mi cabeza gracias a la pasión y dedicación con la que nos enseñaba física en el instituto.

Contents

Summary

This thesis collects the research work developed in the field of Physics about the different interaction processes between cosmic radiation and the atmosphere. It examines the experimental aspects of the object of study by exploring its practical applications for atmospheric sciences, as well as giving a theoretical viewpoint obtained through numerical modeling as it is necessary to validate results or test new hypotheses.

Nowadays, the research of cosmic rays is no longer devoted exclusively to the field of astronomy or astrophysics. During the last few years, a large number of significant results have opened the door to everyday applications of cosmic rays. One of the most remarkable cases was the discovery of a hidden chamber in the Great Pyramid of Giza using muon tomography, a technique similar to radiography that allows discerning the internal structure of dense objects. Other related practical applications also include the use of cosmic rays in volcanology to obtain images of volcanos' innards or the detection of possible nuclear waste in the transport of cargo containers. All this has been possible thanks to progress in the development of new detectors and measurement techniques in nuclear and particle physics.

Cosmic rays, contrary to what their name suggests, are not rays but radiation in the form of high-energy subatomic particles that reach the Earth from outer space in all directions. Their origin is very diverse, the ones with the lowest energies come from the Sun, whereas the most energetic cosmic rays originate in other parts of our Galaxy and even in much more distant places, such as other galaxies. The most energetic cosmic radiation has its origin in the most violent and extreme processes in the Universe, such as supernovae or black holes.

When these high-energy particles (also called *primary* cosmic rays) reach the atmosphere, they immediately interact with air molecules triggering a series of nuclear reactions from which new particles emerge, which in turn repeat the same process giving rise to a cascade of secondary particles that travels through the atmosphere until it reaches the Earth's surface. Cosmic rays are therefore ubiquitous particles in the atmosphere and, in particular, muons, one of the products created when a primary cosmic ray hits atmospheric nuclei. This kind of particle has a great penetrating power that makes it perfect for the applications mentioned above, especially because muons can pass through objects without damaging them. Moreover, they are of natural origin and do not depend on any artificial source for their generation, so they are available anywhere and any time.

In the first part of this dissertation, we consider the use of cosmic rays for atmospheric monitoring, in particular as a tool for measuring the vertical profile of atmospheric temperatures. The idea is to employ cosmic radiation traversing the atmosphere analogously to how weather satellites work. Satellites are able to record the temperature of different layers of the atmosphere by measuring the electromagnetic radiation of different frequencies radiating from it, which depends on the atmospheric state. Thus, we propose to use surface cosmic-ray measurements performed at different observation angles and energies for the same purpose. This idea arises

from the discovery of the correlation between variations of the cosmic-ray flux measured both at the Earth's surface and underground with temperature variations at different heights. The cause lies in the development of cosmic-ray cascades throughout the atmosphere, which depend on the air density along the path, affecting the production and absorption of secondary particles. As a consequence, cosmic-ray rates measured at the surface are not constant and vary over time in correlation with the atmospheric temperature profile and atmospheric pressure.

In this work, we analyze the experimental data obtained with a high resolution 2 m^2 cosmic-ray detector located at the Faculty of Physics (University of Santiago de Compostela). The objective is to study in detail the variations of cosmic-ray rates measured with the device in order to determine and characterize variations of atmospheric origin in the data. Measurements of correlations between cosmic rays and temperature are usually performed with underground detectors with large areas and volumes or at the surface with detectors of moderate sizes. The former type of device is installed underground to reduce the influence of cosmic-ray radioactivity on the measurements since the ultimate goal of their research is usually related to particle, nuclear, neutrino, or dark matter physics. Regarding ground-based detectors, they have been placed in countless locations around the world. In fact, a Global Muon Detector Network (GMDN) was created to continuously monitor cosmic-ray variations. This global network is used for space weather applications, such as forecasting large geomagnetic storms. Their work also covers the analysis of the atmospheric effect in the observed cosmic-ray data, however, the reason for its characterization is the removal of such effect from the data so that they can observe only the variations associated with space weather. Our challenge is to achieve the opposite, we want to isolate the atmospheric variations present in the data obtained with a small ground-based detector. It should be noted that this is the first time that a multigap timing RPC detector (MtRPC) has been used in the study of such correlations. In addition, we have implemented a program for the simulation of cosmic-ray air showers that allows the introduction of real atmospheric profiles. We simulate the atmospheric effects to corroborate and understand the experimental results.

Next, we focus on a practical application by designing a monitoring station aimed to obtain the vertical temperature profile of the atmosphere from cosmic-ray measurements. To date, despite the improved understanding of the influence of the atmosphere on cosmic-ray rates, the technological potential of such a possibility has been barely explored. In this thesis, the limits of the cosmic-ray inversion problem for temperature estimation are examined, presenting a configuration that combines a ground-based and an underground detector placed at an optimal depth. In addition, unlike previous works, we use the angular information.

The last part of the thesis is devoted to a slightly different research topic: the influence of cosmic rays on atmospheric processes. In particular, we study how the ionization produced by cosmic rays as they pass through the atmosphere affects cloud formation. At the end of the last century, significant correlations were found between solar activity and global cloud cover. The proposed hypothesis argued that during periods of low solar activity, since the Sun's magnetic field weakens, cosmic radiation of galactic origin can more easily penetrate the solar system and reach the Earth with a higher flux. Hence, atmospheric ionization increases and through some mechanism that is not yet fully understood is able to favor cloud formation. During peaks of maximum activity, the opposite will occur. The finding of these correlations, if the causality was confirmed, would mean that cosmic rays could play a role in climate variation because any significant alteration in global cloud cover modifies the terrestrial albedo causing changes in global warming or cooling. One of the biggest uncertainties in climate predictions

is the influence of clouds and how they vary under different conditions. The reason is that contrary to what one might think, the exact mechanisms of cloud formation are hardly known in detail. These uncertainties lead to a large dispersion in the predictions regarding the average temperature increase by the end of the century, which ranges from 1.4°C to 4.5°C. In the latter case, we would be talking about an extreme scenario with catastrophic consequences for the climate and human beings. It is therefore vital to forecast temperature change as accurately as possible. Thus, it is essential to go deeper into the study of cloud formation processes.

Cloud formation is caused by the presence in the air of small particles (or "cloud seeds") that act as condensation nuclei for water vapor. These tiny particles are atmospheric aerosols. However, there are many unanswered questions about how aerosols form in the atmosphere and how they affect clouds. Recent studies have found strong correlations between solar activity and aerosol properties, even though other similar analyses were not able to reproduce these results. Thus, this topic is quite controversial and has not yet helped to clarify the link between cosmic rays and clouds. In this thesis, we study the effect of charged aerosols due to cosmic-ray ionization in the condensation and coagulation processes of aerosols. We implement some mathematical models and numerical methods in order to carry out computational simulations of complex atmospheric physics and chemistry. For such purpose, we use the state-of-the-art GEOS-Chem atmospheric simulation program that includes a highly accurate microphysics scheme for the description of aerosol growth processes. Furthermore, the program features the option to vary atmospheric ionization to simulate a period of maximum or minimum solar activity. We launch pairwise simulations to contrast the results of both types of scenarios. The difference between both cases will give us information about the relevance of the change of the cosmic-ray flux due to solar activity in the formation of aerosols.

Resumen

Esta tesis recoge el trabajo de investigación desarrollado en el campo de la Física sobre distintos procesos de interacción que se dan entre la radiación cósmica y la atmósfera. Para ello, se enfoca el objeto de estudio desde un punto de vista experimental, explorando sus aplicaciones prácticas para las ciencias atmosféricas, y también desde un punto de vista más teórico a través de la modelización numérica, necesario para validar resultados o comprobar nuevas hipótesis.

En la actualidad, el estudio de los Rayos Cósmicos ya no se centra exclusivamente en el campo de la astronomía o astrofísica. Durante los últimos años, se han obtenido una gran cantidad de resultados significativos que han abierto la puerta a la aplicación de los rayos cósmicos en la vida cotidiana. Uno de los casos con más repercusión ha sido el descubrimiento de una cámara oculta en la Gran Pirámide de Guiza a través de la tomografía de muones, una técnica similar a la radiografía que permite discernir la estructura interna de objetos densos. Entre las aplicaciones prácticas relacionadas también cabe mencionar su uso en la vulcanología para obtener imágenes del interior de los volcanes, o la detección de posibles residuos nucleares en el transporte de grandes contenedores. Todo ello ha sido posible gracias al avance en el desarrollo de nuevos detectores y técnicas de medición en la física nuclear y de partículas.

Los rayos cósmicos, al contrario de lo que su nombre sugiere, no son rayos, sino que son una radiación en forma de partículas subatómicas de alta energía que llegan a la Tierra procedentes del espacio exterior y en todas direcciones. Su origen es muy diverso, las de menor energía proceden del Sol, mientras que las de mayor energía se originan en otras partes de nuestra Galaxia e incluso en lugares mucho más distantes, como en otras galaxias. La radiación cósmica más energética tiene su origen en los procesos más violentos y extremos del Universo, tales como supernovas o agujeros negros.

Cuando estas partículas de gran energía (también denominados rayos cósmicos *primarios*) entran en contacto con la atmósfera, interaccionan inmediatamente con las moléculas del aire desencadenando una serie de reacciones nucleares de las que emergen nuevas partículas, que a su vez repiten el proceso generando una cascada de partículas secundarias que viaja por la atmósfera hasta llegar a la superficie terrestre. Por lo tanto, los rayos cósmicos son partículas omnipresentes en la atmósfera y, en especial, los muones, uno de los productos que se crean cuando un rayo cósmico primario impacta con los núcleos atmosféricos. Esta clase de partículas tiene un gran poder de penetración que hace que sean perfectos para las aplicaciones mencionadas con anterioridad, sobre todo, porque atraviesan los objetos sin dañarlos. Asimismo, son de origen natural y no dependen de ninguna fuente artificial para su generación, por lo que están disponibles en todo momento y en cualquier parte.

En la primera parte de esta tesis, se considera el uso de los muones para la monitorización atmosférica, en concreto, como herramienta para medir el perfil de temperatura de la atmósfera. La idea es utilizar la radiación cósmica que atraviesa la atmósfera de forma análoga al funcionamiento de los satélites de observación. En su caso, los satélites son capaces de

registrar la temperatura de diferentes capas de la atmósfera a través de la medición de la radiación electromagnética de diferentes frecuencias que radia de esta y que depende de su estado. De este modo, se propone usar las medidas de rayos cósmicos en superficie realizadas a diferentes ángulos de observación y energías (equivalente a profundidad bajo tierra) para el mismo propósito. Esta idea surge del descubrimiento de la correlación de las variaciones de rayos cósmicos medidos en superficie y bajo tierra con las variaciones de temperatura a diferentes alturas. Su causa radica en la evolución de las cascadas de rayos cósmicos a lo largo de la atmósfera, que dependen de la densidad del aire a su paso, afectando a la producción y absorción de las partículas secundarias generadas en las diferentes interacciones nucleares. Como consecuencia, las tasas de rayos cósmicos medidas en superficie no son constantes y varían con el tiempo en correlación con las temperaturas y la presión atmosférica. La clave está en que los muones cósmicos de diferentes energías se ven afectados de forma diferente por las variaciones de temperatura, siendo los rayos cósmicos más energéticos mucho más sensibles a la temperatura de la estratosfera, por ejemplo. Esta peculiaridad se puede aprovechar para construir un modelo que permita resolver el problema inverso y reconstruir la temperatura de la atmósfera a partir de la información proporcionada por los diferentes "canales" de detección de rayos cósmicos. Los "coeficientes de temperatura" son unos pesos que se calculan de forma teórica y que proporcionan información sobre cómo afecta la variación de temperatura en cada capa de la atmósfera a la tasa medida a un cierto nivel de observación. Además, estos coeficientes dependen del ángulo de observación y la energía de los muones. A lo largo de la tesis, estos coeficientes juegan un papel fundamental para el desarrollo de las diferentes metodologías de análisis.

En este trabajo, se analizan, por un lado, los datos experimentales obtenidos con un pequeño detector de rayos cósmicos de alta resolución y 2 m^2 de superficie situado en la facultad de Física (Universidad de Santiago de Compostela). El objetivo consiste en analizar en detalle las variaciones de las tasas de rayos cósmicos medidas con el dispositivo con el fin de determinar y caracterizar las variaciones de origen atmosférico en los datos. Las medidas de las correlaciones entre rayos cósmicos y temperatura se realizan normalmente con detectores bajo tierra que cuentan con grandes áreas y volúmenes de detección o en la superficie con detectores de tamaños más reducidos. En relación al primer tipo de detectores, se instalan bajo tierra para reducir la influencia de la radiactividad de los rayos cósmicos en las medidas ya que el objetivo de estas investigaciones está relacionado con la física nuclear, de partículas, de neutrinos o la física de la materia oscura. En cuanto a los detectores en superficie, se instalaron una gran cantidad en diversas localizaciones alrededor del mundo. De hecho, la Red Global de Detección de Muones (en inglés, GMDN) fue creada para monitorizar de forma continuada las variaciones de rayos cósmicos. Un detector en superficie es mucho más sensible a las variaciones atmosféricas, además también está afectado por fenómenos relacionados con la actividad solar. Esta red global de detectores se usa para aplicaciones de clima espacial, como por ejemplo, para la predicción de grandes tormentas geomagnéticas. También analizan el efecto atmosférico presente en los datos medidos de rayos cósmicos con el objetivo de eliminarlo y así poder observar solamente las variaciones asociadas al clima espacial. Por lo tanto, mientras que otros experimentos están interesados en el estudio de las correlaciones atmosféricas para su posterior eliminación de las medidas, nuestro reto consiste en conseguir lo contrario, aislar las variaciones atmosféricas presentes en las medidas obtenidas con un detector pequeño en superficie. Cabe destacar que esta es la primera vez que se consigue reproducir tales correlaciones con un detector basado en cámaras de placas resistivas de múltiples bandas

(MtRPC). Esta tecnología consiste en detectores gaseosos de respuesta rápida formado por dos placas paralelas cargadas de forma opuesta y hechas con un material altamente resistivo. Entre las dos placas se encuentra el gas, donde interaccionará la partícula incidente. Esta clase de detectores tiene la característica de proporcionar una buena resolución temporal y espacial, muy necesario para un dispositivo de pequeño tamaño cuyo objetivo es la detección de rayos cósmicos en superficie.

Para este trabajo, se mide la correlación entre las tasas medidas y la presión atmosférica en superficie, que se caracteriza con la intención de eliminar las variaciones relacionadas con ella de las tasas y poder así estudiar mejor las variaciones de temperatura, que podrían quedar apantalladas en caso contrario. El uso de un algoritmo específico para dicha tarea también nos permitirá eliminar de los datos las variaciones relacionadas con eventos interplanetarios derivados de la actividad solar. Finalmente, se estimarán los coeficientes de temperatura específicos del detector de forma experimental aplicando una técnica estadística basada en el Análisis de Componentes Principales. Esto nos permitirá discernir las variaciones de temperatura inherentes en los datos, tanto estacionales como otras variaciones inusuales con periodos más cortos duración.

De forma adicional, se ha desarrollado la implementación de un programa para la simulación de cascadas de rayos cósmicos en la atmósfera que permite introducir datos reales de perfiles atmosféricos. Otro software de simulación de cascadas disponible (AIRES, CORSIKA,...) tiene la desventaja de usar un modelo de atmósfera estándar, el cual no permite el estudio de los fenónemos que intentamos observar de forma experimental. Es por ello que nuestra intención consiste en desarrollar un código nuevo desde cero para poder validar la parte experimental. Por lo tanto, se han escrito una serie de rutinas simplificadas que permiten simular las cascadas de partículas en la atmósfera. Con esta metodología, intentaremos entender lo que sucede en la atmósfera y cuáles son los factores relevantes que afectan la evolución de las cascadas. El propósito final es obtener un programa que nos permita introducir datos reales de la atmósfera para simular el flujo de muones que alcanzaría nuestro detector.

En la segunda parte de la tesis, más enfocada en la aplicación práctica, nos centramos en el estudio del desarrollo de una estación de monitorización para la obtención de la temperatura de la atmósfera a partir de rayos cósmicos. Hasta la fecha, a pesar de la mejora en la comprensión de la influencia de la atmósfera en las tasas de rayos cósmicos, apenas se ha explorado el potencial tecnológico de dicha aplicación. En esta tesis, se examinan los límites del problema de inversión de rayos cósmicos para la estimación de la temperatura, presentando como propuesta una configuración que combina una estación de detección en superficie y otra bajo tierra a una profundidad óptima. Además, a diferencia de anteriores trabajos, usamos la información angular de las medidas. La metodología del estudio consiste en simular tasas de rayos cósmicos que contengan las variaciones inducidas de temperatura, utilizando como datos de entrada los coeficientes de temperatura teóricos junto con perfiles reales de temperatura obtenidos de la base de datos de reanálisis del ERA5 (ECMWF). Para obtener una muestra realista de datos, también se incluyen las fluctuaciones de origen estadístico así como el efecto de la absorción de los muones en la roca. La serie temporal resultante se usa en el problema inverso para obtener el perfil de temperaturas que será comparado con los datos de temperatura originales. En la resolución del problema inverso, se analizan diferentes escenarios y los resultados se contrastan con trabajos previos. El objetivo de este estudio es establecer una línea de trabajo para futuros proyectos experimentales que tengan como meta la construcción de una estación de sondeo de la atmósfera a partir de rayos cósmicos.

La última parte de la tesis está dedicada a una temática de investigación ligeramente distinta: la influencia de los rayos cósmicos en los procesos atmosféricos. En concreto, estudiamos cómo la ionización que los rayos cósmicos producen a medida que atraviesan la atmósfera afecta a la formación de nubes. A finales del siglo pasado, se observaron correlaciones significativas entre la actividad solar y la cobertura global de nubes. La hipótesis planteada razona que en periodos de baja actividad solar, puesto que el campo magnético del Sol se debilita, la radiación cósmica de origen galáctico puede penetrar con más facilidad en el Sistem Solar y llegar hasta la Tierra con un flujo mayor. Como consecuencia, la ionización atmosférica aumenta y mediante algún mecanismo aún desconocido es capaz de favorecer la formación de nubes. Así, en periodos mínimos de actividad solar, la cobertura de nubes del planeta será mayor, mientras que en picos de actividad máxima ocurrirá lo contrario. El hallazgo de estas correlaciones, de confirmarse la causalidad, significaría que los rayos cósmicos estarían jugando su papel en la variación del clima. Esto se debe a que cualquier alteración significativa en la cobertura global de nubes modifica el albedo terrestre provocando cambios en el calentamiento o enfriamiento del planeta. Una de las mayores incertidumbres en las predicciones climáticas es la influencia de las nubes y cómo estas varían bajo diferentes condiciones. El motivo es que al contrario de lo que uno pueda pensar, apenas se conocen con detalle cuáles son los mecanismos exactos por los cuales se forman las nubes. Estas incertidumbres provocan una gran dispersión en los resultados de las predicciones del aumento de la temperatura media a finales de siglo, que varían entre el 1.5° y 4.5°C. Cabe destacar que este rango de incertidumbre en las predicciones no se ha conseguido reducir a lo largo de los últimos años. En el segundo caso pronosticado, estaríamos hablando de un escenario extremo con consecuencias catastróficas para el clima y el ser humano. Por lo tanto, resulta vital proyectar con la mayor exactitud posible el cambio en la temperatura. Así que es imprescindible ahondar en el estudio de los procesos de formación de nubes.

La formación de las nubes se produce gracias a la presencia en el aire de pequeñas partículas (o "semillas de nube") que actúan como núcleos de condensación para el vapor de agua. Estas minúsculas partículas son los aerosoles atmosféricos, que pueden ser de origen natural o antropogénico, como por ejemplo, partículas de sal procedentes del mar, material volcánico, polvo del desierto, productos de incendios forestales o la quema de combustibles, etc. Sin ellos, las nubes no existirían en la Tierra y el clima sería radicalmente diferente. Además, no existiría la vida. Sin embargo, existen muchas preguntas sin resolver acerca de cómo se forman los aerosoles en la atmósfera y su efecto en las nubes.

En los últimos 20 años, se ha estudiado más a fondo las correlaciones entre la actividad solar y las nubes, incluyendo también los aerosoles en el análisis. Mientras que algunos trabajos encontraron correlaciones significativas entre datos de cobertura de nubes y propiedades de los aerosoles, otros análisis similares no fueron capaces de reproducir dichos resultados. Así, este tema resulta bastante controvertido y aún no ha ayudado a esclarecer el vínculo entre rayos cósmicos y nubes.

Sin embargo, un imporante experimento llevado a cabo en el CERN y denominado CLOUD, tiene como objetivo estudiar dentro una gran cámara con condiciones atmosféricas controladas la creación y el crecimiento de los aerosoles. Una de las misiones principales de este proyecto consite en investigar la relación que existe entre los rayos cósmicos y las nubes. Para ello, se utiliza como fuente de radiación partículas aceleradas en el sincrotrón para emular la ionización producida por los rayos cósmicos galácticos en la atmósfera. Con los primeros resultados publicados en el 2011, este experimento se ha convertido en uno de los

primeros en demostrar una relación directa entre radiación cósmica y aerosoles. Aunque los resultados demuestran que los rayos cósmicos no juegan un papel fundamental en el cambio climático, sí son relevantes en una pequeña proporción para el proceso de nucleación los aerosoles. Y se demuestra que bajo ciertas condiciones atmosféricas, pueden favorecer de manera significativa su crecimiento. Por lo tanto, no se debe descartar su efecto. Los modelos empíricos derivados de este experimento han sido puestos a prueba en modelos informáticos de química atmosférica para simular con precisión los procesos de formación de los aerosoles y su influencia en la nubosidad. Con ello se ha observado que la ionización afecta a los pequeños aerosoles pero estos cambios no son lo suficientemente eficaces como para trasladarse a las partículas más grandes que forman los núcleos de condensación. A pesar de todo ello, esto no descarta por completo la influencia de los rayos cósmicos en los aerosoles. Otros procesos como la condensación o la coagulación de los aerosoles también parecen estar afectados por la ionización y han sido explorados en menor medida. En la última parte de la tesis, vamos a tener en cuenta estos dos últimos procesos y los implementamos en GEOS-Chem, un programa de simulación atmosférica que incluye un esquema de microfísica de gran precisión en la descripción de los procesos de crecimiento de los aerosoles. Este modelo es uno de los más completos y accesibles que se pueden encontrar, además de que está elaborado por cientos de científicos alrededor del mundo. Esto hace que sea uno de los más actualizados y complejos de su campo. En concreto, GEOS-Chem es un modelo diseñado para el transporte químico tridimensional que permite realizar simulaciones de la composición atmosférica a una escala global o regional. Además, se puede acoplar con otros modelos climáticos o meteorológicos, como puede ser el modelo WRF (uno de los más utilizados en el mundo para la predicción regional a corto plazo). Otra de las características más destacables es que ya tiene implementado el efecto de los iones generados por la radiación cósmica en el proceso de nucleación de los aerosoles. La nucleación es una de las fuentes más importantes de partículas atmosféricas y consiste en la agregación de pequeños conglomerados moleculares desde la fase gaseosa y se sabe que este proceso puede ser estimulado por la presencia de iones. En este caso, el modelo GOES-Chem cuenta con una parametrización de la nucleación que depende de varios parámetros entre los que se encuentran la tasa de ionización atmosférica.

La nucleación es un proceso que involucra a las partículas más pequeñas, por el contrario, la condensación y coagulación son los procesos responsables de que los pequeños grupos de partículas crezcan a tamaños superiores. Si tenemos en cuenta la presencia de iones atmosféricos, estos condensan sobre los aerosoles proporcionándoles carga. Así, los aerosoles pueden acumular un variado número de cargas en su superficie. Como consecuencia, esta distribución de cargas en los aerosoles va a afectar al proceso de coagulación, puesto que si dos aerosoles que colisionan tienen cargas de idéntico signo, aparecerá una fuerza de repulsión que inhibirá su unión. Por el contrario, si los aerosoles transportan cargas de signo contrario, su coagulación estará más favorecida. De esta forma, resulta relevante incorporar la distribución de cargas en el modelo. Sin embargo, introducir de forma explícita la distribución de carga de las partículas es más complejo y haría que el cálculo fuese extremadamente lento. Esto se debe a que el modelo divide la distribución de tamaño de los aerosoles en cuarenta *bins* y para cada uno resuelve un par de ecuaciones en cada paso de tiempo, una que calcula el número de aerosoles en el *bin* y otra que calcula su masa. Así que el modelo tiene que resolver 80 ecuaciones en cada paso de tiempo y en cada punto del espacio (o malla espacial del modelo). Si suponemos que las partículas solo pueden transportar una carga negativa o positiva, eso significaría tener que triplicar los *bins* para que también se tenga en cuenta el número de partículas cargadas en

cada momento y poder calcular mejor la coagulación. Por lo tanto, el número de ecuaciones a resolver aumentaría considerablemente y ralentizaría mucho los cálculos. Pero la realidad es aún más complicada puesto que los aerosoles pueden transportar más de una carga (de hecho pueden llegar a ser más de 100 cargas) y en esa situación el número de ecuaciones a resolver sería inmenso. Por suerte, existen técnicas que permiten aproximar el número de cargas mediante una función que depende de ciertos parámetros, como el tamaño de la partícula, y que hace que ya no sea necesario la implementación explícita de todos los *bins* de carga. Además, también permite acelerar la velocidad de cómputo.

Nuestro objetivo consiste en implementar el cálculo de las cargas y su efecto en la coagulación para ver como la ionización afecta al crecimiento de los aerosoles. Una vez implementados los cambios oportunos en el código, puesto que el programa tiene como característica la opción de variar la ionización atmosférica inducida por los rayos cósmicos para simular un periodo de actividad solar máxima o mínimo, lanzamos simulaciones a pares para contrastar los resultados de ambas situaciones. La diferencia entre ambas nos dará información acerca de la relevancia del cambio del flujo de rayos cósmicos debido a la actividad solar en la formación de los aerosoles.

Resumo

Esta tese recolle o traballo de investigación levado a cabo no campo da Física sobre distintos procesos de interacción que se dan entre a radiación cósmica e a atmosfera. No traballo enfócase o obxecto de estudo dende un punto de vista experimental, explorando as súas aplicacións prácticas para as ciencias atmosféricas, e tamén dende un punto de vista máis teórico a través da modelización numérica, necesario para validar resultados ou comprobar novas hipóteses.

Na actualidade, o estudo dos Raios Cósmicos xa non está centrado exclusivamente no campo da astronomía ou astrofísica. Durante os últimos anos, obtivéronse unha gran cantidade de resultados significativos que abriron a porta á aplicación dos raios cósmicos na vida cotiá. Un dos casos con maior repercusión foi o descubrimento dunha cámara oculta na Gran Pirámide de Guiza a través da tomografía de muóns, unha técnica similar á radiografía que permite disnernir a estructura interna dos obxectos densos. Entre as aplicacións prácticas relacionadas tamén cabe mencionar o seu uso na vulcanoloxía para obter imaxes do interior dos volcáns, ou a detección de posibles refugallos nucleares no transporte de grandes contedores. Todo isto foi posible grazas ao avance no desenvolvemento de novos detectores e técnicas de medición na física nuclear e de partículas.

Os raios cósmicos, ao contrario de que o seu nome suxire, non son raios, senón que son unha radiación en forma de partículas subatómicas de alta enerxía que chegan á Terra procedentes do espazo exterior e en todas direccións. A súa orixe é moi diversa, as partículas de menor enerxía proceden do Sol, mentres que as de maior enerxía orixínanse noutras partes da nosa Galaxia e incluso en lugares moito máis afastados, como noutras galaxias. A radiación cósmica máis enerxética ten a súa orixe nos procesos máis violentos e extremos do Universo, tales como supernovas ou buratos negros.

Cando estas partículas de grande enerxía (tamén denominadas raios cósmicos *primarios*) entran en contacto coa atmosfera, interaccionan inmediatamente coas moléculas do aire desencadeando unha serie de reaccións nucleares das que xorden novas partículas, que á súa vez repiten o proceso xerando unha fervenza de partículas secundarias que viaxa pola atmosfera ata chegar á superficie terrestre. Polo tanto, os raios cósmicos son partículas ubicuas na atmosfera e, especialmente, os muóns, un dos productos que se crean cando un raio cósmico primario impacta cos núcleos atmosféricos. Esta clase de partículas ten un gran poder de penetración que fai que sexan perfectas para as aplicacións mencionadas con anterioridade, sobre todo, porque atravesan os obxectos sen causarlles dano. Así mesmo, son de orixe natural e non dependen de ningunha fonte artificial para a súa xeración, polo que están dispoñibles en todo momento e en calquera parte.

Na primeira parte desta tese, considérase o uso dos muóns para a monitorización atmosférica, en concreto, como ferramenta para medir a temperatura da atmosfera. A idea é utilizar a radiación cósmica que atravesa a atmosfera de forma análoga ao funcionamento dos satélites de observación meteorolóxica. Os satélites son capaces de rexistrar a temperatura de

diferentes capas da atmosfera a través da medición da radiación electromagnética de diferentes frecuencias que radian dela e que depende do seu estado. Deste modo, proponse usar as medidas de raios cósmicos en superficie realizadas a diferentes ángulos de observación e enerxías (equivalente á profundidade baixo terra) para o mesmo propósito. Esta idea xorde do descubrimento da correlación das variacións de raios cósmicos medidos en superficie e baixo terra coas variacións do perfil de temperatura a diferentes alturas e a presión atmosférica. A súa causa radica na evolución das fervenzas de raios cósmicos ao longo da atmosfera, que dependen da densidade do aire ao seu paso, afectando á producción e absorción das partículas secundarias creadas nas diferentes interaccións nucleares. Como consecuencia, as taxas de raios cósmicos medidas en superficie non son constantes e varían co tempo en correlación coas temperaturas ou a presión atmosférica. A chave está en que os muóns cósmicos de diferentes enerxías vense afectados de forma diferente polas variacións de temperatura, sendo os raios cósmicos máis enerxéticos moito máis sensibles á temperatura da estratosfera, por exemplo. Esta peculiaridade pódese aproveitar para construir un modelo que permita resolver o problema inverso e reconstruir a temperatura da atmosfera a partir da información proporcionada polas diferentes "canles" de detección de raios cósmicos. Os "coeficientes de temperatura" son uns pesos que se calculan de forma teórica e que proporcionan información sobre como afecta a variación de temperatura en cada capa da atmosfera á taxa medida a un certo nivel de observación. Ademais, estes coeficientes dependen do ángulo de observación e da enerxía dos muóns. Ao longo desta tese, estes coeficientes xogan un papel fundamental para o desenvolvemento das diferentes metodoloxías de análise.

Neste traballo, analízanse, por un lado, os datos experimentais obtidos cun pequeno detector de raios cósmicos de alta resolución e 2 m^2 de superficie situado na Facultade de Físicas (Universidade de Santiago de Compostela). O obxectivo consiste en analizar con detalle as variacións das taxas de raios cósmicos medidas co dispositivo coa fin de determinar e caracterizar as variacións de orixe atmosférico nos datos. As medidas das correlacións entre raios cósmicos e temperatura realízanse normalmente con detectores baixo terra que contan con grandes áreas e volúmenes de detección ou na superficie con detectores de tamaños máis reducidos. No referido ao primeiro tipo de detectores, instálanse baixo terra para reducir a influencia da radioactividade dos raios cósmicos nas medidas xa que o obxectivo destas investigacións está relacionado coa física nuclear, de partículas, de neutrinos ou a física da materia escura. En relación aos detectores en superficie, instaláronse unha gran cantidade deles en diversas localizacións arredor do mundo. De feito, a Rede Global de Detección de Muons (GMDN) foi creada para monitorizar de forma continuada as variacións de raios cósmicos. Un detector en superficie é moito máis sensible ás variacións atmosféricas, ademais tamén está afectado por fenómenos relacionados coa actividade solar. Esta rede global de detectores úsase para aplicacións de clima espacial, como por exemplo, para a predición de grandes tormentas xeomagnéticas. Tamén analizan o efecto atmosférico presente nos datos medidos de raios cósmicos co obxectivo de eliminalo e así poder observar soamente as variacións que estén asociadas ao clima espacial. Polo tanto, mentres que esta clase de experimentos están interesados no estudo das correlacións coa atmosfera para a súa posterior eliminación das medidas, o noso reto consiste en conseguir o contrario, illar as variacións atmosféricas presentes nas medidas obtidas cun detector pequeno en superficie. Cabe destacar que esta é a primeira vez que se consegue reproducir tales correlacións cun detector baseado en cámaras de placas resistivas de múltiples bandas (MtRPC). Esta tecnoloxía consiste en detectores gaseosos de resposta rápida formados por dúas placas paralelas cargadas de forma oposta e feitas cun

material altamente resistivo. Entre as dúas placas atópase o gas, onde interaccionará a partícula incidente. Esta clase de detectores ten a característica de proporcionar unha boa resolución temporal e espacial, moi necesario para un dispositivo de pequeno tamaño cuxo obxectivo sexa a detección de raios cósmicos en superficie.

Para este traballo, mídese a correlación das taxas medidas coa presión atmosférica en superficie, que se caracteriza coa intención de eliminar as variacións relacionadas con ela das taxas e poder así estudar mellor as variacións de temperatura, que poderían quedar ocultas en caso contrario. O uso dun algoritmo específico para a realización desta tarea tamén permite eliminar dos datos as variacións relacionadas con eventos interplanetarios derivados da actividade solar. Finalmente, vanse estimar os coeficientes de temperatura específicos do detector de forma experimental aplicando unha técnica estadística baseada na Análise de Compoñentes Principais (PCA). Isto permítenos discernir as variacións de temperatura inherentes nos datos, tanto estacionales como outras variacións inusuais con períodos máis curtos de duración.

De forma adicional, implementouse un programa para a simulación de fervenzas de raios cósmicos na atmosfera que permite introducir datos reais de perfís atmosféricos. Outro software de simulación de fervenzas dispoñible (AIRES, CORSIKA...) ten a desvantaxe de usar un modelo de atmosfera estándar, o cal non permite o estudo dos fenómenos que intentamos observar de forma experimental. É por isto que a nosa intención consiste en desenvolver un código novo dende cero para poder validar a parte experimental. Polo tanto, escribíronse unha serie de rutinas simplificadas que permiten simular as fervenzas de partículas na atmosfera. Esta metodoloxía permítenos entender o que sucede na atmosfera e cales son os factores relevantes que afecta a evolución das fervenzas. O propósito final é obter un programa que nos permita introducir datos reais da atmosfera para simular o fluxo de muóns que alcanzarán o noso detector.

Na segunda parte da tese, máis enfocada á aplicación práctica, centrámonos no estudo do desenvolvemento dunha estación de monizotirazación para a obtención do perfil de temperatura da atmosfera a partir de raios cósmicos. Ata agora, pese á mellora na comprensión da influencia da atmosfera nas taxas de raios cósmicos, apenas explorouse o potencial tecnolóxico de tal aplicación. Nesta tese, examínanse os límites do problema da inversión de raios cósmicos para a estimación do perfil de temperatura, presentando como proposta unha configuración que combina unha estación de detección en superficie e outra baixo terra situada a unha profundidade óptima. Ademais, en contraste con traballos anteriores, usamos a información angular das medidas. A metodoloxía do estudo consiste en simular taxas de raios cósmicos que coteñan as variacións inducidas de temperatura, utilizando como datos de entrada os coeficientes de temperatura teóricos xunto cos perfís reais de temperatura obtidos da base de datos de reanálisis do ERA5 (ECMWF). Para obter unha mostra realista de datos, tamén se incluen as fluctuacións de orixe estadístico así como tamén o efecto da absorción dos muóns na roca. A serie temporal resultante úsase no problema inverso para obter o perfil de temperaturas que será comparado cos datos de temperatura orixinais. Na resolución do problema inverso, analízanse diferentes escenarios e os resultados contrástanse con traballos previos. O obxectivo deste estudo é establecer unha liña de traballo para futuros proxectos experimentais que teñan como meta a construcción dunha estación de sondaxe da atmosfera a partir de raios cósmicos.

A última parte da tese está dedicada a unha temática de investigación lixeiramente distinta: a influencia dos raios cósmicos nos procesos atmosféricos. En concreto, estudamos como a ionización que os raios cósmicos producen a medida que atravesan a atmosfera afecta á

formación de nubes. A finais do século pasado, observáronse correlacións significativas entre a actividade solar e a cobertura global de nubes. A hipótese planteada razoa que en períodos de baixa actividade solar, dado que o campo magnético do Sol debilítase, a radiación cósmica de orixe galáctico pode penetrar con máis facilidade no Sistema Solar e chegar ata a Terra cun fluxo maior. Como consecuencia, a ionización atmosférica aumenta e mediante algún mecanismo aínda descoñecido é capaz de favorecer a formación de nubes. Así, en períodos mínimos de actividade solar, a cobertura de nubes do planeta será maior, mentres que en picos de actividade solar máxima ocurrirá o contrario. O achado destas correlacións, de confirmarse a causalidade, significaría que os raios cósmicos estarían xogando un certo papel na variación do clima. Isto débese a que calquera alteración significativa na cobertura global de nubes modifica o albedo terrestre provocando cambios no calentamento ou enfriamento do planeta. Unha das maiores incertezas nas predicións climáticas é a influencia das nubes e como estas varían baixo diferentes condicións. O motivo é que ao contrario do que un poida pensar, apenas se coñecen con detalle cales son os mecanismos exactos polos cales se forman as nubes. Estas incertezas provocan unha gran dispersión nos resultados das predicións do aumento da temperatura media para finais de século, que varían entre 1.5°C e 4.5°C. Cabe destacar que este grao de incerteza nas predicións non se conseguiu reducir ao longo dos últimos anos. No segundo caso pronosticado, estariamos falando dun escenario extremo con consecuencias catastróficas para o clima e os seres vivos. Polo tanto, resulta vital proxectar coa maior exactitude posible o cambio na temperatura. Así que resulta imprescindible afondar no estudo dos procesos de formación de nubes.

A formación de nubes prodúcese grazas á presenza no aire de pequenas partículas (ou "sementes de nube") que actúan como núcleos de condensación para o vapor de auga. Estas minúsculas partículas son os aerosois atmosféricos, que poden ser de orixe natural ou antropoxénico, como por exemplo, partículas de sal procedentes do mar, material volcánico, po do deserto, produtos de incendios forestais ou a queima de combustibles, etc. Sen os aerosois, as nubes non existirían na Terra e o clima sería radicalmente diferente. Ademais, non existiría a vida. Así a todo, existen moitas preguntas sen resolver acerca de como se forman e medran os aerosois na atmosfera e o seu efecto nas nubes.

Nos últimos 20 anos, estudiouse máis a fondo as correlacións entre a actividade solar e as nubes, incluindo tamén os aerosois nas análises. Mentres que algúns traballos atoparon correlacións significativas entre datos de cobertura de nubes e propiedades dos aerosois, outras análises similares non foron quen de reproducir os mesmos resultados. Así, este tema resulta bastante controvertido a aínda non axudou a esclarecer o vencello entre raios cósmicos e nubes.

Porén, un importante experimento levado a cabo no CERN e denominado CLOUD, ten como obxectivo estudar dentro dunha gran cámara con condicións atmosféricas controladas a creación e crecemento dos aerosois. Unha das misións principais deste proxecto consiste en investigar a relación existente entre os raios cósmicos e as nubes. Para tal propósito, utilízase como fonte de radiación partículas aceleradas no sincrotrón para emular a ionización producida polos raios cósmicos galácticos na atmosfera. Cos primeiros resultados publicados no 2011, este experimento convertiuse nun dos primeiros en demostrar unha relación directa entre radiación cósmica e os aerosois. Aínda que os resultados demostren que os raios cósmicos non xogan un papel fundamental no cambio climático, si que son relevantes nunha pequena proporción para o proceso de nucleación dos aerosois. Demóstrase que baixo certas condicións atmosféricas, poden favorecer de xeito significativo o seu crecemento. Polo tanto, non se debería descartar o seu efecto. Os modelos empíricos derivados deste experimento foron postos

a proba en modelos informáticos de química atmosférica para simular con precisión os procesos de formación dos aerosois e a súa influencia na nubosidade. Grazas a isto, observouse que a ionización afecta aos pequenos aerorois pero estes cambios non son suficientemente eficaces como para trasladarse ás partículas máis grandes que forman os núcleos de condensación. A pesar de todo, isto non descarta por completo a influencia dos raios cósmicos nos aerosois. Outros procesos como a condensación ou a coagulación dos aerosois tamén parecen estar afectados pola ionización pero foron explorados en menor medida. Na última parte da tese, vamos ter en conta estes dous últimos procesos e os implementamos no GEOS-Chem, un programa de simulación atmosférica que inclúe un esquema de microfísica de gran precisión na descripción dos procesos de crecemento dos aerosois. Este modelo é un dos máis completos e accesibles que se poden atopar, ademais de que está elaborado por centos de científicos arredor do mundo. Isto fai que sexa un dos más actualizados e complexos de seu campo. En concreto, GEOS-Chem é un modelo deseñado para o transporte químico tridimensional que permite realizar simulacións da composición atmosférica a unha escala global ou rexional. Ademais, pódese acoplar con outros modelos climáticos ou meteorolóxicos, como pode ser o modelo WRF (un dos máis utilizados no mundo para a predición rexional a curto prazo). Outra das características máis salientables é que xa ten implementado o efecto dos ións xerados pola radiación cósmica na atmosfera no proceso de nucleación dos aerosois. A nucleación é unha das fontes máis importantes de partículas atmosféricas e consiste na agregación de pequenos conglomerados moleculares dende a fase gaseosa e sábese que este proceso pode ser estimulado pola presenza de ións. Neste caso, o modelo GEOS-Chem conta cunha parametrización da nucleación que depende de varios parámetros entre os que están a taxa de ionización atmosférica.

A nucleación e un proceso que involucra ás partículas máis miúdas, pola súa contra, a condensación e coagulación son os procesos responsables de que os pequenos grupos de partículas medren a tamaños superiores. Se temos en conta a presenza dos ións atmosféricos, estes condensan sobre os aerosois proporcionándolle carga. Deste xeito, os aerosois poden acumular un variado número de cargas na súa superficie. Como consecuencia, esta distribución de cargas nos aerosois vai afectar ao proceso de coagulación, posto que se dous aerosois que colisionan teñen cargas de idéntico signo, aparecerá unha forza de repulsión que inhibirá a súa unión. Pola contra, se os aerosois transportan cargas de signo contrario, a súa coagulación estará máis favorecida. Deste xeito, resulta relevante incorporar a distribución de cargas no modelo. Non obstante, introducir de xeito explícito a distribución de carga das partículas é moi complexo e faría que o cómputo fose extremadamente lento. Isto débese a que o modelo divide a distribución de tamaño dos aerosois en corenta *bins* e para cada un resolve un par de ecuacións en cada paso de tempo, unha que calcula o número de aerosois no bin e outra que calcula a súa masa. Así que o modelo ten que resolver oitenta ecuacións en cada paso de tempo e en cada punto do espazo (ou malla espacial do modelo). Se supoñemos que as partículas só poden transportar una carga negativa ou positiva, isto significaría ter que triplicar os *bins* para que tamén se teña en conta a carga destas partículas en cada momento e poder calcular mellor a coagulación. Polo tanto, o número de ecuacións a resolver aumentaría considerablemente e retardaría moito os cálculos. Pero a realidade resulta aínda máis complexa posto que as partículas poden transportar máis dunha carga (de feito poden chegar a ser máis de 100 cargas) e nesta situación o número de ecuacións a resolver sería inmenso. Por sorte, existen técnicas que permiten aproximar o número de cargas mediante unha función que depende de certos parámetros, como o tamaño da partícula, e que fai que xa non sexa necesario a implementación

explícita de todos os *bins* de carga. Ademais, tamén permite acelerar a velocidade de cómputo.

O noso obxectivo consite en implementar o cálculo das cargas e o seu efecto na coagulación para ver como a ionización afecta ao crecemento dos aerosois. Unha vez implementados os cambios oportunos no código, posto que o programa ten como característica a opción de variar a ionización atmosférica inducida polos raios cósmicos para simular un período de actividade solar máxima ou mínimo, corremos simulacións a pares para contrastar os resultados das dúas situacións. A diferenza entre ámbalas dúas daranos información acerca da relevancia do cambio do fluxo de raios cósmicos debido a actividade solar na formación dos aerosois.

Nomenclature and Abbreviations

α_T	Effective Temperature Coefficient
α_{MSS}	Mass-weighted Temperature Coefficient
$\mu^{\pm}$	Muon
$\pi^{\pm}$	Charged Pion
E_{th}	Threshold Energy
R_c	Geomagnetic Cutoff Rigidity
T_{eff}	Effective Temperature
W_T	Temperature Coefficient
CCN	Cloud Condensation Nuclei
CME	Coronal Mass Ejection
CR	Cosmic Rays
EAS	Extensive Air Shower
FD	Forbush Decrease
GCR	Galactic Cosmic Rays
GeV	Gigaelectronvolt
GMDN	Global Muon Detector Network
mwe	meter water equivalent
PCR	Principal Component Regression
RMSE	Root-mean-square Error
RPC	Resistive Plate Chamber
SSW	Sudden Stratospheric Warming
UHECR	Ultra-high-energy cosmic ray

List of Figures

List of Tables

List of Publications

The following list indicates the publications derived from this research that were used to create this thesis. I declare that I am the main author of all these publications, I am properly authorized to use these articles in this context, and they were not used in any other theses. I also declare that there is a non-doctoral co-author (D.G.C.) who participated in the first publication.

- I. Riádigos, D. García-Castro, D. Gonzáles-Díaz, and V. Pérez-Muñuzuri. Atmospheric temperature effect in secondary cosmic rays observed with a 2 m^2 ground-based tRPC detector. *Earth and Space Science*, 7(9), p. e2020EA001131, 2020
  Impact Factor (JCR): 2.900 (2020)
  Quartile (JCR): Q2 (Geosciences, Multidisciplinary)

- I. Riádigos, D. González-Díaz, and V. Pérez-Muñuzuri. Revisting the limits of atmospheric temperature retrieval from cosmic-rays measurements. *Earth and Space Science*, 9, e2021EA001982, 2022.
  Impact Factor (JCR): 2.900 (2020)
  Quartile (JCR): Q2 (Geosciences, Multidisciplinary)

- I. Riádigos et al. The charge on aerosols from Cosmic Rays and the enhancement of cloud condensation nuclei formation. *In preparation*, 2022.

My contribution to both published publications included the analysis, design, code implementation, development of the methodology, generation of plots and tables, and writing of the original drafts. Co-author D.G.C. was responsible for the correction and preparation of the data as well as the part of the barometric effect analysis reported in the first publication.

Chapter 2 and 4 of this thesis are based on the results of the first and second articles, respectively. These articles are open access with permissions to be used in this thesis. The uses-permission for all the results taken, modified, or derived from these publications can be verified under the following link: `https://agupubs.onlinelibrary.wiley.com/hub/journal/23335084/open-access.html`. These permissions are included in order to avoid any legal issues related to plagiarism or self-plagiarism.

The next list indicates other publications derived from the thesis research, but they were not included as part of the manuscript:

Proceedings

- J. A. Garzón, J. Collazo, J. Cuenca-García, D. Castro, J. Otero, M. Yermo, J. J. Blanco, T. Kurtukian, A. Morozova, M. A. Pais, A. Blanco, P. Fonte, L. Lopes, G. Kornakov,

H. Álvarez-Pol, P. Cabanelas, A. Pazos, M. Seco, I. Riádigos, V. Pérez-Muñuzuri, A. Gómez-Tato, J. C. Mouriño, P. Rey and J. Taboada. TRAGALDABAS. First results on cosmic ray studies and their relation with the solar activity, the Earth magnetic field and the atmospheric properties. *Proc. of the XXV European Cosmic Ray Symposium 2016*, arXiv preprint arXiv:1701.07277. 2017.

- I. Riádigos. Analysis of the atmospheric effect on the TRAGALDABAS high resolution Cosmic Ray detector. *Proc. of the 36th International Cosmic Ray Conference (ICRC2019)*, Vol. 36, p. 132, 2019.

Motivation and Objectives

Cosmic Rays. The first time one hears these words they may sound fanciful or even seem like something out of science fiction, but nothing could be further from the truth. Cosmic rays or cosmic radiation is what it sounds like: radiation from outer space. We usually tend to assume that the biggest mysteries of the Universe are unattainable and way out there, far away from us. However, this is not always the reality, and the great unkowns may be closer than we imagine. Just like hidden phantoms, they surround us, permeate us, and we cannot even manage to see or perceive a hint of them. Cosmic rays are one of those mysteries. Certainly, I am not referring to anything mystical or metaphysical. They are tiny chunks of atoms, invisible to our eyes and yet they can be found everywhere. They pose a mystery because scientists still do not know with certainty their origin.

It is somewhat difficult to try to explain something that we cannot see with our own eyes. In ancient Greece, they already suspected that matter had to be composed of small elements, however, it was not until the 19th century that we were actually able to experiment and recognize the first atoms. Later, at the beginning of the last century, cosmic rays were discovered. Nowadays, because of the progress of science, we understand almost everything about them: what they are, what they look like and how to observe them. Although, as we have already pointed out, there are still some open questions about some aspects of their origin, some of them linked to the largest, most violent and bizarre phenomena in the cosmos, such as black holes. Anyways, this thesis does not pretend to solve any great mystery rather than finding innovative ways to research the everyday, and maintaining that connection between the science of the great and the mundane. For example, it is funny to realize that if Einstein's theory of special relativity were not true, this thesis could not have been done or, at least, its conclusions would be radically different.

A lot of fancy things can be done with cosmic rays and that is why their study is becoming a research field of great interest in many areas: space weather, high-energy physics or tomography, to mention a few. One of our main motivations for the study of cosmic rays arises from the discovery that the variations of the temperature of the atmosphere are strongly correlated with cosmic-ray variations measured at the Earth's surface or underground [24]. Patrick Blackett was the responsible for this discovery and was awarded the Nobel Prize for Physics in 1948. This finding was corroborated by several experiments carried out after this relation was found. In particular, the MACRO and MINOS experiments located deep undergound reported strong correlations between high-energy cosmic-ray fluxes and seasonal variations of upper atmospheric or stratospheric temperatures [10, 6]. Another important experiment which has served as inspiration for this work is the IceCube located at the South Pole (2010) [154]. Not only did it demonstrated the correlation between the upper atmosphere and high-energy muons, but it also observed that low-energy cosmic rays measured at the surface are negatively correlated with the temperature of the lower layers of the stratosphere. Furthermore,

it could correlate cosmic-ray fluxes with the long- and short-therm variations of the South Pole atmosphere.

In view of the above, it is attractive to study the feasibility of developing an alternative technique for the measurement of meteorological conditions through the detection of cosmic-ray variations, and explore its intrinsic limits. These results lead to the possibility of using cosmic-ray detectors for meteorological applications. Despite extensive research on the relationships between atmospheric conditions and cosmic rates, most experiments focus on their characterization for subsequent removal from the measurements since they are more interested in investigating other physical phenomena not related to the atmosphere, for example the Global Muon Detector Network (GMDN) that specializes in the study of space weather [133].

Moreover, the experiments described require, very frequently, large, complex and expensive infrastructures for cosmic-ray detection: in mines, under the ice of Antarctica, etc. This motivated us to wonder if we would be able to obtain similar or better results with smaller detectors carefully designed for atmospheric studies. In addition, since we had seen that cosmic rays of different energies are affected by different layers of the atmosphere, we asked ourselves whether a detector capable of discriminating different cosmic-ray populations would be able to obtain the temperature for different layers of the atmosphere.

The recent development of small, high-resolution and affordable detectors with higher accuracy has opened the door to further investigate the aforementioned possibility [109, 124, 173]. In our case, a 2×2 m^2 detector has been deployed at the Faculty of Physics of the University of Santiago de Compostela (Spain), devoted to the measurement of cosmic rays at the surface [26]. With this in mind, our first aim is to evaluate and validate the correlations between the atmospheric temperatures and cosmic-ray data obtained with such a small and high resolution surface detector. The purpose is to determine whether this kind of devices could be used in the future as atmospheric monitoring stations. Following this study, our objective also include establishing from which parts of the atmosphere we can retrieve the temperature, solving what is known as the inverse problem, and determining how this can be better achieved: identifying the required set of observations, the features of the detectors, etc.

As previously mentioned, cosmic rays are always shrouded in mystery. Indeed, there is another intricate question about cosmic rays that is still unsolved: their link with climate change. We first came across this issue when in 2016 the results of the CLOUD experiment at CERN, one of the most important experiments investigating this topic, revealed clues about the effect of cosmic rays on the growth of atmospheric aerosols, which are small particles precursors of cloud droplets [54]. This information was crucial because, believe it or not, we know very little about how clouds form even though we know that they play an important role in the Earth's climate. About two-thirds of our planet are covered by clouds and they can affect climate in several ways. Mainly, cloud cover has a big impact on the temperature of the planet. Clouds reflect sunlight during the day, and at the same time they can prevent surface radiation from being lost to space at night by reflecting it back to Earth. In both situations, the average temperature is caused to decrease or rise, respectivelly. Hence, clouds can have both a cooling or warming effect. Globally, they have a cooling effect but the balance between clouds and climate is quite complex.

There is much uncertainty in climate models when it comes to predicting global temperature rise by the end of the century. One of the reasons is the great uncertainty in several factors, such as cloud formation. Therefore, any small improvement in the understanding could help to significantly improve the accuracy of climate predictions.

Since it is quite challenging to perform experiments to analyze in detail how cosmic rays affect cloud formation, our goal is to introduce these effects into a model of atmospheric chemistry. So far, they have hardly been taken into consideration in the development of such models, one of the reasons being the lack of theoretical and experimental models describing the effect of cosmic ionization on aerosols. However, in recent years, there has been advances in the field that provide the necessary information to include the impact from cosmic rays on cloud formation [54, 149, 168].

Thesis structure

The main topic addressed in this thesis is the interplay between cosmic rays and the atmosphere. We consider cosmic rays both as an object of research as well as a research tool. With this intention, the present work is divided into five chapters accompanied by a general introduction and final conclusions.

Chapter 1 begins by laying out the theoretical foundations of the research, and provides all the essentials needed to properly follow the content of the thesis.

Chapter 2 follows the introductory part and contains experimental work related to one of the main objectives of this thesis. It assesses the variations of cosmic-ray data related to atmospheric effects measured with a 2×2 m^2 4-plane tRPC station (TRAGALDABAS), located at the University of Santiago de Compostela.

Chapter 3 examines and characterizes the limits of atmospheric temperature retrieval from cosmic-ray measurements. This study was performed with simulated cosmic-ray data that made it possible to evaluate different scenarios for solving and optimizing the inverse problem.

Chapter 4 presents the development of a numerical model and the results obtained from simulating the passage of cosmic rays through the atmosphere, using real data of atmospheric profiles as input. This study helps to corroborate the results obtained in **Chapter 2**.

The thesis will then go on to the last topic, the effects of cosmic rays on the atmosphere. Thus, **Chapter 5** covers the analysis of the results obtained with a global 3-D model of atmospheric chemistry, GEOS-Chem. Here, we implement in the model the effects of atmospheric charged particles derived from cosmic-ray ionization that influence aerosol evolution processes.

The last chapter includes the **General Conclusions** that summarize and reflect the final impressions of all the work developed in the thesis. In addition, we add recommendations for future work on the different topics that have been covered.

At the end of the thesis, a series of Appendices are included:

Appendix A contains a detailed explanation of some concepts related to the atmospheric dynamics of the Sudden Stratospheric Warming events.

Appendix B shows information and supplementary calculations that were used in the development of the main chapters.

Finally, **Appendix C** covers some mathematical derivations related to the numerical simulations of air showers.

Chapter 1

INTRODUCTION

Abstract: *This chapter will introduce the main concepts about Cosmic Rays of relevance to the topics addressed in this thesis. As a first step, the most basic notions of this research field will be covered in order to provide the necessary background to go deeper into the subject. This will include a brief overwiew of the historical studies of the relation between cosmic rays and the atmosphere as well as a summary of the state of the art. Finally, specific and technical details concerning the work of this thesis will be presented.*

1.1 What are Cosmic Rays?

In the era of multi-messenger astronomy, the study of the cosmos is no longer constrained by the information gathered solely from visible light. The diverse sources of information include "messengers" such as gravitational waves, neutrinos, all kinds of light, and cosmic rays. Each of these signals coming from the Universe provides powerful information about the most unknown, bizarre, and extreme phenomena. Black holes or neutron stars collisions, for example, are currently attracting the interest of the scientific community. However, cosmic rays can also give us information tailored to a more mundane scale closer to everyday life, as we will see in the following.

Cosmic rays (CR), or cosmic radiation, refer to a collection of high-energy subatomic particles that are constantly raining down upon the Earth's atmosphere. They travel through space at near-light speeds and can have different origins. They can come from the Sun, from different regions of our galaxy, and even from much more distant places such as other galaxies.

Most CR striking the top of the atmosphere comprise charged nuclei, of which roughly 90% are protons, 9% helium (alpha particles), and the remainder includes heavier nuclei and all stable charged particles. Regarding the latter, it is worth mentioning that there is a minor component of antimatter too, for instance, antiprotons and positrons [75].

CR population covers a wide range of energies from nearly their rest mass up to ultra-relativistic energies of 10^{20} eV ($\sim$20 J).[1] This is one hundred billion times more energetic than the rest mass energy of a proton and equivalent to a killer tennis serve.

[1] Within the framework of relativistic physics, a relation is established between the total energy and the momentum plus the rest mass of a particle: $E^2 = (pc)^2 + (m_0c^2)^2$. An ultrarelativistic particle will have all its energy attached to the momentum, such as $E \approx cp \gg m_0c^2$.

The broad range of energies stems from the diverse types of sources that originate CR. For this reason, CR are typically categorized into several groups according to their origin. A small part of them (ranging from few tens of keV to several GeV) are generated in the Sun during periods of intense solar flares or caused by interplanetary phenomena (shock waves) associated with coronal mass ejections. The Galactic Cosmic Rays (GCR) represent the bulk of the spectrum. With energies as high as 10^{16} eV, they are created in supernova explosions, pulsars, double stars, and other objects in the galaxy. However, there are still many open questions about their origins and some aspects remain still unknown [51, 65]. The extragalactic CR are particles with exceptionally high energies (up to 10^{21} eV) and also the least common and enigmatic, they are referred to as ultrahigh-energy cosmic rays (UHECRs). Very little is known about their origins and what mechanism is accelerating them. The reason is the lack of statistics in the observation of this kind of particles. Above 10^{16} eV, the flux of CR drops to below one extragalactic particle per square meter per year. Large detectors would be required to collect a sufficient number of them. In any case, some of the candidates that are being considered to explain their origin are pulsars, neutron stars, gamma-ray bursts and jets from active galactic nuclei, to mention a few [99].

We know that some of the extreme phenomena reported above must be responsible for generating the most energetic particles ever measured here on Earth. In fact, the most powerful particle accelerators in the world have been able to accelerate protons to a record energy of 7 TeV, a far cry from the fastest CR [44]. In conclusion, cosmic radiation can provide us with new insights into the nature of the Universe.

1.1.1 Energy Spectrum

Cosmic rays reaching the top of the atmosphere are called primary cosmic rays. As we will see later, primary cosmic rays interact with the nuclei of the elements that populate the atmosphere, giving rise to a flux of secondary particles, or secondary cosmic rays. The incoming flux of cosmic rays is not constant over time and depends on several factors. On the one hand, the flux of low-energy particles is modulated by the solar wind, i.e., by the solar activity [165]. Some of these variations are connected to the 11-year solar cycle and show a solid anticorrelation with CR flux. The solar wind is a constant flow of plasma (energetic charged particles) released from the Sun. The heliospheric magnetic field is embedded in it and fills the Solar System like some sort of protecting bubble, preventing lower-energy Galactic Cosmic Rays from entering. Therefore, as the strength of the solar wind weakens during periods of minimum solar activity, the flux of GCR increases. Apart from the modulation effect of the solar activity cycle, there are some sporadic moments when the flux of the low-energy region may also change. Spontaneous powerful solar flares or coronal mass ejections are some of the events that can cause changes in cosmic rays with energies between the range of MeV and GeV.

Importantly, the variation of the Earth's magnetic field plays an important role because it deflects the charged particle fraction whithin cosmic rays along their path towards the Earth's surface. The ones with the weakest energy will either be reflected into space or will be trapped in the intricate magnetic field lines, prevented from reaching the ground. In spite of this, if the incident particle has enough energy, it will follow a nearly straight path towards the surface. Hence, the cosmic-ray flux has a dependence on latitude, longitude and zenith angle of observation, which is a consequence of the shape of the Earth's magnetic field. The geomagnetic cutoff rigidity, R_c, is the quantity that defines the rigidity value above which the incoming

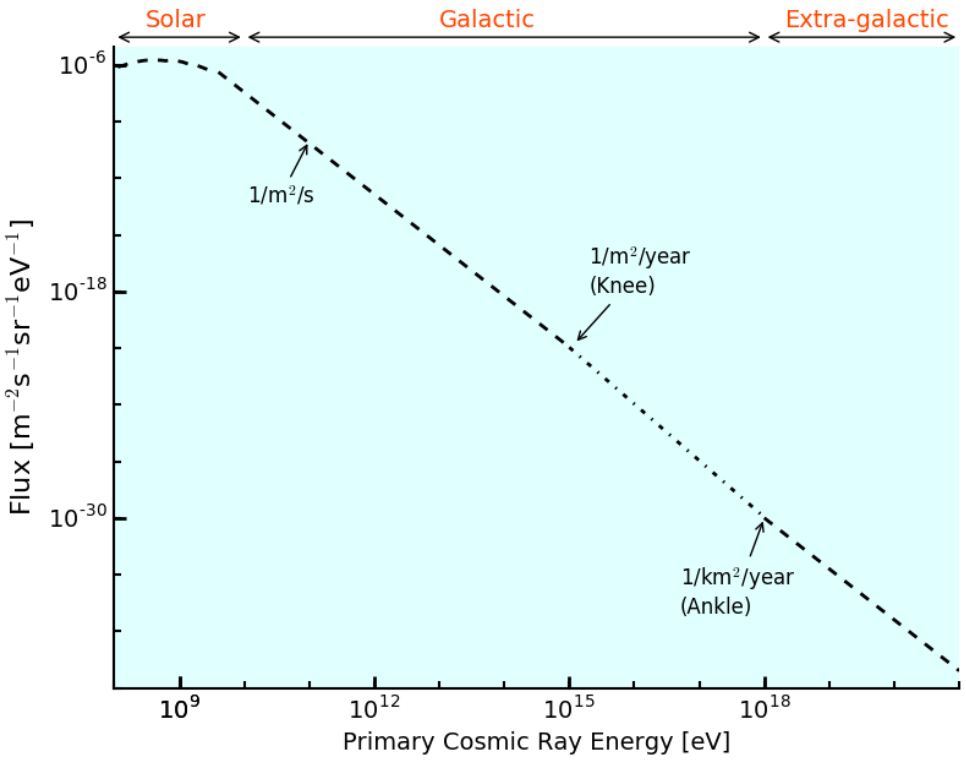

Figure 1.1: The energy spectrum of the primary cosmic radiation.

cosmic-ray particle will have an allowed trajectory. But, it should be noted that this is not a fixed value either, since the magnetosphere also varies with time.

Finally, the GCR intensity also suffers variations due to the change in the rate of supernovae explosions in the solar neighborhood. However, these changes occur on long time scales of millennia and it can be assumed to remain fairly constant in this context.

All these combined effects that have been mentioned above contribute to the total flux of cosmic rays. The intensity of primary cosmic rays as a function of energy is given in Figure 1.1. This energy spectrum features two prominent transition regions where the slope changes. Its shape is so steep that the flux of particles above 100 GeV is much larger than that above 10^{11} GeV by sixteen orders of magnitude. One particle per square meter arrive in a year with energies of 10^{7} GeV. A small detector flown at the top of the atmosphere with an area of 1 m^2 would have to wait one year to measure a particle above that energy.

There is an increment of the slope in the interval between 10^{6} and 10^{7} GeV. This region is generally called the *knee*. It also exhibits a flattening at higher energies above 10^{9} GeV, known as the *ankle*. The origin of these structures is still unclear, but it is assumed to be related to the different mechanisms of generation of cosmic-ray populations. It is suggested that GCR below the *knee* are accelerated in the shock waves of supernova remnants (SNR) [86], while particles between the *knee* and the *ankle* come from different galactic sources, such as pulsars [28]. The most energetic cosmic rays (UHECRs) with an energy greater than 1 EeV are created outside the Galaxy but, as pointed before, with an uncertain origin [22].

The spectra of primary nucleons can be approximated by an inverse power law in energy for the range between several GeV and tens of EeV:

$$I_N \propto E^{-(\gamma+1)} \frac{particles}{m^2\, s\, sr\, GeV} \tag{1.1}$$

where E is the energy and $\gamma \approx 1.7$ is the integral spectral index. It is also very common to define $\alpha = \gamma + 1$ as the differential spectral index. Above the *knee* the spectrum steepens with an index value of $\gamma \sim 2$.

1.2 Cosmic Rays in the Atmosphere

We have previously mentioned that any particle pelting the Earth will encounter the magnetic field, which acts as a natural barrier to the weakest CR. The primary radiation that penetrates this shield is hazardous to organic life forms, and this is one of the reasons why astronauts cannot stay for long periods in outer space. Nevertheless, any particle permeating the magnetic field still has to face the atmosphere, our second natural shield against cosmic radiation.

These primary particles will seldom reach the ground, rather they will interact with an atmospheric nuclei, usually in the upper atmosphere [71]. If the primary cosmic ray has enough energy, its collision will produce a large number of new particles and nuclear fragments, triggering a chain of nuclear interactions that are capable of generating up to billions of secondary particles. As implied by the description itself, these are generally called secondary cosmic rays. All these particles compose what is known as an Extensive Air Shower (EAS) and propagate randomly through the atmosphere until some of them eventually reach the ground. In some cases, they can cover a surface area of several hundred square kilometers. These particles can be measured using sophisticated detectors placed on the ground.

The secondary particles lose energy due to interactions as they move downwards in the atmosphere. At the first stage of the cascade, the number of particles increases dramatically, reaching a maximum at a height of about $\sim$20 km (called *Pfotzer maximum*) [18]. However, the daughter particles will have less energy than their predecessors by conservation of energy. Eventually, they will not be capable of generating new particles and will be absorbed along the way. As a result, only a small fraction of the total amount of particles generated will arrive at the surface. In addition, the number of secondary cosmic rays that are produced in a shower will depend on the available energy of the primary cosmic ray. The more energy it has, the more particles can be created. Considering the energy spectrum of primary CR, those which have the capacity of yielding bigger air showers are the most energetic but also the scarcest ones. Low-energy CR (below a few GeV) will barely have enough energy to initiate a cascade. Regardless of this, it must be kept in mind that the Earth is constantly being hit by lots of CR, and even though only a small part of the secondary particles reach the ground, they are enough to produce a flux of ten particles per second passing through a surface the size of a hand. The secondary component of CR is a part of the natural radioactivity present in the environment in which we live.

As can be seen in Figure 1.2, different kinds of interactions occur in a cascade that result in the creation of all types of subatomic particles: muons, pions, kaons, neutrinos, neutrons, electrons, positrons, or gamma rays. After the first collision of the primary CR (usually a proton) with an air nucleus, a lot of mesons are produced. In particle physics, mesons refer to a category of subatomic particles which are distinguished by being composed of a quark and an antiquark. Baryons are the other category that encompasses heavier particles formed by quark

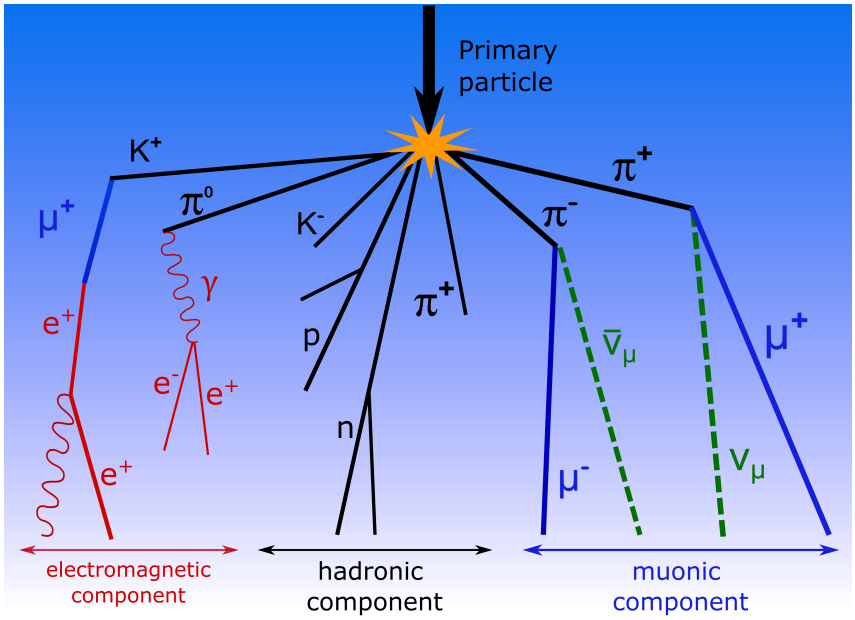

Figure 1.2: Illustration of an atmospheric air shower initiated by a primary cosmic-ray particle interacting with an atmospheric nucleus. The cascade of secondary particles is divided into the muonic component (blue), the hadronic component (black), the electromagnetic component (red), and the neutrino component (green), undetectable for practical purposes.

triplets, such as the well-known protons and neutrons. Baryons and mesons are both hadrons, the family that includes any particle composed of quarks.

Returning to the formation of the air shower, we had mentioned before that in the first interaction a lot of mesons are produced, namely the so-called pions. In addition, kaons (another type of meson, having a "strange" quark inside it) and other baryons can also be created. Pions and kaons are not stable and they are susceptible to decay into other particles rather than interact. Charged pions ($\pi^{\pm}$) decay into elementary particles called muons ($\mu^{\pm}$) and neutrinos (ν). However, mesons that live longer also have the probability to collide with another atmospheric nucleus before decaying and produce a bunch of new particles.

The neutral pions (π^0) have a very short lifetime as well and tend to decay rapidly into gamma rays. The latter may in turn create electron-positron pairs through interaction with the field of a nucleus. At the same time, electrons and positrons may produce more gamma rays through bremsstrahlung radiation in the field of a nucleus too. Muons from the hadronic component of the CR shower, which are produced mainly by pions and kaons, are far less interacting and can decay to electrons and positrons [75]. All these phenomena give raise to the so-called electromagnetic component of a CR shower. Table 1.1 summarizes the most relevant particle processes in an air shower.

Therefore, it is clear that an air shower is composed of a great variety of particles resulting from the multiple interactions that take place as the cascade develops. For a complete picture, the flux of secondary cosmic rays in the atmosphere is typically divided into three components:

- Hadronic component: including protons, neutrons, pions, kaons...
- Electromagnetic component: consisting of gamma rays, electrons and positrons.
- Muonic component: muons.

Interactions	Decays
$p+A \rightarrow p+n+\pi^0+\pi^{\pm}+...$	$\pi^+ \rightarrow \mu^+ + \nu_\mu$
	$\pi^- \rightarrow \mu^- + \bar{\nu}_\mu$
	$\pi^0 \rightarrow \gamma+\gamma$
$\pi^{\pm}+A \rightarrow \pi^0+\pi^{\pm}+...$	$\mu^+ \rightarrow e^+ + \nu_e + \bar{\nu}_\mu$
	$\mu^- \rightarrow e^- + \bar{\nu}_e + \nu_\mu$
	$\gamma \rightarrow e^- + e^+$

Table 1.1: Most relevant particle processes in a cosmic ray air shower.

One of the most relevant components is the one that refers to muons since they represent the largest number of charged particles that reach the Earth's surface. In fact, the muonic component will cover most of the scope of this dissertation.

Figure 1.3 shows some examples of atmospheric air showers obtained using CORSIKA (a Monte Carlo program employed to simulate air showers [57]). The cascades are created by protons of different incident energies: 10 TeV (Fig. 1.3a) and 100 GeV (Fig. 1.3b). It can be seen from the illustrations that the primary cosmic ray with the highest energy is capable of generating much more particles that also cover a wider area when they reach the surface. In addition, it has its first interaction at a height of ∼15 km, whereas the less energetic proton interacts at a much lower altitude (∼8 km).

1.2.1 Muons

Most muons are produced in the upper atmosphere at an altitude of about ∼15 km. Compared to their relatives, they are much heavier particles: muons have a mass of 105.7

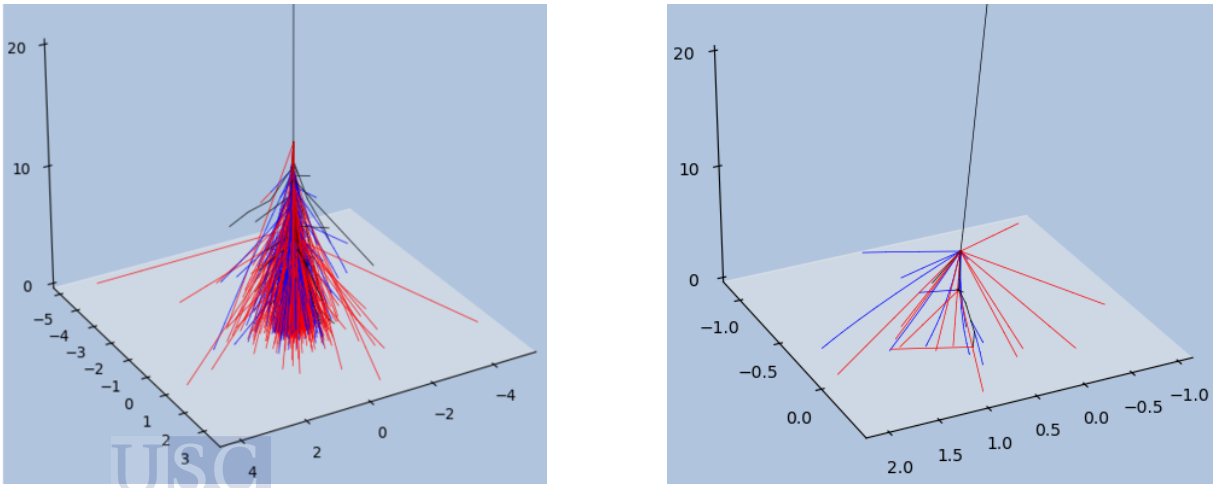

(a) 10 TeV **(b)** 100 GeV

Figure 1.3: 3D development of air showers triggered in the atmosphere by different incident protons. The *XYZ* coordinates are given in km. The lines represent the trajectories of muons (blue), hadron particles (black), and gamma rays and electrons/positrons conforming the electromagnetic component (red). The showers were simulated using the Corsika software [57].

MeV/c^2, which is approximately 200 times greater than that of the electron ($m_e = 0.511$ MeV/c^2) [75]. Muons are very weakly interacting particles and lose energy by primarily emitting bremsstrahlung radiation as they travel through the atmosphere. This radiation, composed of photons, is produced when a charged particle is deflected by another charged particle, such as an atmospheric nucleus. The amount of energy emitted here is inversely related to the mass of the particle, which accounts for why muons can penetrate far deeper into matter than electrons. By way of illustration, the mean energy of muons created at the site of production is 6 GeV and they lose about 2 GeV before reaching the ground.

Muons are relativistic particles moving at nearly the speed of light ($\sim$ 0.999c) and also feature a very short mean lifetime, $\tau = 2 \times 10^{-6}$ s. From a classical point of view (distance traveled equals speed multiplied by time), a muon produced at a height of 10 km would only travel 600 m before decaying, implying that muons would never reach the surface. In contrast, it is observed that they do. Then, what is misunderstood? The answer is that relativistc effects have not been taken into consideration. Time dilation, which is involved in those cases, requires the Lorentz factor ($\Gamma \equiv 1/\sqrt{1-\beta^2}$, where $\beta = \upsilon/c$ is the particle velocity relative to the speed of light) to be considered. It indicates how much the temporal characteristics of an object that is moving (in particular its lifetime) change for an independent observer, especially at very high speeds. This factor will have a value close to one for classical speeds but becomes higher than one for relativistic scenarios. For those special cases, which include muon movement through the atmosphere, time dilation makes its mean lifetime to be larger, 1.4×10^{-4} s for the example discussed (muon with an energy of 6 GeV), and therefore the distance traveled would be 42 km instead (relativistic effect in length is $l = \Gamma\beta c\tau$). This allows them to reach the surface before decaying and even go deep underground.

To conclude, muons rain down on every single square centimeter of the Earth's surface and their average energy at the ground is $\sim$4 GeV [142]. Their penetrating power makes them a suitable tool for imaging dense and large materials without causing any damage to them. As muons travel through objects, they are absorbed in different amounts depending on the density of the material and the energy of the incident particles. Scientists can compare the flux measured after traversing the obstacle with that expected without it, to reconstruct the inner density ("muon imaging" or muography) [30]. This property has made it possible for muons to be used in different research areas to carry out the most astonishing discoveries. In 2017, a group of archeologists discovered a hidden chamber in Egypt's Great Pyramid by scanning its interior with the help of cosmic muons passing through it [116]. Furthermore, this technique has also been employed in the area of volcanology to reveal the density profile of a volcano to foresee how an eruption could develop [153].

We will see later how this technique can also be applied to retrieve information from the atmosphere.

1.3 Cosmic Ray Measurements

There are different methods for cosmic-ray detection that depend mainly on the component to be studied as well as the part of the spectrum (i.e., range of energies) to be covered. On the one hand, direct detection of primary cosmic rays is possible thanks to particle detectors placed on orbiting spacecrafts or the International Space Station. Along with it, balloon-borne instruments reaching high altitudes are launched for the same purpose. However, this kind of detection only allows measurements of low-energy primary CR.

Balloons can also be deployed to register the secondary radiation as a function of altitude as they rise in the atmosphere. Aircraft can be considered for these cases as well. On the other hand, there are several ground-based techniques to measure secondary CR.

Firstly, neutron monitors are widely used to monitor variations of neutron rates in the energy range between 500 MeV and 20 GeV [145]. A standard neutron monitor consists of a set of counter tubes made of several layers of materials. The outer layer protects the measurements from external sources of noise and allows neutrons from the cascade to pass through. The incident neutron generates additional neutrons via nuclear interactions in the following layer made of lead. Eventually, when they reach the innermost layer, they can be captured by the nuclei of the gas that fills it, emitting other particles that are easier to detect and transform into electrical pulses. This kind of detector is typically used in astrophysics to monitor the Sun's activity [115]. In this regard, it is a kind of indirect detection of primary CR. Neutron detectors are also used in the field of hydrology to measure the soil water content over wide areas or reveal mountain snowpacks [45, 95, 90, 105].

Another type of detector most frequently used is that which measures muons. There are plenty of different techniques to detect them and the equipment employed is usually very diverse in design and performance. The most basic detectors may consist of ionization chambers or scintillation counters. In the first case, the particles that enter the detector ionize the gas inside it, creating charges that are collected using an electric field. In the second case, a scintillating material that emits photons in response to ionizing radiation is used. The released photons are then converted into electrons via the photoelectric effect, then they are accelerated to strike a series of dynodes that yield more electrons, and so amplifying the initial signal. The resultant output is a pulse proportional to the energy of the traversing particle [162].

The detectors mentioned above are very versatile but they only measure the integrated flux of CR coming from all directions. Anyhow, better performance can be achieved by installing several of these devices in specific layouts. Muon telescopes assemblies involve several detectors (scintillators for instance) positioned along a straight line from smallest to largest thickness. Identification of the type of particle (i.e., its mass and charge) is possible by measuring the energy deposited in each detector. Such detectors are usually rigid structures that can be rotated in the zenith and azimuth directions. Moreover, depending on the detector layout, they require the particle to have a minimum energy (i.e. threshold energy) to be able to pass through the entire detector assembly and be recorded [52].

Multi-directional telescopes are a more attractive alternative that include angular resolution and allow measurements of CR from different directions (e.g., [14]). Generally, the system configuration consists of two arrays of detectors, one on top of the other. Figure 1.4a shows an example of a multi-directional telescope. This type of layout enables the identification of particle trajectories (tracking) by means of signal coincidences. When a particle hits two detectors in each of the layers within a coincidence window of a few nanoseconds, a signal is assigned to the particle that has crossed them. In CR experiments, the particles involved are relativistic, and hence the required time window to establish a coincidence between a couple of detectors spaced by tens of centimeters will be a few nanoseconds. As the window increases, so does the probability of random coincidences, as well as the possibility of several interesting events occurring inside the same window and being missed.

To sum up, when a coincidence is recorded, the trajectory of the particle can be determined. The number of detection directions is constrained by the geometry of the setup and the angular resolution relies both on the size of the individual detectors that compose the arrays and the

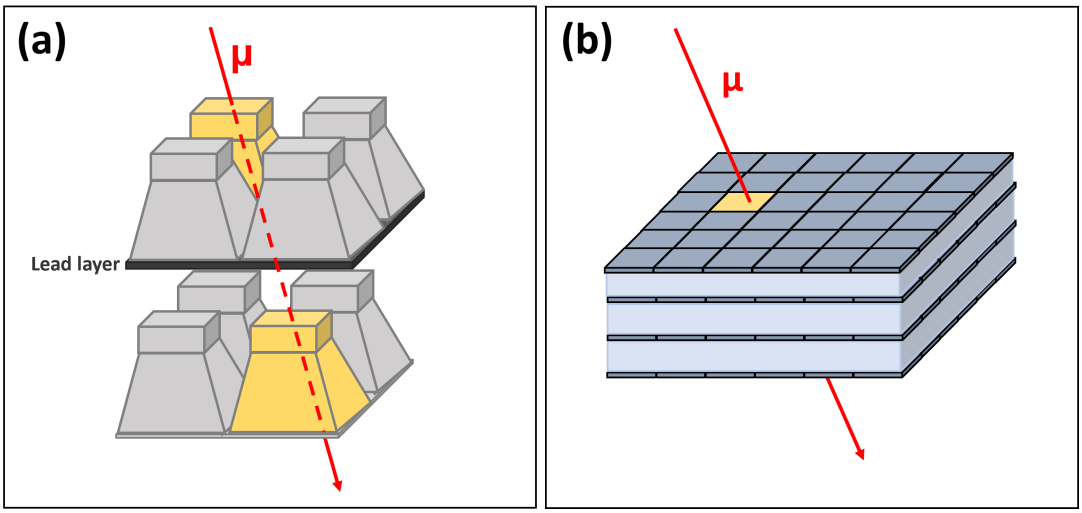

Figure 1.4: Scheme comparing a multi-directional muon telescope with a muon hodoscope. (a) A simple multi-directional telescope assembling formed by two horizontal layers, each one with 4 individual scintillator detectors. A lead layer is located below the upper layer to absorb low-energy brackground radiation. The estimation of the direction of the incident particle is quite limited by the detector configuration. (b) Hodoscope consisting of 4 layers, each one with an array of 6×6 individual detectors. The particle track can be estimated with high accuracy from the number of individual detectors that are hit when the particle crosses the 4 planes.

distance between layers. In this context, detection directions are fixed and the threshold energy of such telescopes is a function of the zenith angle since the particles' path increases with it. On the other hand, traditional telescopes do not have counting rates sufficiently high and tend to have large sizes in order to retain measurement statistics.

Muon hodoscopes took the next step in the development of CR detectors by improving the accuracy and resolution of tracking particles with new approaches. One of the main features of hodoscopes is that they can track charged particles from virtually any direction of the upper hemisphere. This provides a continuous measurement of the angular distribution of the particle flux. The arrangement of a muon hodoscope consists of arrays of many segments (i.e. detectors) located at two or more parallel planes. A track can be inferred from the number of segments that light up a signal (trigger) when they are hit by a particle as it passes through the planes. Obviously, the spatial resolution of these detectors is limited by the segment size. Figure 1.4b illustrates the layout of a muon hodoscope.

An example of an hodoscope is URAGAN, which operates at the National Research Nuclear University in Moscow. This detector is the first large area muon hodoscope in the world and is made of four independent modules. Each of them is an assembly of eight planes of small discharge tubes equipped with a two-coordinate system of external readout plates (strips). Every layer contains 320 tubes and the total area covered is 3.5×3.5 m^2. The system detection requires the coincidence of signals from at least four of the strips of the detection planes within a time window of 250 ns. In addition, the range of threshold energies goes from 0.2 to 0.6 GeV. With all these features, URAGAN allows high accuracy measurements of the surface muon distribution [16].

In general, the detectors mentioned so far are suitable to study secondary cosmic-ray fluxes at the surface and at low energies. We have previously remarked in Section 1.1.1 that high-energy CR are far rarer and their arrival rate per square kilometer is very low. For this reason, a detector of a gigantic area would be needed to measure at least one of those energetic

particles. The assembly of such a device would be nonsensical. Fortunately, there are other ingenious ways to detect these cosmic rays.

The study of CR in the high-energy region can only be made in practice by observing the air showers that they produce. As the secondary particles pass through the atmosphere, their interaction with the atmospheric molecules produces different kinds of radiation. On the one hand, they excite the gas molecules, mostly nitrogen, resulting in the emission of visible and ultraviolet radiation. The fluorescence light is produced isotropically and can travel several kilometers through the atmosphere to be detected by an optical telescope (fluorescence detectors) [1].

On the other hand, electrons and positrons travel faster than the speed of light in air and hence emit Cherenkov radiation that is measured by the so-called Cherenkov telescopes. This kind of detector comprises a large segmented mirror that concentrates the Cherenkov radiation it receives towards an array of photomultiplier tubes. Apart from this, electrons and positrons can also emit electromagnetic radiation with frequencies of tens of MHz, one of the reasons being their interaction with the Earth's magnetic field (synchrotron radiation). These radio signals are pointed sharply downwards relative to the shower development and can be recorded locating antennas at the ground level [89].

Finally, another method to detect the secondary products of highly energetic CR is to deploy big arrays of surface detectors over a wide area ($\sim$100 km^2). Such arrays can observe a vast part of the celestial hemisphere. And what's more, they are often built as hybrid observatories, incorporating other types of complementary detectors (e.g. Cherenkov telescopes and fluorescence detectors) to carry out a more complete study of the cascades. The surface array samples the distribution of charged particles at the ground, whereas the other kind of telescope supplies simultaneous measurements of the longitudinal development and lateral distribution of particles (i.e., particle density over a plane normal to the shower axis). This combination of measurements gives very valuable information about the primary cosmic ray, making it possible to reconstruct its energy, mass composition, and direction of arrival, for example.

One of the biggest array experiments for the detection of UHECR is the Pierre Auger Observatory in Argentina. It is located in the vast plain of Pampa Amarilla in Mendoza Province and its array of surface detectors currently consists of more than 1600 water tanks distributed over an area of 3000 km^2 (about 30 times the size of Paris) accompanied by 27 fluorescence detectors. It was designed for a high statistics study of UHECR and retrieve both their energy and arrival direction. It has been taking data since 2004 [104].

Another interesting example of a big array is the IceCube Neutrino Observatory constructed in Antarctica. The experiment counts with thousands of sensors placed deep in the ice and distributed over a cubic kilometer. The set of detectors can be found at depths between 1450 and 2450 m, and they are based on photomultiplier technology. The observatory also includes the IceTop, a surface array with $\sim$ 162 tanks of ice to measure showers of secondary particles. Its construction began in 2005 and, since then, it has been continuously incorporating new improvements [64].

The Antarctic observatory is committed to the search for neutrinos, which are nearly massless particles quite challenging to detect. The most energetic population of these particles originates from the most violent astrophysical sources: gamma-ray bursts, black holes, and neutron stars. Therefore, their study provides information for surveying these fascinating astrophysical phenomena.

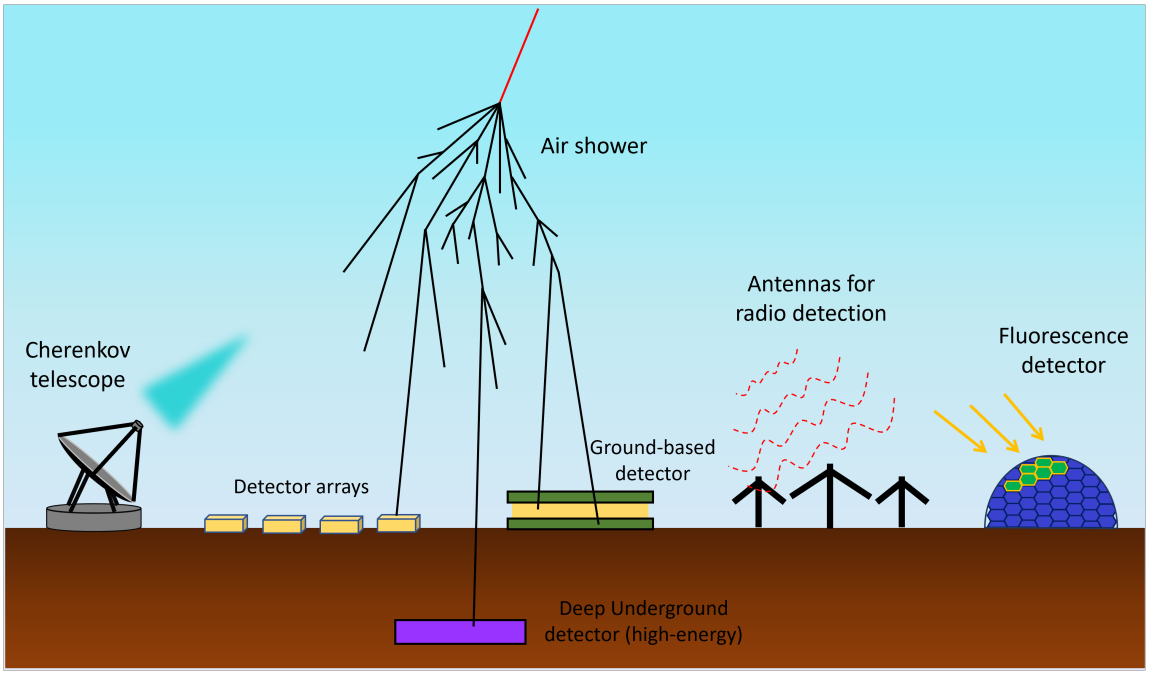

Figure 1.5: Simplified diagram of cosmic ray showers detection techniques. Muons or neutrons are measured with ground-based particle detectors; the electromagnetic component is measured with another kind of detectors by means of Cherenkov and fluorescence light, or antennas for the radio pulses; deep underground detectors are devoted to high-energy muons measurements; big arrays cover wide areas to study extensive air showers from ultrahigh-energy cosmic rays.

The challenge of neutrino detection is that they seldom interact with matter. Nevertheless, when they do interact with the water molecules in the ice, several particles such as muons or electrons are created. These charged particles leave a characteristic signal as they pass through the ice that can be recorded by the sensors.

In the same fashion, CR can be studied underground. Hadrons, electrons, and gamma-rays are immediately absorbed by the rock when they reach the ground level given that it is denser than atmospheric air. Contrarily, high-energy muons can penetrate deep underground and be detected at great depths. Considering the energy loss processes of the muon passage through matter (ionization of the medium, bremsstrahlung, etc.), the minimum energy required for a muon at the surface to reach a certain depth X can be estimated with the following equation [65]:

$$E_{th} = \varepsilon \left(e^{X/\xi} - 1 \right) \tag{1.2}$$

where ε defines a critical energy that equals 500 GeV for muons in rock and $\xi \approx 2.5 \cdot 10^5 \text{g/cm}^2$.

Therefore, if we are interested in studying muons with energies above a specific threshold, the best way to do it is to place an underground detector at the corresponding depth. An alternative approach would be to incorporate a lead shield of a predetermined thickness in a surface detector that only allows higher energy muons to pass through. Clearly, this technique is only feasible for low threshold energies, since higher energies require a greater thickness of lead.

Some of the most relevant underground experiments are located at depths greater than 250 m. MINOS is an experiment at the Soudan Underground Mine State Park in Minnesota

(USA). Its far detector is located 0.72 km underground and, for this reason, detects muons with energy at the surface above 0.73 TeV [5]. MACRO is another particle physics detector at the Gran Sasso Laboratory in Italy and is covered by 1400 m of rock. It measures muons in the energy range between 1 and 20 TeV, which depend on the topographical profile [8].

To sum up, Figure 1.5 provides a sketch summarizing some of the secondary cosmic ray detection techniques mentioned so far.

1.3.1 RPC detectors

Resistive Plate Chambers (RPC) based detectors offer another option to measure secondary radiation. They are addressed in forthcoming chapters of the present work, so a more detailed description feels mandatory. RPCs are low-cost detectors with good spatial and temporal resolution. An RPC is basically a small gas chamber sandwiched between two parallel plate electrodes made of a high resistivity material, where one acts as the anode and the other as the cathode. The charges in the plates cause a high voltage and thus an electric field inside the chamber (or gas gap) [136, 34].

When a charged particle passes through the chamber interacts with the gas atoms causing ionization and releasing the external electrons of the molecules that generate clusters of electron-ion pairs. The number of electrons included in each cluster depends on the energy transferred during the collision by the incident particle. The resulting electrons and ions drift towards the anode or cathode, depending on their charge. The particles are accelerated by the electric field along their path acquiring enough energy to ionize more gas atoms. As a consequence, an avalanche of electrons is generated. The signal produced by the electrons is picked up by the electrodes often routed to the amplifying electronics through metallic strips [132].

Similar to the aforementioned hodoscope configuration, the RPCs employ readout strips placed along the cell on both faces, positioned perpendicular to each other to register the $x-$ and y-coordinate of the incident particle. The strips cover the outer part of the electrodes, whilst the inner face has a layer of graphite paint where the high voltage is applied. The resistive material of the electrodes is usually glass or bakelite. Figure 1.6 shows a sketch of an RPC detector with an avalanche being produced in the gas gap.

The efficiency of this kind of technology depends essentially on the number of primary ionization clusters created in the gas. Since the primary ionization is a random process following Poisson statistics, the efficiency of an RPC relies on the fraction of signals that is produced close enough to the cathode to produce a detectable signal. An efficient RPC must be able to produce a signal that is detectable, and the strongest signals take place when the first ionizations occur in the vicinity of the cathode. As RPC gaps become smaller also the number of effective electron-ion clusters does, however they are capable of sustaining higher fields, thus leading to better time resolutions.

RPCs have been intensively developed at CERN for the large hadron collider (LHC). The conventional RPC involved a 2 mm gas gap filled with a mixture of freon, argon and isobutane. However, the demand for RPC with improved temporal resolutions spawned the development of multi-gap RPCs [185]. The objective was to keep good timings, characteristic of narrow-gap RPCs, with the fundamental virtues of a wide gas gap. Regarding this reduction of the gap width, the applied electric field can be greater in such case, and thus the ionization rate is much faster, which implies a faster signal response. The first proposed multi-gap configuration

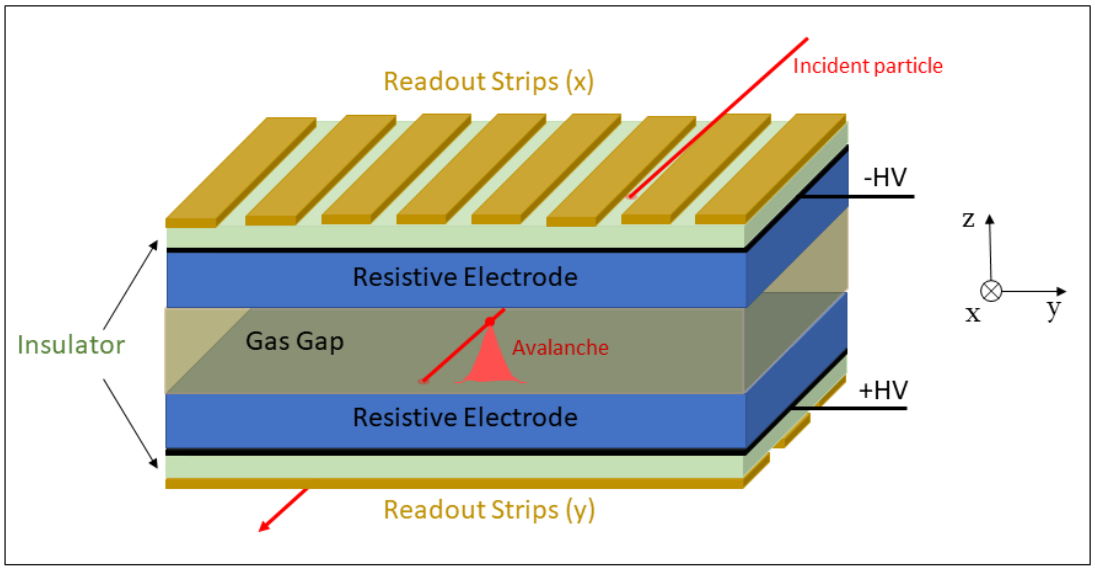

Figure 1.6: Principal scheme of a typical single gap RPC and the formation process of an avalanche produced by a charged particle traversing the detector.

included three gaps of 3 mm replacing a single 9 mm gap. More gaps increase the total gap thickness of the detector and the number of primary clusters generated. In such a case, the particle entering the detector will produce an ionization at least in one of the gas gaps and a stronger signal could be obtained combining the avalanches generated in each of the gaps. In other words, when an individual signal is not able to overcome a detection threshold, the combined signal can. This methodology makes it possible to obtain efficiencies close to 100 % and time resolutions of hundreds of picoseconds.

Although the design of the detector may seem simple, the physics in multi-gap RPCs is far more complicated. When the avalanches develop and start to become too large, the big aggregation of electrons will cause a significant local field, whose magnitude can be as high as the applied electric field but having the opposite direction. As a result, the cascade will eventually saturate destabilizing the normal avalanche growth and leading to undesired high order phenomena, dubbed "streamers". This effect can be prevented by reducing the applied electric field that might render the detector inefficient, the time resolution insufficient or both. A much more attractive method is that of including electronegative gases such as SF6 (sulfur hexafluoride) in the gas mixture, which absorb some of the electrons generated and limit the amount of free charge in the gas, allowing stable operation deep into the space-charge region. In the multi-gap configuration, the high voltage is only applied to the external resistive plates, while the intermediate ones are electrically floating. To separate the high voltage electrodes from the readout electrodes, a thin insulating sheet is added. More information about multi-gap RPCs and their performance can be found in [43] and [61].

Timing RPC (tRPC)

With the improvements mentioned above, new applications for RPCs were developed. The Time-of-Flight (TOF) technique employed with other detectors to identify particle types could now be applied using RPCs. This approach allows determining the velocity of the incident charged particle by recording the time needed to travel (flight) from one detector to another.

If the momentum of the particles is known, particles with different masses but with the same momentum will have different TOFs, allowing to extract their mass and thus their nature. The TOF technique required high timing accuracy at a quite reduced cost and RPCs proved to be the perfect candidates. Some of the underlying reasons for this choice are that they are relatively simple in structure, made of commercially available materials, and meet the necessary technical requirements [62].

Timing RPCs (tRPCs) are used in several experiments at CERN and elsewhere, for instance at GSI Helmholtz Centre for Heavy Ion Research in the HADES experiment (High Acceptance Di-Electron Spectrometer) [125]). HADES has been designed to investigate the nuclear matter at high pressures to shed light on the properties of particles constituents. Its TOF walls covers an area of 8 m^2. The time it takes for a particle to travel from the diamond detector placed directly in the beam to the TOF wall is recorded to calculate the particle's velocity. At the same time, the momentum is measured using a superconducting magnet and MDCs (multiwire drift chambers) to reconstruct the particle trajectory, in order to identify the particle.

The promising performance of the RPC technology made it appealing for CR research, especially for large area coverage. However, it should be considered that RPCs performance is affected by variations of temperature and humidity, and hence they need to be adapted to outdoor environmental conditions. Even indoors, room climate should be kept as stable as possible. In recent years, it has been proven that the above requirements can be fulfilled and RPCs can be run outdoor with low maintenance. Numerous experiments all around the world were already equipped with this technology for the study of cosmic rays. The Daya Bay underground experiment in China has assembled RPCs to shield background CR from the detection of neutrinos [39]. The HADES RPC wall has also been tested to measure air shower properties such as particle density, arrival time distribution or arrival detection [20]. An array of timing RPCs was also installed as part of the EEE project (Extreme Energy Events) in Italy, paving the road to smaller hodoscopes, like the one that constitutes the core of this thesis. EEE employs a network of tracking detectors installed all over Italy, each one with a detection size of $\sim$2 m^2. This project is devoted to the study of air showers and the primary cosmic rays that generate them [11].

Despite these developments, the study of the atmospheric effect remains a residual activity in view of these detectors' grand goals in the field of particle physics. In fact, prior to this thesis, no multigap RPC detector had been used to atmospheric sensing. The technology presents an interesting novelty, as it is the fastest technology (i.e., with best time resolution) used for the task up to this date, with demonstrated capability to reach 50-60 ps in m^2 areas [170, 27].

1.4 Atmospheric influence on Cosmic Rays

Recalling Section 1.1.1, it was mentioned that primary cosmic ray flux undergoes variations of different kinds, for instance, solar activity. Naturally, these variations of the primary CR affect the rates of secondary particles at the surface as well. With this in mind, it should be noted that the atmospheric conditions also influence rates, primarily through density changes which directly affect particle interaction and decay probabilities. If meteorological effects did not affect the particle flux, primary variations could be derived directly from secondary CR modulations observed at the surface. If these variations of atmospheric origin are large enough, they can genuinely mask the primary variations and lead to misunderstandings when unfolding phenomena of extraterrestrial origin. For this reason, it is essential to know the influence of

meteorological effects on the CR flux. In this section, we will review the most important aspects of the atmospheric effects on CR intensities.

1.4.1 Barometric effect

The effect of the atmospheric pressure, usually referred to as the barometric effect, is considered one of the major factors influencing secondary cosmic ray flux. In the case of muons, it affects energies ranging from 10 to 100 GeV. This effect was discovered in the mid-1920s, followed by the discovery of the temperature effect 10 years later, which will be explained in the next sections. At that time, it was observed that CR variations were inversely proportional to changes of air pressure at ground level, i.e., there was an anticorrelation between the two variables. In a first attempt to find an explanation, this phenomenon was attributed to an absorption effect of muons in the atmosphere. Later, in the 1950s, Dorman described this effect in more detail in his work with a one-dimensional approximation of the development of the cascades. Here, it was reinterpreted as three effects: absorption, decay, and generation effects [48]. According to the theory, the barometric effect decreases with increasing muon threshold energy, and it can be considered negligible for high-energy muons.

Experimentally, the change of the intensity N of the secondary muon component with small variations of surface pressure can be expressed as:

$$dN = -\mu dP \tag{1.3}$$

where μ is the absorption coefficient for the secondary component and P is the surface pressure. For $\beta \equiv -\mu = constant$, the equation becomes

$$N = N_0 e^{\beta \Delta P} \tag{1.4}$$

where N_0 is a reference intensity corresponding to a reference pressure P_0, and $\Delta P = P - P_0$. This can be converted into the well-known expression where β is defined as the "barometric coefficient":

$$\ln\left(\frac{N}{N_0}\right)_P = \beta \Delta P \tag{1.5}$$

and the value of the barometric coefficient can be obtained experimentally by means of a linear regression between measurements of CR and atmospheric pressure.

In broad terms, the barometric effect stems from the absorption of cosmic radiation in the atmosphere through energy loss of the particles created. A higher pressure implies a greater amount of air mass traversed. Because of this, fewer particles will reach the surface. Another factor to take into account is the decay of muons, which will also increase under the same considerations. The last effect to be considered is related to muon production, which is going to be increased for higher pressures. The parent mesons will interact more and eventually decay producing low-energy muons. The latter effect has a positive magnitude but it is smaller than the other two, giving as a result barometric coefficients with negative values for low-energy muons. Moreover, these effects have no impact on high-energy muons [135].

For muons at the ground level ($E_{th} \sim 0.4$ GeV), the barometric coefficient is approximately equal to $\beta = -0.15$ %/hPa. Considering that the amplitude of the annual pressure variations may be about 30 hPa, the variations in CR due to the barometric effect would have an amplitude

of $\sim$4.5 %, comparable or even exceeding typical solar phenomena like Forbush Decrease events (found later in the text).

After the theory stated by Dorman, multiple measurements of the barometric effect were carried out and the values seemed to agree with the theory. However, around 1980, several experiments reported unusual values in their retrievements. It turned out that the theory was incomplete. In 1986, Sagisaka recalculated the barometric coefficients for different threshold energies and angles of observation [135]. The values of the barometric coefficients investigated presented larger values than expected. Sagisaka found out that this discrepancy was due to the influence of the temperature effect in the analysis. They were not properly taking into account the temperature changes.

1.4.2 Temperature effect

Discovering the seasonal variation at the surface

In the early 20th century, the scientific community already knew that CR intensity observed at different parts of the world exhibited a yearly modulation inverse to the surface temperature variation. In 1938, Blackett proposed a theory relating this effect to muon decay in order to justify the decrease of the CR intensity as a consequence of the longer distance muons would have to travel to reach the surface in a warmer atmosphere, owing to its expansion. In such situation, muons would be generated higher in the atmosphere and so would have a greater chance of decaying before reaching the sea level. To corroborate such theory, Blacket pointed out that CR variations should be correlated with the average temperature of the atmosphere up to the generation height of mesons (free atmosphere) rather than the local ground temperature as had been done in the past [24].

Later, Duperier would verify that the mean temperature of the free atmosphere up to 16 km does correlate better with CR intensity than the surface temperature. In addition, to evaluate the relevance of such correlation, he also estimated the partial correlation coefficients, that is to say, the correlations between the CR intensity and one of the temperatures whilst the changes in the other are assumed constant. This proved that the mean temperature of the free atmosphere is the one controlling the temperature effect seen in CR data. Furthermore, if the mean temperature was calculated up to any other height rather than 16 km, for instance, 10 or 20 km, the correlation was found to be appreciably worse [56].

These results supported the theory formulated by Euler and Heisenberg that there existed a maximum of muon production around 15 km [58]. At that time, the estimated value of the coefficient that related the mean temperature of the free atmosphere with the CR variations at the surface was $\alpha \approx -0.18$ %/°C [55].

It is worth mentioning that in 1940, as opposed to previous results, Beardsley observed that the correlations between CR measured in Cheltenham (USA) and temperatures up to 10 km were not significantly different than the ones obtained with the surface temperature. The sign of the latter correlation was negative with a value close to one. Furthermore, correlations with heights above 10 km (i.e., lower stratosphere) seemed to decrease and changed signs. Further radio-sonde balloons observations elucidated the reason behind this discrepancy. It was reported that temperature changes for different heights up to 10 km followed very close those near the surface in contrast to greater heights, where changes are somewhat different. This revealed a special condition of the seasonal atmospheric evolution in Cheltenham [19]. Besides, it was a

reminder that temperature variations throughout the vertical of the atmosphere were complex, and a different approach was required to get a complete picture of the temperature effect.

Cosmic Ray Variations Underground

In parallel, Barrett was studying the correlations between CR rates measured underground (high-energy muons) and atmospheric temperature. Since the driving mechanism for the generation of high-energy muons is the decay of pions, it was hypothesized that there should be a positive correlation between the underground intensity and the atmospheric temperature, contrary to the negative effect seen for muons measured at the ground level (low-energy muons), which was directly related to their decay. The negative effect could be neglected for high-energy muons. However, since muons come from the decay of pions, there should be a strong correlation: an increase in temperature causes an expansion of the atmosphere, which in turn enhances the decay probability of a high-energy pion before it interacts. Consequently, the production of muons increases [17].

If the atmosphere was isothermal, i.e., if the temperature were constant with height, it could be characterized by an absolute temperature T and the coefficient correlating the intensity variations with the temperature changes would be defined as $\alpha = \Delta N/N \cdot \Delta T$. However, the atmosphere is not isothermal. With this in mind, Barrett showed in his work that it was possible to take into account the vertical distribution of temperatures in the atmosphere using a weighted mean temperature. In this weighted average for the case of high-energy muons, the temperature at the pressure levels of the highest altitudes should weigh more compared to lower levels. The reason is that the fate of mesons is always determined in the first few kilometers they travel from the moment they are created since they immediately decay or interact ($\tau_{\pi^{\pm}} = 2.6 \times 10^{-8}$ s). Owing to this, few mesons live long enough to reach low altitudes. Alternatively, if a high-energy meson has been able to reach the regions of highest density in the lower atmosphere, it is very unlikely to decay.

On the other hand, when daily temperature variations were studied as a function of height, it was observed that there were certain levels whose temperature varied in anticorrelation with respect to others. As a consequence, the effects due to temperature variations were compensating. Since muons are created throughout the atmosphere instead of at a single level, one should expect a weak correlation between daily variations of CR and the temperature at an individual level (height). Barrett also noted at that time that temperatures at 80-125 hPa differed in properties from the rest of the atmospheric levels. First, the lowest atmospheric temperatures are found at those levels, even lower than in the upper stratosphere (20-40 hPa). Second, their seasonal variations appeared in antiphase with the seasonal variations above and below that range of pressures.

Last but not least, Barrett assumed that the CR variations were merely caused by temperature changes and random statistical errors. This assumption could be tested after computing the temperature effect, removing it from the rate variations, and then observing whether the residual fluctuations were as small as expected from statistical fluctuations alone. By the time he calculated the temperature effect, he did found a positive correlation with CR rates which was consistent with the considerations mentioned above. Apart from this, to support his hypotheses, he also analyzed the diurnal CR variations. Seeing that the lower region of the atmosphere showed considerably large daily temperature variations, if evidence was found of a diurnal variation in CR intensities with the appropriate phase, it would indicate that there would be a significant production in the lower atmosphere of particles capable of penetrating

underground. Nonetheless, when tested, no significant variation was found. This reinforced the notion that the most important production processes of high-energy muons take place only in the upper parts of the atmosphere.

All things considered, we have seen so far that for high-energy muons there is a positive correlation due to the decrease in air density when temperature increases (positive effect), giving as a result that more pions will decay into muons; for low-energy muons on the other hand, a negative correlation is found due to a similar dependency of the muon decay on air density changes (negative effect).

Method of weighted temperature

As discussed earlier, the real temperature variations are not uniform throughout the atmosphere, and the production of muons or pions cannot be approximated to take place at a single level. As a solution, a weighted or "effective" temperature T_{eff} can be calculated, which is the equivalent to the temperature that an isothermal atmosphere would have in order to produce the same modulation of the muon intensity as an atmosphere with the actual temperature distribution $T(X)$.

An example of an *ad hoc* expression proposed for the effective temperature was [17]

$$T_{eff} = \left(T_{20} + T_{40} + T_{80} + T_{125} + T_{250} + \frac{1}{2} T_{500} \right) / 5.5 \tag{1.6}$$

Here, more weight is being given to upper atmospheric levels (20, 40, 80, 125 and 250 hPa) [17]. The formulation could be improved later by employing sophisticated models for nuclei and meson generation and propagation in the atmosphere.

Anyway, this definition of effective temperature is very useful to study the effect of temperature variations in underground detectors. In such case, while the temperature of the troposphere undergoes considerable daily variations, the temperature of the stratosphere remains practically constant (except for occasional abrupt variations). On a seasonal scale, the slow variations of the temperature of the stratosphere and the decrease of the air density will reduce the probability of mesons to interact and a larger fraction of them will decay into muons. As underground rates are largely oblivious to the troposphere conditions, an underground detector will be sensitive to the small seasonal variations in the temperature of the upper atmosphere.

Temperature coefficients

Over the years, numerous attempts have been made to correlate CR intensity variations with atmospheric variations to obtain the partial temperature coefficients, in lay terms, the distribution of temperature coefficients as a function of height that relates the temperature variation in each layer to the corresponding variation of the total measured rates. However, in practice, it was very difficult to obtain the correct values.

In 1986, the temperature effect had already been estimated for different seasons. Admittedly, far from completely solving the problem of the temperature effect, some underground experiments detected several anomalies in their values. Particularly, they had observed a semi-annual modulation in the muonic intensity measured at the Matshushiro station. This semi-annual variation displayed a very striking contrast compared to the annual

variations commonly observed at other underground stations closer to the surface (e.g., Misato or Sakashita) [135].

The distribution of temperature coefficients had previously been calculated theoretically by several researchers (e.g., [49]) and satisfactory results had been obtained under certain measurement conditions. Their calculations, however, were based on simplified models of the propagation of nuclei and pions and using a muon production spectrum deduced from surface experiments. These considerations proved to be insufficient. In 1986, Sagisaka recalculated the coefficients both for the barometric and temperature effect, solving the anomalies observed in other stations [135]. In his review, Sagisaka expressed the partial temperature coefficients as the sum of two terms: one representing the negative effect and the other the positive effect. In this way, he attributed the reason for the semi-annual variation found in Matsushiro to the dependence on the muon threshold energy of the atmospheric temperature effect. Furthermore, it was remarked once again that the temperature deviations varied with altitude in a complex way at each season. Proof of this is that the variation of the tropopause's temperature is nearly opposite in sign to that in the troposphere (antiphase). Considering the partial temperature coefficients introduced by him as $\alpha_i(h)$, where $i = 1,2$ corresponds to low and high threshold energies, respectively; and the seasonal variations of the atmospheric temperatures as $(\Delta T(h))_j$ for $j = 1,2,3,4$ being the seasons; the different products $\alpha_i \cdot (\Delta T)_j$ can be estimated. By integrating each of these products from the top of the atmosphere to the surface, the total temperature effect can be obtained for both underground and shallow detectors. Figure 1.7 shows an schematic view of the products as explained in Sagisaka's work [135]. In the low-energy case ($E_{th} \sim 1$ GeV), the distribution of coefficients α_i has negative values and is nearly independent of the atmospheric height (Fig. 1.7 top). Thus, the contribution of the product $\alpha_1 \cdot (\Delta T)_j$ in the troposphere to the integral $(\Delta I)_j$ dominates compared to the contribution of the stratosphere (the troposphere has a higher air mass percentage). As a consequence, the temperature effect is opposite to the surface temperature, giving rise to an annual variation with its peak in winter. This can be appreciated in Figure 1.7 where the magnitude of the effect is positive for $\alpha_1 \cdot (\Delta T)_1$ and $\alpha_1 \cdot (\Delta T)_2$, which correspond to the winter and spring months.

On the other side, in the case of deep underground detectors, the contribution of the product $\alpha_2 \cdot (\Delta T)_j$ in both the stratosphere and tropopause sets the seasonal trend. The tropopause temperature peaks towards the end of the spring, much earlier than the troposphere, thus the maximum muon rate occurs during the warmest months. The example shown has been done with mid-latitude temperatures. In the Matsushiro's location, the temperature variations in the upper atmosphere have a different behaviour than the ones showed in Figure 1.7. In their case, the contribution of the product $\alpha_2 \cdot (\Delta T)_j$ in both the troposphere and stratosphere to the integral are almost compensated by each other throughout the seasons. The minor differences in the balance between the two contributions yield a semi-annual variation with two maxima, one in summer and the other in winter. This revealed that the aforementioned balance was very sensitive to the height of the tropopause ($\sim$200 hPa), the temperature profile of the stratosphere, and the shape of the distribution of the temperature coefficients as well.

Given these points, it should be noted that there exists a competition between the processes of interaction and decay that will determine the evolution of the air showers and thus the muon rates at the ground. This competition mainly concerns mesons because protons, gammas, and electrons do not decay. On the one hand, the decay process depends on the mean lifetime τ of the particle. On the other hand, the interaction depends on the amount of traversed matter, that

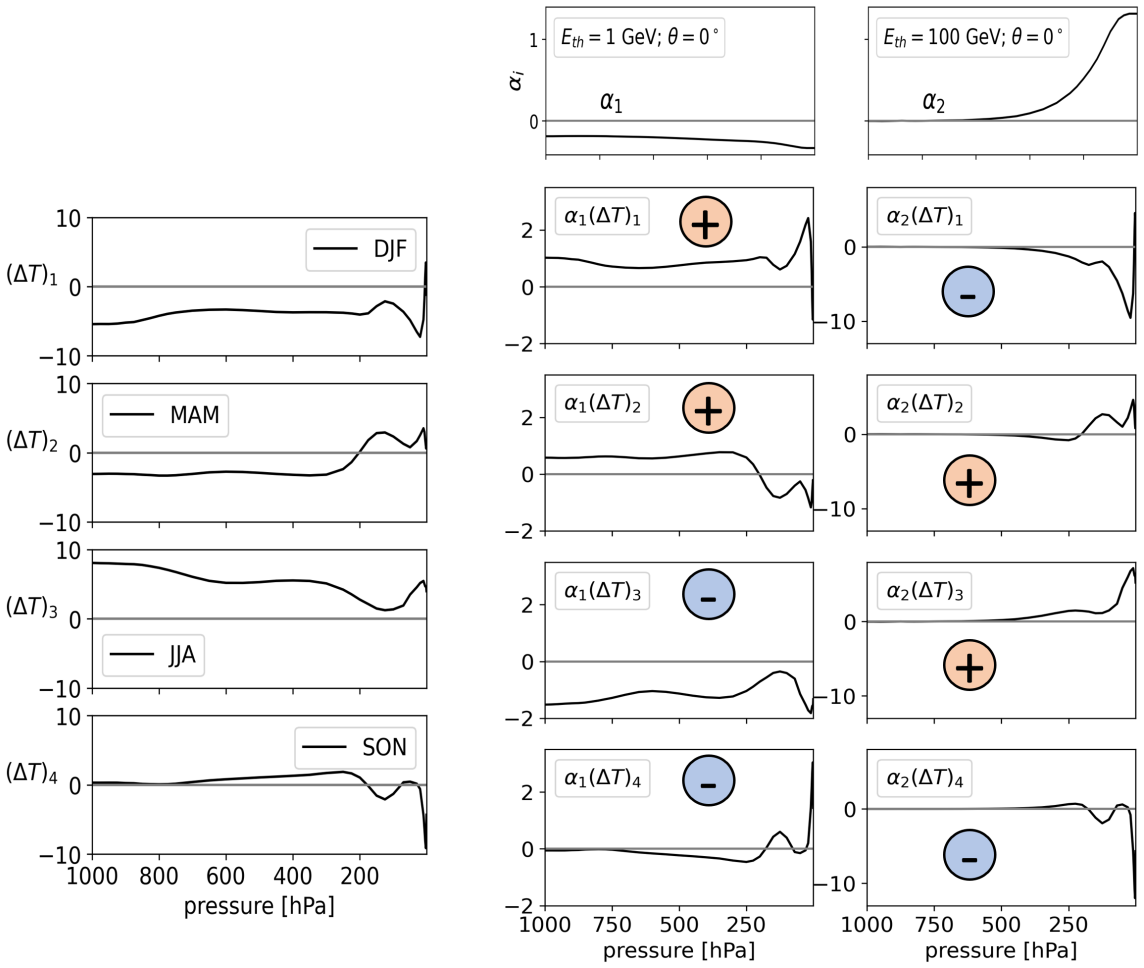

Figure 1.7: Schematic representation of the atmospheric temperature effect on the muon intensity observed at surface and underground as explained in [135]. (Top) α_i ($i = 1,2$) are the partial temperature coefficients for two energy thresholds $E_{th} = 1$ GeV and $E_{th} = 100$ GeV corresponding to surface and underground locations, respectively. (Left) $(\Delta T)_j$ ($j = 1,2,3,4$) are the seasonal variations of the atmospheric temperature from the yearly average at a mid-latitude location (40°). The seasons are grouped by: December-January-February (DJF), March-April-May (MAM), June-July-August (JJA), and September-October-November (SON). (Right) The products $\alpha_i \cdot (\Delta T)_j$ are plotted for each combination of i and j together with the magnitude of the temperature effect, which is shown with a colored circle: the red circles with the plus sign represent the positive and the blue ones with the minus sign the negative.

is, it is a function of the density of the medium.

By way of illustration, Table 1.2 provides typical values for pion interaction and decay lengths. As can be seen from the table, if the decay length is bigger than the hadronic interaction length, $d_{dec} \gg \lambda$, mesons can live long enough to interact and produce other mesons. In contrast, when $d_{dec} \ll \lambda$, mesons decay before interacting and generate: gamma-rays in the case of neutral pions; muons and neutrinos in the case of charged pions (contributing to the muonic component of the cascade).

Meson	Decay Channel	Decay Length $d = \beta\Gamma c\tau \simeq \Gamma c\tau$ [cm]	Interaction Length at 10^{12} eV [g/cm^2]	E_{dec} [eV]
$\pi^{\pm}$	$\pi^{\pm} \to \mu^{\pm}\,\nu_{\mu}$	$d_{\pi^{\pm}} \simeq 780 \cdot \Gamma$	$\lambda_{\pi^{\pm}} \simeq 120$	$7 \cdot 10^{18}$
π^0	$\pi^0 \to \gamma\,\gamma$	$d_{\pi^0} \simeq 2.5 \times 10^{-6} \cdot \Gamma$	$\lambda_{\pi^0} \simeq 120$	$2 \cdot 10^{10}$

Table 1.2: Values of the interaction and decay lengths for pions as well as decay energies. Γ is the Lorentz factor: $\Gamma = E/(m_{\pi}c^2)$.

The competition is going to depend on the energy of the particle E and the density ρ of the upper atmosphere (above ∼15 km). Hence, the energy E_{dec} at which the decay and interaction compete needs to be calculated. Comparing the interaction length d_{int} with the decay lenght $d_{dec} = \lambda/\rho$, we have:

$$d_{dec} = d_{int} \Rightarrow \Gamma c\tau = \frac{\lambda}{\rho} \Rightarrow \frac{E_{dec}}{mc^2} c\tau = \frac{\lambda}{\rho} \tag{1.7}$$

where the decay energy is given by

$$E_{dec} = \frac{\lambda}{c\tau\rho} mc^2 \tag{1.8}$$

Now, if $E \gg E_{dec}$, then the particle will live long enough to interact. But if $E \ll E_{dec}$, the particle will decay.

Table 1.2 provides the results obtained for a pion with $E = 10^{12}$ eV. In this example, for an air shower initiated by a primary cosmic ray with energy E_0, neutral pions will not decay unless $E > 7 \cdot 10^{18}$ eV, whereas charged pions having $E < E_{dec} \sim 2 \cdot 10^{10}$ eV will tend to decay.

Building on the works of Dorman and Sagisaka, refined calculations have been seen recently, in particular those of Dmitrieva *et al.* in 2011, leading to a modern formulation of the above problem [47]. According to these studies, these processes can be embedded in a single function $W_T(E_{th}, X, h, \theta)$, or DTC (*Differential Temperature Coefficient*), which provides information on how much an atmospheric layer at an altitude h contributes to the variations in the flux of muons arriving at a zenith angle θ, with an energy greater than E_{th}, and at an observation level X. According to Dmitrieva *et al.*, if the atmospheric temperature changes as $\Delta T(h)$, the standard muon intensity $N_0(E_{th}, X, \theta)$ at a certain observation level X will be changed by an amount $\Delta N_T(E_{th}, X, \theta)$. Therefore, the relative variation of the muon intensity can be written as:

$$\frac{\Delta N_T(E_{th}, X, \theta)}{N_0(E_{th}, X, \theta)} = \int_0^X W_T(E_{th}, X, h, \theta)\Delta T(h)dh \approx \sum_i W_T(E_{th}, X, h_i, \theta)\Delta T(h_i)\Delta h_i \tag{1.9}$$

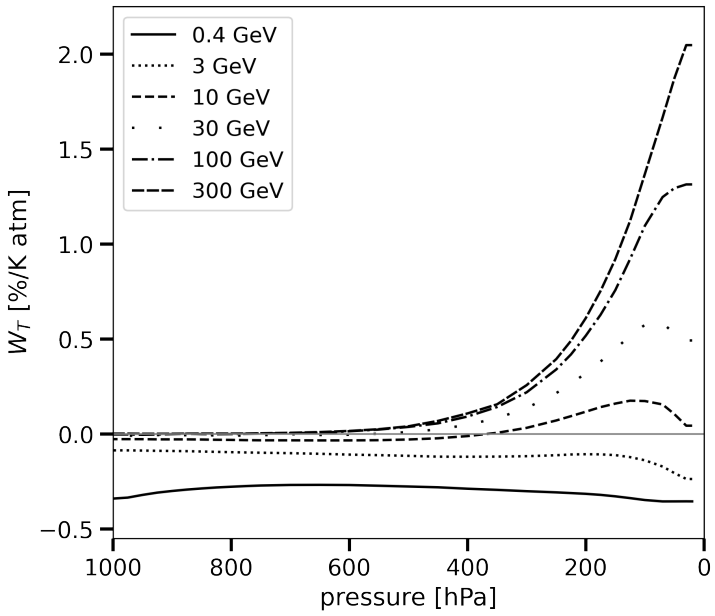

Figure 1.8: Differential temperature coefficients W_T for vertical direction ($\theta = 0°$) at several threshold energies [47].

Figure 1.8 provides some examples of temperature coefficients as a function of atmospheric height for $\theta = 0°$ and several values of threshold energies. The shape of the distributions illustrates how muons with high threshold energies are very sensitive to the stratospheric temperatures ($h < 200$ hPa). In simple terms, small changes in the temperature of the stratosphere significantly affect the intensity of high-energy muons reaching the surface. A simplified schematic view of the temperature effect is shown in Figure 1.9 as well.

Temperature variations in the atmosphere

When estimating the correlation between CR rates and the temperature at a certain atmospheric level ($\frac{\Delta N}{N} = \alpha_p \frac{\Delta T_p}{T_p}$), the slopes α_p of this regression cannot be compared between detectors with similar arrangements but located in different places. The reason is that the atmospheric configuration differs from one place of the planet to another and the variations in ΔT_p correlate with the rest of the atmosphere in different ways, impacting the CR variations. For instance, a colder and denser air forms a more compact atmosphere at the poles. Furthermore, these regions are outside of the General Circulation Zone of the atmosphere, so seasonal variations are smoother, with a consistent low-pressure area that weakens towards summer. The polar vortices isolate Antarctica and North Pole from the atmospheric effects of the mid-latitudes (alternation of cyclones-anticylones, etc). Therefore, the atmosphere is preserved in a stable situation which may only be interrupted during some exceptional events called Sudden Stratospheric Warmings (SSWs) (see more information in Appendix A.1) [31]. Also, the tropopause is located at a lower altitude there, around 9 km, while at the equator (with a warmer atmosphere) it is above 17 km. Translated into pressure levels, 225 hPa is the global standard reference level for the tropopause. However, this can be misleading since the tropopause can exist at any position between 100 and 400 hPa over the year [107].

Not only the position of the layers must be taken into account but also the correlations

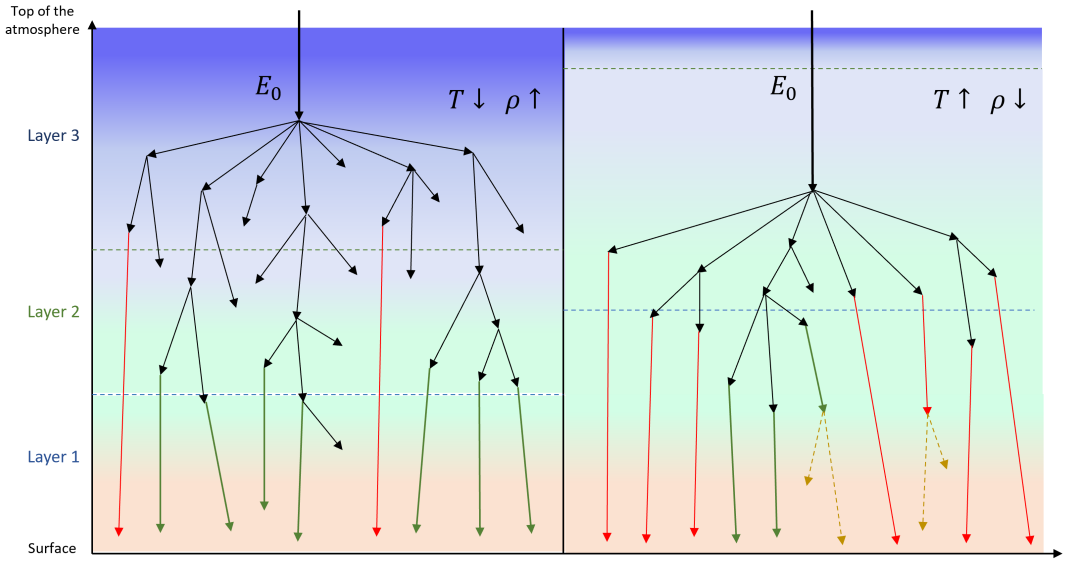

Figure 1.9: Illustration of the temperature effect for an air shower with initial energy E_0 during winter (left) and (summer). Initial particle and charged mesons are drawn with black lines; red lines are high-energy muons; green lines are low-energy muons; and dashed lines represent electrons and neutrinos. The positive effect is represented by more charged mesons decaying in a less dense atmosphere (right) and the negative effect is seen when more low-energy muons generated lower in the atmosphere can reach the ground level before decaying (left).

of temperature variations between different levels. Due to this, comparisons should not be made between the α_p of different detectors for the same pressure levels, since they depend on the regional characteristics of the atmosphere. In general, it is convenient to use an effective coefficient α_T for this purpose. The use of such coefficient provides a net value of the total atmospheric effect, thus removing the constraints not only of the differences in pressure levels but also of the diverse correlations between atmospheric layers that occur for different geographical locations. Therefore, the CR variations due to temperature changes can be expressed in terms of the effective temperature coefficient as follows:

$$\frac{\Delta N_T}{N_0} = \alpha_T \Delta T_{eff} \tag{1.10}$$

and α_T and the effective temperature T_{eff} are defined as

$$\alpha_T = \sum_{i=1}^{n} W_T(E_{th}, X, h_i, \theta) \Delta h_i \tag{1.11}$$

$$T_{eff} = \frac{\sum_{i=1}^{n} W_T(E_{th}, X, h_i, \theta) \Delta T_i \Delta h_i}{\sum_{i=1}^{n} W_T(E_{th}, X, h_i, \theta) \Delta h_i} \tag{1.12}$$

This will be addressed in more detail in Chapter 2.

1.5 Influence of Cosmic Rays on the Atmosphere

In the previous section, we considered the problem of the influence of the atmosphere on CR rates. However, one can ponder the opposite question of whether or not CR influence the

atmosphere.

The interaction of CR particles with the atmosphere can lead to a host of interesting effects, several of which can have a big impact on the planetary environment. It is a well-known fact that CR have an influence on atmospheric electric field and, as a consequence, on thunderstorms as well [146]. Moreover, given that CR ionize the atmosphere as they pass through, their connection with the ionosphere is direct. The ionosphere is a layer of the upper atmosphere (from 80 to 1000 km) ionized by high-energy radiation from the Sun and CR. By means of illustration, during the night, without the influence of the Sun, only CR produce the ionization and hence the ionosphere is much less charged at nighttime. Consequently, any variation in the CR flux will undoubtedly affect this part of the atmosphere [169].

CR also influence atmospheric chemistry when they interact with gas particles, triggering a series of physicochemical chain reactions that alter the composition of the atmosphere. For example, the electrons arising from CR ionization can break N_2 molecules, causing the formation of NO_x. This NO_x molecules are potentially dangerous because they can deplete or generate ozone, depending on the conditions. Besides, the change in NO_x concentrations can affect numerous chemical processes by competing with their reactants.

Altogether, CR can modify atmospheric chemistry, create an ionosphere, influence atmospheric lightning, produce organic molecules in the atmosphere, destroy stratospheric ozone, and so on. For this reason, when studying the atmospheres of other planets (exoplanets), models that take into account the influence of CR are proposed to investigate their potential habitability [74].

Despite all this, we are more interested in the influence of planetary cloud covering and its possible effect on climate, in the short and long term. This topic will be covered in the last chapter of this thesis. On this occasion, we need to understand the background of this influence and its basic concepts.

1.5.1 The Variability of Solar Activity

The main source of energy for the Earth's surface comes from the Sun. The amount of energy received by a particular location varies over time, especially over the seasons. The reason is the Earth's motion around the Sun and the tilt of its axis. However, the irradiance, which is the flow of energy radiated by the Sun, could be considered constant. Eventually, it was found that the Sun has cycles of activity and its irradiance can vary too [172].

Solar activity is measured by the number of sunspots on its surface. Namely, sunspots are dark regions that temporarily appear on the Sun and that are colder than their surroundings areas. These regions can be very large, reaching planetary sizes, and are caused by the interaction of the magnetic fields generated by the motion of the Sun's gases in the outermost layers [144]. These processes generate a lot of activity on its surface, which is known as solar activity. Therefore, sunspots can be considered as an useful indicator of the activity of the star.

In the same way as weather on Earth varies from season to season, the Sun's activity also has its phases, the solar cycles. Granted that solar activity can have an impact here on Earth, scientists need to monitor its status on a regular basis. Sunspots have a lifecycle of the order of weeks and follow the rotational motion of the Sun itself, which lasts 27 days on average. The number of spots in the Sun's surface has been counted since the beginning of the seventeenth century, by the time the telescope was invented. Thanks to these measurements, it was possible to see that the number of sunspots followed a cycle of about 11 years. The beginning of a

cycle is a solar minimum when the Sun presents the least sunspots. Over time, the number of sunspots increases until it reaches a peak, the solar maximum. The cycle ends with the return to the minimum [166].

The irradiation of the Sun changes according to this cycle, although it should be emphasized that this variation is small, in the order of 0.1 %. The effect of this change of the long-term solar irradiance is generally considered to be too small to have any effect on the current climate change [97]. Indeed, they are meant to be negligible only for the last 150 years, approximately, due to the greater magnitude of anthropogenic climate change [186].

On the other hand, large eruptions occur on the Sun, such as solar flares and coronal mass ejections (CMEs), that increase as the Sun approaches the solar maximum. Solar flares happen because the magnetic field lines of the sunspots often twist, cross, and reorganize, causing explosions of energy. These flares release a lot of electromagnetic radiation into space that, if directed towards the Earth, can interfere with radio communications [171].

Solar flares are often followed by a coronal mass ejection. In such a case, a huge amount of plasma (gas of charged particles) from the solar corona with its corresponding strong magnetic field is released. These Sun's disturbances generate solar storms that travel across the interplanetary space affecting the planets found in their path. Especially, when these charged particles hit the Earth, they are deflected by the Earths's magnetic field towards the poles, where they interact with the upper layers of the atmosphere producing the auroras. When CMEs are particularly strong, the resulting geomagnetic storms can produce strong induced electric fields which can affect the electrical transmission lines, causing massive power outages. In addition, solar storms can damage satellite electronics and affect terrestrial communications.

The whole series of phenomena related to solar activity form what is known as Space Weather. Researchers work hard to improve space weather monitoring and forecasting in order to protect our communications, keep astronauts safe, etc.

1.5.2 Cosmic Rays and the Solar Cycle

The intensity and energy spectrum of GCRs is modulated by solar activity. The Sun constantly emits a stream of charged particles called the solar wind. As the solar wind spreads out filling the interplanetary space, it creates an environment of radiation and magnetic fields, forming a giant bubble around the star and planets, known as the heliosphere. This acts as a shield, protecting the planets from galactic cosmic radiation. Additionally, Earth is protected by its own magnetic field, which has several benefits. In Section 1.2, it was mentioned that the magnetosphere is shielding Earth from cosmic radiation. Similarly, it also prevents the atmosphere from being degraded over time by the collision of the solar wind with it. Indeed, planets without magnetic fields, such as Mars and Venus, are exposed to high radiation levels and their atmosphere is gradually vanishing. In the case of Mars, this process is at a very advanced stage, with an atmosphere so rarefied that yields high surface radiation which should be taken into consideration for future space missions [73].

The expansion of solar ejections into interplanetary space produces plasma overdensities at the solar maxima. Therefore, the heliosphere becomes more effective in scattering high-energy GCR entering the solar system. Thus, the flux of GCR arriving at the Earth is reduced, leading to its anticorrelation with the sunspot number [80].

Together with these long-term variations in the flux of GCR, sudden short-term variations can also happen. Forbush Decreases (FDs) are one of the main phenomena responsible for this.

A Forbush Decrease is produced by a CME and refers to a sudden decrease in GCR intensity. They are caused by the heliospheric magnetic shock driven ahead of a CME that sweeps away some of the incoming GCR when it reaches the Earth. FDs also vary in amplitude, ranging from 3 to 20 %, and usually last several days. They can be most easily observed at the Earth's surface with neutron monitors. A FD is characterized by having several phases. The decrease phase starts with the arrival of the shock and may be preceded by a small increase of 2 or 3 %. This preincrease has a very short duration of few hours. The intensity drop is very abrupt and happens in approximately 24 hours. After this stage, a gradual recovery phase occurs in the following days [129].

1.5.3 Link between cosmic ionization and cloud-covering

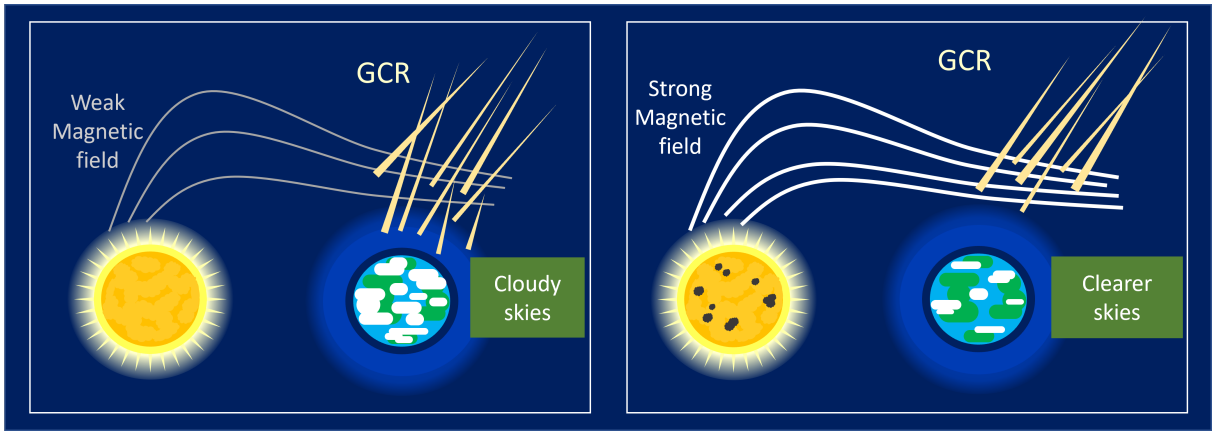

Figure 1.10: Illustration of the possible link between GCR and cloud-covering: a lower solar activity produces a weaker solar magnetic field that deflects much less GCR and thus more clouds will form due to atmospheric ionization (left). The opposite would yield clearer skies (right).

It has been previously pointed out that cosmic ionization of the atmosphere can alter its physical and chemical processes. Because of this, it has been suggested on numerous occasions that solar variability could be correlated with cloud-covering and, therefore, be a contributing factor for climate change by modifying the Earth's average albedo. However, the effect of the Sun's activity on the climate is a controversial question, and there is no clear consensus as there are studies that contradict each other. Figure 1.10 shows a sketch of the possible relation between solar activity and cloud cover.

At the end of the last century, several papers were published in which they observed cloudiness variations at mid-latitudes associated with Forbush Decreases [127, 128]. In 1997, the first correlation between global cloud cover and CR intensity was reported [151]. The cloud cover seemed to be inversely correlated with the solar activity. Five years of satellite data had been analyzed, in coincidence with a solar minimum, and found variations of 3-4 % in the cloud cover. Apart from this, it was also apparent that the observed variation was larger at higher latitudes than in the Tropics, in agreement with the lower values of the rigidity of the Earth's magnetic field. Against the significance of this correlation, other scientists argued that it was very difficult to attribute the correlation to cosmic rays because the actual microphysical explanation for such effect was still lacking. Subsequent reassessments of the trends showed divergent results: strong correlations in Forbush Decrease events [157, 78] against weaker or

no correlations [147, 100, 158]. Furthermore, some analysis also showed the impact of the methodology used on the differences in results (e.g., [102]).

In 1993, Tinsley *et al.* had already suggested that a possible mechanism to explain the linkage between solar activity and climate could be the atmospheric electricity variations caused by the solar wind and that involve the charging of supercooled water droplets and aerosols (small atmospheric particles) at clouds [156]. Later, Svensmark *et al.* presented a work where they found correlations not only with cloud cover but also with cloud and aerosol properties during several FDs [148]. These results might be evidence that cloud changes could be driven by changes in aerosols. Yet, the studies did not clarify whether the effect could be the other way around, clouds could be affecting aerosols. Again, a subsequent similar survey found no evidence of significant correlations [32].

Clouds have a strong influence on the Earth's energy budget, absorbing and reflecting radiation from the Sun and the Earth's surface. Therefore, small changes can have a big relevance for the climate. However, detailed studies on cloud formation are difficult to carry out because it is not straightforward to replicate cloud formation in laboratories.

1.5.4 The CLOUD Experiment

The CLOUD (Cosmics Leaving Outdoors Droplets) project at CERN is a huge experiment that was created to elucidate the possible links between GCR and cloud formation. The experiment focuses on the study of the formation and growth of aerosols that lead to the condensation of cloud droplets. The experiment is performed in a huge chamber (26 m^3) equipped with a wide range of sensors to track the evolution of clouds inside. The CERN Proton Synchrotron provides the artificial and adjustable source of "cosmic rays" through a pion beam. The entire setup allows tuning the chamber's conditions to duplicate those of the real atmosphere, such as temperature, humidity, or levels of ionization. In its more than 10 years of activity, CLOUD has made many striking discoveries. In particular, it was the first experiment to demonstrate a clear relationship between GCR ionization and aerosols formation. In truth, they have found a relatively weak dependence on ion concentrations and that, in the present-day atmosphere, CR intensity cannot meaningfully affect climate via aerosol growth [54]. In spite of this, it has been discovered that ions from GCR can strongly promote the formation rate of biogenic vapors emitted by trees up to a factor of 100. These findings reveal that CR may have played an important role in cloud formation in pre-industrial times [94]. Besides, they demonstrated that nucleation rates could be enhanced thanks to ions under certain conditions. Some of the findings reported are: the enhancement of neutral nucleation caused by cosmic ionization can reach a factor of 15 at the temperatures of the low troposphere; and, in general, ion-induced nucleation is the dominating process in most parts of the troposphere. Nevertheless, it should be taken into account that proving that nucleation of particles is affected by GCR does not imply that this will affect cloud formation.

The work of the CLOUD experiment has shed light on our understandings of aerosol nucleation, growth, and their link with clouds and climate. However, they had not yet addressed the connection between GCR and clouds. Alternatively, they have integrated their experimental results in global aerosol models to test the roles of the different processes of atmospheric particle growth and formation [54, 70, 69]. In these investigations, they estimated that ions from GCR are accounting for about half of the nucleation in both the present-day and pre-industrial atmosphere.

Overall, there is still a long way to go in the understanding of cloud formation. Although the CLOUD experiment has closed the door on certain theories, there are still many uncertainties and mysteries to be solved. Furthermore, it is still unknown whether CR can influence atmospheric processes through other mechanisms (e.g., [150]). For instance, we have already mentioned that Tinsley *et al.* proposed a theory where the atmospheric electric field could play a main role involving both the global atmospheric electrical circuit and cloud microphysics [155].

1.5.5 Ionization Effect on Aerosol growth

Aerosols are tiny particles present in the atmosphere. They can be liquid or solid and have varied chemical compositions. Their sizes also range from small molecular clusters of less than one nanometer to diameters greater than 10 μm. These particles can be emitted directly to the atmosphere (primary aerosols) by different natural or artificial sources or produced in the atmosphere via the conversion of precursor gases (secondary aerosols). Aerosols can be classified into several classes: inorganic (e.g., salts, metals), organic components, carbonaceous compounds, and water. Some of the most common chemical compositions of aerosols are sulfates (SO_4^{2-}), nitrates (NO_3^-), and sea salt (NaCl) [140].

Primary aerosols come from the seas, desert dust, volcanic eruptions, mineral dust and smokes from forest fires. Whereas secondary species are condensed in the atmosphere, such as sulfates and nitrates. It should be emphasized that most of the atmospheric aerosols are anthropogenic in origin, for instance, products of fossil fuels and biomass burning. Moreover, many aerosols are nonvolatile, i.e., once deposited in the aerosol phase, they stay there until the particle is finally removed from the atmosphere via different processes (gravitational sedimentation, wet removal, etc).

Obviously, the geographical location is going to influence the type of species present in the local atmosphere: marine, continental, rural, polar, desertic, etc. Their composition varies as well in different zones of the atmosphere, where one can differentiate between tropospheric and stratospheric aerosols. The former are mixed in the lower atmosphere by turbulent processes and travel through it by the large air masses. The latter are mainly sulfur-based compounds from volcanic injections, which are one of the major sources of stratospheric aerosols.

Atmospheric aerosols can evolve in time and space: they can change in size and composition due to microphysical processes, they are transported through the atmosphere following the circulation of large air masses and they can be removed from the atmosphere, for example being captured when water droplets gravitationally fall and reach the surface.

The most relevant microphysical transformation processes that aerosols undergo are nucleation, condensation, and coagulation. In this way, secondary aerosols are created from precursor gases by condensation of vapors on pre-existing particles. A diagram of the different processes can be seen in Figure 1.11.

Nucleation is the first step in aerosol formation. It refers to the process by which gas molecules in the atmosphere aggregate to form a cluster, i.e., a new fine aerosol. When the cluster grows and reaches a critical size, it becomes stable and can keep growing by condensation. Ions have long been known to enhance nucleation. Several schemes have been proposed to account for this effect in aerosol models. One of them is the ion-mediated nucleation (IMN) mechanism based on a kinetic approach, which is consistent with several experimental observations [183]. Against homogeneous nucleation, which involves the clustering of small neutral molecules, nucleation onto ions is promoted because charged clusters

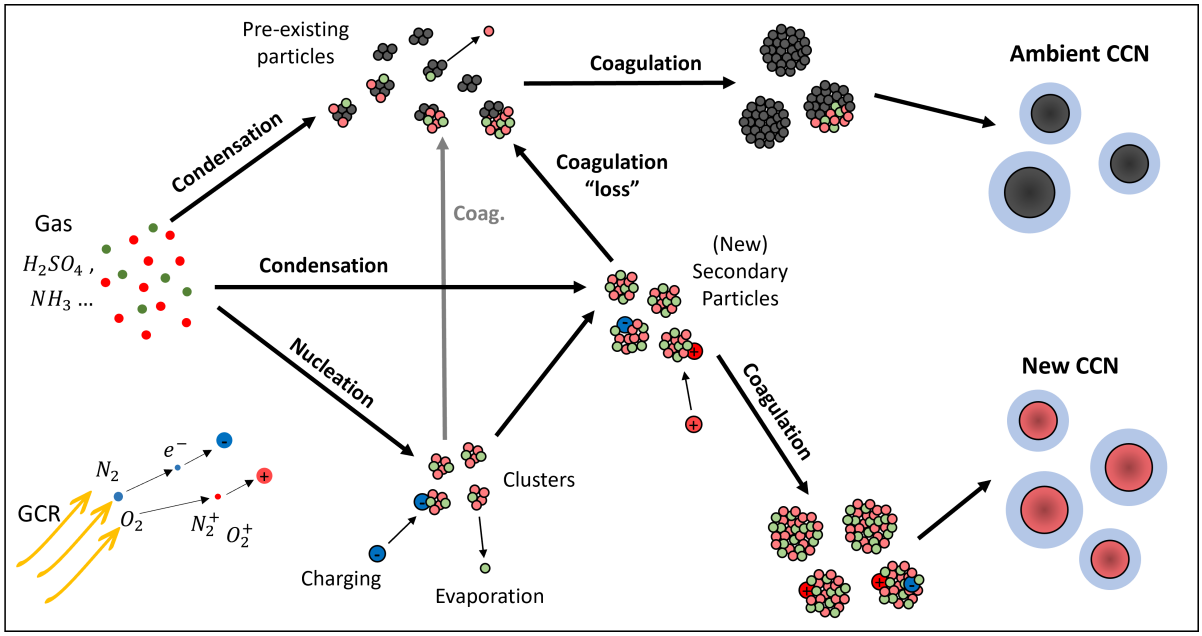

Figure 1.11: Diagram of aerosol processes in the atmosphere including nucleation of clusters for new particle formation and their growth to cloud condensation nuclei (CCN) (lower path). Pre-existing aerosols also compete for condensable gases and grow to CCN via coagulation with the newly formed particles (upper path). Some particles may be lost along the way through evaporation, and ions produced by the impact of GCR with atmospheric nuclei can influence processes by charging aerosols.

are usually much more stable thermodynamically than neutral ones [179, 180]. Additionally, the initial growth of ionized clusters is faster due to the dipole-charge interaction between the ionic core and the dipolar condensing molecules [117]. Owing to this, the initial growth stage of particles up to ∼1.5 nm is strongly enhanced. However, this acceleration decreases for particles larger than that. The 1 nm new particles must grow to sizes of at least 50-100 nm in order to act as cloud condensation nuclei (CCN). An aerosol CCN acts as a seed on which water vapor condenses. The change in the number of CCNs can affect climate.

The method by which new particles grow to larger sizes is called *condensation*. If aerosols are able to grow quickly through this process instead of being lost by coagulation with other pre-existing particles, then they will impact the number of CCNs. Hence, it is mandatory to understand how the different vapors interact with the aerosols. Until recently, there was a lot of uncertainty about this issue. However, the CLOUD team showed that the vapors of sulfuric acid, ammonia, and water are the main ingredients involved in this process [54].

Finally, aerosols can also grow by sticking to each other through a process called *coagulation*. This occurs when particles collide with one another. It should be highlighted that this process is a sink for aerosols loss because it leads to an increase in diameter but the total number of particles decrease. In other words, it favours reaching CCN sizes but, at the same time, the final number of CCNs will be smaller.

As we have seen in the previous sections, the flux of cosmic rays has been reported to correlate with cloud-covering and aerosol properties. One proposed mechanism to explain these correlations is the "ion-aerosol clear-sky" mechanism [122]. It states that an increase in GCR causes an increase of small ions in the atmosphere. This increment may enhance the nucleation rates of ∼1 nm diameter aerosols. Next, if these small particles are able to grow to larger sizes (>50-100 nm) via condensation of vapors, they can act as CCN. Even so, this growth must

take place before the new particles are lost by coagulation with existing aerosols. Eventually, if the number of CCN particles is increased, the number of cloud droplets also increases, which may lead to an enlargement of the cloud albedo and cloud cover, affecting the climate through a cooling effect.

Furthermore, there are other factors that can dampen the growth effect resulting from GCR. The growth of 1 nm aerosols to CCN is going to be constrained by the amount of condensable material. Thus, an increase in nucleation rates results in a decrease of the 1 nm particles that survive up to CCN sizes because growth becomes slower. In such a scenario, coagulation of the new particles with the existing CCN is faster and no new CCN will be formed. Moreover, the response of the cloud droplet concentrations to these effects is not linear with respect to changes in the CCN concentrations.

Therefore, the final effect of the GCR increase in clouds will be determined by several factors that will vary depending on the circumstances. So far, several studies have shown that the influence of GCR on clouds is very weak [122, 143, 182, 53].

Chapter 2

Atmospheric Temperature with a High-Resolution Cosmic Ray Detector

Abstract: *Cosmic-ray observations are affected by several meteorological factors. One of the most challenging to extract is the effect of temperature variations throughout the atmospheric profile. In this chapter, we examine in detail the cosmic ray variations measured with a 2 m^2 high-resolution detector, based on tRPC cells, located at ground level. We find the specific temperature coefficients for the detector from the experimental data by applying a statistical technique based on Principal Component Analysis (PCA). Subsequently, we disentangle the related temperature modulations, both seasonal and short-term.*

*This chapter includes content from the following article: I. Riádigos, D. García-Castro, D. Gonzáles-Díaz, and V. Pérez-Muñuzuri. Atmospheric temperature effect in secondary cosmic rays observed with a 2 m^2 ground-based tRPC detector. *Earth and Space Science*, 7(9), p. e2020EA001131, 2020.

2.1 Introduction

Cosmic rays may provide valuable information for different research areas, such as space weather, high-energy physics, and cosmology [123, 79]. Specifically, ground-based instruments give us the chance to study the products of the interactions between primary cosmic rays and the nuclei in the atmosphere. These secondary particles traverse the atmosphere carrying information about its inner structure, as in a radiography, providing information about its properties. Secondary muons, in particular, are affected by atmospheric pressure and temperature (see Section 1.4). These induce local modifications of the atmospheric density and its depth, thereby changing the balance between particle production, absorption, and decay, affecting the muon rates at ground [51]. Since modern muon detectors are mostly committed to the study of solar activity and other astrophysical phenomena, such effects are regularly removed with simple techniques, as part of a calibration procedure [41]. Our work is concerned with a deeper comprehension of such atmospheric effects.

The temperature effect can be nearly one order of magnitude smaller than its pressure counterpart, requiring a much better control on systematic effects of instrumental origin and high statistics (detector size) in the first place. A precise estimate of the atmospheric temperature effect involves an implementation of the “integral method”, which requires, on the

one hand, knowing the temperature profiles above the detector and, on the other hand, knowing the distribution of temperature coefficients (W_T), the latter accessible by theoretical means [47]. Given that the detector used in this work was conceived to potentially make use of both the soft (electron) and hard (muon) cosmic ray component, the temperature coefficients (calculated for muons) are not known a priori. As discussed afterwards, the effect of the material overburden can not be completely neglected, nor easily characterized, either in the present case.

The main purpose of this work is to experimentally obtain the temperature coefficients for secondary cosmic rays at ground, resorting to a technology not used previously in this kind of studies. We will show how, despite the much higher dark rates customary of gaseous detectors as compared to plastic scintillators, two $\sim$2 m^2 planes of multigap timing RPCs operating at ground level are sufficient to isolate the temperature effect, a fact that results largely from the superb timing characteristics of the device.

2.2 The Cosmic Ray Detector

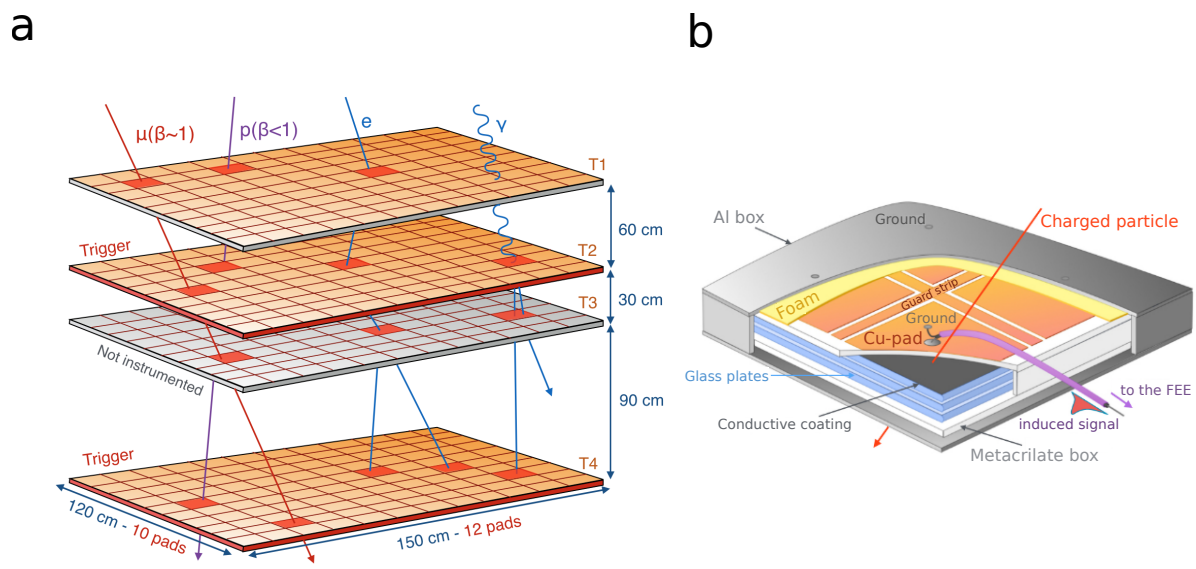

Figure 2.1: (a) Drawing of the cosmic-ray detector at Santiago de Compostela, showing the tRPC layout with some illustrative examples of different particle interactions. In the present analysis only the T2 and T4 RPC planes are used. (b) Inner view of the detector.

The tRPC technology was introduced to particle physics back in 2000 as a byproduct of the R&D program of the ALICE experiment at the Large Hadron Collider [62]. Indeed, multigap tRPCs have been adopted already for the study of high-energy cosmic rays by the EEE collaboration [2], but no study on the temperature effect has been reported by the collaboration yet. tRPCs are generally characterized by the use of thin sub-mm gas gaps operated in "fast" well-quenched gas mixtures at very high electric fields (up to $\sim$ 150 kV/cm). Stability of operation requires the use of insulating materials with high surface quality, something conventionally achieved through soda-lime glass. tRPCs can make optimal use of the multi-gap

technique [185], which allows for the systematic stacking of several gas gaps, in order to achieve time resolutions down to 20 ps in special configurations [12]. In fact, tRPCs have recently demonstrated the capability of reaching 60 ps on 2×2 m^2 areas, with a modest number of electronic readout channels around 160, and a position resolution at the cm-scale [170] (review Section 1.3.1 for more details).

At the University of Santiago de Compostela (Spain), a medium-size tRPC detector (1.2 $\times$ 1.5 m^2) with a space and time resolution of $\sigma_{x,y} \sim 3$ cm and $\sigma_t \sim 300$ ps, respectively, has been installed circa 2014 as part of the Trasgo Project [21, 26]. It is named TRAGALDABAS (TRAsGo for the AnaLysis of the nuclear matter Decay, the Atmosphere, the earth B-Field And the Solar activity), and it has been designed and built at LabCAF in collaboration with LIP (Laboratory of Instrumentation and Experimental Particel Physics at Coimbra) (e.g., [3]). The angular resolution with its present vertical layout is 2-3° and the maximum zenith angle of the accepted tracks is close to 50° (Figure 2.1a). Unlike other cosmic ray detectors, TRAGALDABAS has a relatively small active area of 1.8 m^2. For comparison, the MuSTAnG detector [83] had a surface of 4 m^2 and all four telescopes of the Global Muon Detector Network (GMDN) extend over around 15-30 m^2 [133]. The TRAGALDABAS detector setup can be seen in Figure 2.2.

The detector consists of four RPC planes with a total height of 1.8 m (Figure 2.1a). Each plane's inner design is based on three plates of 2 mm glass with a 1 mm gas gap interleaved, placed inside a gas-tight acrylic box. Tetrafluoroethane, a type of freon (R134a, CF_3CH_2F), is used as the active medium, at a very low flow, just sufficient to keep the detector efficiency constant over time. It operates at a pressure of a few mbar over atmospheric pressure (in order to mitigate air back-flow at the exhaust, but at the same time avoiding mechanical stress). The external sides of the outer glass plates are covered with a semi-conductive coating (acrylic paint) to which a $\pm$ 5600 V high voltage is applied. Electrical pick-up signals, stemming from the avalanches produced in the gas upon the passage of a charged particle, are induced in some of the 120 copper pads (each one with an area of 111×116 mm^2) placed outside of the acrylic box (Figure 2.1b). Those signals are processed with fast $\sim$ 1 GHz BW electronics [21] and, if above an adjustable threshold, a digital LVDS (low-voltage differential signaling) signal is produced, marking the passage of the particle (we will refer to the associated pad and plane as "fired"). A flexible trigger condition can be formed for any number of fired planes and pad multiplicity per plane, a digital signal formed, correspondingly, and sent to the acquisition in order to store the cosmic ray candidate. The telescope is placed at $\sim$260 m above sea level, 42°52'N 8°33'W, at a geomagnetic rigidity cutoff of $R_c \sim$5.5 GV, on the first floor of a two-story building. It is running since 2015 with a room temperature stable at 20 $\pm$ 1°C.

Finally, any background noise that may affect the recorded rates must also be taken into consideration. The neutron albedo could be an unwanted source of noise. This refers to neutrons generated by collisions of secondary CR with land surface materials such as soil, water, snow, biomass, etc. They can backscatter and pass through the detection area. It is important to highlight that, except in special configurations (e.g., [25, 111]), RPC detectors have intrinsically a very low detection efficiency for neutrons below 10 MeV, not exceeding 0.1%. Moreover, neither the products from neutron interactions nor electrons from neutron decay at these energies can traverse a second detection plane, as required in the present analysis. Hence, if assuming a typical albedo neutron flux of $\sim$1 kHz/cm^2 [88], the detector can be effectively considered as neutron-blind, for the purposes of the present analysis.

Figure 2.2: Photo of the TRAGALDABAS detector at the Faculty of Physics of the Univ. of Santiago de Compostela (Spain).

2.3 Input data and processing

We report here data from the commissioning phase and early physics run (from October 2015 to January 2017), where only two detector planes, stacked over a height of 120 cm, were used (T2 and T4 in Figure 2.1a). A trigger condition was defined as "at least one fired pad per plane, in time coincidence". During data analysis, a standard equalization is performed automatically, aimed at the correction of the channel-by-channel variations in the time offsets and signal amplification along the lines of [98]. Provided both charge and time information are stored for each pad, noise signals (displaying zero-charge) can be removed in the next

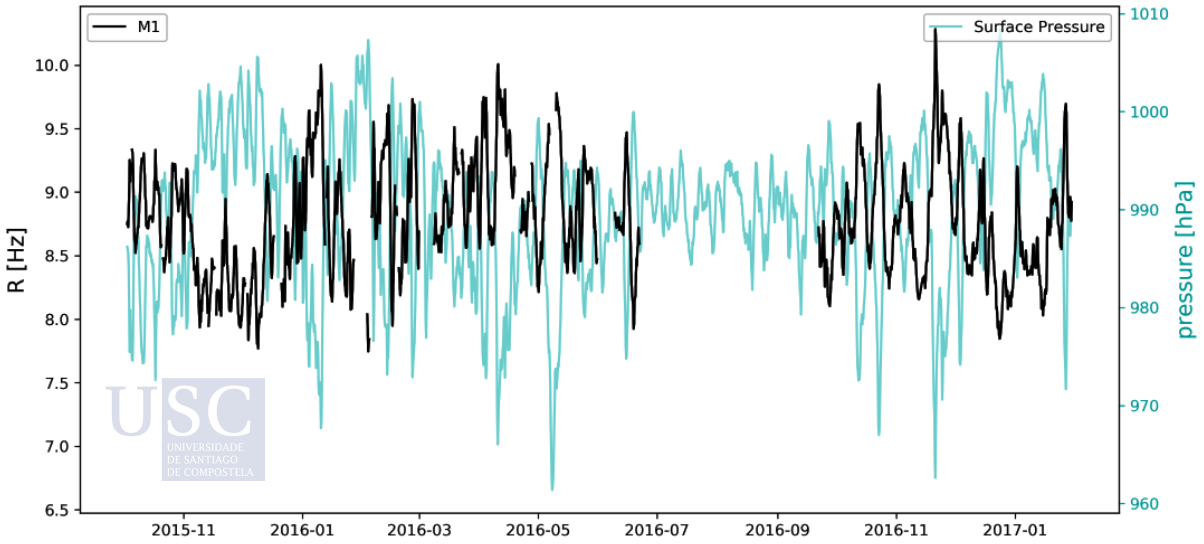

Figure 2.3: Cosmic ray rate for single vertical tracks as observed with the muon telescope (black curve) and ground-level pressure (blue curve).

processing step. Finally, "particle tracks" are formed by combinatorially matching the fired pads in both planes with a velocity compatible with the speed of light, within a 3-σ_t interval, σ_t being the time resolution of the detector. This produces the final data sample ready for physics analysis, where any instrumental effects should be greatly minimized. We use in this work a data sub-sample, corresponding to events with a single track (multiplicity $M = 1$), and a zenith angle θ lower than 13°. The former condition means that only cases with one fired pad per plane have been considered. The resulting mean rate is R= 9.05 Hz.

The complete data taking period, displayed in Figure 2.3, may be conveniently divided into three phases:

- From October 2015 to June 2016. During this first period the detector was run semi-autonomously (several interventions were needed) and problems related to faulty front-end electronics and high voltage instabilities were observed.
- From June 2016 to October 2016. Maintenance work was carried out, the faulty electronics modules were replaced, and an online monitor was developed.
- From October 2016 to January 2017. The detector run in stable conditions, in a fully autonomous way.

Concerning the atmospheric variables, the vertical temperature profiles were retrieved from the European Centre for Medium-Range Weather Forecast (ECMWF) reanalysis, ERA-Interim [42], for the 1979-2017 period, at 37 isobaric levels (1000, 975, 950, 925, 900, 875, 850, 825, 800, 775, 750, 700, 650, 600, 550, 500, 450, 400, 350, 300, 250, 225, 200, 175, 150, 125, 100, 70, 50, 30, 20, 10, 7, 5, 3, 2, 1 hPa), with a horizontal spatial resolution of 0.125° and a temporal resolution of 6 h.

The surface pressure data is provided by a weather station of the Galician Regional MetOffice (MeteoGalicia) located at ∼100 m from the detector.

Two exemplary temperature profiles for summer and winter at the Santiago de Compostela location are shown in Figure 2.4. Two important features are revealed from this image. Firstly, we can see how in the wintertime, the atmosphere is more compact and colder, and, as a consequence, the location of the tropopause is lower in the atmosphere (∼300 hPa). Sencondly, the tropopause region (100-300 hPa) is found much cooler in summer than in winter. We will see later how this circumstance becomes relevant.

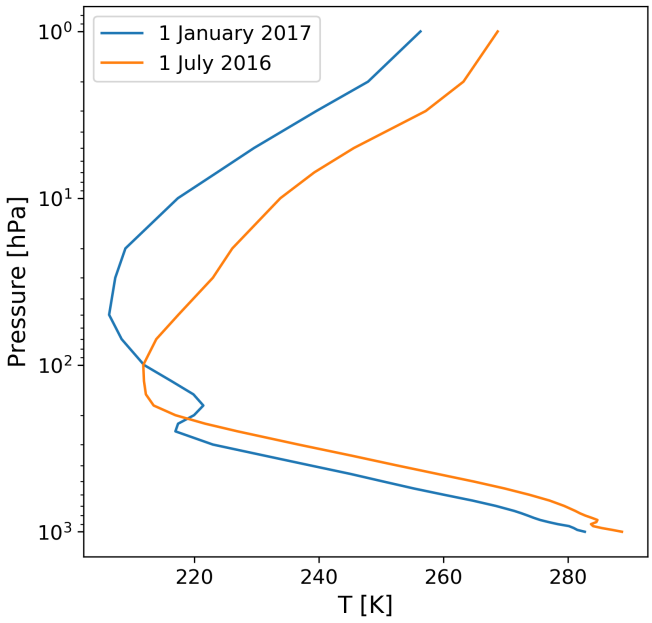

Figure 2.4: Examples of ERA-INTERIM atmospheric temperature profiles for Santiago de Compostela, summer (1 July 2016) and winter (1 January 2017).

2.4 Analysis of Atmospheric Effects

As mentioned before, several methods can be used to take into account the temperature effect of secondary cosmic ray particles in the atmosphere [24, 23, 51, 56, 135]. The integral method is one of the most precise [40, 46] but it requires knowing the distribution of the temperature coefficients in the atmosphere, $W_T(h)$. These can be theoretically calculated for different threshold energies, zenith and azimuth angles of incidence [47], or extracted from CR data [177]. In this work, we compare both approaches.

An experimental determination of $W_T(h)$ is not straightforward, and requires special statistical techniques, given the presence of strong correlations between the temperatures of the different atmospheric layers. For illustration, Figure 2.5a shows a scatter plot of the temperatures corresponding to two different layers, from January 2015 to December 2016, and Figure 2.5b shows the pairwise correlation matrix obtained for the temperatures of the different atmospheric layers on top of the detector for the same period. In general, the low stratosphere ($\sim$250-70 hPa) behaves opposite to the troposphere ($\sim$1000-250 hPa) and high stratosphere ($\sim$70-1 hPa). This is because the boundary layer ($\sim$925 hPa) is positively correlated with the rest of the troposphere through convection, while an increase in its temperature will generally result in the low stratosphere cooling down. This is a typical condition observed for latitude regions above 40° [107].

In the troposphere, heating is associated with convection in the tropics, while the cyclone-anticyclone dynamics in the mid-latitudes is the one forcing the air mixing. Colder regions have a lower tropopause because convection is limited there, for instance, in the polar regions. In general, if the tropopause rises, its temperature decreases. In mid-latitude regions, the cyclonic structures are characterized by a low tropopause, in association with a relatively cold troposphere and a warm lower stratosphere. In contrast, anticyclones uplift the tropopause and relate to a warm troposphere and a cold lower stratosphere. This explains the

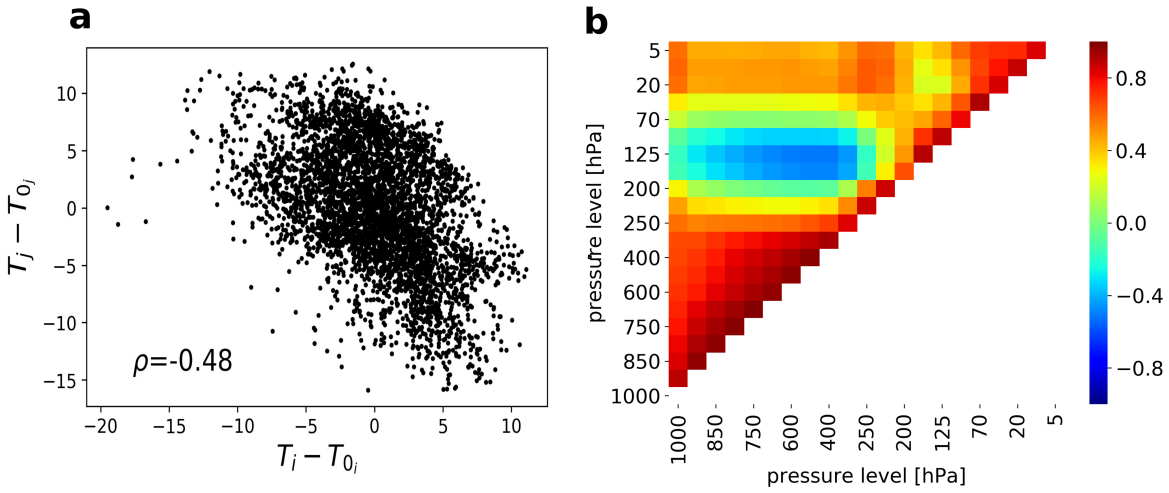

Figure 2.5: (a) Correlation between temperatures for the atmospheric layers i=125 hPa and j=700 hPa ($T_{0i,j}$ is the mean value of each layer). (b) Pairwise correlations between temperatures of the different pressure levels considered in this analysis for Santiago de Compostela (from January 2015 to December 2016).

paradox that tropopause temperatures are lowest where the surface temperatures are highest. To repeat, the extratropical tropopause temperature changes are positively correlated with the lower stratosphere and negatively correlated with those in the troposphere [139].

Figure 2.6 displays the correlations obtained for a high latitude location where the atmospheric conditions are radically different (Novosibirsk, Russia, 55°N 82°55'E). On this occasion, the correlations look quite different, especially in the mid-atmosphere.

Given these points, any attempt to obtain the temperature coefficients by means of a multivariate regression will result in coefficients whose values do not correspond to the actual values. If explanatory variables of a multiple regression model are strongly correlated, they provide redundant information and violate the condition of non-collinearity required in a least-squares regression. The coefficients will also be highly sensitive to small changes in the model and their sign will be dramatically dependent on the variables considered. In other words, slightly different models might lead to different conclusions. In this way, we would never know the actual effect of each variable. Clearly, any phenomenological model aimed at reliably describing the measured rates needs to start from a sensible set of uncorrelated temperature variables, that need to be obtained beforehand. We adapt for the task the Principal Components Regression (PCR) analysis, which has been successfully used before for this type of studies in [177, 137].

2.4.1 Barometric Effect

Being much subtler, the temperature effect must be analyzed once the pressure effect has been removed. Moreover, in the case of gaseous detectors, the efficiency is a function of the ratio of the applied electric field E and pressure P (represented by E/P and dubbed reduced field), so even a high voltage and T-controlled environment is not sufficient to stabilize the detector response completely [108]. The above dependency means that the detector efficiency is anticorrelated with pressure and will add to the barometric effect at ground. Considering the atmospheric effect first, the relative change in the secondary CR rate caused by variations of the

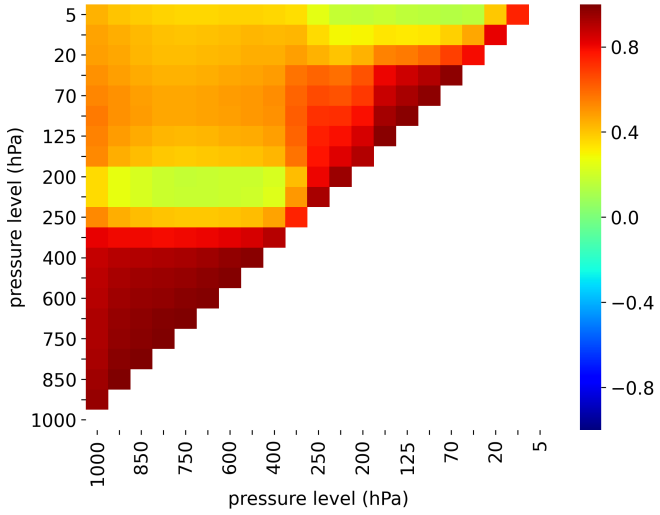

Figure 2.6: Pairwise correlations between temperatures of the different pressure levels for a location at a latitude of ∼55°N.

ground-level pressure has an exponential dependence. To first order approximation, it can be expressed through a linear relation:

$$\frac{R}{R_0} = e^{\beta_{atm}\cdot\Delta P} \rightarrow \left.\frac{\Delta R}{R_0}\right|_P \approx \beta \cdot \Delta P \tag{2.1}$$

where $\left.\frac{\Delta R}{R_0}\right|_P$ is the relative variation of the CR rate due to the pressure effect, R_0 represents its average value over the period under consideration, $\Delta P = P - P_0$ is the deviation of the ground-level pressure with respect to its mean value (P_0) over the same period, and $\beta = \beta_{atm} + \beta_{det}$ is the barometric coefficient, with β_{atm} representing the atmospheric effect and β_{det} the detector contribution.

The barometric coefficient was obtained separately for four different sub-periods, that displayed slightly different stability conditions (Table 2.1). An iterative linear fit was performed, with data outside a 2-σ interval removed from the fit (Figure 2.7). Compatible barometric coefficients were obtained, whose mean value was determined to be $\beta = -0.59 \pm 0.02$ %/hPa. This methodology allows us to remove any outliers in the data caused by detector instabilities and occasional space weather effects such as Forbush decreases or interplanetary events.

Finally, the barometric effect is removed using:

$$\left.\frac{\Delta R}{R_0}\right|_T = \left.\frac{\Delta R}{R_0}\right|_{obs} - \left.\frac{\Delta R}{R_0}\right|_P \tag{2.2}$$

where $\left.\frac{\Delta R}{R_0}\right|_{obs}$ are the experimental CR variations and $\left.\frac{\Delta R}{R_0}\right|_T$ the remaining variations due to the temperature effect.

2.4.2 Temperature effect

Variations of the measured rate of the secondary cosmic component due to the atmospheric temperature effect can be approximated by a linear combination of some temperature

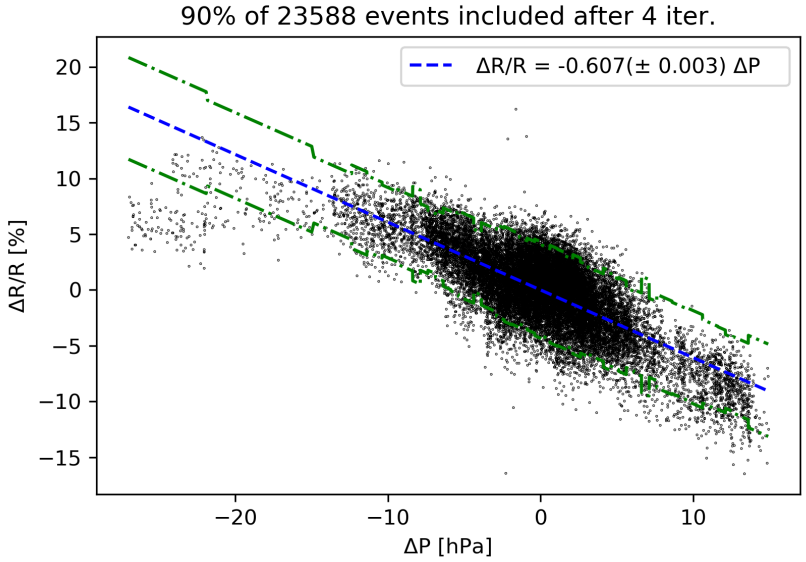

Figure 2.7: Example of the linear fit method used to obtain the barometric coefficient for one of the subperiods (3 October to 23 December 2015). The green lines delimit the points left out of a 2-σ interval after an iterative procedure. The blue line is the resulting regression line.

Period	β **[%/hPa]**
3 October 2015 - 23 December 2015	-0.607 $\pm$ 0.003
24 December 2015 - 20 September 2016	-0.602 $\pm$ 0.002
21 September 2016 - 22 November 2016	-0.583 $\pm$ 0.003
23 November 2016 - 10 January 2017	-0.568 $\pm$ 0.002

Table 2.1: Barometric coefficients for the different sub-periods.

coefficients and the temperature variations at n atmospheric layers [47], as discussed in Section 1.4.2 of the introductory chapter. Again, the corresponding expression is:

$$\left.\frac{\Delta R}{R_0}\right|_T = \sum_{i=1}^{n} W_T(h_i)\Delta T_i \Delta h_i \tag{2.3}$$

where $\left.\frac{\Delta R}{R_0}\right|_T$ are the relative variations due to the temperature effect; W_T, given in % K^{-1} atm^{-1}, is the corresponding temperature coefficient for the atmospheric layer i at pressure h_i; $\Delta T_i = T_i - T_{0_i}$ are the temperature variations within the same layer with respect to its mean value (T_{0_i}), and $\Delta h_i = h_{i-1} - h_i$ is the layer thickness, in atm.

Defining $k_{x_i} = W_T(h_i)\Delta h_i$, equation (2.3) can be rewritten as

$$\frac{\Delta R}{R_0}\Big|_T = \sum_{i=1}^{n} k_{x_i}\Delta T_i \tag{2.4}$$

that we denote formally as

$$\mathbf{y} = \mathbf{X}\mathbf{k_x} \tag{2.5}$$

where $\mathbf{y}$ is the vector of the measured relative variations $\frac{\Delta R}{R_0}\Big|_T$; $\mathbf{X}$ is the $(m \times n)$ data matrix of the temperature variations whose columns are the temperature variations of the i^{th} pressure level and $\mathbf{k_x}$ refers to the vector of temperature coefficients, that we want to estimate.

As mentioned earlier, the coefficients of this model can not be obtained by an ordinary regression. For our purpose, we decided to use the Principal Component Regression (PCR) technique [91]. This method is applied when a dataset of variables shows multicollinearity, in our case, the temperature variations. The idea is to build new uncorrelated variables (called principal components), maintaining the information conveyed by the original ones, and use them as the new predictors to estimate the unknown regression coefficients of the model.

The PCA consists of an orthogonal linear transformation that converts the original variables to a new coordinate system. The principal components (PCs) represent the directions of the data containing the highest variance. So, the first step is standardizing the ΔT_i measurements in $\mathbf{X}$, dividing them by their standard deviations (over the analyzed period). This standardization is needed to prevent the variables with the highest variance from dominating. It causes a change in the notation, too. To keep it simple, we maintain the current notation but taking into account that all the following calculations are based on standardized variables.

The principal components are the eigenvectors (directions) obtained from the covariance matrix of $\mathbf{X}$ and sorted by the amount of explained variance. This set of orthogonal vectors forms a new basis in the new coordinate system. The matrix $\mathbf{X}$ can be transformed using the matrix of eigenvectors, defined as $\mathbf{A}$ $(n \times n)$, in the following way

$$\mathbf{P} = \mathbf{X}\mathbf{A} \tag{2.6}$$

where $\mathbf{P}$ is now the matrix $(m \times n)$ containing the new variables in the new space. We got a set of uncorrelated variables because they were built using orthogonal eigenvectors. As a consequence, a new model can be built using variables $\mathbf{P}$:

$$\mathbf{y} = \mathbf{P}\mathbf{k_p} \tag{2.7}$$

Now, the new set of coefficients $\mathbf{k_p}$ can be obtained directly using least-squares regression. Taking into account equation (2.6), we can write

$$\mathbf{y} = \mathbf{X}\mathbf{A}\mathbf{k_p} \tag{2.8}$$

The regression coefficients $\mathbf{k_p}$ can be transformed back into the original space using equation (2.5) and (2.8)

$$\mathbf{k_x} = \mathbf{A}\mathbf{k_p} \tag{2.9}$$

and multiplying by standard deviations in order to go back to the original scale.

The year-to-year variability of the temperature data may affect the determination of the

principal components, particularly if exceptional temperature changes took place during the data acquisition period, such as Sudden Stratospheric Warmings (see more information in Appendix A.1). This can be seen in Figures 2.8 and 2.9, where several stratospheric temperature anomalies (warmings and coolings) can be seen during winter periods. Therefore, as a first step, we use a training dataset from a time series of the last 30 years to determine the PCs of the temperature data and avoid the influence of outliers corresponding to exceptional events.

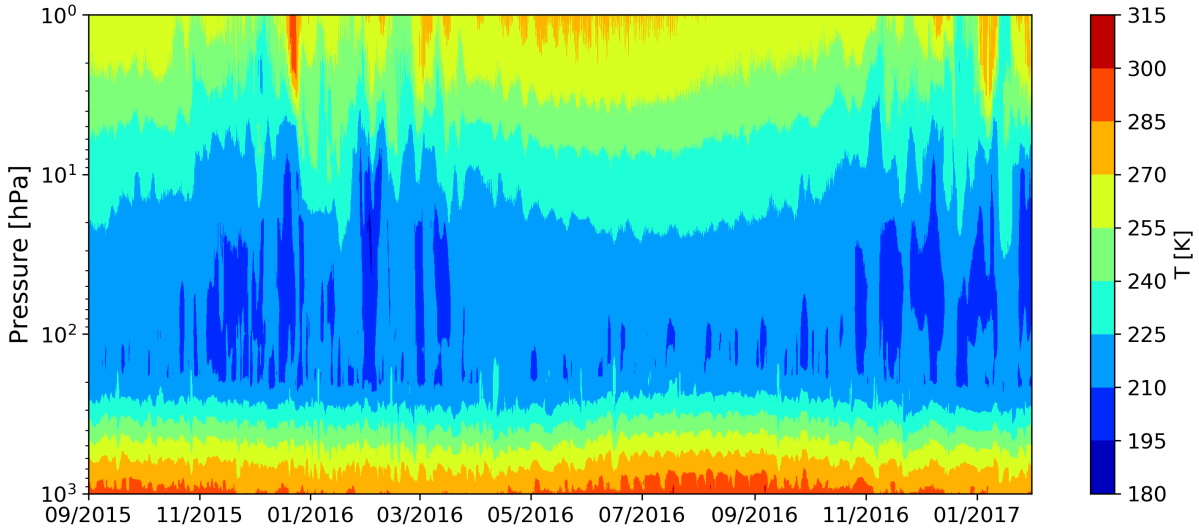

Figure 2.8: Temperature time series of the atmosphere in Santiago de Compostela from October 2015 to January 2017.

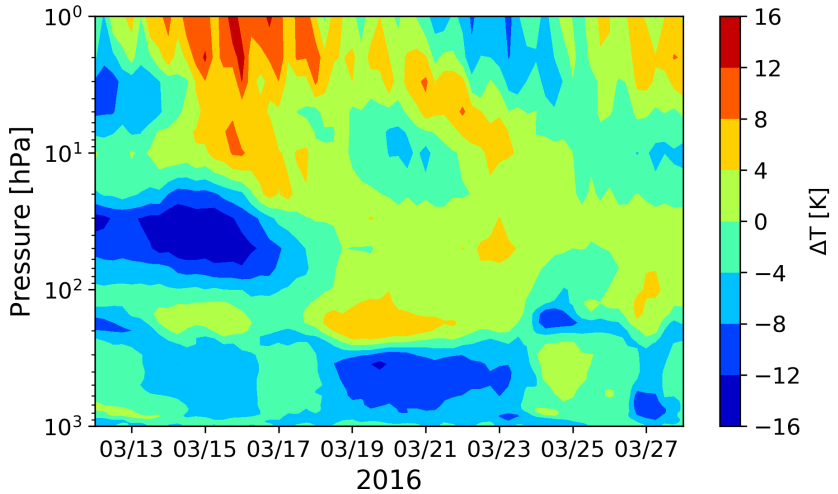

Figure 2.9: Temperature anomaly for March 2016 were an example of a Sudden Stratospheric Warming is observed in the first half of the month. The upper stratosphere warms rapidly in a few days propagating way down into the troposphere in the next weeks.

PCR typically uses only a significant subset of all the principal components $\mathbf{P}'$ to increase reliability. The components with higher variances are usually selected as the regressor variables for being the most important. No standard method exists for deciding how many components to retain. Anyhow, a good number of components should carry a high percentage of the total

variance ($> 70\%$). In order to decide the number of PCs to keep, we previously performed an analysis with reconstructed cosmic ray variations using a theoretical distribution of the temperature coefficients as a proxy [47]. These variations represent ideal data (i.e., without noise) only affected by the atmospheric temperature. Then, we apply the PCR method to these data to see how many PCs need to be kept in order to retrieve the original coefficients. To make this study more realistic, we follow the typical procedure of adding extra noise to the original data in three levels (low, medium, and high) to be able to analyze the performance of the technique. It was observed that with two components it is possible to restore the correct values of the coefficients until an acceptable level of noise. Including more components destabilizes the result (further details of the analysis can be found in Appendix B.1.1).

Finally, the vector of coefficients $\mathbf{k}'_{\mathbf{p}}$ is estimated by regressing the observed vector of cosmic ray data on the selected principal components $\mathbf{P}'$ using least-squares regression. So equation (2.7) is reduced to

$$\mathbf{y} = \mathbf{P}'\mathbf{k}'_{\mathbf{p}} \tag{2.10}$$

where $\mathbf{P}'$ is now a matrix $(m \times r)$ whose columns are the corresponding subset of columns of $\mathbf{P}$ (and $r < n$).

Using equation (2.9), $\mathbf{k}'_{\mathbf{p}}$ can be transformed back to the space of the actual temperature variables, providing the regression coefficients $\mathbf{k}_{\mathbf{x}}$ that characterize the original model. Also, the relation $k_{x_i} = W_T(h_i)\Delta h_i$ introduced before is taken into account when converting the estimated regression coefficients to the distribution of temperature coefficients W_T, having a dimension %/K·atm.

It must be noted that Partial Least Squares (PLS) regression could be an alternative to this technique because it is similar to PCR in that both select components that explain the most variance in the model. The difference is that PLS incorporates the response variable (the CR rate, in this case) into the analysis. One of the main reasons for not using this method is that our set of CR measurements is limited to a period of just two years, which would prevent a robust analysis.

2.5 Results and Discussion

Figure 2.10a shows the distribution of temperature coefficients for the secondary cosmic component recorded at sea level for vertical incidence (blue line), where only events with a zenith angle θ lower than 13° were selected. The PCR method was applied to four different sub-periods of the data in order to account for systematic effects, expected to be mostly of instrumental origin at this stage, but also any remaining space weather phenomena having similar timescales to temperature variations. The average value and error bars are obtained from this combined analysis.

As mentioned, the detector is placed in the first floor of a two-floor building. Therefore, the composition of the overburden material has been taken into account to estimate the value of the muons threshold energy, $E_{th} \sim 0.15$ GeV, which is important to compare our coefficients with the theoretical ones (these can be found on the basis of integrations of the distributions describing muon production and propagation in the atmosphere). For illustration, the theoretical distributions for different muon energy thresholds and zenith angle $\theta = 0^\circ$ (grey lines in Figure 2.10a) as given in [47] are shown. A good agreement with the ones obtained with PCR is

observed for low thresholds, while above 0.75 GeV a systematic deviation appears, specially close to ground level.

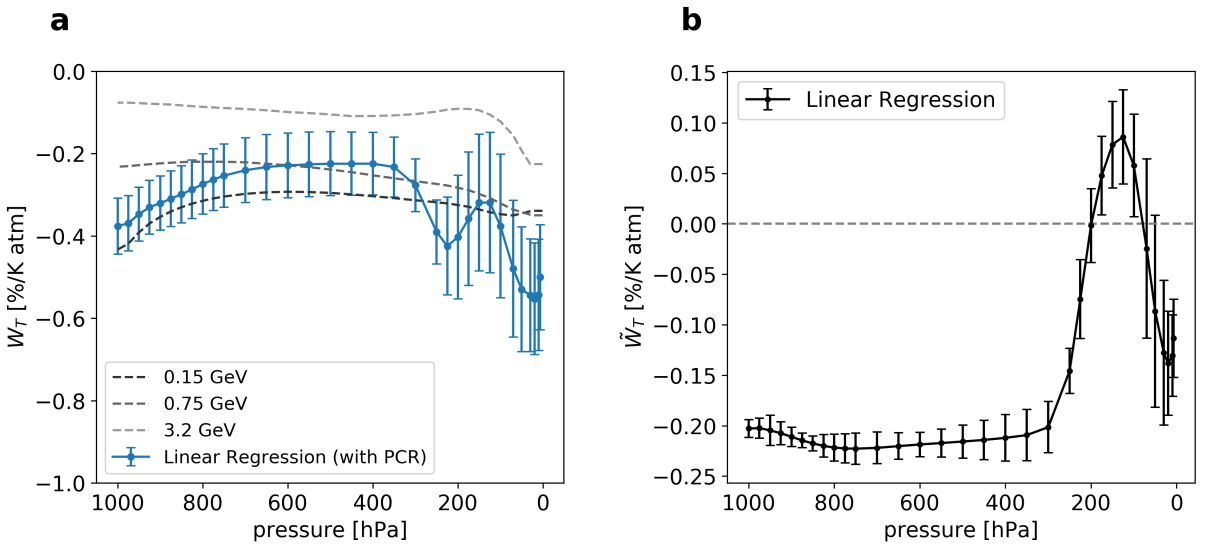

Figure 2.10: (a) Distribution of temperature coefficients obtained with PCR for vertical tracks and comparison with the theoretical distribution energy thresholds: 0.15, 0.75, and 3.2 GeV. (b) Slopes $\tilde{W}_T$ obtained through a direct linear regression for the same data sample ($\theta < 13°$)

Although being compatible, the estimated values in the troposphere (>300 hPa) are systematically above the theoretical ones. This might be a consequence of the method itself but could as well reflect the presence of the soft component in the measured rates, given that it anticipates a positive correlation with the lower layers of the atmosphere [51]. The values also differ at high altitudes, in this case due to the constraint in the selection of the number of principal components in the analysis. The PCR method computes the principal components taking into account the variance in the temperature data. Then, the first components reproduce the general variations in the troposphere and stratosphere (seasonal changes). Variations in the high atmosphere are considerably more complex than in the surface, as illustrated in Figure 2.5. Increasing the selected number of components would help to reduce this effect in an ideal situation. However, the optimum number of selected components in our case is the one that allows to obtain the best results of the coefficients without the solution being destabilized by noise and other instrumental effects. On the other hand, it should be noted that the accuracy of the ECMWF reanalysis is worse at high altitudes (0-200 hPa) due to the lack of data (less satellite/balloon observations, etc), so the temperatures have an inherent source of error that surely increases the difficulties in obtaining the coefficients at those heights.

Figure 2.10b shows for illustration the slopes determined before applying the PCR. Each coefficient $\widetilde{W}_T$ is obtained by direct regression between the relative variations of the CR intensity and the temperature variations for different layers:

$$\left.\frac{\Delta R}{R_0}\right|_T = \widetilde{W}_T(h_i)\Delta T_i \Delta h_i \tag{2.11}$$

These coefficients are dominated by the multiple correlations between the atmospheric layers. In particular, the slopes in the troposphere are negative, become positive in the low stratosphere, and return to negative values in the high stratosphere. The distribution of temperature

coefficients, $W_T(h)$, indicates that the contribution of the troposphere to the total rate variation is higher than the rest ($\sum_{i=1}^{trop}\Delta h_i/\sum_{i=1}^{n}\Delta h_i \sim 75\%$) and the values of the coefficients for this layer are negative. Therefore, when a direct regression is performed, the slopes $\widetilde{W}_T$ in the troposphere will be negative with values close to the real ones, W_T. The observed slopes in the high stratosphere will be negative due to the positive correlation with the troposphere (Figure 2.5). And the slopes in the low stratosphere are slightly positive due to the anticorrelation with the troposphere. A comparison with Figure 2.10b illustrates that these correlations have been largely removed with the PCR method.

Once the distribution of temperature coefficients W_T has been calculated, we can study the temperature effect. For this purpose, equation (2.3) can be used to build the so-called "effective temperature", which allows to consider the entire atmospheric temperature profile through an unique parameter:

$$\frac{\Delta R}{R_0}\Big|_T = \sum_{i=1}^{n} W_T(h_i)\Delta h_i \cdot \frac{\sum_{i=1}^{n} W_T(h_i)\Delta T_i \Delta h_i}{\sum_{i=1}^{n} W_T(h_i)\Delta h_i} = \alpha_T \Delta T_{eff} \tag{2.12}$$

Here the temperature coefficient α_T and the effective temperature T_{eff} are defined as

$$\alpha_T = \sum_{i=1}^{n} W_T(h_i)\Delta h_i \tag{2.13}$$

$$T_{eff} = \frac{\sum_{i=1}^{n} W_T(h_i) T_i \Delta h_i}{\sum_{i=1}^{n} W_T(h_i)\Delta h_i} \tag{2.14}$$

The definition of the effective temperature makes it possible to approximate the atmosphere as an isothermal body with a temperature T_{eff}, which is nothing but an average weighted by the product between the temperature coefficients and the atmospheric depth. It can be calculated using equation (2.14) with the corresponding temperature coefficients W_T. Moreover, the theoretical value $\alpha_{T_{theor}} = -0.319$ %/K is obtained using equation (2.13) for $E_{th} = 0.15$ GeV. In our case, it can be experimentally calculated using the values of W_T obtained by the PCR method:

$$\alpha_{T_{exp}} = -0.279 \pm 0.051 \ \%/\mathrm{K}$$

That is compatible with the theoretical one and also hints at the presence of the soft component, which could be the reason for the slight increase.

A complementary approach exists using the so-called mass-weighted temperature T_{MSS} and its corresponding coefficient α_{MSS} [40]. In this case, the CR variations due to the temperature effect are approximated by

$$\frac{\Delta R}{R_0}\Big|_T = \alpha_{MSS}\Delta T_{MSS} \tag{2.15}$$

$$T_{MSS} = \sum_{i=1}^{n} T_i \cdot \left(\frac{x(h_i) - x(h_{i+1})}{x(h_0)}\right) \tag{2.16}$$

where $x(h_i)$ is the atmospheric depth at the same altitude. Indeed, a very recent study from the GMDN [113] found a relation between the mass-weighted temperature coefficient and the cutoff rigidity (R_c) and latitude (L) for vertical incidence:

	Theoretical (Dmitrieva *et al.* [47])	This work (PCR)	$\Delta\alpha$
α_T (%/K)	-0.319	-0.279 $\pm$ 0.051	0.040 $\pm$ 0.051
	Mendonça *et al.* [113]	This work	$\Delta\alpha$
α_{MSS} (%/K)	-0.271	-0.233 $\pm$ 0.045	0.038 $\pm$ 0.045

Table 2.2: Values of the temperature coefficients α_T and α_{MSS} obtained in this work, together with the deviation from independent estimates, dubbed $\Delta\alpha$. (For comparison, the value obtained using a direct linear regression from Fig. 2.10b gives α_T=-0.163 $\pm$ 0.005 %/K)

$$\alpha_{MSS} = -0.304 + 0.0389 \cdot \ln R_c - 0.0488 \cdot \sin L \tag{2.17}$$

Introducing in this equation the values for R_c and L corresponding to the location of our detector, we anticipate a temperature coefficient of -0.271 %/K. On the other hand, the application of a linear regression to our data following equation (2.15) gives $\alpha_{MSS} = -0.233 \pm 0.045$ %/K, which again points to contamination from the soft component. Our analysis is summarised in Table 2.2, highlighting the deviation from the other two estimates discussed in this work ($\Delta\alpha$). The fact that $\Delta\alpha$ is similar for both α_{MSS} and α_T, suggests a common origin to the observed excess, despite its small statistical significance.

Figure 2.11 shows the secondary CR after pressure correction compared with the estimated temperature effect modeled through our two main PCs and their corresponding regression coefficients. The evolution of the effective temperature is shown as well. It is possible to appreciate the typical seasonal behavior reported by other detectors: CR rate reaches its maximum in winter when the atmosphere is colder while it declines towards summer when it is warmer. Moreover, the procedure is able to interpolate the temperature effect in those periods of missing data, such us July and August of 2016. Overall, the estimated temperature effect is able to reproduce $\sim 77\%$ of the variability of the observed data, demonstrating that the PCR is a reasonable method to recover the seasonal variability.

A significant behavior is also observed at the end of 2016: rates show an abrupt decrease followed by a major increase (see zoom in Figure 2.11). The PCR method is able to reproduce this trend as well. If the temperature variations of this period are analyzed, several cooling and warmings are observed: a Sudden Stratospheric Warming in the high stratosphere takes place, followed by a great cooling of at least -40 K. However, an opposite behavior is observed in the low stratosphere.

The sign of the calculated distribution of the coefficients W_T (Figure 2.10a) indicates that the negative temperature effect dominates throughout the atmosphere. This means that if the temperature varies in any atmospheric layer, the measured rate will vary in inverse proportionality to that indicated by the corresponding coefficient. Bearing this in mind, we can expect a measured rate decrease due to the increase of temperature in the troposphere and high stratosphere. However, the reduction of the temperature of the low stratosphere, given the presence of correlations between layers, will tend to increase the rates. The effective

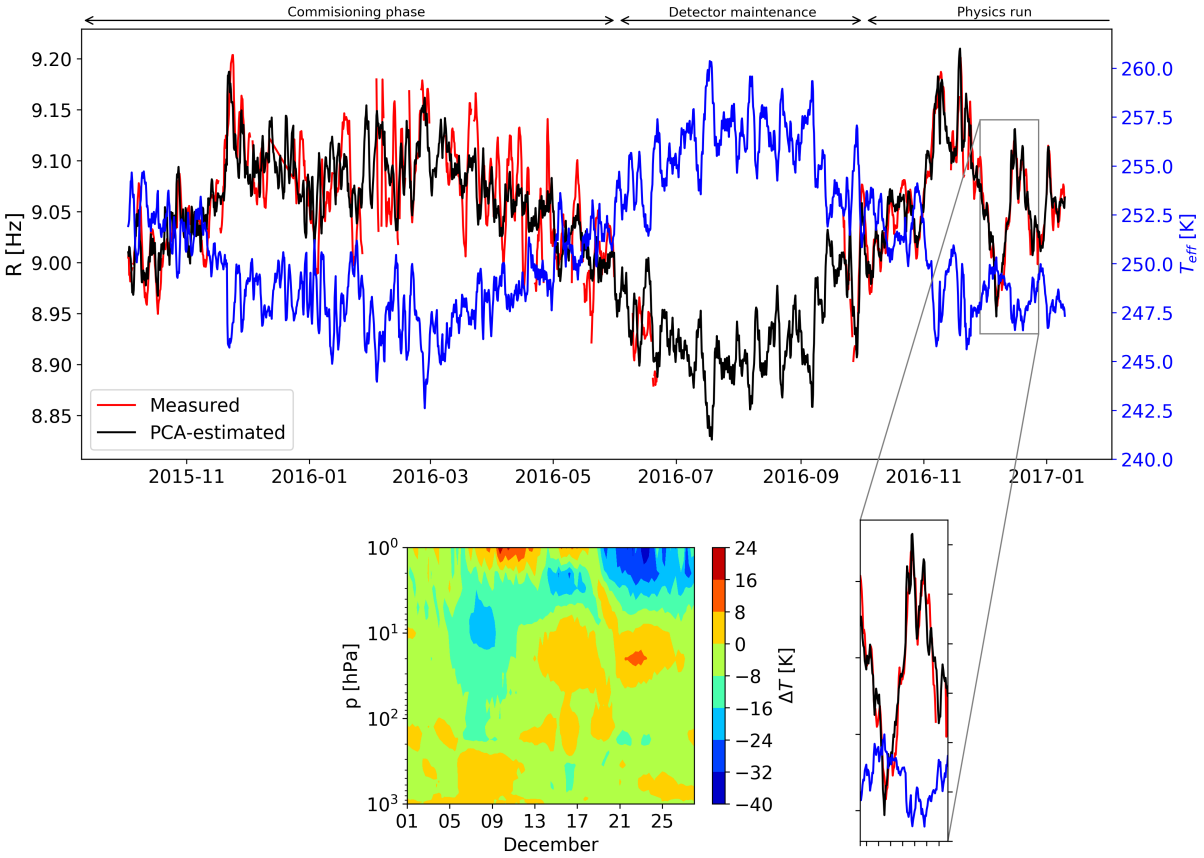

Figure 2.11: (Top) Cosmic ray rate corrected by pressure as observed by the TRAGALDABAS detector (red curve) and calculated via PCR method (black curve) compared with the effective temperature (blue curve). (Bottom) Zoom into the December 2016 sudden stratospheric warming event, and P, ΔT map on that period.

temperature describes the global effect of these different temperature variations. In this case, as the layers of the troposphere have more weight ($\sim$75% of the total atmospheric mass) with respect to the stratosphere, their effect is dominant, and that is why the seasonal evolution of the effective temperature in Figure 2.11 is similar to the surface temperature and appears anticorrelated with the observed rates.

To sum up, this is the first demonstration that the multigap timing RPC technology can be successfully applied to studies about the atmosphere condition, in particular its temperature profile. With the commissioning phase already over and the detector fully operative, additional work could focus on carrying out differential studies on the angular response as well as carefully correcting for space weather phenomena.

2.5.1 Monitoring a Forbush Decrease

The distribution of temperature coefficients can be used, along with the barometric coefficient, to remove the atmospheric effects and analyze space weather phenomena. This is briefly described in this section with the analysis of a Forbush Decrease since a more detailed analysis is pending for future work.

As mentioned in the introduction of this chapter, CR measurements provide valuable data for different research areas, in particular space weather. But as we have seen so far, when analyzing variations in CR intensity using ground-based detectors, atmospheric effects cannot be ignored. The pressure and temperature effects produce significant variations. Therefore, it is important to remove those in order to study any solar or interplanetary phenomena [51].

In June 2015 the Sun was very active and produced a significant number of coronal mass ejections towards the Earth, initiating a large FD event (more information at the Soho/Lasco CME Catalog [68]). A FD may be caused when a solar wind disturbance travels away from the Sun towards the Earth, affecting the galactic cosmic ray flux, which conveys the most energetic particles coming from outside the heliosphere. Such disturbance will produce a region of suppressed CR density located downstream of the coronal mass ejection, behind the interplanetary shock which this fast ejection produces in the medium ahead of it. In such a case, the CR intensity at ground shows a fast decrease, reaching a minimum within about a day, followed by a slow recovery phase lasting for several days (see Sections 1.5.1 and 1.5.2) [33].

The decrease in the TRAGALDABAS counting rate on 22 June 2015 corresponds to the the first FD registered over the period from 2015 to 2017. Figure 2.12 shows the relative variations before corrections (grey), corrected only by pressure (blue) and corrected by both temperature and pressure (red) in the period from 18 June to 6 July 2015. A fast decreasing phase is observed after pressure corrections, reaching a minimum in a couple of days of about $\sim$4%, and followed by a slow recovery phase during the next days. Without atmospheric corrections, this characteristic FD behavior is not discernible.

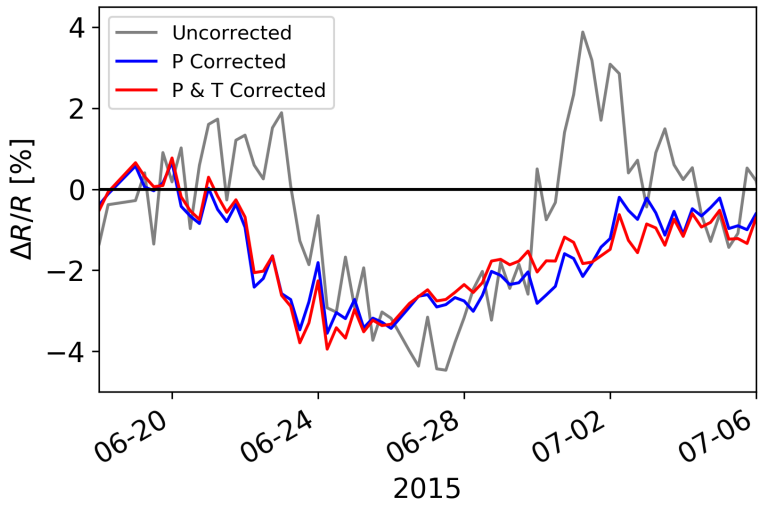

Figure 2.12: Forbush Decrease event on 22 June 2015: uncorrected (gray curve), only pressure corrected (blue curve), and pressure and temperature corrected variations (red curve).

2.6 Conclusions

The work presented in this chapter was designed to analyze in detail the atmospheric effects on cosmic-ray measurements at the surface performed with a small-size multigap timing RPC detector.

Using the specific Principal Component Regression technique designed to deal with the presence of multiple correlations in the atmospheric data, we were able to experimentally obtain the temperature coefficients $W_T(h)$ as well as the effective parameter $\alpha_{T_{exp}} = -0.279 \pm 0.051$ %/K, and compare them with the theoretical values. As a result, we were able to determine the effective atmospheric temperature and thereby identify its seasonal modulation along with short-term events known as Sudden Stratospheric Warmings. Furthermore, the results are consistent with a clear dominance of the hard component and a small contribution from the soft component.

The results of this study support the idea that small-size multigap tRPC detectors, which are more affordable and practical compared to larger assemblies, could be a good choice for ground-based cosmic-ray monitoring and its related atmospheric research.

Chapter 3

Revisting the limits of atmospheric temperature retrieval from cosmic-ray measurements

Abstract: *A priori, cosmic-ray measurements offer a unique capability to determine the vertical profile of atmospheric temperatures directly from surface measurements. However, despite the increased understanding of the impact of the atmosphere on cosmic-ray rates, attempts to explore the technological potential of the latter for atmospheric physics remain very limited. In this Chapter, we examine the intrinsic limits of the process of cosmic-ray data inversion for atmospheric temperature retrieval, by combining a detection station at ground with another one placed underground at an optimal depth, and making full use of the angular information. With that aim, realistic cosmic-ray data with the temperature-induced variations included has been simulated using atmospheric profile databases and will be used as input for the inverse problem. Different aspects of the configuration and combinations of angular channels are examined using this data. Following this, the obtained temperatures are compared to the original temperature data. We analyze how the method presented for retrieving temperatures compares with previous works and how it exhibits a significant improvement in terms of temporal and spatial resolution.*

*This chapter includes content from the following article: I. Riádigos, D. González-Díaz, and V. Pérez-Muñuzuri. Revisting the limits of atmospheric temperature retrieval from cosmic-rays measurements. *Earth and Space Science*, 9, e2021EA001982, 2022.

3.1 Introduction

Cosmic rays have offered an exceptional way to observe the world around us from different points of view. As we have seen in the previous chapter (Chapter 2), the major factors influencing CR rates at ground are surface pressure and the temperature profile of the atmosphere. The "temperature effect" associated with the latter is described through the so-called temperature coefficients, $W_T(h, \theta, E_{th})$. These are given as a function of height, depending on the angle of incidence and the threshold energy of the muons.

An analogy can be drawn between satellite and cosmic-ray measurements when targeting atmospheric temperature retrieval. Weather satellites employ the observations of electromagnetic radiations emitted by the atmosphere, that depend on its state. Temperature-dependent weighting functions, based on competing emission and absorption processes, need to be established beforehand for each atmospheric layer. Besides, they depend on the energy of the measured radiation [60]. The inverse problem of retrieving the atmospheric temperature profile can be solved by combining several energy channels. By the same token, CR measurements at different angles and energies (ground/underground) may be used for the same purpose.

The following section will introduce a real case of data inversion, which will serve as an illustration to understand the constraints that must be taken into account when solving the inverse problem. Subsequently, we will proceed to characterize and evaluate in detail the methodology for retrieving the atmospheric temperatures.

3.2 A Case Study of Inverse Problem: Canfranc (LSC)

Flux and angular distribution of high-energy muons have been measured underground at Canfranc Underground Laboratory (LSC), located under Mount Tobazo (1980 m) in the Aragonese Pyrenees [161]. Figure 3.1 shows the characteristic mountain profile along the railway tunnel under Tobazo, where the laboratory is located. To measure the CR flux, a muon monitor based on an array of scintillators arranged in 3 planes has been installed [101]. This station has the capability to track the muon trajectories and thus extract the angular distributions. It is worth mentioning the relatively small size of the detector, with an active area of 0.95 m2. Figure 3.2 shows the angular distribution of the muon flux measured in the LAB2400 as a function of the zenith and azimuth angle. The experiment used a sample recorded between October 2015 and March 2018. The asymmetry seen in the figure corresponds to the profile of the mountain above the laboratory. Muons are absorbed as they pass through the rock, so the more slant depth traversed, the less intensity detected in that particular direction. As a matter of fact, the maximum intensity observed corresponds to the direction of the Rioseta valley.

These intensity values correspond to the average obtained during the period of

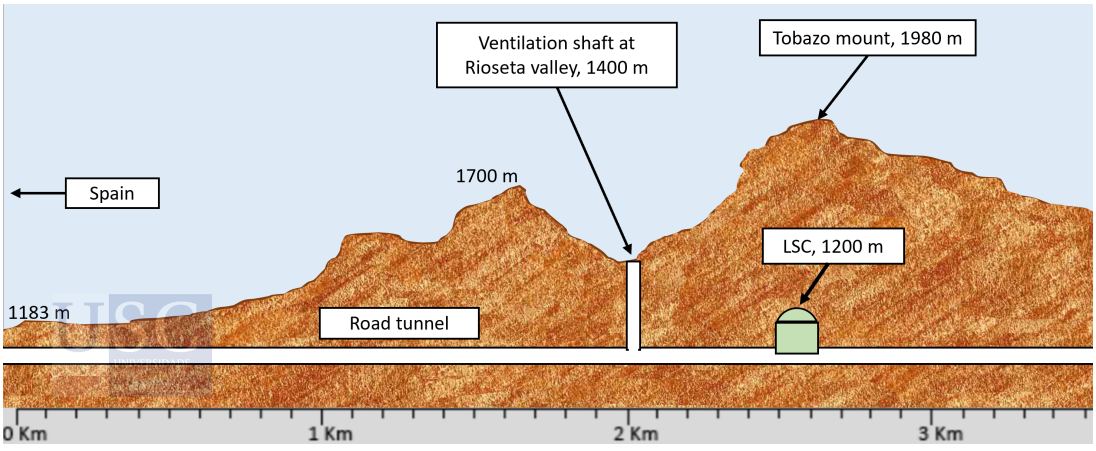

Figure 3.1: Mountain cross section along the railroad tunnel that joins Spain and France under Mount Tobazo (1980 m). The LSC can be found at ∼800 m under Tobazo.

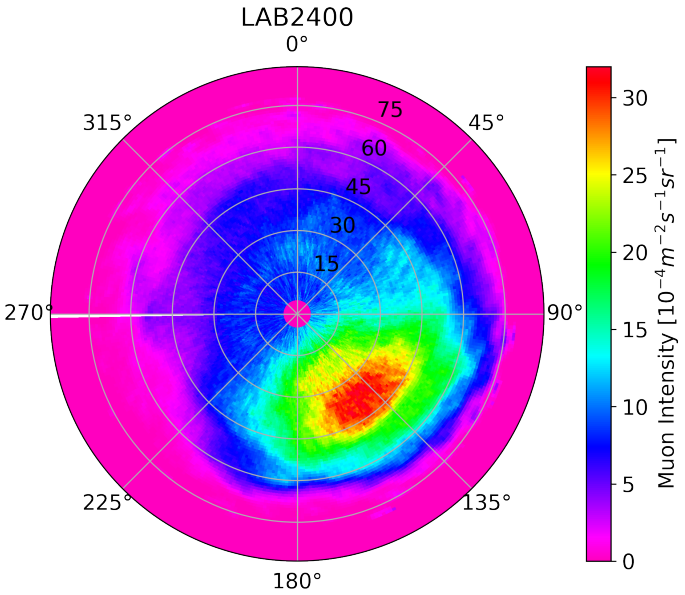

Figure 3.2: Muon intensity measured at Cranfanc Underground Laboratory (LAB2400) as a function of the zenith and azimuth angle (θ, ϕ). The maxima observed around $\theta = 40°$ and $\phi = 150°$ corresponds to the direction of the Rioseta valley [161].

measurement. Now, we would like to estimate the corresponding temperature effect in this data. To do this, we first need to know the threshold energies of the observations.

There is an empirical relation that correlates the muon intensity from a given direction with the slant depth [106, 9]:

$$I(X) \approx I_u \left(\frac{X_0}{X}\right)^{\eta} e^{-\frac{X}{X_0}} \tag{3.1}$$

where $I_u = 2.15 \pm 0.08 \times 10^{-6}$ cm^{-2}s^{-1}sr^{-1}, $\eta = 1.93^{+0.20}_{-0.12}$ and $X_0 = 1155^{+60}_{-30}$ mwe (meter water equivalent) [7].

At the same time, we have seen in the Introduction (Section 1.3) the equation that gives the minimum energy, namely threshold energy, required for a muon at the surface to reach a depth X (Eq. 1.2).

Therefore, we can estimate the depth for the different directions of the data displayed in Fig. 3.2 using equation 3.1 and then calculate the threshold energy by means of equation 1.2. Once we obtain the threshold energies for each angular bin in Fig. 3.2, we can plot a histogram grouping values of similar threshold energies to evaluate the statistics of the measurements. For the purpose of the analysis, we transform intensity rates to number of counts, N:

$$N = I \cdot A \cdot \Delta t \cdot \Delta\Omega \quad (\equiv R_0 \Delta t) \tag{3.2}$$

where I is the intensity in units of cm^{-2}s^{-1}sr^{-1}, A is the area of the detector, Δt is the measurement time, and $\Delta\Omega$ corresponds to the solid angle of the angular bin. The statistical fluctuations associated to N are then given by $\sqrt{N}$. Assuming a measurement time of 24 h and including the detector size, we obtain the number of muons recorded for each angular bin, that we group with $E_{th} \cdot cos\theta$, as shown in Figure 3.3. The bars represent the errors associated with

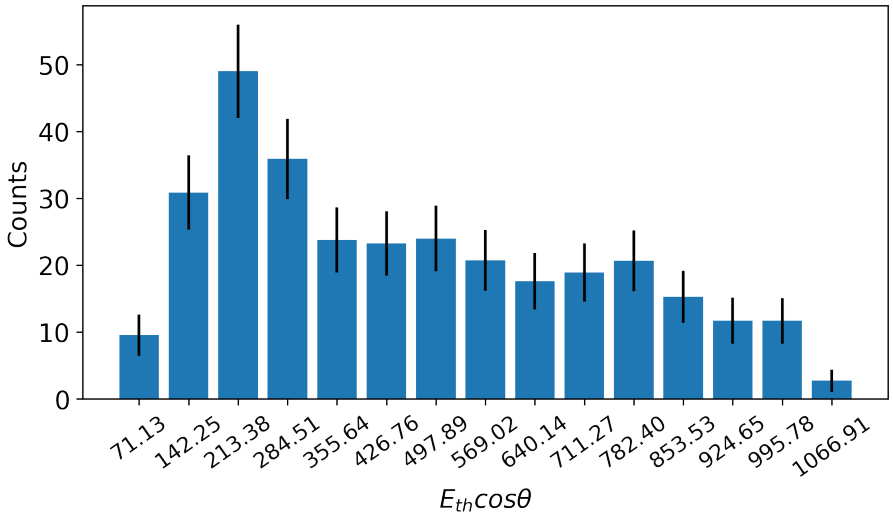

Figure 3.3: Estimated number of muons for each energy threshold $E_{th} \cdot cos\theta$ for a time step of 24 h at the LSC site. The error bars represent the standard error for Poisson counting.

counting. Figure 3.3 gives us an idea of the daily counting values of the detector as well as the features of the measurements. First of all, it is apparent from this plot that Canfranc has the potential to measure a wide range of threshold energies, from ∼70 GeV to ∼1000 GeV. It should be recalled that this is a consequence of the unique profile of the mountain. Secondly, the counting values are about 20 on average but there is a significant difference between the maximum and the minimum counting. Furthermore, these estimated values are relatively small and thus have statistical errors of ∼20 %.

Now, we are interested in determining the temperature-induced variations at Canfranc location. Using the values of $E_{th} \cdot cos\theta$, we can compute the corresponding effective temperature using the analytic expression given for high energies [6]:

$$T_{eff} \simeq \frac{\sum_{n=0}^{N} \Delta X_n T(X_n)(W_n^{\pi} + W_n^{K})}{\sum_{n=0}^{N} \Delta X_n (W_n^{\pi} + W_n^{K})} \tag{3.3}$$

where $W^{\pi,K}(X)$ are weights, i.e. temperature coefficients, depending on pressure level X_n and $E_{th}cos\theta$:

$$W^{\pi,K} \simeq \frac{(1 - X/\Lambda'_{\pi,K})^2 e^{-X/\Lambda_{\pi,K}} A^1_{\pi,K}}{\gamma + (\gamma+1) B^1_{\pi,K} K(X) (\langle E_{th} cos\theta \rangle / \varepsilon_{\pi,K})^2} \tag{3.4}$$

The parameters $A^1_{\pi,K}$ and $B^1_{\pi,K}$ refer to meson production and attenuation in the atmosphere, $1/\Lambda'_{\pi,K} \equiv 1/\Lambda_N - 1/\Lambda_{\pi,K}$ relates the attenuation lengths of the primary cosmic rays, pions and kaons, which are Λ_N, Λ_π and Λ_K, respectively. The temperatures values at different pressure levels included in the expression 3.3 are obtained from ERA5 reanalysis database for the Canfranc location [81].

The point is that we have to take into account the different variations that affect the real CR measurements if we want to use the data to access the temperature profile through the inverse problem. As we have seen in the previous chapter (Chapter 2), muon intensities are subject to variations of different origins. Here, we only assume those due to the temperature effect

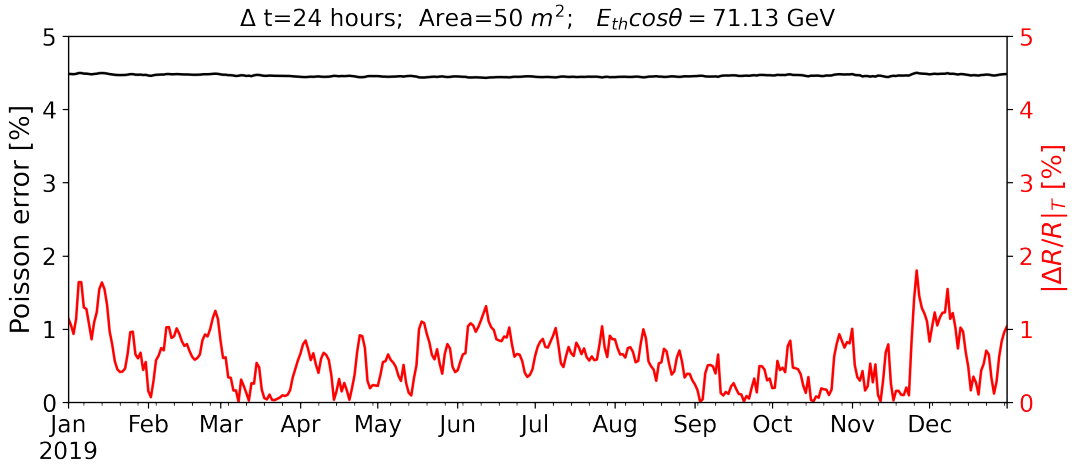

Figure 3.4: The black line represents the statistic variations over time corresponding to the muon intensity of the threshold energy 71.13 GeV, for an area of 50 m^2 and a measurement time of 24 h; while the red line corresponds to the absolute temperature variations related to the same threshold energy. Part two and one of eq. 3.5, respectively.

(systematic) and those referring to the statistical fluctuations of the measurement (error):

$$\left(\frac{\Delta R}{R_0}\right)_{obs} = \left(\frac{\Delta R}{R_0}\right)_T + \left(\frac{\Delta R}{R_0}\right)_{err} = \alpha_T \frac{\Delta T_{eff}}{T_{eff_0}} + \left(\frac{\Delta R}{R_0}\right)_{err} \tag{3.5}$$

In this equation, it is mandatory to have low statistic variations in order to measure with good accuracy the temperature variations. If statistic fluctuations are higher than temperature variations, we won't be able to obtain any temperature information. From equation 3.2, two ways of dismissing statistic variations, i.e. increase counting, can be deduced: increase the measurement time or the size of the detector. Obviously, $\Delta\Omega$ can be increased as well, but in the case of Canfranc, the relation between $\Delta\Omega$ and the observation threshold is fixed by the mountain topology.

Figure 3.4 presents the variations corresponding to $E_{th} = 71.13$ GeV for time steps of 24 hours and assuming that the LSC detector has an area of 50 m^2. In this scenario, the mean counting is 502.7, which has an error of 4.46 %. The black line represents the statistic variation as a function of time. It can be appreciated that whereas temperature variations (red line) are below 2 %, statistic fluctuations are so much higher (>4 %).

In the original case (A=0.95 m^2), the mean counting for the same threshold energy is 9.55 with an error of 30 % (see Fig. 3.3), making it even harder to retrieve any information of the temperature. It would be necessary to reach particle countings higher than ∼40000 (with an associated error of 0.5 %, similar to MINOS experiment [6]) to be able to obtain any valuable information. The only remaining option would be to increase the measurement time to more than two months, which is clearly not usable for temperature monitoring. As a consequence, we have shown that it would not be possible to observe the temperature variations in the real data with the current configuration of the LSC.

The above can be written more formally as follows. Assuming a certain rate R measured in a time Δt, then the counting is $N = R \cdot \Delta t$ and the standard deviation $\Delta N = \sqrt{N} = \sqrt{R\Delta t}$. Therefore,

$$\frac{\Delta N}{N_0} = \frac{1}{\sqrt{R\Delta t}} \tag{3.6}$$

If we want to estimate the temperature variations associated with the rates, we use the well-known relation $\Delta R/R = \alpha_T \Delta T_{eff}/T_{eff_0}$. So, it must be fulfilled that:

$$\frac{\Delta N}{N_0} \lesssim \frac{\Delta R}{R_0} = \alpha_T \frac{\Delta T_{eff}}{T_{eff_0}} \tag{3.7}$$

that can be rewritten using equation 3.6:

$$\frac{1}{\sqrt{R\Delta t}} \lesssim \alpha_T \frac{\Delta T_{eff}}{T_{eff_0}} \tag{3.8}$$

and we get

$$\left(\frac{\Delta T_{eff}}{T_{eff_0}}\right)^2 \Delta t \geq \frac{1}{R\alpha_T^2} \tag{3.9}$$

Considering that temperature variations are of the order of $\frac{\Delta T_{eff}}{T_{eff_0}} \sim 10^{-2} - 10^{-3}$, then

$$\left(\frac{\Delta T_{eff}}{T_{eff_0}}\right)^2 \sim 10^{-4} - 10^{-6} \tag{3.10}$$

From equation 3.9 and assuming that $\Delta t \sim$ *hours* and $\alpha_T \lesssim 1$, we can obtain the value of the rates that we should have:

$$R \sim 10^2 \text{ muons/s} \sim 10^5 - 10^6 \text{ muons/h}$$

Therefore, this is the limit to being able to retrieve temperature variations.

Figure 3.5 shows how the data would look with real variations (gray line) for the case of 50 m^2, where it can already be seen that the noise prevents discerning the temperature variations that are shown, by comparison, with the red line. To give a more quantitative idea of the dissimilarity, the correlation coefficient between both time series represented in the figure is $R = 0.11$.

Last but not least, it should also be noted that despite the potential of the LSC location, which allows accessing a wide range of threshold energies, and apparently to different effective temperatures, the reality is rather different. Figure 3.6 compares the effective temperatures corresponding to the maximum and minimum threshold energies of Canfranc data for two different periods, a "standard" atmospheric period and a Sudden Stratospheric Warming event. Both variations are practically identical and reflect the variations of the stratospheric temperature because the distributions of temperature coefficients associated with both threshold energies peak in the stratosphere (see the high threshold energies in Figure 3.7). As a result, both effective temperatures are supplying information about the same area of the atmosphere. And this is not very useful since our objective is to obtain the atmospheric temperatures at different levels.

So far, we have seen that the temperature coefficients give us information about how the observed rates vary for each degree of temperature change at a given atmospheric level h. Moreover, we have seen that the coefficients are the sum of two terms: the positive effect

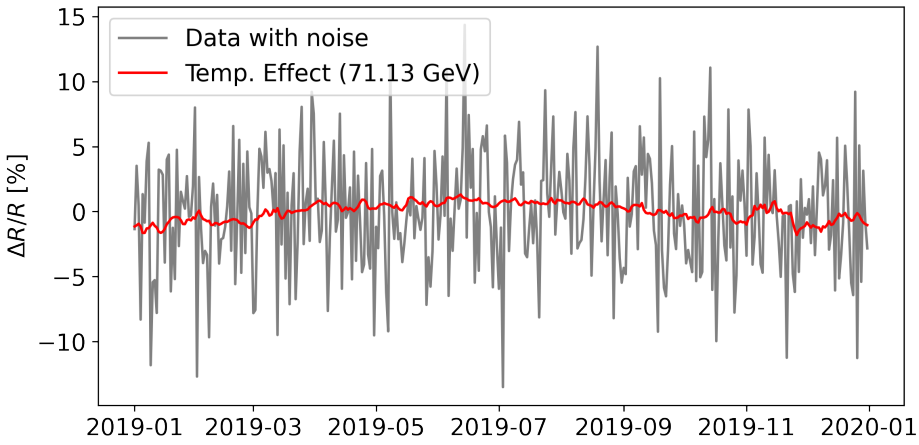

Figure 3.5: Rate variations corresponding to the temperature effect (red line) compared with data that includes both temperature and statistical variations (grey line). For $E_{th}cos\theta$=71.13 GeV, A =50 m^2 and Δt=24 h.

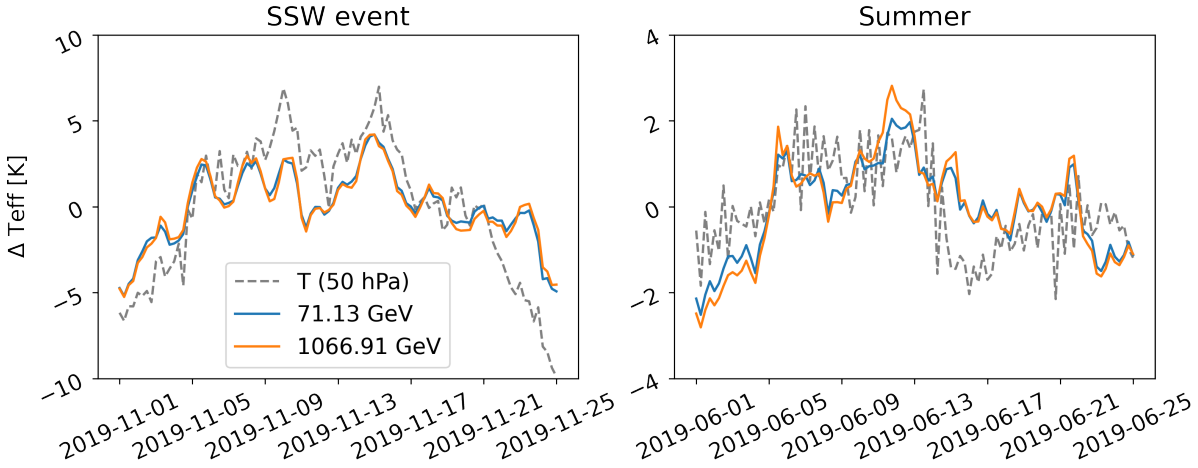

Figure 3.6: (Left) ΔT_{eff} for two different threshold energies (71.13 GeV and 1066.91 GeV) during a SSW event. (Right) Same but for a "standard" atmospheric situation, such as summer. The black dashed line represents the variation of temperature at 50 hPa.

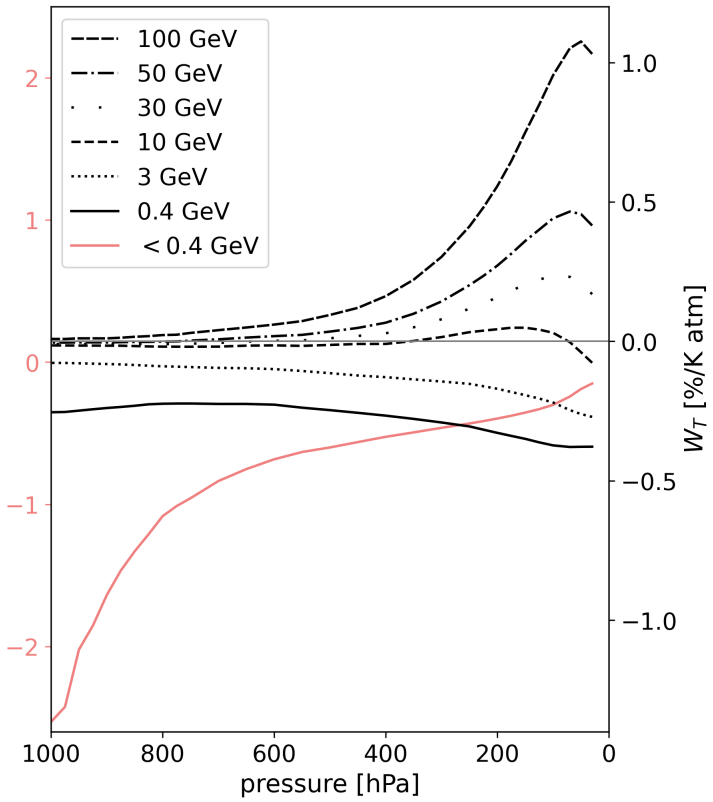

Figure 3.7: Temperature coefficients for vertical direction (θ=0°) at several threshold energies corresponding to different underground depths [135], shown in black on the right axis. Coefficients for vertical muons observed at ground, tagged respectively by passage or absorption in 10 cm-lead and labelled as "hard" ($E_{th} = 0.4$ GeV) and "soft" ($E < 0.4$ GeV) are shown by continuous lines (black and red, respectively). The latter have been obtained from [51], and have axis on the left with the same units as the one on the right.

related to mesons and the negative effect associated with muons. The sign of the coefficient gives information about the net value of the total effect produced by each layer, which depends on E_{th}. In the case of low threshold energies, the negative effect dominates, which means that for every temperature increase in that layer, the measured change in rates will have the opposite sign. However, as the threshold energy increases, the positive effect prevails. The latter effect becomes prominent around 100 hPa ($\sim$15 km) where the peak of meson production takes place. This can be appreciated in Figure 3.7. As seen also in this Figure, selection by threshold energy (equivalently, depth) is the most natural way to separate the positive and negative effects in the weights, allowing a priori a higher sensitivity to the behaviour of the different atmospheric layers.

One of the first attempts to estimate the atmospheric temperature profile using CR measurements with multiple detectors was carried out by [96]. By combining measurements at ground for soft muons (stopped in 10 cm of plastic scintillator), hard muons (passing through 10 cm of lead) and underground muons (80 mwe) performed with 1m^2-area detectors they claimed a daily accuracy in the range 2-2.5 K for the atmospheric regions corresponding to 100, 500, and 900 hPa, over a period of about half a year. The detector suite was accompanied by measurements from a neutron monitor, in order to independently identify solar or interplanetary events that could bias the temperature estimate. Despite the sophistication of the approach, neither the depth of the detector was optimized nor angular information was used. In the

light of those very promising results, it is surprising for us that such natural extensions were not pursued. In fact, more recent studies have endeavored to obtain the temperature for more atmospheric layers by using a single detector and measurements at different angles (for example, [176, 178, 175]).

Clearly one early limitation was detector complexity, as measurements were done over large areas by resorting to large scintillator tiles. However, multi-directional muon detectors (sometimes called hodoscopes) are nowadays common-place and available as part of the Global Muon Detector Network (GMDN) [133], for instance. Furthermore, the revival of the fields of muon tomography [126] and muography [116] has led to the adaptation of new technologies from particle physics, including for instance the development of extruded plastic scintillator [124], micropattern gaseous detectors [67, 109], as well as classic [15] and timing [173] resistive plate chambers (RPCs), just to name a few. They all offer affordable ways to cover large areas at high angular resolution. As an example, we have already seen in Chapter 2 that the effective atmospheric temperature has been measured at ground with a 2 m^2 timing RPC station, the first time that this technology, capable of time resolutions down to 50-60 ps and precise angular reconstruction on areas of several m^2 [170, 27], has been used for the task. In view of these powerful technological assets, the existence of new detailed calculations of the atmospheric coefficients, as well as the latest generation of accurate temperature data from the European Centre for Medium-Range Weather Forecast (ECMWF), reassessing the technological potential of cosmic rays for atmospheric temperature forecast seems very timely if not imperative.

3.3 Methods

3.3.1 Temperature effect

Even for a perfect detector, cosmic-ray rates are subject to variations of diverse origins: those due to changes in the solar activity and in the atmosphere thermodynamic state are the most important. The former act as a potential systematic bias to the atmospheric temperature estimate, and in the remainder of this work we will assume implicitly that they can be isolated and eliminated. Although a natural way to perform this task is through the complementary use of neutron detectors (highly insensitive to atmospheric temperature variations), underground muon detectors (as the one proposed in text) may be sufficient, as solar and interplanetary events have less influence at underground depths. This occurs because interplanetary phenomena affect low-energy primary cosmic rays (in the range of a few MeV and GeV), which in turn are responsible for originating the low-energy secondary muons at sea level [65, 51]. Along these lines, changes in the measured CR rates induced by temperature variations can be approximated by the expression already presented in previous chapters (see equation 1.9).

3.3.2 Cosmic-ray intensity simulation

For a mid-latitude location around 40°, the intensity of vertical muons at ground is typically $I_g \approx 70\ \mathrm{m^{-2}s^{-1}sr^{-1}}$ [72, 76], the value used hereafter. In this case, the angular dependence has been parameterized as $dN/d\cos(\theta) \propto (\cos\theta)^2$ for either soft (< 0.4 GeV) or hard (> 0.4 GeV) muons (e.g., [131]). Given the very high statistics for any angular bin, the particular choice of this distribution does not influence the temperature retrieval for muons reconstructed at ground level.

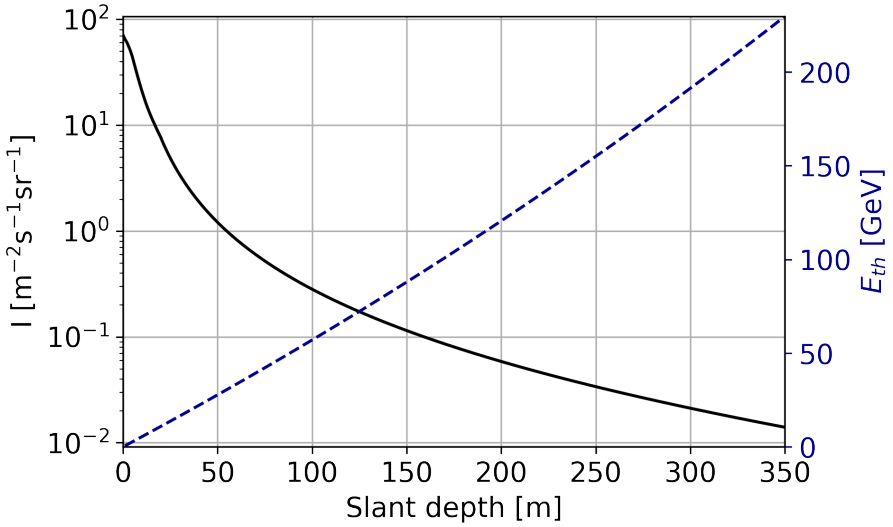

Figure 3.8: Parameterizations used in this work: vertical muon intensity (left axis) and threshold energy (right axis) as a function of vertical slant depth. A typical soil density of $\rho = 2.7$ g/cm^3 has been assumed.

In the case of underground measurements, expression 3.1 has shown a simple relation between muon intensity and slant depth, X. Since this parameterization is not accurate for shallow depths (< 20 m) it has been complemented here by the one presented in [29], which is obtained from an approximation of the surface muon spectrum together with muon range tables. Figure 3.8 shows the muon intensity (in units of m^{-2}s^{-1}sr^{-1}) as a function of slant depth using the aforementioned parameterizations for an average soil density of 2.7 g/cm^3.

For the simulation of underground muons we have assumed in the following an isotropic distribution impinging on a homogeneous soil slab, with rates and threshold energies for each angle obtained from eqs. 3.1 and 1.2. The "slab" denomination is because for each zenith angle θ_k, the corresponding depth ρ_k is calculated with $\rho_k = \rho_0/\cos\theta$ (see Figure 3.9)

For a given detector with a fixed detection area, the number of counts measured over a period of time and solid angle is given by equation 3.2. For simplicity, the detection efficiency and acceptance have been assumed to be angle-independent and close to 1. The statistical fluctuations associated to N are then given by $\sqrt{N}$. On account of that, the variations of CR rates can be expressed as previously indicated by equation 3.5, where $(\Delta R/R_0)_{obs}$ are the experimental CR rate variations, $(\Delta R/R_0)_T$ the changes due to the temperature effect, and $(\Delta R/R_0)_{err}$ the associated statistical fluctuations. Specially underground, the detector area and measuring time become critical variables. Based on a preliminary analysis, and practical considerations, we set for a detector area of 4 m^2, and a time interval of 6 h, although the impact of these choices in our analysis is evaluated at the end of the work.

In sum, the procedure followed for the simulation of CR variations over a specific period of time can be sketched as:

- For underground detectors, CR intensity and threshold energy are estimated using Eq. 3.1 and 1.2, respectively, for a certain slab thickness over the detector (depth). The approximation of [29] is used to calculate intensities for depths shallower than 20 m. Isotropic emission at ground level is assumed, for muons reaching underground.

- For surface detectors, a vertical CR intensity of $I_g \sim 70$ m^{-2}s^{-1}sr^{-1} is assumed, following

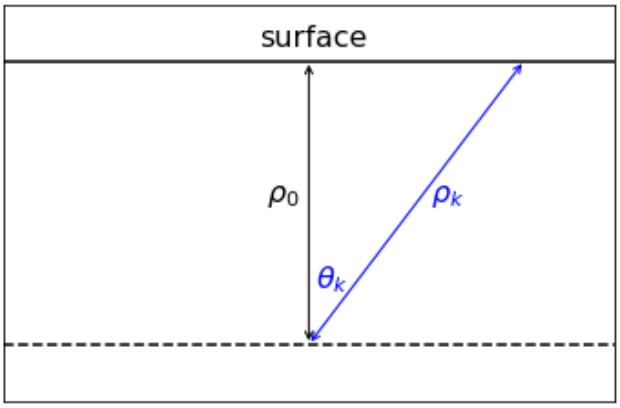

Figure 3.9: Relations of depths for a certain zenith angle θ_k in the slab assumption. ρ_0 is the vertical slant depth.

an angular distribution like $dN/d\cos(\theta) \propto \cos(\theta)^2$. For the soft component, the value of the intensity is assumed to be about a fraction 0.4 of the hard component [51].

- Counting rates, N, are calculated for a fixed detector size, time interval and solid angle as indicated in Eq. 3.2.
- Variations in CR rates due to the temperature effect are calculated with Eq. 1.9 using the temperature time series from ERA5 and the temperature coefficients for the corresponding energy, E_{th}, and angle, θ (linearly interpolated when needed). A more detailed discussion of the estimation of these coefficients is presented below in Section 3.3.4.
- Poisson noise with a mean value of N was added.

3.3.3 Temperature data

Vertical profiles of atmospheric temperatures were retrieved from ECMWF reanalysis, using the ERA5 dataset which offers 37 isobaric levels (1000, 975, 950, 925, 900, 875, 850, 825, 800, 775, 750, 700, 650, 600, 550, 500, 450, 400, 350, 300, 250, 225, 200, 175, 150, 125, 100, 70, 50, 30, 20, 10, 7, 5, 3, 2, and 1 hPa), with a horizontal spatial resolution of 0.25° and a temporal resolution of 6 h [81]. A mid-latitude location at 40° was chosen, in this case corresponding to Santiago de Compostela (Spain).

3.3.4 Temperature coefficients

The distributions of temperature coefficients (W_T) have been calculated before by several authors. Dorman supplied the most extensive calculations for a wide variety of threshold energies and zenith angles [50]. These estimates were later re-evaluated by Sagisaka and Dmitrieva [135, 47]. The former provided coefficients for various combinations of threshold energy and zenith angle whereas the latter introduced up-to-date parameters in the calculations to give a vast database of coefficients, focused on threshold energies for surface hodoscopes.

In the following, Dorman's coefficients will be used whenever the soft component at ground is involved, as he is the only one to provide them; underground coefficients for different angles will be taken from Sagisaka's work; for the hard component at ground, the coefficients supplied by Dmitrieva *et al.* will be adopted. In this latter case, a back-to-back comparison with Dorman and Sagisaka's weights is possible and will be discussed in text. Illustratively, a compilation of the atmospheric weights in case of vertical incidence is shown in Figure 3.7. They will be used for the single-channel (single-angle) analysis in section 3.4.1. For stations with angular resolution, weights as a function of angle are needed, and they will be introduced in section 3.4.2.

3.3.5 Formulation of the inverse problem for temperature retrieval from cosmic-ray data

The inverse problem of estimating the vertical distribution of atmospheric temperature from CR observations will be performed in this work through a simple linear regression. Thus, the temperature at the i-th layer of the atmosphere can be estimated from the CR rate variations as:

$$\Delta\hat{T}_i = \sum_{k=1}^{n_{st}} \sum_{j=1}^{n_{ch}} c_{jki} \frac{\Delta R}{R_0}(E_{th,jk}, \theta_j)\Big|_k \tag{3.11}$$

where c_{jki} are the coefficients of the least squares minimization and $\frac{\Delta R}{R_0}(E_{th,jk}, \theta_j)\big|_k$ are the relative variations of CR rates for a certain detector station k (if several assumed) and angular bin j, with the threshold energy taken to be different for each station and angular bin (for stations detecting soft muons the threshold energy must be understood as a maximum energy). Rates have been simulated according to the procedure described in subsection 3.3.2.

It must be noted before the start that, to date, various underground experiments have attempted to retrieve the temperature of the stratosphere from CR data, a particularly attractive possibility as the underground component is strongly influenced by the temperature of the upper atmospheric layers [17, 10, 119, 154]. Nevertheless, the statistical fluctuations in the counting process as well as the need of deep underground facilities play an important role that limits the practical use of this approach for atmospheric physics. Rate variations due to the temperature effect when deep underground are indeed around $\sim$1.5 %, and therefore statistical fluctuations need to be much lower than this in order to retrieve information about the atmosphere. By way of illustration, the MINOS experiment (located 720 m underground) has a mean counting of $\sim$40000 muons per day that results in error bars of the order of just 0.5 %, thanks to an imposing acceptance of 691 m^{2}sr. In this way, seasonal rate variations caused by the temperature effect could be observed in [6]. On the other hand, we have seen that a dedicated campaign carried out at the Canfranc Underground Laboratory characterized the muon flux inside the experimental halls with a muon monitor of just 0.95 m^2 [161]. Despite the great precision achieved in the reconstruction of the flux as a function of azimuth and zenith angles, with $\sim$400 muons per day and a statistical uncertainty of $\sim$5 %, observing the temperature effect became impossible.

The above facts highlight the main limitations of a single-channel (single-angle) analysis, therefore an alternative approach to the inversion of cosmic-ray data is proposed in this work, based on eq. 3.11. First, three detector stations of small area are considered (two could be indeed part of the same one, sitting at ground level, devoted to hard and soft muon reconstruction), all around 2×2 m^2 in size, following a similar approach as presented in [114].

Additionally, and contrary to that work, the angular information will be considered explicitly and the depth of the third (underground) station will be left as a free parameter during the optimization.

The root-mean-square error for each atmospheric layer i (RMSE_i) is introduced in order to quantify the deviations of the temperature estimated values from the real ones, and used hereafter:

$$\sigma(\hat{T}_i - T_i) = \sqrt{\frac{\sum_{l=1}^{n_t}(\hat{T}_i|_l - T_i|_l)^2}{n_t}} \equiv RMSE_i \tag{3.12}$$

where $\hat{T}_i$ is the estimated (retrieved) temperature, T_i the corresponding temperature data from ERA5, and the l index runs in the temporal data series up to the number of measurements n_t. Similarly, the intrinsic time spread of the layer is defined as the standard deviation from its mean value $T_{i,0}$:

$$\sigma(T_i) = \sqrt{\frac{\sum_{l=1}^{n_t}(T_{i,0} - T_i|_l)^2}{n_t}} \tag{3.13}$$

3.4 Results

3.4.1 Single-channel

In order to compare with previous studies, we estimate the temperature of the 37 available pressure levels using eq. 3.11 for j=1, i.e., single-channel (only vertical direction, $\theta = 0\text{-}10^\circ$) and k =1-3 stations, depending on whether we analyze the components separately or combined. Expression 3.11 becomes:

$$\Delta\hat{T}_i = \sum_{k=1}^{n_{st}} c_{ki} \frac{\Delta R}{R_0}(E_{th,k}, 0^\circ)\Big|_k \tag{3.14}$$

For instance, the expression for the estimation of temperatures using only the hard component is:

$$\Delta\hat{T}_i = c_i \frac{\Delta R}{R_0}(E_{th}, 0^\circ)\Big|_{hard} \tag{3.15}$$

In this case, only one variable is used as an estimator of the temperature. However, it is also possible to use the expression including several components, such as:

$$\Delta\hat{T}_i = c_{1i} \frac{\Delta R}{R_0}(E_{th,1}, 0^\circ)\Big|_{hard} + c_{2i} \frac{\Delta R}{R_0}(E_{th,2}, 0^\circ)\Big|_{soft} \tag{3.16}$$

Figure 3.10a shows the RMSE for the hard (blue line) and soft (red line) components individually, together with their combination (black line). The underground component is the only one that allows the inspection of different depths (Figure 3.10b). The hard muon component has a threshold energy of 0.4 GeV, corresponding approximately to muons traversing 10 cm of lead. Temperature coefficients are nearly flat in this case (Figure 3.7, continuous black line), which means that rates are similarly affected by all atmospheric layers. As a consequence, it is the troposphere, the largest region of the atmosphere by weight, the one that dominates the variations of CR rates. Temperatures between 1000 and 300 hPa are in this way

reasonably well estimated from hard muon rates (RMSE $\sim$ 3 K), however accuracy is lost in the tropopause and stratosphere (Figure 3.10a, dashed-blue line). Since the soft muon component at ground ($E < 0.4$ GeV) is much more affected by the temperature of the lower layers of the atmosphere (Figure 3.7, continuous red line), it becomes more precise as a temperature estimator below 300 hPa (Figure 3.10a, dotted-red line) by suppresing the negative correlation between troposphere and tropopause regions (as seen in Section 2.4). The combination of both components gives a marginal improvement at this point (black line).

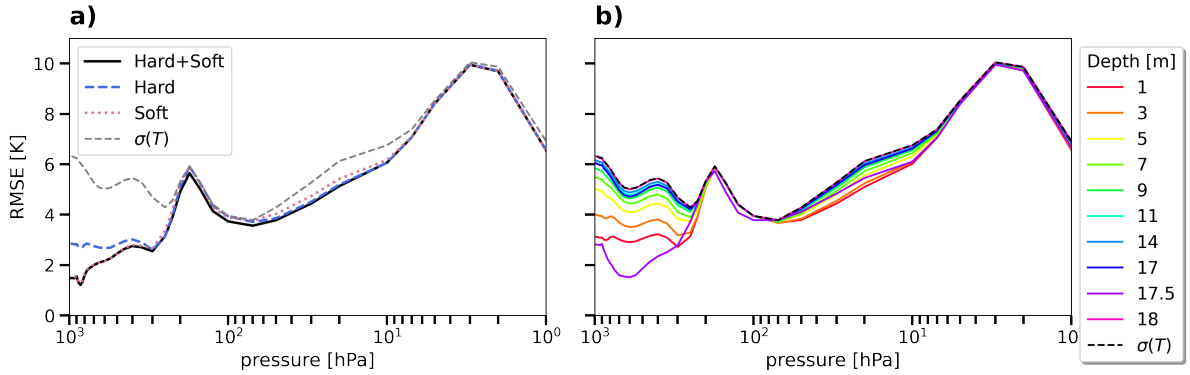

Figure 3.10: RMSE between estimated and real temperature, plotted as a function of the pressure level after cosmic-ray data inversion. The detector area is 2 m$\times$2 m and the analysis has been performed in 6 h intervals. A single-channel analysis based on vertical muons has been assumed: (a) using the hard (blue line) and soft (red line) muon component, with the combination of both components shown in black; (b) using the underground muon component at different depths. The standard deviation of the temperature of each layer is overlaid in both cases (dashed grey line). The 1m-depth situation is already almost indistinguishable from the hard muon analysis shown in left. At a "magic depth" of 17.5 m the sensitivity to the troposphere becomes maximal and slightly improves in the stratosphere, as explained in text.

The temperature estimate from the inversion of underground rates is now shown in Figure 3.10b for different depths. In general, accuracy is lost with depth due to the loss of statistics as well as weights becoming closer to zero. For depths greater than 18 m the variability of the temperature estimate is indistinguishable from the temperature variability of the layer itself (dashed line in the figure). However, and similar to earlier investigations [114], even for a single-channel analysis we see some preference towards the third station being placed well underground yet at relatively shallow depths, specifically, at 17.5 m. Although this value may seem somewhat artificial, it emerges from the behaviour of the temperature coefficients at that particular depth ($E_{th} \sim 10$ GeV). It happens when the temperature coefficients in the tropopause region (100-200 hPa) reach values close to zero while still having enough weight in the troposphere to dominate the CR rate variations. As temperatures in the 100-150 hPa region are anticorrelated with both the troposphere and stratosphere, minimizing their contribution results in the best possible estimator for the tropospheric temperature, with a mild improvement in the stratosphere too. This delicate balance of the correlation/anti-correlation effects between troposphere, tropopause and stratosphere results in a very narrow plateau of optimum depths (10's of cm) and is highly sensitive to the weight shapes. As we will show, it achieves its full potential when angular information is considered, thereby involving a wider range of angles and thus optimal depths than seen in a single-channel analysis. Given that calculations like the ones presented here depend on weights that are theoretically estimated, a wide depth-plateau is a desirable feature to have at the outset.

In all three analyses, a peak around the tropopause region is noticeable. Here the estimates are generally poor because the variations of temperatures in this part of the atmosphere are strongly anti-correlated with the surface variations, whose contribution to the observed rates is dominant. In addition, the temperatures of the upper stratosphere ($<$ 50 hPa) are also particularly difficult to capture. The reason is that this region corresponds to few percent of the total atmospheric mass. So unless the temperature coefficients would peak at that specific region and become essentially zero in the rest of the atmosphere, the effect of the remaining layers will always be dominant (i.e. they will have more weight in eq. 1.9).

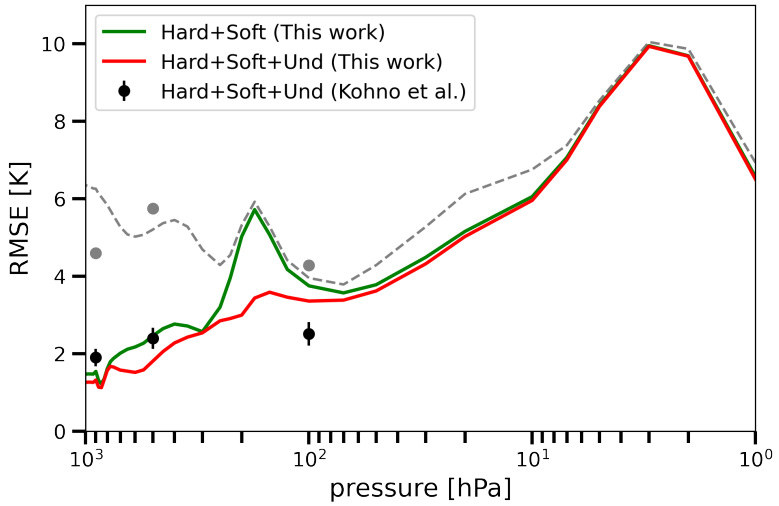

Figure 3.11: RMSE between estimated and real temperature, plotted as a function of the pressure level after cosmic-ray data inversion. The detector area is 2 m$\times$2 m and the analysis has been performed in 6 h intervals. A single-channel analysis based on vertical muons has been assumed (θ below 10 deg.). The results for the combination of the hard and soft component are shown by the green line. Inclusion of a third underground station at an optimal depth around 17.5 m improves the results for layers below the 80 hPa one (red line). For comparison, the experimental results obtained around the Tokyo area in [96], also with a three-station configuration, are overlaid (black markers). The standard deviations of the temperature of each layer as seen in our data (dashed line) as well as the one on their study [96] (grey points) are included too.

Finally, Figure 3.11 shows the simulation results for two (green) and three (red) stations, the latter for the optimal depth obtained in our study. The daily RMSE obtained from an analogous three-station (1 m^2) configuration in [96], with measurements performed over a 5 month period within Tokyo area, is overlaid (black points). Despite the different atmospheric conditions, the intrinsic temperature variations of the layers studied are comparable (grey points vs grey dashed line), as well as the reconstructed temperature (black points vs red line), giving support to the present analysis. Importantly, a first hint of the possibility of achieving good temperature retrieval at critical regions like the tropopause, through the combination of ground/underground stations is already indicated through the red line. As already mentioned, this possibility reaches its full potential when considering angular information.

3.4.2 Multi-channel

As muon stations can be easily built nowadays with a high angular resolution of the order of a degree, and given the strong dependence of atmospheric weights with zenith angle, a vast amount of additional information can be made in principle available to the inverse problem (eq.

3.11). For simplicity, we chose to bin the zenith angle in 10 degree-steps (channels) ranging from 0° to 70°. Clearly, there must exist more optimal ways to use the angular information, ideally keeping a reasonable statistics for each angular channel for each depth and detector area considered. Realistically, an angle-averaged W_T for each channel should be used too. The straightforward binning and linear regression model chosen here aims at merely illustrating the potential (and intrinsic limits) of combining angular information with an optimal depth, hinting at which depth that is, and for which detector size.

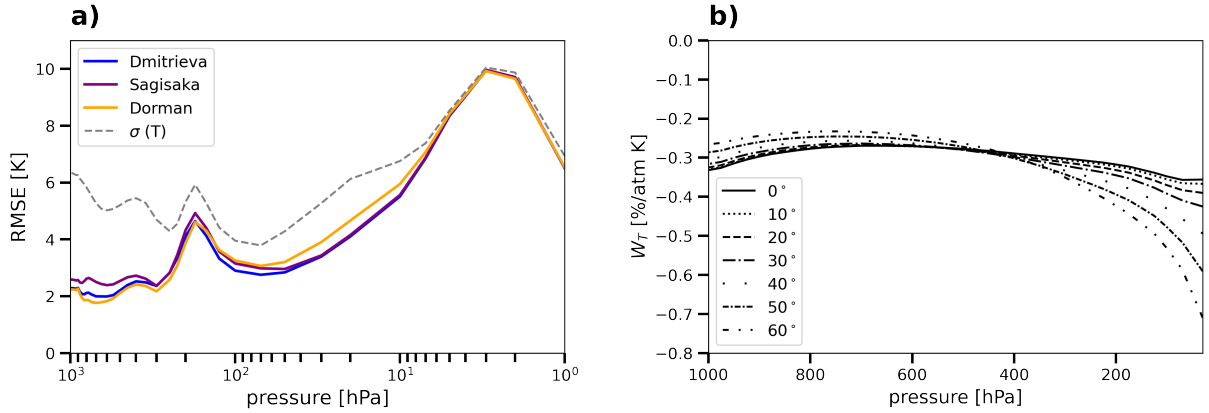

Figure 3.12: (a) RMSE between estimated and real temperature for each atmospheric pressure level, using the hard component. Each curve refers to the results obtained using the different databases of coefficients: [135, 51, 47]. (b) Distribution of temperature coefficients for hard muons, at several angles [47].

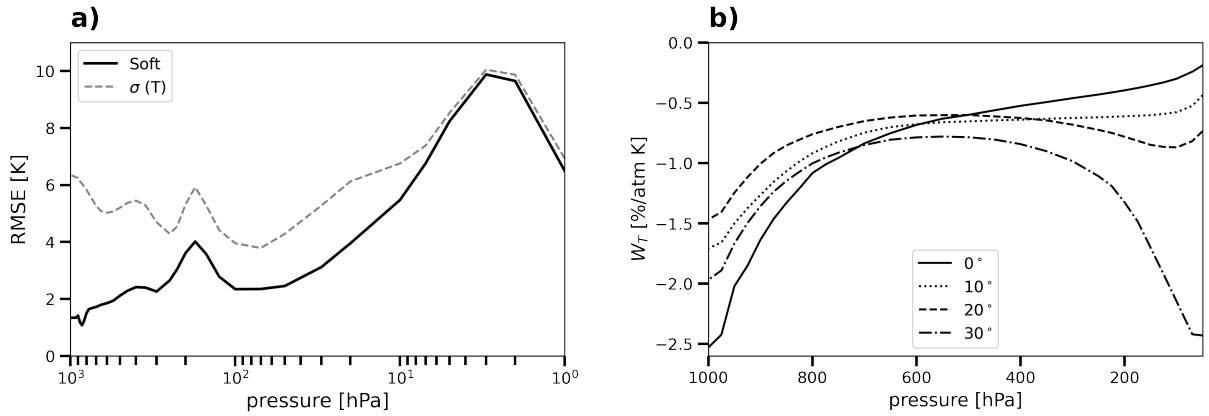

Figure 3.13: (a) RMSE between estimated and real temperature for each atmospheric pressure level, using the soft component. (b) Distribution of temperature coefficients for soft muons, at several angles [51].

First of all, the results for muons reconstructed in the ground station (tagged as before as hard ($E > 0.4$ GeV) and soft ($E < 0.4$ GeV)) are shown in Figures 3.12 and 3.13. As for the single-channel analysis, a typical station area of 2×2 m^2 has been assumed. In the case of hard muons, Figure 3.12a shows the temperature predictability (RMSE, eq. 3.12) calculated employing the temperature coefficients from the three databases available to us [135, 51, 47]. Calculations based on Sagisaka's and Dmitrieva's coefficients are in approximate agreement, while Dorman's deviate slightly in the low stratosphere. Already at this point, the multi-channel analysis of hard muons significantly outperforms the single-channel analysis in

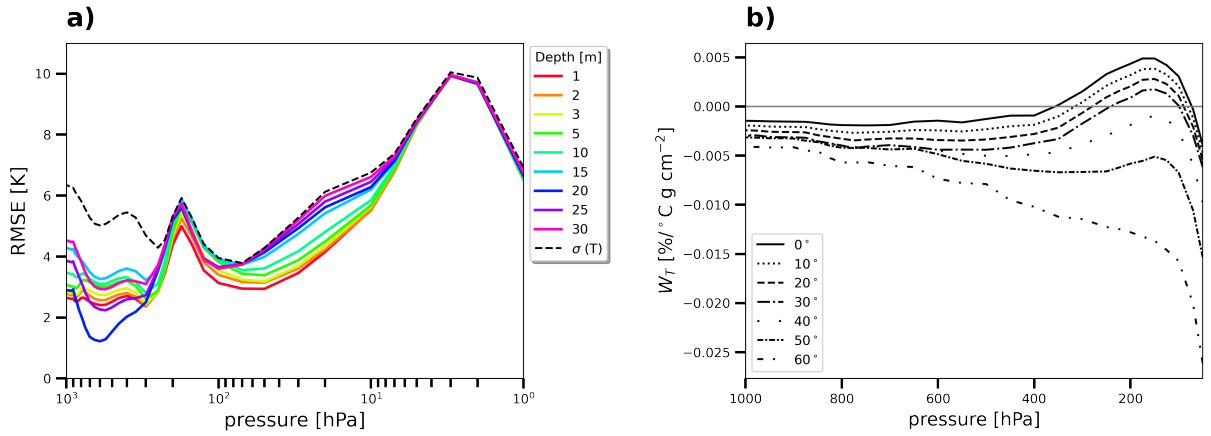

Figure 3.14: (a) RMSE between estimated and real temperature for each atmospheric pressure level, using underground muons. (b) Distribution of temperature coefficients for muons above 10 GeV, at several angles [135].

the high atmosphere (above the level of 100 hPa) even with the latter performed through three detection stations (previous section, Figure 3.10). When performing the multi-channel analysis for the soft component (Figure 3.13a), for which only Dorman's weights seem to exist (Figure 3.13b), the result is even slightly better. So, with independence from the specific shape of the weights (Figure 3.12b and 3.13b) the use of multiple angles within a single station represents a far better strategy when aiming at temperature retrieval in the high atmosphere than using multiple stations.

Figure 3.14a shows now the RMSE for underground stations placed at different depths, assuming a uniform-thickness soil slab. As in the single-channel analysis, statistics limits the station capabilities quickly as a function of depth, and so for 30-m depth a $2 \times 2\text{m}^2$ detector is already insensitive to temperatures above the tropopause (magenta line). As the distribution of temperature coefficients gets more peaked at small zenith angles the deeper the station is placed, the usefulness of multiple angular bins becomes more limited and the best global description is obtained again (as in the single-channel analysis) for near-surface detectors (1 m deep, red line). Indeed, the RMSE for a 1 m-deep station is very close the one obtained in Figure 3.12 for hard muons. Interestingly, however, a 20 m-deep station would perform significantly better for tropospheric levels below 300 hPa. This reproduces the effect observed in the single-channel analysis, although for a broader range of depths. It becomes even more apparent when combining several stations (Figure 3.15): weight coefficients in the range 19-20 m, despite showing a low sensitivity to temperature (up to $\times$ 100 less than weights at ground) exhibit a strong dependence with angle and atmospheric height, going from positive to negative values in the tropopause region. This can be used beneficially in the regression to minimize the correlation/anti-correlation effects in the troposphere-tropopause-stratosphere regions. At the same time, the relatively shallow depth of the station is compatible with a moderate statistical noise in counting, even for angles far from the vertical.

The combined analysis of the different muon components/stations is shown in Figure 3.15 for the following two cases: hard + underground (Figure 3.15a) and hard + soft + underground (Figure 3.15b). While the inclusion of soft muons brings a sizeable improvement in the troposphere region, it does not seem critical to the observation that an optimum depth exists.

At first glance, the optimum depth derived from this analysis would seem to be in agreement with that chosen in the three-station/single-channel simulation of [114]. In their work they

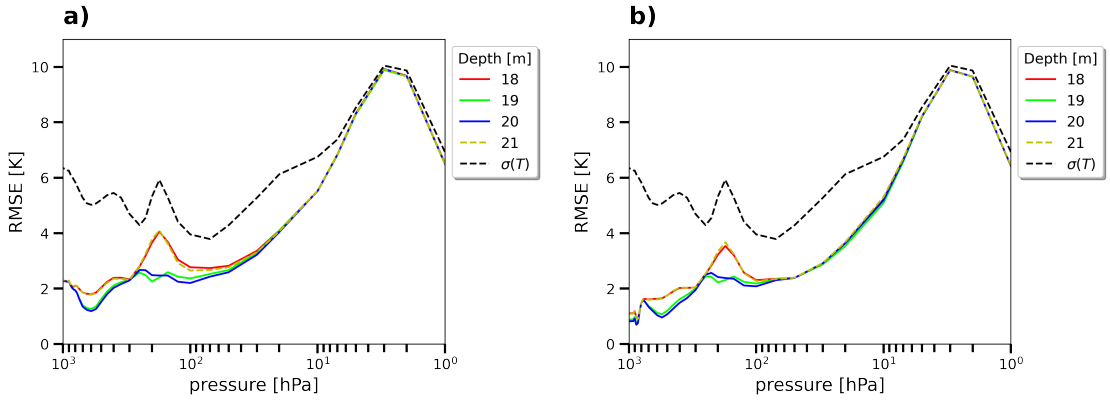

Figure 3.15: RMSE between estimated and real temperature for each atmospheric pressure level, in the multi-channel analysis. (a) Hard + underground muons at different depths. (b) Hard + soft + underground muons at different depths. Depths smaller than 18 m and larger than 21 m are excluded because they do not exhibit any discernible difference compared to those.

selected a depth of 55 m.w.e, which is equivalent to a threshold energy of ∼11 GeV or, in other words, to a soil-thickness of 20 m. However, the early temperature coefficients there assumed are much more peaked than the ones used here, and would correspond to a threshold of 50 GeV (80 m-depth) if resorting to more modern estimates as those shown in Figure 3.7. The performance of the two methods is very different too, as can be appreciated in Figure 3.16 where the RMSE from the three-station/single-channel analysis as proposed in Miyazaki and Wada (black dashed line) is compared with the present one (blue line). Despite the assumed depth is the same in both cases, the difference in the assumed weights makes all the difference, allowing us to establish the relevance of the 20 m-depth as an actual optimum for atmospheric studies. The improvement is even more apparent when considering a multi-channel analysis (orange line): up to a factor of two or more can be gained in critical atmospheric regions like the tropopause and stratosphere compared to earlier simulation work. The reconstruction reaches a best value of 0.8 K at 850 hPa and a worse one around 2.2 K for the tropopause region and up to 50 hPa, becoming the temperature intrinsically inaccessible above the 10 hPa layer. Moreover, Miyazaki and Wada estimated RMSE-values between 1 and 3 K when disregarding statistical noise from counting, for seven pressure levels between 1000 and 100 hPa. Interpreting that as the intrinsic limit to the inversion problem and comparing to the analogous result in our analysis (red-dashed line in Figure 3.16), it can be concluded that a three-station/multi-channel analysis with optimized depth provides an overall improvement of around a factor 2 also in that situation.

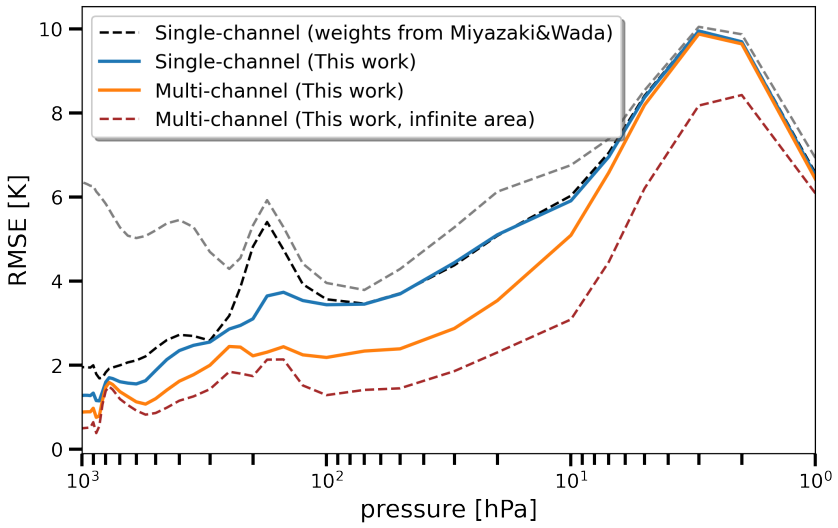

Figure 3.16: RMSE between estimated and real temperature for each atmospheric pressure level. Observations performed in 6 h time intervals and for 2 m $\times$ 2 m detection area. Black dashed: three-station/single-channel analysis using weights from [114]. Blue: three-station/single-channel analysis at an optimized underground depth. Orange: three-station/multi-channel analysis at optimized underground depth. Dashed red: three-station/multi-channel analysis at optimized underground depth, neglecting statistical fluctuations in particle counting. The grey dashed line represents the intrinsic spread of the temperatures for each atmospheric layer.

3.5 Discussion

Within the relatively simple inversion algorithm proposed in this work, the width of the optimal-depth plateau in Figure 3.15 exhibits a non-trivial dependence with the chosen angular binning. For depths around the optimal one, this is exacerbated since the overall correlation between rates and temperature (eq. 2.12) changes sign (hence, it vanishes) as a function of the angular channel. It does so in a way that is both abrupt and critically dependent on the precise shapes of the weights. While this fact suggests that a finer resolution is desirable (1 degree is technically possible without great effort), we opted to leave such a study outside this work. The reason is two-fold: i) the binning becomes too thin compared to the four angular bins available for our underground coefficients in [135], and so, in the absence of new calculations of those, the present simulation work would depend largely on the interpolation method and ii) the $\times 10$ increase in the number of fitting parameters would require of a more dedicated optimization study than intended here. In our case we have relied on the python package *Statsmodels*, and the Ordinary Least Squares method included in it, without constraints in the fitting parameters (some examples of regression plots can be found in Figure B.3 of Appendix B.2.1). The results were little sensitive to the method chosen or how the regression was conditioned (initial values, parameter range, function tolerance and linear constraints between variables). Studies performed with a mildly increased binning (5 degrees) show indeed that the results of the regression within the 19-20 m plateau become much more stable.

Once the existence of an optimal depth-plateau has been established, it is important to understand how the performance of the inversion algorithm depends on the size of the detection area and the presence of systematic errors in particle counting (that we have simulated getting random samples from a Gaussian distribution with the width being a certain percentage of the average rate and subsequently adding them to the data series). To make the latter more

realistic, we follow the typical procedure of adding extra noise to the data in different levels (low, medium, and high) to analyze the performance of the technique.

Figure 3.17 seems to show a preference towards areas at the scale of few m^2, as there are just marginal gains compared to the case of infinite area (a condition well fulfilled for practical purposes above 300 m^2), whereas performance deteriorates very perceptibly below 1 m^2. A larger detector will be more resilient against systematic variations in counting too, with a 4 m^2 detector able to tolerate up to $\sim$0.3% additional fluctuations in counting, assuming they are uncorrelated at every time step (Figure 3.18). This poses a very stringent requirement for the detection system, whose overall efficiency should be kept stable within these values. From this point of view, plastic detectors coupled to photon sensors represent a most natural choice, although a gaseous detector with redundant layers could become more affordable/practical at the expense of a larger design complexity.

Results presented here are difficult to interpret from an atmospheric physics perspective, so in order to get a better grasp of how the minimization process works, a close examination of what we define here as "combined temperature coefficients" will show to be useful. For that we rewrite equation 3.11 taking into account expression 1.9:

$$\Delta\hat{T}_i = \sum_{k=1}^{n_{st}} \sum_{j=1}^{n_{ch}} c_{jki} \left(\sum_{p=1}^{n_l} W_T(E_{th,jk}, \theta_j, h_p) \Delta T_p \Delta h_p \right) \Bigg|_k \tag{3.17}$$

Rearranging the terms for the same pressure level p we obtain:

$$\Delta\hat{T}_i = \sum_{p=1}^{n_l} \left(\sum_{k=1}^{n_{st}} \sum_{j=1}^{n_{ch}} c_{jki} W_T(E_{th,jk}, \theta_j, h_p) \right) \Delta T_p \Delta h_p \tag{3.18}$$

from where we define the combined temperature coefficient as:

$$W_{pi} \equiv \sum_{k=1}^{n_{st}} \sum_{j=1}^{n_{ch}} c_{jki} W_T(E_{th,jk}, \theta_j, h_p) \tag{3.19}$$

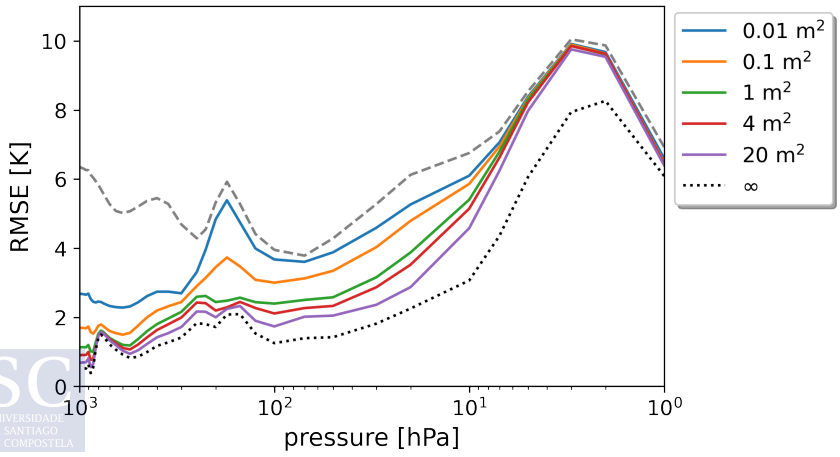

Figure 3.17: RMSE between estimated and real temperature for each atmospheric pressure level, for a three station/multi-channel analysis at an optimal depth. Each line represents a different value of the size of the detectors. The grey dashed line represents the standard deviation of the temperatures for each atmospheric layer.

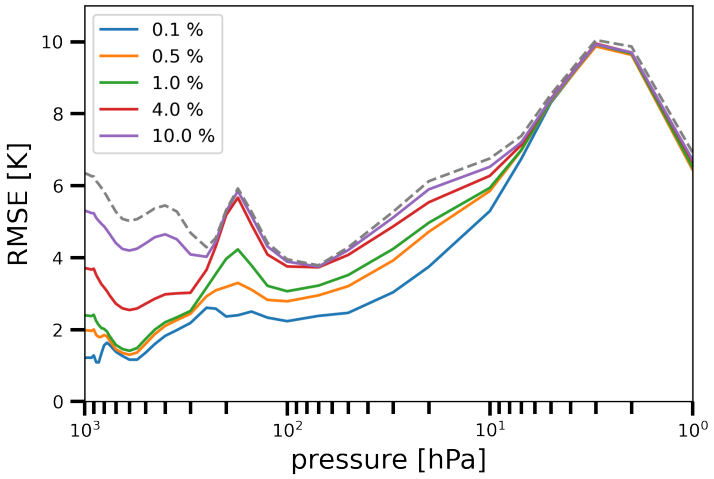

Figure 3.18: RMSE of the estimation of temperature for each atmospheric pressure level, for a three station/multi-channel analysis at an optimal depth. Different levels of Gaussian noise have been aggregated to the rates: 0.1, 0.5, 1, 4, and 10%. The grey dashed line represents the standard deviation of the temperatures for each atmospheric layer.

When solving the inverse problem for the temperature of a certain pressure layer, one may expect that the coefficients c_{jki} of the regression should in principle have values such that in eq. 3.18 the combined coefficients are able to enhance the p-term of the same temperature layer (i), minimizing the contribution from the rest. As the shapes of the temperature coefficients are not flexible enough to accommodate this condition for any arbitrary layer, the correlation between atmospheric layers becomes an essential ingredient. Figure 3.19 shows some examples of the combined coefficients obtained for the retrieval of the temperature at 50, 150, 200, 500, 850, and 1000 hPa for different depths of interest: 15, 19, 20, 21, and 100 m.

For the highest and lowest atmospheric layers (1000 and 50 hPa, represented at bottom right and top left in Fig. 3.19 botton right, respectively), the combined coefficients have indeed the highest value on that layer. The presence of a significant contribution from the other atmopsheric layers limits temperature reconstruction here. Indeed, the effect of the width of the combined coefficients can be seen in the reconstruction of the 850 hPa layer (chosen since it corresponds to the layer with the lowest RMSE in the analysis) that is very similar to the 1000 hPa one.

On the other hand, the combined coefficients for the case of 200 and 500 hPa (middle subplots in Fig. 3.19), especially at optimal depths, rely strongly on the correlation between layers. In the case of 200 hPa for 15, 21, and 100 m detector depths, the regression has chosen to give positive weight to the stratospheric levels and negative one to the tropospheric ones. As these temperatures are correlated, this approach minimizes both contributions enhancing the ones for the intermediate layers. The combined coefficients for 19 and 20 m use the atmosphere information differently, which is a consequence of the better use of the underground component included in the regression. That is, for 20 m ($E_{th} \sim 10$ GeV), the troposphere exhibits positive combined coefficients and even softly peaks in the corresponding 200 hPa layer. As the temperatures at 200 hPa are still correlated with the tropospheric ones a better sensitivity ensues, inherited from the weights' shapes at underground depths (Figure 3.14b).

Another interesting example is the situation for the 500 hPa level. The depths of 15, 21, and 100 m prefer to rely on coefficients from layers above 200 hPa to predict the temperature.

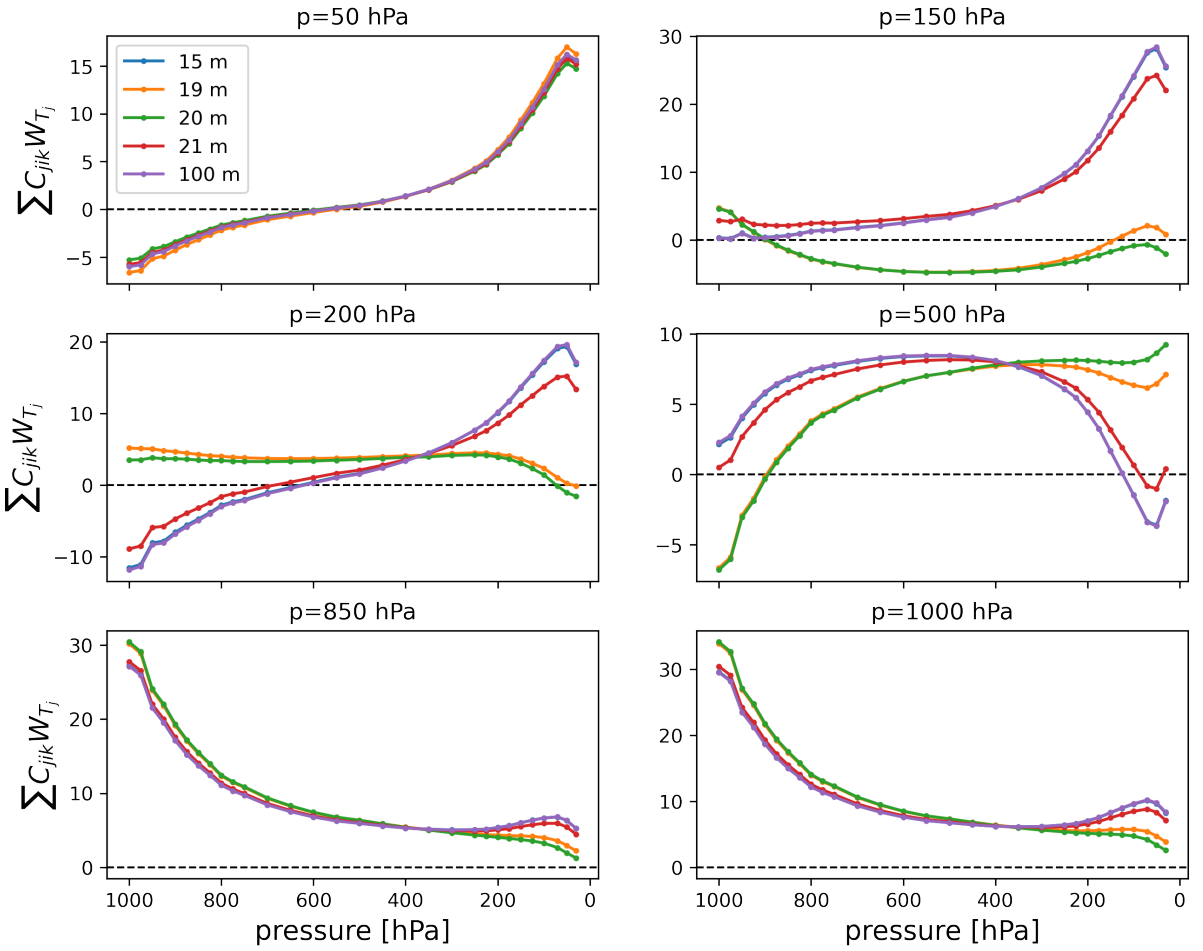

Figure 3.19: Combined temperature coefficients calculated for the atmospheric pressure levels of 50, 150, 200, 500, 850, and 1000 hPa in the three-station/multi-channel configuration. The curves represent different depths of the underground station: 15, 19, 20, 21, and 100 m.

However, a better accuracy can be achieved if relying on coefficients from layers below 800 hPa (depths 19-20 m), as this makes use of the positive correlation between troposphere and stratosphere and thus it balances both contributions to the temperature of the 500 hPa layers. Even more extreme is the case of the 150 hPa level (top right in Fig. 3.18), which is strongly anticorrelated with the high stratosphere and troposphere. The regression is succesfully able to use this information for the depths of 10 and 20 m, even allowing the coefficients to peak in the nearby region around 100 hPa (19 m depth). By comparison, the regression performed for other depths attempts desperately to give weight to all the stratospheric levels down to 200 hPa, in order to achieve some sensitivity to the 150 hPa one. As the high stratosphere is anticorrelated with the 150 hPa layer, the strategy is bound to fail, producing the large peak-structure on the RMSE observed in this region for non-optimized depths, and that has been presented abundantly throughout the text.

As a consequence of the above observations, it becomes clear that the cosmic-ray method for atmospheric temperature retrieval involves a suitable weighting of the information from the entire atmosphere, for each layer whose temperature is being resolved. In particular, the fact that the variations in the lowest part of the stratosphere and around the tropopause (∼100-200 hPa) are partly anticorrelated with the variations in the troposphere and upper stratosphere

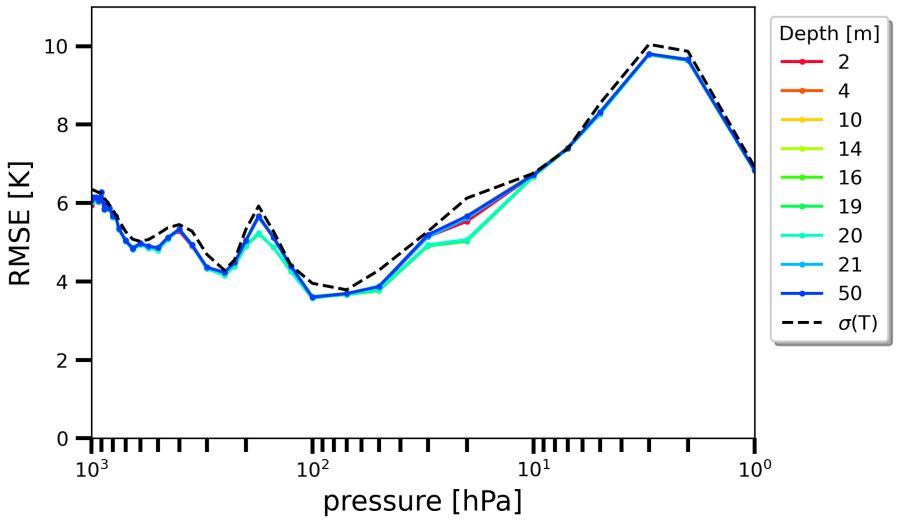

Figure 3.20: RMSE of the estimation of temperature for each atmospheric pressure level, for a three-station/multi-channel analysis. The simulated temperature variations have been taken from data but introduced in uncorrelated fashion, for each 6 h interval. σ(T) is the standard deviation of temperatures.

(∼70-1 hPa) determine the shapes of the combined coefficients for intermediate atmospheric layers. Simulating a custom atmosphere with uncorrelated temperature variations allows to better illustrate the situation. In this case the total spread of each layer is kept, and assigned randomly at each time interval. With 37 layers, and in light of the broad W_p's obtained above, this should represent a very harsh situation for the linear regression, as shown in fact in Figure 3.20. It is relevant to see that the weights in the region 19-20 m still offer the highest sensitivity, confirming that a higher variability of shapes of the temperature coefficients distribution in that region plays a part in the overall performance of the regression. The dominant contribution, however, must come from the long-distance correlations between different layers, and the ability of the weights to accommodate them, as indicated by Figure 3.19.

Overall, our study shows that the introduction of different angles into the analysis of the inverse problem helps improving the estimates of the atmospheric temperature profile dramatically. A temperature predictability (RMSE) ranging from 0.8-1K in the low troposphere to 2.2 K in the 50 hPa level was obtained, deteriorating for higher stratospheric layers. For a temperature monitoring emplacement dedicated to improve atmospheric forecasts, this range of heights is more than enough since the most interesting atmospheric phenomena occur in the tropospheric layer. However, there is a unique phenomenon that takes place in the stratosphere and is attracting a lot of atmospheric scientists due to its capacity to modify the weather at the surface. We are referring to Sudden Stratospheric Warmings (SSW). A SSW is an event that occurs in polar vortices when the stratospheric temperature suffers an abrupt increase in a short period of time. In such events, the vortex may collapse, releasing cold air towards lower latitudes that could impact the surface weather. This situation is more likely to happen in the northern hemisphere (see more information in Appendix A.1). In many cases, the monitoring of the temperature at 10 hPa (for which a modest 5 K RMSE was obtained in this analysis) is useful when a major event occurs. Still, the observation of any other lower stratospheric level provides very valuable information about these events. In such a case, the setup proposed in this work would be at least complementary to this kind of research. For illustration, a comparison between the input temperatures and the ones estimated with the inversion method proposed in

text is shown in Figure 3.21. The difference between the observed and estimated temperatures is also included in Figure 3.22. The bias calculated for these predictions is zero for the pressure levels presented. However, it can be seen that the upper atmosphere displays the most significant errors, which correspond to the occurrence of the aforementioned SSW events. The model loses detail when capturing these events, as we have mentioned above, yet it is able to reproduce its influence on lower levels (between 20 and 200 hPa).

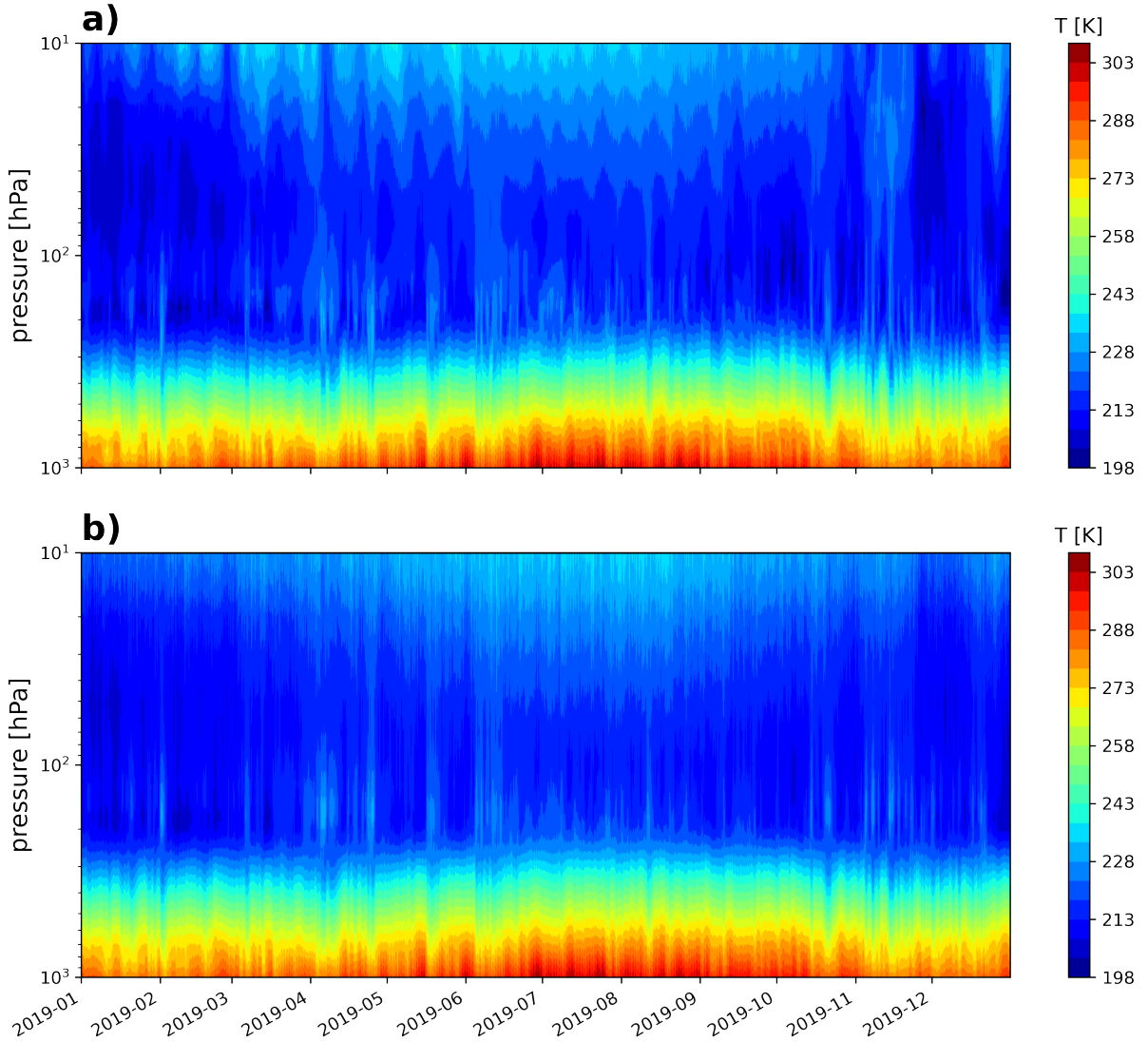

Figure 3.21: (a) Observed temperature for 2019. (b) Estimated temperature for 2019 using the detector configuration and data analysis discussed in text.

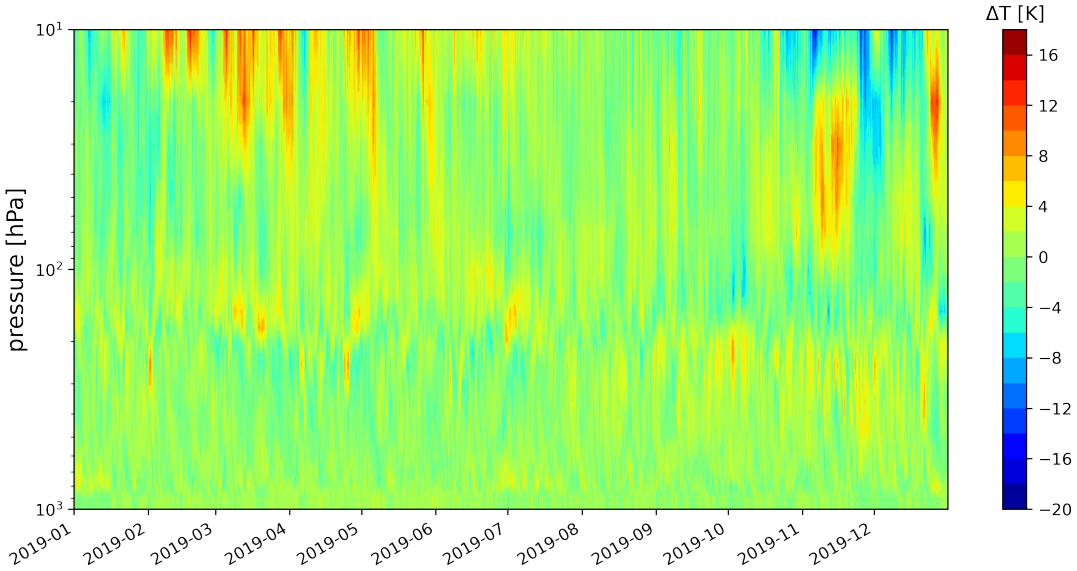

Figure 3.22: Difference between observed and estimated temperature for 2019 using the detector configuration and data analysis discussed in the text.

3.6 Conclusions

The purpose of the present study was to determine the best configuration of a monitoring station integrated by cosmic-ray telescopes. One of the most significant findings to emerge from this study is the possibility to retrieve the temperature of the atmosphere from the surface with good accuracy up to a considerable height ($\sim$ 20 km). An implication of this is that atmospheric muon detectors can be used in scientific research beyond the field of astrophysics.

Returning to the question posed at the beginning of this chapter, it is now possible to state that multi-directional telescopes can enhance the estimate of atmospheric temperatures. Our results have shown that one can achieve a high degree of accuracy with error margins between 0.8 and 2.2 K that could be improved in practice applying more advanced statistical techniques such as those employed in satellite observations [59, 134]. For 4 m^2-scale detectors, this performance requires of an outstanding detector stability (below 0.3% on its counting efficiency). While detector inefficiencies to minimum ionizing particles down to 0.1% are not alien to particle physics instrumentation, the requirement will pose significant constraints on the chosen technology and detector design.

On the other hand, the current work was limited by the use of simulated CR data and further work needs to be done in the area of experimentation to evaluate the actual limits of the estimates. In spite of this, our findings establish several courses of action for future research. A good line for future work would be to contrast the retrieved temperatures from real cosmic-ray data against temperature data from balloon measurements. Additionally, we have found evidence of an optimal depth to place one of the detectors. Depths of 19-20 m seem feasible and affordable, with no need to go deep into a mountain as is done for other CR research. Such an underground station could be easily located in dams, tunnels or subway stations for instance. Moreover, continuous measurements of vertical temperature provided in this way would no doubt complement satellite measurements, as this technology would be much more affordable and easy to assemble and maintain.

Chapter 4

Simulating the atmospheric effects with a dummy model

Abstract:

In this chapter we present the atmospheric effects analyzed by means of a cosmic-ray air shower simulation code. This tool serves as an additional testing to corroborate and better understand the correlations between cosmic-ray variations at the surface and atmospheric properties.

4.1 Introduction

Chapter 2 has paved the way for introducing the influence of the atmosphere on the observations of CR at the surface. We have seen how tricky it can be to identify the individual effects in the total rates, especially when the atmosphere exhibits a complex behavior.

Over the past decades, a number of works have studied in detail the correlations between CR observations and atmospheric variations [e.g., 120, 23, 184, 118]. However, it can be difficult to make a correct interpretation of these relationships when there are so many factors at play. Numerical simulations of EAS can provide a deeper insight into the CR variations, especially because the influencing factors can be controlled. For example, the primary CR spectrum can be fixed, which makes it possible to exclude variations caused by space weather.

4.2 Simulation Overview

Numerous programs are available for the realistic simulation of EAS [65, 82]. Some of the most widely used are CORSIKA and AIRES [57, 138]. These programs consist of a series of routines and subroutines that track the paths in the atmosphere followed by the particles created in the cascade produced by a high-energy primary cosmic ray. Figure 1.3 in the introduction section shows a pair of examples of 3D air showers simulated with CORSIKA.

As we have seen so far, the Earth's atmosphere is the medium in which air showers propagate and, therefore, their evolution strongly depends on its state (density, temperature, etc). Thus, the program must incorporate a realistic model of the atmosphere so that the simulations are as accurate as possible. All programs that simulate EAS use what is known as *US Standard Atmosphere* as a model [13]. It is based on experimental data and constitutes

an international standard since it represents an average atmosphere. The model provides the values of the atmospheric pressure, density, and temperature as a function of altitude. For instance, it considers that the values of the surface temperature and pressure are $T_0 = 288.15$ K and $P_0 = 1013.25$ hPa, respectively. The Linsley's parameterization gives the mathematical approach that fits these data. It divides the atmosphere into five layers represented by an exponential function that allows to compute the atmospheric depth X as a function of height. The parameterization covers a range of heights up to $\sim$113 km.

This model is not a wrong approximation of the state of the atmosphere when what we are interested in knowing about the air showers has nothing to do with atmospheric physics. However, for our purpose, this model is not useful because it does not adequately represent a real changing atmosphere. Several studies have attempted to reproduce the temperature effect in CR indirectly by comparing the results obtained using two different parameterizations of the standard atmosphere: Linsley and Keilhauer [92]. These parameterizations differ slightly in the calculated atmospheric profile, and therefore they provide two different values of the effective temperature (eq. 1.12). As a consequence, the temperature effect can be examined in a quantitative manner [159].

Another alternative is to use a scaling factor to change the parameterization values at certain atmospheric layers, emulating the density changes of the atmosphere in different seasons [38]. This method makes it possible to know, for example, what would happend to the CR rates at the surface when a region of the stratosphere increases its density by a specific percentage. Nonetheless, it is still an approximate approach that is not the modeling the real variations of the atmosphere as a function of height.

For academic purposes, we have decided to develop our own air shower simulation program that allows us to introduce real temperature profiles. The model is a simplification as it involves only the interactions of the muonic component developed in a one-dimensional atmosphere. The code has been written in Python language and is divided into several libraries that manage different parts of the simulation. Figure 4.1 shows a diagram of the blocks that integrate the program:

1. The input file contains the main parameters for the run process: number of air showers to be generated, energy of the primary cosmic ray, atmospheric model, etc.

2. In the second step, the program preprocesses the real data files (downloaded from ERA5 [81]) to provide an array with the temperature values as a function of height.

3. The atmospheric density and depth are calculated using the temperature data.

4. The fourth block contains the code that simulates the interactions of the cascade.

5. The desired results are stored in a file according to the specifications given in the input file: number of muons arriving to the ground, muon energy, height of creation, etc.

4.2.1 Primary Cosmic Ray

The interaction model assumes that the primary particle is a proton. Moreover, the total number of showers to be simulated in one run can be specified. Regarding the primary energy, a fixed value can be indicated or sampled whithin the interval $[E_{min}, E_{max}]$ with the probability distribution derived from the primary spectrum with exponent γ also specified. The energy is

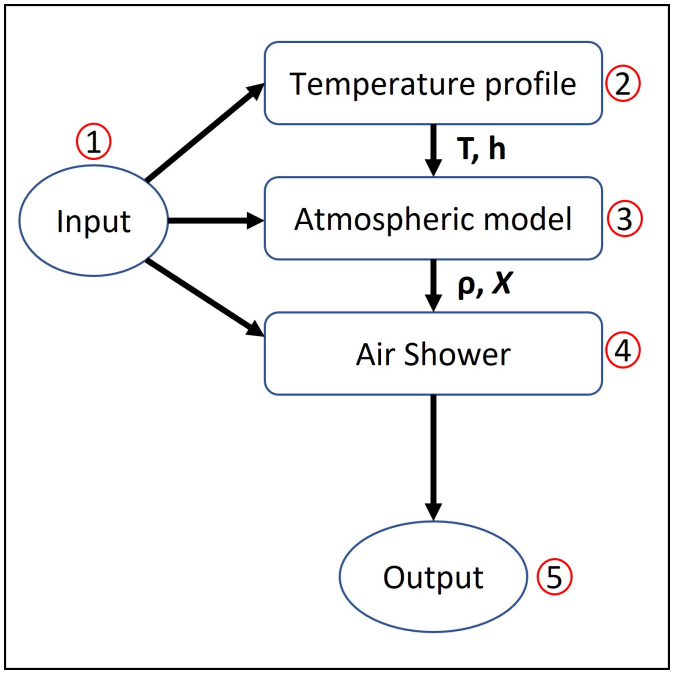

Figure 4.1: Schematic flow chart for the air shower simulations.

selected from the following probability distribution (see Appendix C.1 for a detailed derivation of the sampling distribution):

$$p(E) = NE^{-(\gamma+1)} \tag{4.1}$$

where N is a normalization factor.

4.2.2 Particle's fate

In a cosmic-ray simulation, which is based on Monte Carlo, a particle that has been created in the cascade can undergo different pathways, such as decaying or interacting with an atmospheric nucleus. Each interaction is characterized by its mean free path λ. For decaying, we have already seen in the introduction the corresponding expression (Table 1.2). For the case of nuclear interactions, the mean free path can be alternatively stated as the effective cross section, σ. Both are related as follows:

$$\lambda = \frac{m_{air}}{\sigma} \tag{4.2}$$

where $m_{air} = 14.54$ g/mol is the air atomic weight (not to be confused with the molecular weight). The mean free path λ is usually expressed in units of g/cm^2, so the correct expression would actually read as

$$\lambda = \frac{m_{air}}{N_{av}\sigma} \tag{4.3}$$

where N_{av} refers to the Avogadro's number. The effective cross section is a function of the particle energy.

Regardless of the type of interaction, it is mandatory to sample the corresponding

probability distribution to evaluate the actual path of the particle, which in this case corresponds to an exponential:

$$p(X) = \frac{1}{\lambda} e^{-X/\lambda} \tag{4.4}$$

where X_i corresponds to the mass thickness (g/cm^2). Integrating gives the survival probability:

$$P(X) = \int_0^X \frac{1}{\lambda} e^{-X'/\lambda} dX = e^{-X/\lambda} \tag{4.5}$$

and X can be expressed as:

$$X = -\lambda \, lnP \tag{4.6}$$

being P a random number between $(0, 1]$.

For each kind of interaction that the particle can undergo, X_i is sampled from the corresponding distribution to obtain a set of values:

$$X_i \quad i = 1, ..., n$$

The final interaction j that the particle will actually suffer corresponds to the minimum number of the X_i, that is, $X_j \leq X_i$ for all i. Hence, once the particle's fate has been decided, the corresponding interaction process starts [138].

One can imagine that a complete program that simulates CR cascades will have to take into account a myriad of different interactions for a variety of different subatomic particles: bremsstrahlung, electron-positron annihilation, inelastic collisions hadron-nucleus, photoelectric effect, etc., to mention a few. However, in our case we only want to study the atmospheric effect on muons, whose most important interactions are decaying and energy loss by ionization and radiative processes (bremsstrahlung, pair production, and photonuclear interactions). In addition, we also need to include the interactions of the parent particles: charged pions can mainly undergo a hadronic collision with a nucleus, ionization or decay. Regarding protons, we considered only hadronic interactions giving rise to pions.

The splitting of protons and pions are managed by a simple model of hadronic interactions based on the Hillas splitting algorithm (HSA) which is computationally fast [65, 112, 141]. This model handles the process of secondary particle creation in an inelastic hadronic interaction of the proton-air or pion-air type. The number of particles created, i.e. the multiplicity, as well as their energy is calculated with the algorithm. All particles created, whether the interacting particles is a proton or a charged pion, are assumed to be pions: charged $\pi^{\pm}$ or neutral π^0. In this way, as an approximation, the interactions are considered to be perfectly inelastic since all the energy of the initial particle is distributed among the new pions. In addition, each type of pion is produced with a one-third probability. As a consequence, a third of the available energy goes to π^0 production. The energies of the secondary particles are estimated following the HSA model as follows:

1. The available energy of the incoming particle is divided into two parts A and B randomly.
2. A is assigned as the energy that is going to have the incident particle after the interaction.
3. The energy B is split randomly into $J = 2^N$ "branches", where N is a fixed positive integer.

4. One of those branches J is split randomly into two parts A' and B'. The former is selected as the energy of a pion.

5. B' is subdivided at random into two parts: one of them is assigned as the energy of a pion and the other part is redefined as B' again.

6. The previous step is repeated until the energy of B' is less than a predefined critical energy ξ_c, which must be at least as large as m_π. When the critical energy ξ_c is achieved, then the algorithm goes back to step 4 to process the following branch.

The algorithm depends on the number of branches J. The value $J = 4$ has been suggested as a good proxy that fits with other complex hadronic models such as GEISHA and QGSJET (used in AIRES and CORSIKA, for example), that cover the low energy region below a few tens of GeV and the upper region above several hundreds of GeV, respectively [141]. Therefore, the HSA algorithm can cover the energy region treated in our simulations.

Moreover, when a $\pi^\pm$ decays in the cascade, the energy of the products needs to be calculated. In this case, the charged pion produces a muon and a neutrino:

$$\pi^\pm \rightarrow \mu^\pm + \nu_\mu(\bar{\nu}_\mu)$$

so the initial energy must be divided between the two new particles. The energy splitting follows the typical two-body decay theory of particle physics. The energy of the products have flat distributions assuming highly relativistic pions and massless neutrinos. They are given by [141]:

$$\frac{m_\mu^2}{m_\pi^2} \cdot E_\pi \leq E_\mu \leq E_\pi \tag{4.7}$$

$$0 \leq E_\nu \leq E_\pi \cdot \left(1 - \frac{m_\mu^2}{m_\pi^2}\right) \tag{4.8}$$

In this case, the muon will have an energy with probability distributed uniformly within the energy ranges given in equation 4.7, while the remaining energy is assigned to the neutrino. We should recall that in our simulations we only track muons, so neutrinos are discarded.

With the set of processes defined above, which include those involved in the atmospheric effect, it should be sufficient to emulate such effect in the muons arriving at the surface. In this way, we are saving computational cost because simulating a complete shower where millions of particles can be generated becomes very expensive.

4.2.3 Atmospheric model

As mentioned before, the CR simulation programs to date have tended to focus on standard atmospheric models rather than including the real atmospheric profiles. The aim of our program is to evaluate the actual influence of the atmosphere on the cascades in order to compare with real CR measurements. For such purpose, we will use atmospheric data from the ERA5 reanalysis dataset (from the European Center for Medium-Range Weather Forecasts, ECMWF) to be assimilated by our program [81]. This dataset delivers very accurate and consistent data of the atmosphere, combining model data with observations from across the world.

The ERA5 provides 37 isobaric levels from the surface up to the stratosphere (1000, 975, 950, 925, 900, 875, 850, 825, 800, 775, 750, 700, 650, 600, 550, 500, 450, 400, 350, 300, 250, 225, 200, 175, 150, 125, 100, 70, 50, 30, 20, 10, 7, 5, 3, 2, and 1 hPa), with a horizontal spatial resolution of 0.25° and a temporal resolution of 6 h [81]. We have downloaded the temperature and geopotential variables in pressure levels as well as pressure and temperature at ground level.

It is necessary to obtain the pressure and density profile as a function of height from the downloaded variables. It should be taken into account that air density depends on the temperature, which in turn is a function of altitude: $\rho(T,z)$. The equation of state in the case of an ideal gas is given by:

$$p(T) = \rho R_{air} T \tag{4.9}$$

where $R_{air} = R/M$, with $R = 8.3144$ J/(Kmol) is the gas constant and M is the air molar mass. Therefore, ρ can be estimated with:

$$\rho(z) = \frac{p(z)}{R_{air} T(z)} \tag{4.10}$$

where p, T and z are directly obtained from ERA5. Apart from this, the expression for the atmospheric depth as a function of height $X(z)$ needs to be obtained, which will allow us to calculate the height of the interaction for a given particle when its fate has been decided following the procedure indicated in the previous section. The atmospheric depth has units of g/cm^2 and can be obtained integrating the atmospheric density along the path length dz.

The atmospheric pressure represents the force of air per unit area: $p = F/A$. Force F represents the total weight of all air stacked above, which is the air mass multiplied by the gravity acceleration: $F = \int g dm$. At the same time, mass is density times volume. Therefore, we have:

$$F = \int_h^\infty g dm = \int_h^\infty g \rho A dz \approx gA \int_h^\infty \rho dz \tag{4.11}$$

This becomes:

$$gA \int_h^\infty \rho dz = pA \rightarrow p = g \int_h^\infty \rho dz \tag{4.12}$$

and finally, the atmospheric depth is:

$$\frac{p}{g} = \int_h^\infty \rho dz \equiv X \tag{4.13}$$

as we have anticipated, it corresponds to density integrated along a certain path. Thus, the atmospheric depth can be calculated using $p(z)$ data.

Although all this looks very satisfactory, we notice that we only have data for 37 pressure levels. However, when the particle's fate is calculated in the processing of the cascades, it gives a certain value for X. We include a function to linearly interpolate the data in order to determinate the atmospheric height corresponding to this value. Figure 4.2 illustrates a real atmospheric depth profile with some examples of points interpolated with that data.

The user-specified atmospheric data from ERA5 only covers altitudes up to 50 km, but it should go up to 100 km for simulation purposes. We have solved this issue by adding extra layers using the standard atmospheric model. This approximation is reasonable since the

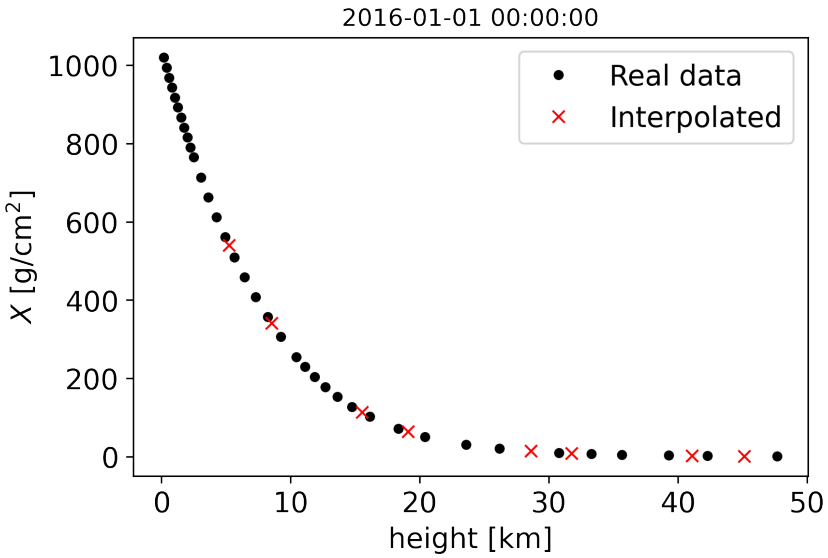

Figure 4.2: Atmospheric depth as a function of height for 1 January 2016 (black points) and some examples of points interpolated with this data (red crosses).

temperature variations at such great altitudes are negligible for the temperature effect induced in the surface CR rates. The reason is that the first interactions of the primary cosmic rays take place much deeper in the atmosphere.

Above the stratosphere, the following atmospheric layers can be found: stratopause, mesosphere, mesopause and the thermosphere. The stratopause and mesopause separate the stratosphere from the mesosphere and the mesosphere from the thermosphere, respectively. According to the definiton of the Standard Atmosphere, the stratopause can be found at an altitude of 47-51 km; the mesosphere spans heights approximately between 51 and 71 km and the mesopause goes from 71 km up to 85 km. The thermosphere, which corresponds to the second-outermost layer of Earth's atmosphere, extends to between 500 and 1000 km above the surface.

The temperature in the mesosphere drops with height, and its temperature-altitude profile can be described by a linear expression:

$$T = T_0 + A(h - h_0) \tag{4.14}$$

where T_0 is the base temperature of the layer, $A = -2.8$ K/km is the lapse rate, h refers to height, and $h_0 = 51$ km is the base altitude of the layer. Here, T_0 will match the value corresponding to the previous layer. In the thermosphere, the temperature profile has the form of an ellipse, which is expressed by:

$$T = T_c + A[1 - ((h - h_0)/a)^2]^{1/2} \tag{4.15}$$

where T_c is the base temperature, $A = -76.32$ K, $a = -19.9429$ km, h is the altitude, and h_0 is the base altitude. Again, T_c has to match the value of the previous temperature layer.

The stratopause and thermopause are described as isothermal layers.

Equation 4.10 can not be used here to calculate the atmospheric density at altitudes above 50 km since we do not have the pressure profiles for these atmospheric regions. Instead, we can first calculate the atmospheric pressure as a function of height using the barometric formula and

the temperatures calculated using equations 4.14 and 4.15:

$$p = p_0 e^{-\frac{gMh}{RT}} \tag{4.16}$$

where p_0 is the surface pressure. Finally, the atmospheric density and depth can be calculated using equations 4.10 and 4.13.

4.3 Simulation Setup

We focus the simulation study on uderstanding the observed atmospheric effects by means of the muon/meson balance in the atmosphere. The pressure and temperature effects are analyzed separately. In each simulation run (i.e., each atmospheric profile), 10^4 primary protons are launched down to the surface. This number has been carefully selected so that the statistical fluctuations of the output data are low enough to allow observation of the atmospheric effects. Then, the energy of the primary particle is selected from the probability distribution 4.1 whithin the interval ranging from 100 to 10^4 GeV.

The recorded outputs are the energy of muons reaching the surface and the production height of pions and muons. For the surface muon energies, we only save the ones having an energy above $\sim$4 GeV.

4.4 Results

4.4.1 Altitude Effects

To study the pressure effect, we have modeled the seasonal variations of the atmosphere during 2015 and analyzed their effects on the muon flux variations at the surface. We have averaged the real data to obtain the atmospheric profiles for the different seasons. For the purpose of this exercise, it is not necessary to analyze the whole time series, day by day. On the one hand, it would be computationally very expensive and, on the other hand, considering only seasonal variations makes it easier to study the barometric effect.

Figure 4.3 shows the simulated results for the barometric effect. In agreement with what we have obtained experimentally, the variations of muon flux are anticorrelated with the surface pressure variations. We have mentioned several times throughout this dissertation that mesons produced in the cascades can either interact or decay into muons. Therefore, we analyze the production heights of pions and muons to understand the reason of the observed seasonal behaviour.

Figure 4.4 displays one example of the distribution of the pion production height. As can be appreciated, our simulation predicts a maximum shower production level at an altitude of 7 km. Although it should be noted that in our case it appears at larger depths than the real one (about 12-15 km). However, we must remember that we are employing a simplified 1D-model. The particles of the cascade are moving vertically downwards in the atmosphere, traversing less amount of atmosphere than if they were traveling with a certain angle of inclination, as in real life, and therefore in our case they travel down deeper in the atmosphere.

The exact value of the peak is obtained by fitting the data with a Gaussian function in the atmospheric region around the maximum (blue line in Fig. 4.4). In the exampled shown, a value of 7.273 km has been obtained, which corresponds to altitudes in the 300 hPa region.

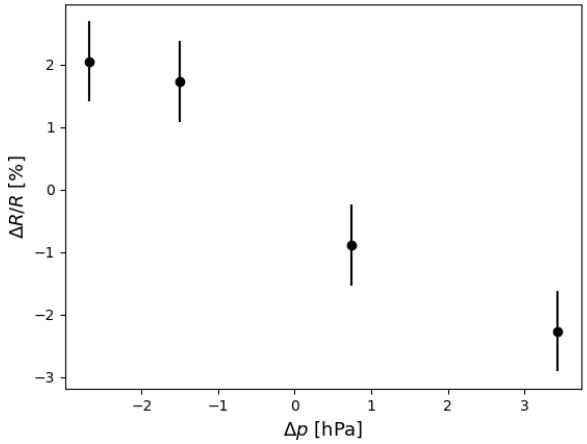

Figure 4.3: Relative variation of muon rates at the surface ($E_{th} = 3.2$ GeV) as a function of the surface pressure variations.

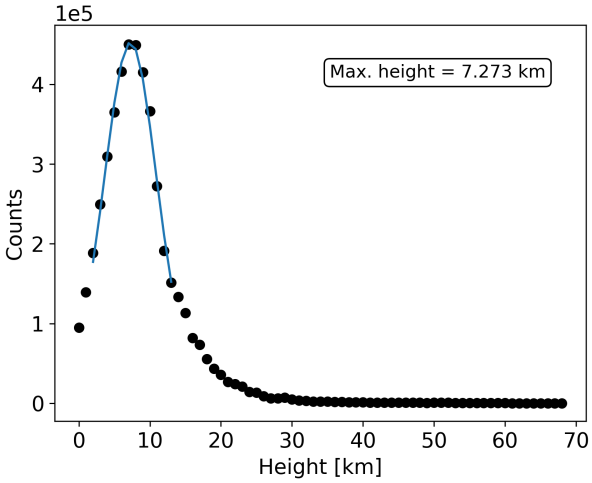

Figure 4.4: Distribution of pion-production height as a function of the atmospheric height. Height zero represents the surface level. The blue line represents the gaussian fit to the data in order to obtain the maximum height of production.

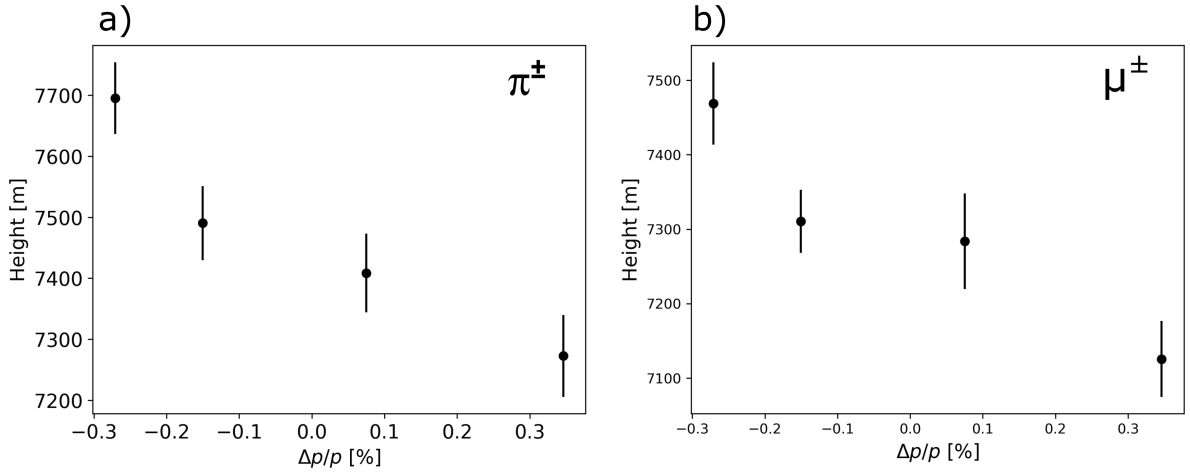

Figure 4.5: Simulated maximum height of production as a function of surface pressure variations for pions (a) and muons (b).

The maximum of production should shift when the surface pressure varies. To analyze its displacement, we fit all the simulated distributions to a Gaussian function in the same way as indicated above. The results are shown in Figure 4.5a as a function of the variations in surface pressure. Note that maximum height of production appears higher for lower surface pressure values.

Figure 4.5b looks at the muon production maximum heights. First of all, the values of the peaks are similar to those of the pions, although slightly lower ($\sim$200 m). This proves that pions are decaying almost immediately after creation, just as expected. As a consequence, the muon production peak shifts in the same way with pressure variations. Further inspection of the results shows that the peak variation is only a few hundred meters between different seasons (raging from 7200 to 7700 m in the case of pions). This is due to the fact that the surface pressure variations between seasons for the year we are analyzing are very small.

The height of the maximum depends on the altitude of interaction of the primary particles. The interaction probability of a proton depends on its energy and the amount of air mass traversed, i.e., atmospheric pressure. If its fate is to interact after traversing 300 hPa of mass, the only thing that changes is the altitude where that specific pressure level is located. As a result, the production height of pions and muons changes according to this. To test this hypothesis, we plot the maximum peak of the muon production versus height variations for the 300 hPa pressure level. The results can be seen in Figure 4.6. The lowest altitudes of the 300 hPa pressure level coincide with the lowest values of the production peak.

4.4.2 Temperature correlations

We simulate a period of one year with steps of 25 days to obtain a small sample of cosmic-rays flux. A full year with 6-hour steps would take a long time, but a shorter period is enough to corroborate the experimental results. The simulated rates are correlated with the temperature variations at different heights to obtain the regression slopes $\widetilde{W}_T$, similar to those obtained in Chapter 2 in Figure 2.10b. Figure 4.7 shows the results of the regression of the simulated data, indicating a good agreement with the expected values based on the theoretical weights W_T by Dmitrieva *et al.* (assuming a threshold energy of 3.2 GeV). The fact that we are

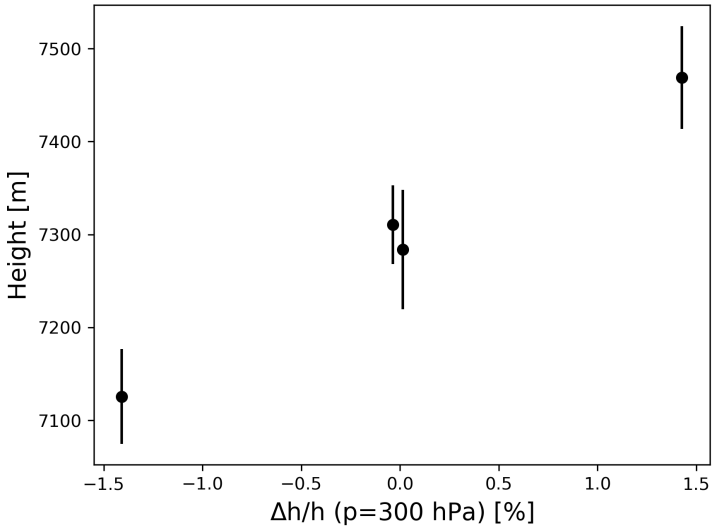

Figure 4.6: Simulated maximum height of production for muons as a function of height variations in the pressure level of 300 hPa.

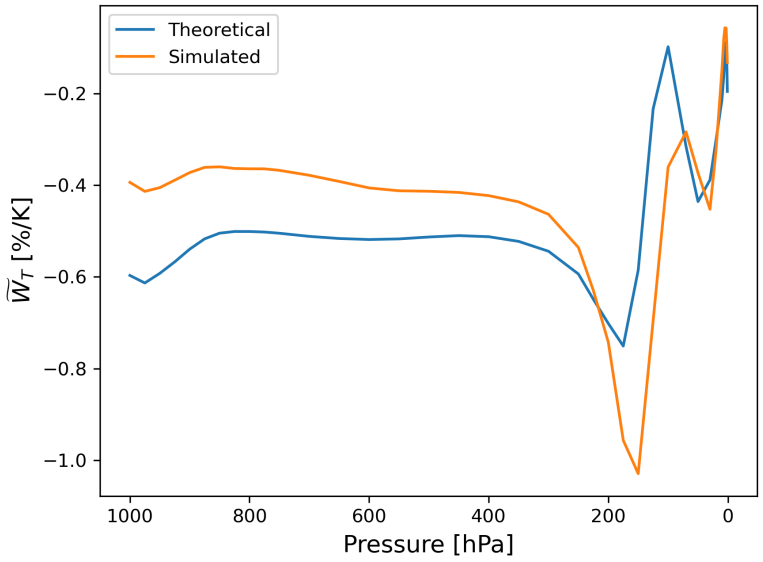

Figure 4.7: Slopes $\widetilde{W}_T$ obtained through a direct linear regression with simulated cosmic ray data (yellow line) compared to the expected values (blue line).

able to reproduce the theoretical results confirms that the atmospheric effects seen in the real data are indeed dominated by the absorption/production processes of the secondary particles in the atmosphere, mainly muons and pions. As already indicated in the discussion of Figure 2.10, when doing a direct regression the correlations between atmospheric layers also play a role, and indeed the strong variations in the region 50-250 hPa are a footprint of the tropopause dynamics.

Chapter 5

Modeling the Influence of Cosmic Rays on the Atmosphere

Abstract: *The flux of cosmic rays in the atmosphere has been reported to correlate with cloud and aerosol properties. Several mechanisms have been proposed and tested to explain this effect, leading to the conclusion that the induced effects were minor. However, these studies did not disprove the link between cosmic rays and clouds (i.e., climate). Since then, some different mechanisms that could be relevant to aerosol growth have been postulated. In this chapter, we use a global chemistry transport model to include the effects of charging on the microphysical development of aerosols. We will compare the variations of cloud condensation nuclei (CCN) concentrations between the solar maximum and solar minimum. This study aims to discover the complex relationship between GCR and aerosols.*

*This chapter includes content from the following article: I. Riádigos et al.. The Charge of aerosols from Cosmic Rays and the enhancement of cloud condensation nuclei formation. *In preparation*, 2022.

5.1 Introduction

In the previous chapters, we have covered the subject of the atmospheric effect on the CR flux measured near the surface. However, as was mentioned in Chapter 1, the charged population of CR can affect those atmospheric processes where the ionization, electric field, or particle charges play an important role. The charging of the atmospheric aerosols and the subsequent creation of CCN, as pointed out in Chapter 1, are among those processes. Thus, in this last chapter, we address the opposite question to the one that has been covered so far in the previous chapters, i.e. how CR can affect atmospheric conditions, in particular those related to cloud formation. It should be also mentioned that while in Chapters 2-4 we were focused mainly on the muon component of secondary CR, in this chapter the entire CR flux is considered to calculate atmospheric ionization rates. Besides, the barometric/temperature effect previously analyzed is direct, however, the CR-cloud effect that we are going to study is considered to be an indirect effect, because there is no linear proportionality between changes in CR flux and the variations of CCN.

One of the most debated aspects of aerosols is the role that Galactic Cosmic Rays play in their growth. We have seen in the introductory part of this thesis (Section 1.5.3)

that numerous studies have reported strong correlations between the cosmic-ray flux and aerosol-cloud properties (e.g., [148]). To date, literature has emerged that offers contradictory findings about this issue [102]. In addition to this, it has not been easy to find the corresponding process to explain such connection. Numerous mechanisms have been proposed but have failed when testing their relevance to CCN formation. One of the most promising hypotheses has been the so-called "aerosol clear-sky mechanism", which involves the nucleation process.

Nucleation is a process affecting the finest atmospheric particles by which they aggregate to form small clusters, giving birth to the smallest aerosols. It is one of the most important processes in the creation of aerosols in the atmosphere. From here, condensation and coagulation are responsible for these small clusters to grow to CCN sizes ($\gtrsim$100 nm). The former causes the growth of aerosols through condensation of vapors (generally sulfuric acid and low-volatility organics), and the latter refers to the attachment of two colliding aerosols to form a larger one. It is well known that the presence of small ions created from the ionization of atmospheric particles by GCR can enhance the nucleation rates. If the newly created particles do not get lost along the way, they can grow to CCN sizes. One of the possible ways of being lost is through coagulation with existing CCN particles. The balance between coagulation losses and growth to CCN will determine how much GCR induced-ionization can influence the number of CCN and eventually cloud cover. These are the fundamentals of the clear-sky mechanism. During the past decade, Jeff Pierce has presented numerous reports and collaborated on several studies to shed light on the relevance of this mechanism in the atmosphere [122, 143, 121].

The state-of-the-art CLOUD experiment at CERN has made significant contributions to our understanding of the relation between aerosol nucleation and GCR. The CLOUD collaboration was the first to experimentally demonstrate the impact of GCR on nucleation rates and has provided parameterizations for this relationship that can be easily incorporated into atmospheric models for further analysis [54]. However, they have determined that the impact of GCR on nucleation (i.e., the clear-sky mechanism) is not sufficient to explain the correlations found between cosmic-ray flux and clouds. These results have opened the door for proposing new mechanisms that can explain this elusive link.

Recently, another group of researchers has explored theoretically and experimentally the possibility that cosmic rays may enhance the condensation rates of aerosols [149]. The proposed hypothesis states that an increase in ionization results in faster aerosol growth by condensation, which prevents them from being lost by coagulating with existing particles. The point here is that the charge that aerosols acquire when ions condense on them has traditionally been neglected. This has been assumed because the flux from neutral molecules (such as sulfuric acid) to aerosols by condensation is much higher when compared to the mass flux from the ions. By illustration, the typical ratio between them is 10^{-3}. Svensmark *et al.* argue that this small ion flux should not be underestimated. So far, only the condensation of neutral molecules in aerosol growth has been taken into account. Svensmark *et al.* also consider that aerosols can be charged by the condensation of ions and at the same time neutral gas can condensate onto charged aerosols. They develop a model where all these interactions are taken into account. This model considers that aerosols can be positively, negatively, or neutrally charged and that the condensible gas contains positive and negative ions from cosmic rays as well. They define β as the interaction or attachment coefficient (in units of m^3/s) between gas molecules and aerosols. The key is that β has different values depending on whether the particles in play are charged or uncharged. If the electrostatic interactions between charged particles are taken into account when computing this coefficient, it is observed that for small particles its value

is greater than the original coefficient of neutral particles. As a consequence, small charged particles would condense faster than neutral ones. In their work, Svensmark *et al.* present experimental results showing that the presence of ions seems to support their hypothesis under some atmospheric conditions. However, when estimating the interaction coefficients they make too many simplifications, such as considering a constant temperature or setting the mass of the neutral gas to a value of 100 AMU. This is only a small representation of the atmospheric conditions.

To test the real impact of this mechanism, the proposed scheme should be incorporated into an atmospheric model. In 2020, Svensmark *et al.* presented a numerical approach for this mechanism that could be implemented in atmospheric models [152]. However, numerous challenges arise when it comes to implementing this model. On the one hand, the calculation of the interaction coefficients for charged particles requires a lot of computational resources. This implies that tables should be previously created with the values of the coefficients as a function of different variables, which could then be used to interpolate the corresponding values in the model. As we will see later in this chapter, there is a much faster and accurate approach to do this calculation. On the other hand, it has been shown that in the real atmosphere particles are capable of acquiring multiple elementary charges [93, 168]. So this must be taken into account and turns out to be one of the objectives of this work.

To take into account that aerosols can accumulate a large number of charges on their surface, their charge distribution must be estimated. The charge distribution affects the coagulation process since if two colliding aerosols carry charges of identical signs, a repulsive force will appear and inhibit their union. In contrast, if the aerosols carry charges of opposite signs, their coagulation will be enhanced. Thus, it becomes relevant to incorporate the charge distribution in the model but, as we will see, doing it explicitly is almost impossible and computationally very expensive. However, there is an approach that can be adopted for this purpose and will be explored in the following.

Improving our knowledge of aerosol growth is important to better understand changes in clouds. Any change in the global cloud cover modifies the terrestrial albedo by increasing or decreasing the warming effect on climate. One of the biggest unknown factors in climate prediction is how clouds vary under different conditions. As we mentioned, one of the reasons is that the exact mechanisms of CCN formation are hardly known in detail. These uncertainties lead to a large dispersion in the climate predictions regarding the average temperature increase for the following decades. Therefore, it is crucial to go deeper into the study of cloud formation processes as climate change is one of the greatest concerns of our generation.

In short, numerical models that describe in detail all aerosol microphysical processes are very demanding from a computational point of view. Expanding upon previous works, we want to include the effects of atmospheric charging from CR in aerosol growth to test and understand the relationship between cosmic radiation and aerosols. The most important processes for aerosol growth are nucleation, condensation, and coagulation. So far, only the former has been parameterized and included in global aerosol models taking into account the effect of ions in the process (ion-induced nucleation) [181, 54, 69]. However, multiple investigations have proven that this mechanism alone is not strong enough to produce substantial changes in the final CCN concentrations (e.g., [143]). Therefore, our work is devoted to introduce the charging effect of ions into the condensation and coagulation processes using a global 3-D atmospheric chemistry model called GEOS-Chem. This model has been designed to simulate atmospheric composition on a global and regional scale. Besides, it can be coupled with other

climatic or meteorological models, such as WRF (one of the most widely used in the world for short-term regional forecasting). GEOS-Chem is one of the most complete and accessible models that can be found, in addition to the fact that it is developed by hundreds of scientists around the world. Therefore, it is one of the most updated and complex models in its field. Another outstanding feature is that it has already implemented the effect of the ions generated by GCR in the nucleation process. Hence, it is one of the most suitable models to carry out our study.

In the following sections, we present the methodology used to achieve our objectives and we will show that the effect of charging on the aerosol processes can be quite relevant and further research should be carried out in this direction.

5.2 Atmospheric Simulations with GEOS-Chem

We use the global chemical transport model GEOS-Chem v12.1.0 (`https://zenodo.org/record/1553349`) with a horizontal resolution of $4^\circ \times 5^\circ$ and 47 vertical layers (from the surface up to 0.01 hPa). The model is driven by assimilated meteorological data from MERRA-2 reanalysis (https://gmao.gsfc.nasa.gov/reanalysis/MERRA-2/). This 3D model includes two aerosol microphysics schemes: TOMAS and APM. In this work, we use the TOMAS (TwO-Moment Aerosol Sectional) package [4, 160]. An advantage of using TOMAS is that it provides a higher resolution for all chemical species, especially for small sizes, which is very relevant to our study. This microphysics model simulates two independent moments (number and mass) of the aerosol size distribution for a number of discrete size bins:

$$N_k = \int_{x_k}^{x_{k+1}} n_k(x)dx \tag{5.1}$$

$$M_k = \int_{x_k}^{x_{k+1}} x n_k(x)dx \tag{5.2}$$

where N_k and M_k are the total number and mass of aerosol in the k bin, $n_k(x)$ is the number of particles with masses between $x + dx$, and x_k is the lowest limit of the k bin.

In addition, the package incorporates modules for computing nucleation, condensation, and coagulation. We use the version of TOMAS40 that includes 30 bins logarithmically spaced ranging from 10 nm to 10 μm to represent the aerosol diameters, plus ten additional sub-10nm bins with a lower limit of 1 nm. The latter provides a high resolution for small particles, which is necessary for the simulations we want to carry out.

Particularly, GEOS-Chem includes the ion-mediated nucleation (IMN) mechanism [180, 181] to calculate the nucleation rates taking into consideration the influence of atmospheric ions. The IMN depends on five key parameters: sulfuric acid concentration, temperature, relative humidity, ionization rate, and surface area of preexisting particles. The nucleation rates as a function of these parameters are extracted from a look-up table that covers a wide range of atmospheric conditions in order to be used as an input for GEOS-Chem. The global atmospheric ion rates due to CR are calculated following the model given by Usoskin and Kovaltsov [167]. The contribution of radioactive materials from soil to ionization rates is also included.

The Usoskin and Kovaltsov approach consists of a very simple numerical model which computes the cosmic induced ionization in the atmosphere from the surface up to the stratosphere, all over the world. The model is parameterized by the modulation potential ϕ

(given in units of GV), which is used to easily calculate the variations in the induced ionization caused by the Sun's activity. This parameter is utilized to determine the energy spectrum of GCR at the Earth's orbit, which is modulated by the solar variations. It takes a typical value of 1 GV at solar maximum and 0.4 GV for the solar minimum. The smaller the value, the more CR enter the atmosphere.

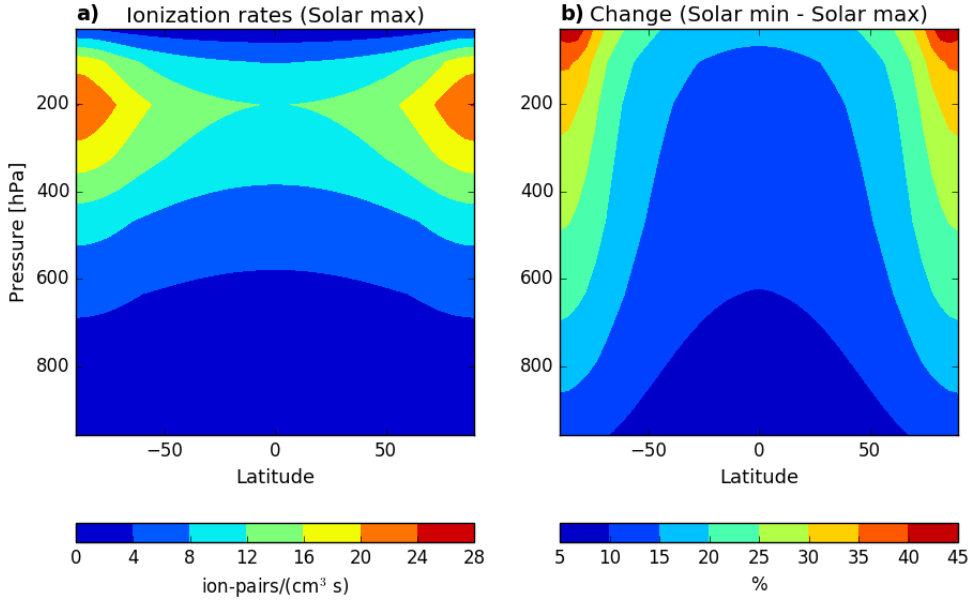

Figure 5.1: **(a)** Zonal-mean CR induced ionization (in units of ion-pairs $\mathrm{cm}^{-3}s^{-1}$) in the atmosphere in the solar maximum ($\phi = 1$ GV). **(b)** Zonal-mean percent change in the induced ionization between the solar minimum ($\phi = 0.4$ GV) and solar maximum. [167]

Figure 5.1a shows the atmospheric ionization rates for the solar-maximum case calculated using the method described in [167]. The rates are averaged over longitude in order to examine the regional differences. As can be seen, the ionization rates in the solar maximum are generally higher in the upper troposphere than near the surface. Furthermore, they are also higher towards the poles because magnetic rigidity is smaller, i.e., the Earth's magnetic field shields much less. Figure 5.1b compares the ion-pair formation rates from CR between the solar minimum and the solar maximum. The changes between both situations reflect how the polar regions are most susceptible to CR changes. Apart from this, it should be remarked that the strongest FDs can cause changes in the atmospheric ionization rates similar to the changes between a solar maximum and solar minimum. Thus, a comparative study between solar peaks can be used to estimate how the changes would look like in a FD event [143].

5.3 Approach to simulate charge distributions

5.3.1 Condensation

Ions produced in the atmosphere by CR can charge aerosols through diffusion charging, which refers to the attachment of ions from the environmental background to the surface of particles [85, 174, 130]. We formulate the interactions governing the temporal dependences of ions and aerosols. The terms for the temporal changes in ion concentrations n^q are:

$$\frac{dn^q}{dt} = \left.\frac{dn^q}{dt}\right|_{production} + \left.\frac{dn^q}{dt}\right|_{condensation} + \left.\frac{dn^q}{dt}\right|_{loss} \tag{5.3}$$

where q=[-,+] denotes the charge. Here, the first term on the right-hand side refers to the production rates of ions in the atmosphere, q, by cosmic rays (estimated according to Usoskin *et al.* [167]) and natural radioactivity that contributes to near-surface ion production from radioactive elemenents in the soil. The second term in the above equation describes the condensation of ions onto aerosols:

$$\left.\frac{dn^q}{dt}\right|_{condensation} = -n^q \sum_k \sum_j \beta^q_{k,j} N_{k,j} \tag{5.4}$$

here, $\beta^q_{k,j}$ represents the interaction coefficient between an ion and an aerosol, being $N_{k,j}$ the number concentration of particles with size k carrying charge j (i.e., j represents the number of elementary charges of particles).

Finally, the third term in equation 5.3 includes the loss rate of ions due to ion-ion recombination:

$$\left.\frac{dn^q}{dt}\right|_{loss} = -\alpha n^+ n^- \tag{5.5}$$

where α is the recombination coefficient of ions.

It should be noted that, while the first term represents a positive contribution to ion rates, both the second and third terms refer to their removal of ions by two different processes, one of them leading to charged-aerosol formation. In particular, the condensation of ions onto aerosols provokes the addition of positive and negative charges to the particles. The variations in the charge distributions of aerosols for a k-bin can be represented by the following interactions:

$$\frac{dN_{kj}}{dt} = \beta^+_{k,j-1} n^+ N_{k,j-1} - \beta^+_{k,j} n^+ N_{k,j} + \beta^-_{k,j+1} n^- N_{k,j+1} - \beta^-_{k,j} n^- N_{k,j} \tag{5.6}$$

the charge j of an aerosol with size on the k-bin is displaced to the left $(j-1)$ when a negative ion is attached to the aerosol but increases $(j+1)$ when it interacts with a positive ion.

In this case, the mean value of the charge distributions can be expressed as

$$J_k = \frac{\sum j N_{kj}}{\sum N_{kj}} \tag{5.7}$$

5.3.2 Coagulation

Particles of size bin k coagulate with the other particles of size bin i. By illustration, an example of a simple model to describe the rate of change for a k-bin when considering only neutral aerosols is [164, 110]:

$$\frac{dN_k}{dt} = \frac{1}{2} \sum_{i=1}^{k-1} K_{i,k-i} N_i N_{k-i} - N_k \sum_{i=1}^{I} K_{i,k} N_i \tag{5.8}$$

where $K_{i,k}$ is the coagulation coefficient between two bins and I is the total number of bins. In the case of TOMAS40, with 40 size bins, the resulting number of equations to solve is 40.

Coupled with them, we would like to include the corresponding differential equations of the charge distributions for each bin: dN_{kj}/dt. However, the number of equations to be solved would be multiplied by the number of charge bins j taken into consideration. For instance, assuming that aerosols can acquire up to ten elementary charges (positive or negative), the resulting set of equations to be solved would be 450. Hence, from the computational point of view, it would be counterproductive and expensive to implement such a model.

In equation 5.8, the coagulation coefficient represents the collision frequencies of the aerosols (units of m^3s^{-1}), alternatively stated as the coagulation rate coefficient. Physically, three regions can be distinguished depending on the ratio of mean free path of the gas molecule to the particle radius (Knudsen number, Kn): continuum, transition, and free molecular [140]. In detail, if the mean free paths are high yielding few collisions ($Kn > 10$), the gas has to be analyzed by the molecular theory. By contrast, the continuum regime covers dense flows with high collision rates ($Kn < 0.01$), where the gas can be treated as a continuous medium. In this situation, fluid properties such as temperature, density, viscosity, etc. can be written as continuous functions of space and time.

The computation of the coagulation coefficients concerns several collision mechanisms, including the interparticle forces (i.e., electrostatic interactions) and the given flow regime. Specifically, the Brownian motion (i.e., resulting from thermal energy) is the dominant mechanism assumed to induce coagulation in TOMAS [103]. The coagulation coefficients are calculated with an interpolation formula considering the coagulation in the different regimes [63]. Therefore, the Brownian interaction coefficient between two aerosols is given by

$$K_{k,i}^{Br} = 4\pi(r_k + r_i)(D_{p,k} + D_{p,i}) \left(\frac{r_k + r_i}{r_k + r_i + \sqrt{g_k^2 + g_i^2}} + \frac{4(D_{p,k} + D_{p,i})}{(r_k + r_i)\sqrt{\bar{v}_k^2 + \bar{v}_i^2}} \right)^{-1} \tag{5.9}$$

where r_k and r_i are the radii of the two interacting aerosols, D_p is the particle diffusion coefficient, g is the particle mean traveling length, and $\bar{v}$ is the average speed of the aerosol in air. However, we want to consider the interaction between charging aerosols. For this reason, coagulation is going to be affected by electrostatic interactions and needs to be taken into account. Charged particles coagulation may be enhanced or inhibited depending on their charges. A straightforward approach to do this is multiplying the Brownian coefficient by a "correction factor", $W_{k,i}$, which is based on a "stability coefficient" that considers Coulomb forces in the continuum regime [140].

The electrostatic potential energy of the interaction between two particles of charge j_k and j_i separated by a distance r is:

$$\phi = \frac{j_k j_i e^2}{4\pi\varepsilon_0 \varepsilon r} \tag{5.10}$$

where e is the elementary electronic charge (1.602×10^{-19} C), ε_0 is the permittivity of vacuum and ε is the dielectric constant of air. Taking this into consideration, the correction factor is given by [63]:

$$W_{k,i} = \frac{\gamma}{e^{\gamma} - 1} \tag{5.11}$$

where

$$\gamma = \frac{j_k j_i e^2}{4\pi\varepsilon_0\varepsilon(r_k + r_i)k_B T} \tag{5.12}$$

Here k_B is the Boltzmann constant and T is the temperature. Comparing with equation 5.10, the constant γ can be seen as the ratio between the electrostatic potential energy and the thermal energy $k_B T$. In the case of particles with similar charges ($j_k j_i > 0$), γ is greater than zero and, therefore, $W_{k,i} < 1$ and the coagulation is inhibited with respect to that of pure Brownian collision. On the other hand, for different charges, the constant gives $\gamma < 0$ and $W_{k,i} > 1$, which implies that the coagulation rate is enhanced. In fact, the factor $W_{k,i}$ is also referred to as the "enhancement factor". Finally, when the charge of either the colliding aerosols approaches zero ($j_k j_i \to 0$), $\gamma \to 0$ and $e^{\gamma} \sim 1 + \gamma$. Thus, $W_{k,i} \to 1$ and the coagulation coefficient restores its original form involving the Brownian mechanism alone.

It was mentioned above that the expression 5.9 was calculated considering the continuum regime. However, there exist correction factors estimated for the rest of the regimes (see [152]). Obviously, the expression presented above is going to be less precise, although it has proven to provide quite good results [87, 93, 168]. Svensmark *et al.* have recently developed a new numerical approach for the growth of charged aerosols where they propose their coefficients but, they turn out to be very expensive to compute explicitly in the code [152]. Besides, the calculation is designed for very specific cases, like-charged coagulation is neglected, they do not handle multiple-charge aerosols, and several constraints are taken into consideration for the estimates. As a consequence, the coefficients presented in their work are system-specific and should be considered as a first approximation. For this reason, we have decided to adopt a more suitable methodology with the combined expressions 5.9 and 5.11, which have already been implemented in several studies and contrasted with real data [110, 93, 168].

At this point, we need an appropriate approach to include the charges in the coagulation process. Several methods calculate the charge accumulation rate of particles with the ion balance and the charge balance model represented by equations 5.4 and 5.6. However, several works have suggested other alternatives in order to save computational costs without loss of accuracy. They have proposed to assume a Gaussian distribution to approximate the charge distributions in aerosols at a steady-state, and the obtained results were successful with an acceptable degree of error [37, 93]. So the charge distributions can be represented like this:

$$N_{kj} = \frac{N_k}{\sqrt{2\pi}\sigma_k} \exp\left(-\frac{(j - J_k)^2}{2\sigma_k^2}\right) \tag{5.13}$$

where J_k is the mean aerosol charge (from eq. 5.7), and σ_k is the standard deviation of the charge distribution for the k-bin, both given by:

$$\sigma_k^2 = \frac{1}{2\omega_k} \qquad J_k = \frac{X - 1}{2\omega_k} \tag{5.14}$$

with $\omega_k = \frac{e^2}{8\pi\varepsilon_0\varepsilon r_k k_B T}$, $X = \frac{\mu_+}{\mu_-}$. Here ω_k describes the effects of the diffusion charging, X represents the mobility ratio between positive and negative ions, and $\mu_\pm$ is the mobility of positive or negative ions ($\mathrm{m^2 V^{-1} s^{-1}}$).

Therefore, with these tools, we are already able to estimate the distribution of charged aerosols at each time step. But we are still missing a key piece: taking into account the charging in the coagulation equation 5.8. One way to do it is to include the effects of the

charge distributions on the coagulation coefficients. The correction factor between particles of size bins k and i presented in eq. 5.11 is replaced by an average correction factor $\overline{W}_{k,i}$, which includes the interaction of all charged particles of size k with any charged particle of size i [37]:

$$\overline{W}_{k,i} = 1 + \frac{\sum_{j_k \neq 0}^{\infty} \sum_{j_i \neq 0}^{\infty} N_{k,j_k} N_{i,j_i} (W_{k,i} - 1)}{\sum_{j_k}^{\infty} N_{k,j_k} \sum_{j_i}^{\infty} N_{i,j_i}} \tag{5.15}$$

If the coagulation is mainly inhibited among aerosols, $W_{k,i} < 1$, the second term in the right-hand side of the above equation will be negative and the average correction factor will be less than one. When the opposite happens, the coagulation between particles of size k and i will be enhanced. This simplified method avoids having to explicitly include the entire calculation in the code.

To summarise, the recipe for implementing the effect of CR charging in the atmospheric 3-D model is as follows: first, the mean aerosol charge J_k and σ_k are calculated for each size bin using equation 5.14; second, the charge distributions are estimated using the Gaussian distribution introduced in the expression 5.13 along with the total number of aerosols N_k calculated in the atmospheric model; third, the average correction factor $\overline{W}_{k,i}$ can be computed in eq. 5.15; and finally, the "standard" coagulation coefficient can be corrected multiplying by the correction factor $\tilde{K}_{k,i} = K_{k,i}\overline{W}_{k,i}$.

Last but not least, a small detail must be taken into account when implementing the calculations in the code. The summation indexes in eq. 5.15 are evaluated to infinity and, in practice, it is usually considered to span $l_k = J_k \pm 5\sigma_k$, as an approximation to determine the summations (which encompasses 99.99994% of the charge values). However, the summations can become too large when aerosols carry a significant number of charges. This fact significantly impacts the computation time at each step and, therefore, demands optimization. In this case, the correction coefficient has to be evaluated at each time step for all combinations of bins, k^2. Considering that the number of terms in the summation becomes $l_k \cdot l_i$, the number of total calculations at each time step scale with $k^2(l_k l_i)$.

To optimize calculations without losing accuracy, Vasilakos *et al.* proposes limiting the iteration interval to $J_k \pm 2\sigma_k$ and additionally employ an adaptive step for the iterator in the summation that will be applied whenever the average charge exceeds the value of 100 [168]. The step is defined as $\Delta n = \frac{|4\sigma_k|}{100} + 1$ and it has been found to considerably reduce the computation time without losing accuracy in the estimation of $\overline{W}_{k,i}$. In our tests, we have been able to reduce the computation time by up to 85% by applying these optimizations.

Figure 5.2 compares the correction coefficients obtained using the exact summations with those estimated using the optimization method. As can be seen, the lines representing the theoretical (red lines) and approximate values (black dashed lines) overlap, indicating that there is no loss in accuracy when using the approximate summation (correction coefficients for $X = 0.7$ and $X = 0.8$ are included in Appendix B.4).

Therefore, the aim of this work is to implement the methodology described throughout these last sections for the very first time in a global aerosol model.

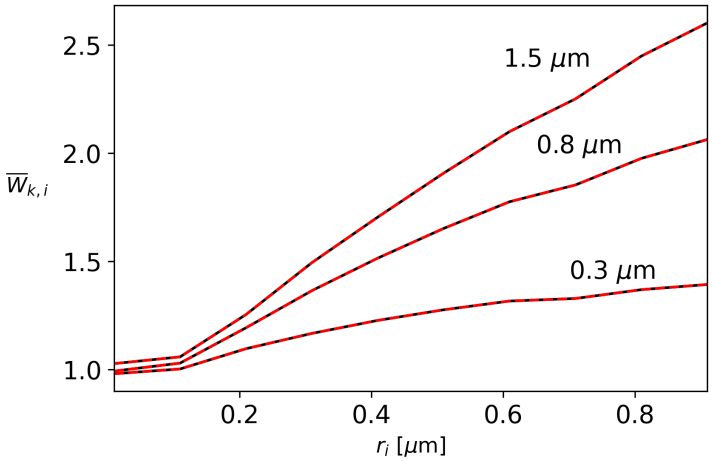

Figure 5.2: Correction coefficients ($\overline{W}_{k,i}$) calculated with the exact summations (red solid lines) together with the optimized computation described in Vasilakos *et al.* (black dashed lines) between particles of size r_k and r_i. The r_k values are the ones indicated in the labels next to the curves: 0.3, 0.8 and 1.5 μm. The following values have been chosen for the calculations: $N_k = N_j = 6 \cdot 10^9$ m^{-3}, $X = 0.8$ and $T = 270$ K. The dashed lines representing the approximate calculation of the coefficients overlap with those of the exact solution, indicating that there is no loss in accuracy when using the approximation.

5.4 Simulation Setup

In this work, we use the TOMAS version of GEOS-Chem that includes 40 bins, as was indicated before. Furthermore, the nucleation model chosen for these simulations is the ion-mediated nucleation (IMN) by Yu (2010). We run pairwise simulations, one with a modulation potential of 0.4 GV (referred as solar minimum) and the other with a modulation potential of 1 GV (referred as solar maximum). In addition to this, we change the value of the ion mobility ratio X to test the sensitivity of the results to this parameter. In typical atmospheric conditions the mobility ratio is $X < 1$, therefore the values examined are: $X = (0.7, 0.8, 0.9)$ [66, 77]. With this, the number of simulations carried out will be 2×3, plus 2 additional ones with the standard cases in which the particle charging will not be taken into account, this will be called the standard case.

We perform two-month simulations corresponding to January and February. The runs have a spin-up period of 1 month, therefore the simulated month is actually February. The results from this month are averaged to analyze the overall effectiveness of the approach. The spin-up period (or initialization period) is necessary because the files with the initial conditions used by GEOS-Chem do not reflect the actual atmospheric state. For simulation cases similar to ours, it has been found that a spin-up of 1 month is sufficient (see [143]).

As a first attemp, we have decided that one-month simulation is enough for our purposes, since once equilibrium is reached with the spin-up period, the results do not vary much over time. Moreover, with the new approach implemented in the code, simulations take two to three times longer to complete even though the calculations has been optimized.

The saved outputs of the simulations contain the nucleation rates in the atmosphere as a function of time as well as the concentrations of the different types of aeorols distributed over the 40 initially specified bins. Afterwards, the total number of particles for different threshold sizes is calculated, that is, the total number of particles larger than a certain size: CN3, CN10, CN40 and CN80. For example, CN10 are the total number of particles larger tan

10 nm. Besides, the CCN concentrations are also computed. CCN are defined as a subset of the aeorol particles that can nucleate water drops at supersaturations less than 0.2%. In the real atmosphere, the number of aerosols activated to become cloud droplets depends on the particle size distribution, composition, and water vapor supersaturation (S). For a $S < 0.2\%$, the ~ 90 % of the aerosol particles activated are in the size range above 100 nm [36].

5.5 Results and Discussions

Figure 5.3 shows the percentage change between the solar minimum and the solar maximum simulations in CN3, CN10, CN40, and CN80 concentrations averaged over various atmospheric regions: lower troposphere (below 700 hPa) and free troposphere (below 200 hPa).

First of all, for all the cases analyzed, the percent change is positive, indicating that the concentration values are always higher in the solar-minimum situation than in the solar maximum. Secondly, the enhancement in concentration for the standard cases range from 0.2 % in CCN to 1.5 % in CN3. Therefore, this enhancement tends to drop as the particle

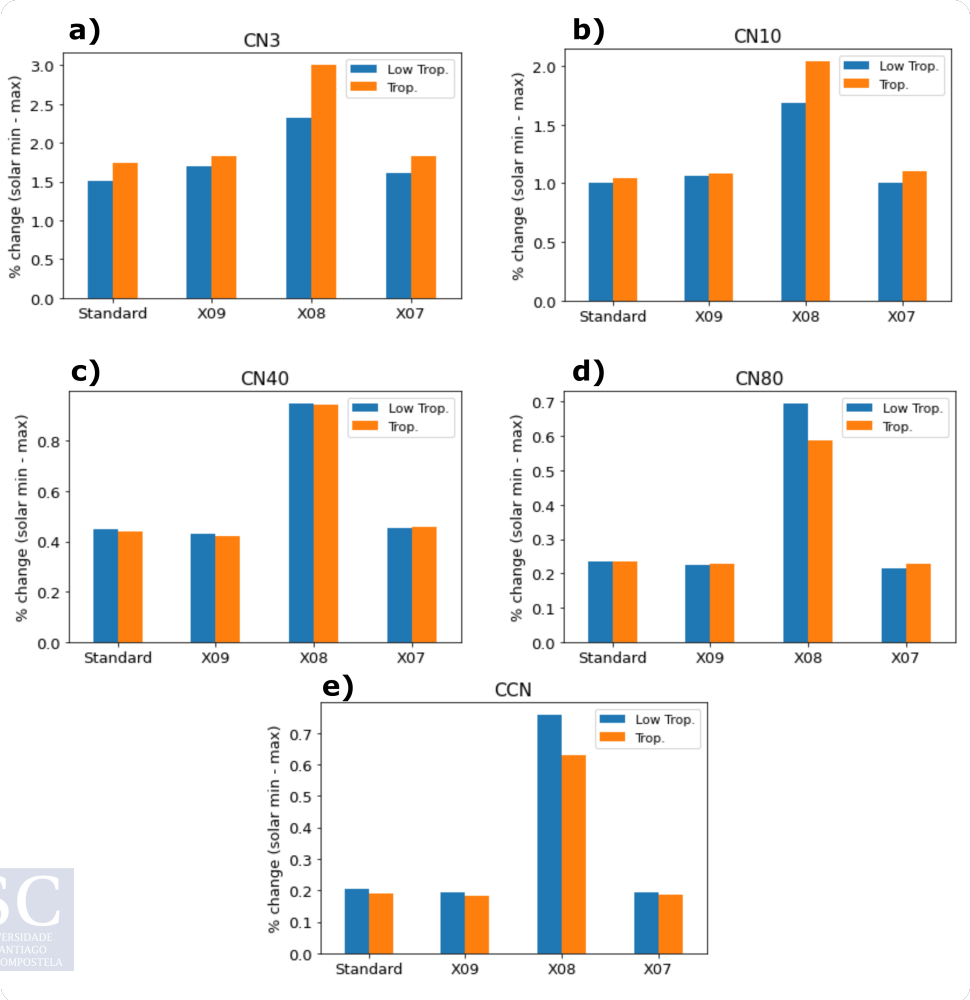

Figure 5.3: Percent change in (a) CN3, (b) CN10, (c) CN40, (d) CN80, and (e) CCN for various atmospheric regions: lower atmosphere (blue bars) and free troposphere (yellow bars). Four different cases are analized (x axis): standard, $X = 0.9$, $X = 0.8$, and $X = 0.7$.

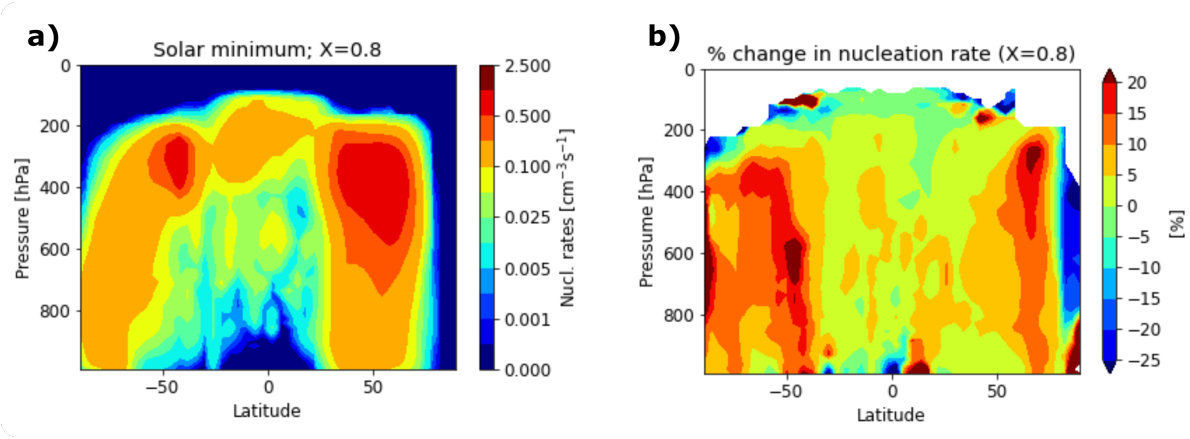

Figure 5.4: (a) Zonal-mean nucleation rates in the $X = 0.8$ simulation for the solar minimum. (b) Percentage change in nucleation rate between the solar-minimum and the solar-maximum simulations for $X = 0.8$. Redish values refer to faster nucleation during the solar minimum case.

size increases. The reason was already explained in previous works (see [143]). The Standard case is characterized by including only the effect of cosmic-rays ionization on the nucleation process, previously referred to as the IMN mechanism (see Section 5.2) and already included in GEOS-Chem. An increase in ionization causes more particles to have the capability to grow to larger sizes. The new small particles created compete for condensable material and start to grow more slowly, taking longer to reach 40 nm and 80 nm. Slower growth rates lead to an increase in the coagulation sink. As a consequence, the increase produced in the concentrations of smaller particles delays in reaching larger particles sizes. That is why CN80 and CCN show the least significant improvements. Surprisingly, this is not the case for $X = 0.8$. Although there is a general decrease in the enhancement from CN3 to CCN, the magnitude of the change is maintained from 40 nm to CCN sizes. Furthermore, CCN concentrations display a slight increase when compared to CN80.

For $X = 0.8$, it is also noteworthy that whereas the change is twice as large as the Standard case for CN3, CN10, and CN40 concentrations, the change is more than three times greater for CN80 and CCN. One of the possible explanations is that diffusion charging is having a significant impact on small aerosols. For such a case, the enhancement or inhibition of small paticles with other size ranges is very dependent on the mobility value (as can be seen comparing the enhancement factors from Figure 5.2 and the ones included in Appendix B.4). As a result, it seems that fewer particles are lost by the coagulation sink and more can survive to CCN sizes.

On the contrary, when the mobility ratio is set to 0.7 and 0.9 this effect disappears. In these cases, it could be that the coagulation is so inhibited that aerosols cannot grow by this pathway and compete for the condensable gases, slowing down their growth.

In the Standard case, there is no major difference between the free troposphere and low troposphere changes. However, when including the charging effect in the simulations, it seems like the free troposphere region presents higher increases for smaller particles and reverses the tendency in CN80 and CCN concentrations. This difference is more pronounced in the case of $X = 0.8$. The free troposphere has lower concentrations of CN40 and CN80 than the boundary layer and hence it might be more sensitive to variations in CN40 and CN80 concentrations. We can take a look at the nucleation rates to have a glimpse of what is happening.

Figure 5.4a shows the zonal-mean nucleation rates for the solar minimum case when $X =$

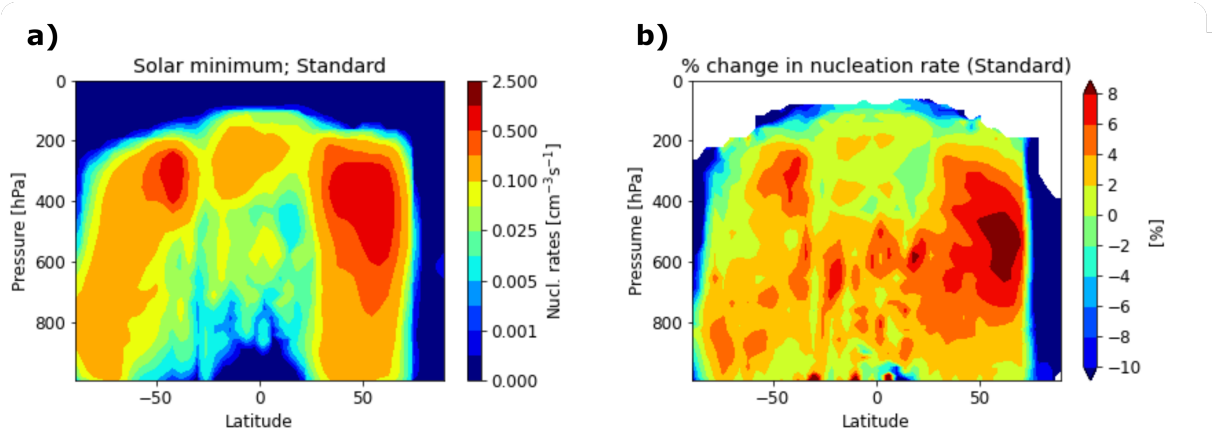

Figure 5.5: (a) Zonal-mean nucleation rates in the standard case for the solar minimum. (b) Percentage change in nucleation rate between the solar-minimum and the solar-maximum simulations for the standard simulations.

0.8. As it can be seen, the highest nucleation values are found above 600 hPa in the mid-high latitude regions. At the same time, Figure 5.4b displays the percentage change in the nucleation rates between the solar minimum and the solar maximum. This percent change in the mid-high latitude regions is 5-15 %, with some peaks with even higher values. Furthermore, the overall percent change shows positive values in practically all regions. The contrast is striking when compared to the standard situation (Figure 5.5b). Here, the spatial distribution of the percent variations is quite different. On the one hand, almost all zonal locations show an increase of 1-6 % with respect to the solar maximum (i.e., higher cosmic-ray intensity). It should be noted that these values are in agreement with those reported in previous studies [181, 143]. On the other hand, the highest difference is seen in the mid-latitudes of the northern hemisphere where the nucleation rates have also the largest values (see Fig. 5.5a). The latter makes sense since the period of the simulation coincides with wintertime in that hemisphere. It is possible that the location of the increase regions might change with other periods. However, in the $X = 0.8$ case, the nucleation rates show the same spatial distribution (Fig. 5.4a) but this does not result in an increase in the northern hemisphere only, rather it can be seen in both (Fig. 5.4b). This is evidence that the charged coagulation is taking effect. The smallest particles are less negatively charged than larger ones. Therefore, the coagulation between the smallest positive particles and the negatively charged larger bins is enhanced, leading to the reduction of the concentrations of the large particles. This could be the reason why in Figure 5.3 the CN80 and CCN concentrations show fewer percent changes in the free troposphere case ($X = 0.8$) than in the lower troposphere.

For illustration, Figure 5.6 shows the results when the mobility ratio is $X = 0.7$. In such case, the percent differences display the same features as in the standard simulations. The $X = 0.9$ case is not included because it displays similar nucleation values.

Figure 5.7 shows the percent change in the zonal-mean CN values between the solar-minimum and the solar-maximum simulations when the mobility ratio is $X = 0.8$ (changes for $X = 0.9$ can be found in Appendix B.3.2). In general, the changes in the concentrations (CN3, CN10, CN80, and CCN) increase during the solar cycle at nearly all zonal regions. Moreover, the biggest changes take place in the same mid-high latitude regions as in Figure 5.4b. Apart from this, changes in CN3 and CN10 are more pronounced in the 400-600 hPa region but the tropical upper troposphere also shows an increase, around 5 %.

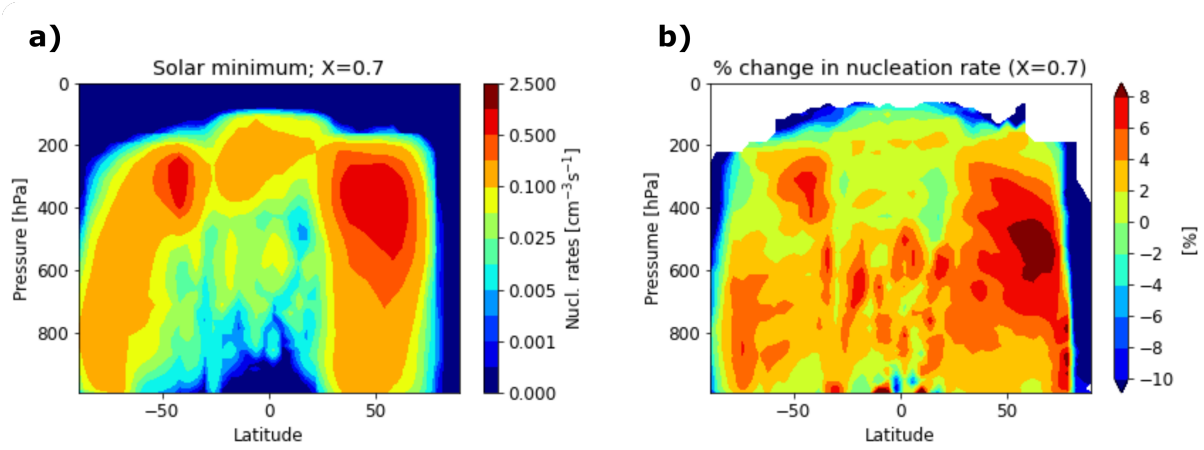

Figure 5.6: (a) Zonal-mean nucleation rates in the $X = 0.7$ case for the solar minimum. (b) Percentage change in nucleation rate between the solar-minimum and the solar-maximum simulations for $X = 0.7$.

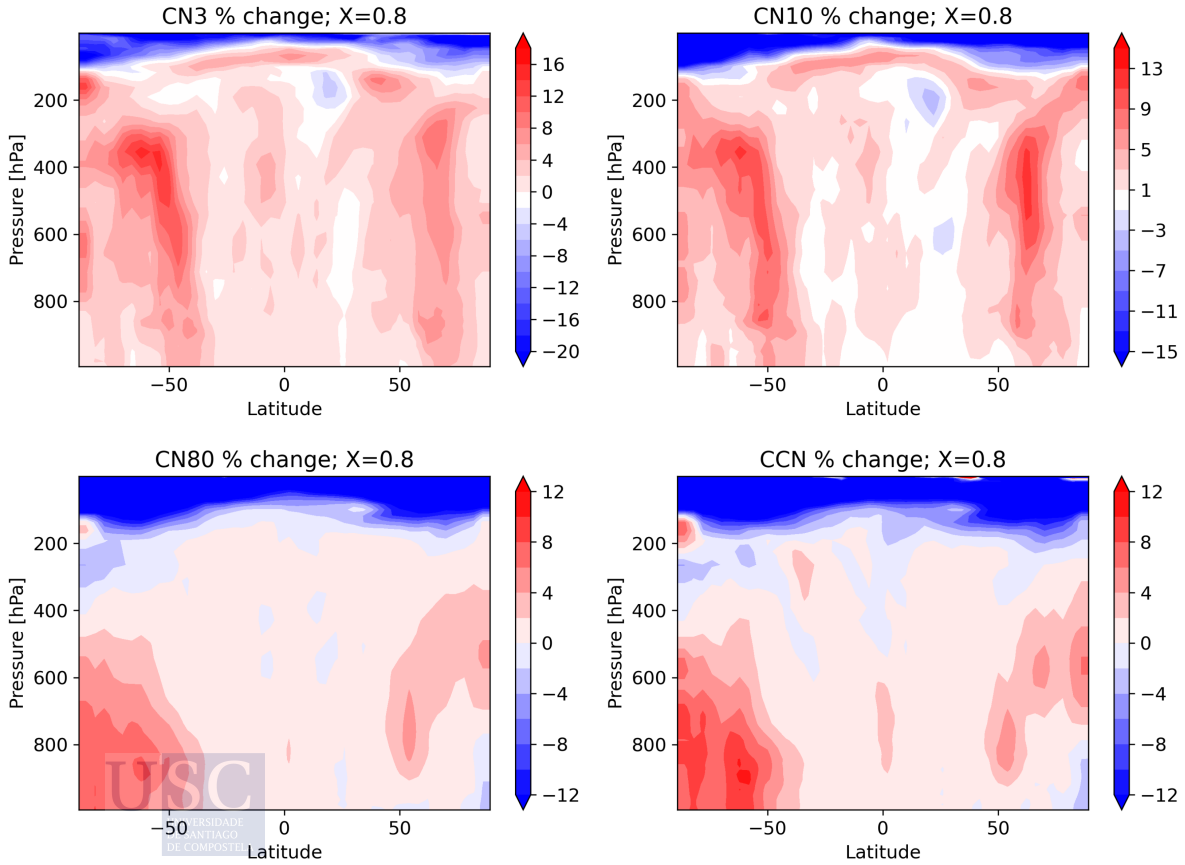

Figure 5.7: Percentage change between the solar-minimum and the solar-maximum case of zonal-mean CN3, CN10, CN80, and CCN concentrations ($X = 0.8$).

However, CN80 and CCN show a zonal sensitivity quite different because the largest variations are shifted to higher latitudes and appear in the lower troposphere.

We observe that changes in the concentrations are a bit less than those found in the nucleation rates. In the mid-high latitudes, Figure 5.4b depicts changes in the nucleations between 10-20 %, whereas it slightly drops to 10-15 % in CN3. The situation for CN80 and CCN changes radically, but it should be noted that the average variations in CCN are 2 % with local changes as high as 10 %. Performing the analysis by regions, the CCN concentrations show the following increases: 4 % for the polar regions, 2.7 % for mid-latitude regions, and 0.82 % for the tropical areas. This would corroborate the theory that the highest changes in ionization rates at polar areas, as seen in Figure 5.1, would result in larger aerosol changes in those regions.

So far, we have determined the response of CCN to changes in cosmic rays. We have just seen above that the changes in ion formation rates do not lead to similar changes in nucleation rates, and in turn changes in nucleation do not cause the same changes in CCN. The reason is that the processes involving the growth of aerosols are complex and compete with each other, giving rise to feedbacks that can enhance or dampen cosmic ray changes. For example, small particles can take two paths: coagulate with larger particles to reach CCN sizes or grow through condensation to form a new CCN.

Previously, it has been proved that when only the effect of cosmic rays on nucleation was taken into account, the processes competed in such a way that the enhancement was depressed under certain conditions [143]. In this work, we are bringing more variables into play that make things more complicated. So, it is difficult to have a clear picture of what is happening but we have been able to draw a general description of the results that give us a lot of information. To illustrate this challenge, one can take a look at the correction factors such as those shown before in Figure 5.2, which are supposed to give information on what is happening with the coagulation of particles of different sizes. However, when compared to corrections factors for the other mobility cases (included in Fig. B.4 of the Appendix), one can appreciate that the differences are in the smallest particles, whose values change drastically from $\overline{W}_{k,i} < 1$ to $\overline{W}_{k,i} > 1$ depending on X. One possible way to understand which particle sizes are determining the fate of the aerosols would be to consider simulations with only the charge distribution on small particles or the opposite situation where only large particles carry charges. This remains pending as future work.

Now, the question is whether changes in CCN that we have been reported in this work can lead to similar changes in cloud albedo or cloud cover. Some other dampened mechanisms may exist that cause CCN to be lost before cloud cover changes. However, it has been stated that in order to produce changes in cloud cover over the solar cycle, one needs changes higher than $\sim$1 % in CCN. In our case, these requirements are met when $X = 0.8$. This opens up the possibility that the processes we have implemented may be the missing link between cosmic rays and clouds. However, we should be cautious with this statement, as there is still a lot of work to be done. For instance, future work will focus on increasing the period of the simulations to ensure that the observed changes hold over time and at different epochs of the year.

Furthermore, we can observe that the value of the ion mobility ratio has a dramatic impact on the results. Here, we have assumed that it has a fixed value throughout the atmosphere, but the truth is that in real life this does not have to be the case. We know that X has values less than 1 in the atmosphere because negative ions have higher mobility than positive ions [84]. However, the sensitivity of the results to this ratio may be the reason behind the discrepancies

in the correlations between solar activity and clouds.

5.6 Conclusions

This part of the thesis has addressed the problem of the influence of cosmic rays on the growth of atmospheric aerosols. Through the methodology previously proposed in other works [93, 168], we have been able to incorporate for the first time the effect of the diffusion charging in the microphysical evolution of atmospheric particles of a state-of-the-art atmospheric model, GEOS-Chem. Thus, the simulations performed with this model have provided a more realistic and detailed view of the indirect effect of cosmic rays on the final concentrations of CCN.

The evidence from this study suggests that the ionization induced by cosmic radiation in the atmosphere may favor the growth of small particles to CCN sizes under certain conditions ($X = 0.8$). We observed that changes in CCN concentrations between the solar maximum and solar minimum (2-10 %) may become significantly relevant for cloud formation. This work will serve as a base for future studies and further research is needed to estimate this effect more accurately.

GENERAL CONCLUSIONS

The impetus for the work discussed in this thesis was to explore the implications of cosmic rays for atmospheric physics. In particular, we have used cosmic rays as a tool to analyze the properties of the atmosphere and showed how the appropriate technology has the potential to deliver the atmospheric profile with good accuracy.

The second major finding to emerge from this dissertation is that cosmic rays may be more relevant than previously thought for aerosol growth and cloud formation. This observation was supported by the simulation results and agrees with the hypothesis posed at the beginning of the study.

In general, the following conclusions can be drawn from the present work:

- In the analysis of correlations between atmospheric variables and cosmic ray measurements, we have commissioned and calibrated a small-size 2 m^2 multigap timing RPC detector devoted to the detailed study of cosmic rays at ground level and performed the first analysis of the atmospheric temperature effect with this kind of technology. By studying a data sample of about one year, it has been possible to estimate the distribution of temperature coefficients ($W_T(h)$), showing that the contribution of the hard component is dominant and in good agreement with theoretical expectations.

  We have seen how the presence of strong correlations among the different atmospheric layers precludes the use of conventional regression methods. A Principal Component Regression (PCR), considering the first two components, is sufficient to capture at least 77% of the temperature variability, giving a good description of the $W_T(h)$ and the global slope parameter $\alpha_{T_{exp}} = -0.279 \pm 0.051$ %/K (compared to a theoretical value of $\alpha_{T_{theor}} = -0.319$ %/K). This results in an anticorrelation with the effective atmospheric temperature, which allows to clearly identify its seasonal cycles as well as short-term exceptional events (such as the tropospheric consequences of a Sudden Stratospheric Warming) through measurements performed at ground level.

- We have developed a 1D-model Monte Carlo tool to simulate cosmic-ray air showers in real atmospheric scenarios. With this tool, we have been able to estimate the atmospheric effects, and probed them to be in qualitative agreement with a theoretical treatment based on weight coefficients $W_T(h)$ as well as data. This study has gone some way towards enhancing our understanding of the measured atmospheric effects by further inspecting the influence of the atmospheric attributes that would be impossible to accomplish with observational data.

- Another study was undertaken to evaluate and establish the limits for obtaining the atmospheric temperature through cosmic-ray data. In that way, we have found the best configuration for a monitoring station integrated by cosmic-ray telescopes. Besides, the

results have shown that it could be possible to retrieve the temperature of the atmosphere from the surface with good accuracy and at several atmospheric layers. An implication of this is the possibility that atmospheric muon detectors can be employed in scientific research beyond the field of astrophysics. Therefore, we have fulfilled one of the main objectives of this thesis which was to exploit the potential of cosmic rays for the development of practical applications for everyday life.

Returning to the question posed at the beginning of the work, it is now possible to state that multi-directional telescopes can improve the estimate of atmospheric temperatures. Multiple analyses have revealed that one can achieve a high degree of accuracy with error margins between 0.8 and 2.2 K up to $\sim$20 km. It was also shown that it is possible to follow strong temperature variations that happen in the low stratosphere, like those taking place during Sudden Stratospheric Warmings.

- With the two previous results, we pave the way for continuous monitoring of cosmic-ray variations using stations equipped with muon telescopes, that would allow real-time atmospheric temperatures to be retrieved for their use in meteorological monitoring or climate quality data records. This kind of station could be part of the global observing system along with the existing weather stations, satellites, and balloon measurements. In addition, it is important to highlight that this could be achieved with more affordable and accessible technology, and much easier to maintain than other alternatives.

- In the study of the influence of cosmic rays on the atmosphere, we have found a possible link between cosmic rays and clouds. The enhancement that we have identified in the CCN concentrations assists in our understanding of the role of charged particles in aerosol growth. Previous works have focused on the study of processes affecting small aerosols, such as nucleation [181, 54, 149], but the results presented in this thesis seem to indicate that other processes such as charging coagulation are of great relevance. Furthermore, the results are in agreement with the theory and consistent with previous works, which increases their robustness. However, we should be aware that there is still room for improvement. It is still too early to claim that we have found the key to the missing link between cosmic rays and clouds. But it is certainly a step forward in understanding the relationship. Furthermore, whether or not this proves to be true in the future, it is undoubtedly a process that appears to have some degree of relevance to aerosol growth and should be accounted for in atmospheric models just as nucleation was once incorporated.

Applicability and Future Perspectives

The discoveries presented in this thesis have many important implications for future practice. On the one hand, the analysis of the temperature retrieval suggests that several courses of action can be pursued and there is still much room for improvement. For instance, the accuracy in temperature retrieval can be improved in practice by employing more advanced statistical techniques such as those employed in satellite remote sensing [59, 134]. Additionally, for 4 m^2-scale detectors, the performance achieved in the analysis requires outstanding detector stability (below 0.3% on its counting efficiency). While detector inefficiencies to minimum

down to 0.1% are not alien to particle physics instrumentation, the requirement will pose significant constraints on the chosen technology and detector design.

Regarding the part of the correction of the variations that are not of atmospheric origin, some experiments have stressed the relevance of complementary neutron detectors to remove those effects related to the primary cosmic ray fluctuations. However, we believe that this would not be necessary as the underground detector could be playing a similar role. Besides, the results of Chapter 2 show that it would not be very complicated to avoid such effects with some specific statistical methods.

Anyway, we observe that there is a definite need for real measurements performed with a realistic setup. The installation of a functional station integrated by a couple of detectors, one ground-based and another underground, would be the ultimate test to see how realistic our proposal is. Furthermore, the temperature estimates obtained could be directly contrasted with balloon-sounding measurements, which would allow determining how accurate these estimates would be.

In the case of the air shower simulations, a straightforward step would be to implement the changes in a complete simulation program, such as AIRES, which already has some built-in functionality to change the atmospheric model. In this way, more realistic simulations can be achieved, and the temperature effect on the soft component could be examined as well, for instance. Moreover, apart from estimating the distribution of the temperature coefficients experimentally or numerically as up to know, one could obtain them through Monte Carlo simulations, without requiring of any simplifying assumption.

Finally, regarding the part of the GEOS-Chem simulations, a new world of possibilities opens up to investigate the consequences of the implementations performed. For example, the CLOUD experiment has shown that cosmic rays could be relevant in pre-industrial times. In particular, they have found that cosmic rays strongly enhance the production of pure biogenic particles by a factor of 10-100 compared to particles without the influence of ions, suggesting that cosmic radiation could have been more relevant for cloud formation in pre-industrial times than in today's polluted atmosphere [94]. Other studies also argue that 1/3 of the warming in the last century was induced by changes in cosmic rays [35]. This could be related to the biogenic particle nucleation since the amount of atmospheric pollution was less than in the present atmosphere. Future work could be to run simulations for past periods with the anthropogenic emissions off and the charged coagulation in order to study the effect on CCN.

Another alternative to test the effects of the charging on coagulation would be to simulate volcanic periods, where coarse aerosols are ejected into the atmosphere. This kind of simulation would serve as a sensitivity test for the implemented approach since it is assumed that for larger particles and high concentrations, the impact of charging can be significant.

Appendix A

Atmospheric Dynamics

Abstract: *We include here some basic concepts about atmospheric dynamics. In particular, the Sudden Stratospheric Warming events are described more in detail in order to have a better understanding of what they are.*

A.1 Sudden Stratospheric Warming

The stratosphere is the layer located immediately above the troposphere. The top of the stratosphere occurs around 50 km. As its name suggests, it is an atmospheric layer stratified into other layers, with the cooler ones located lower in the stratosphere. Indeed, the temperature profile of the stratosphere is characterized by the fact that the temperature increases with height, in contrast with the temperature of the troposphere, which decreases with altitude. The increase in temperature stems from the presence of ozone which absorbs ultraviolet radiation from the Sun. As a result of the temperature stratification of the whole layer, vertical mixing and convection are much rarer than horizontal mixing. Therefore, the layers of air are quite stable [140].

The troposphere is the layer of the atmosphere to which meteorologists pay most attention because it is where most weather phenomena take place. However, interactions between the troposphere and the stratosphere are also closely monitored, as they can deeply impact the weather down at the surface. One of these phenomena is the Sudden Stratospheric Warming (SSW), which has the ability to alter atmospheric patterns.

The stratospheric polar vortex is a large and persistent low-pressure region located in the Poles. It weakens towards summer and gains intensity in winter. SSW events are very common and occur when the polar vortex starts to weaken in late winter. A SSW refers to a rapid and large warming in the stratosphere over a short period of time, usually a couple of days [31].

A normal stratosphere exhibits a polar vortex rotating counterclockwise (similar to cyclones) with very low temperatures. When a SSW takes place, the vortex gets weaker and can split in two or rearrange out of its usual position over the Pole. In the most extreme events, polar winds may even reverse and begin to rotate clockwise.

A SSW is the result of a Rossby wave, also known as a planetary wave, lifting from the troposphere to the stratosphere, carrying a warmer air mass into the upper atmosphere. Atmospheric Rossby waves form primarily as a result of the land's orography. For example, the great mountain systems of the Northern Hemisphere, such as the Himalayas or the Alps, can cause the dominant westerly winds in the mid-latitudes to ripple when they encounter these

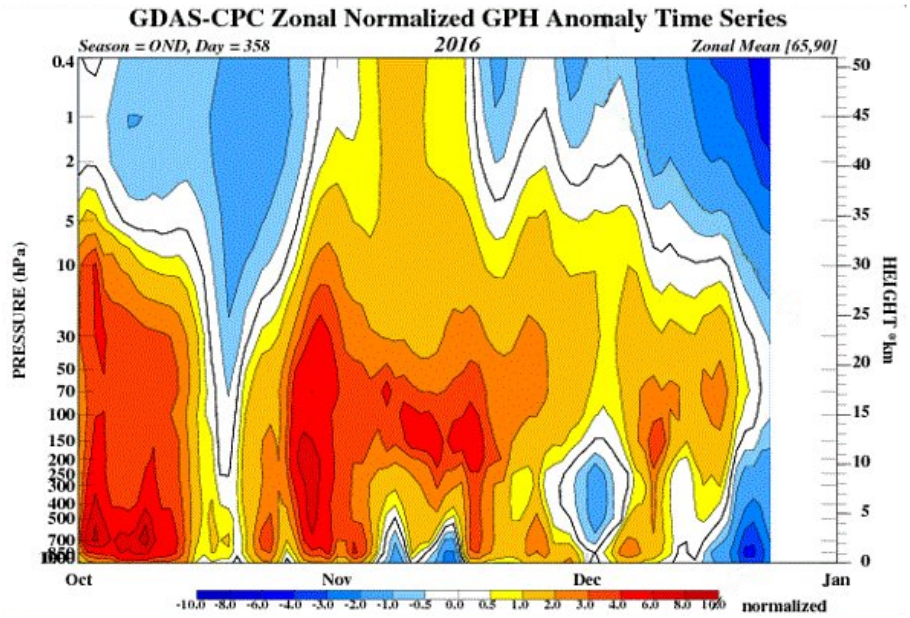

Figure A.1: October-December 2016 timeseries of normalized polar (65°-90°N) geopotential height anomalies from 1000 hPa to 1 hPa (`https://www.cpc.ncep.noaa.gov/products/stratosphere/strat-trop/`).

mountain barriers, forming waves that will move to the West or East.

These disturbances in atmospheric circulation can generate stationary or dynamic waves. Whenever these waves reach enough amplitude, they traverse the tropopause and enter the stratosphere increasing its temperature.

The fact that a SSW occurs does not guarantee an impact on weather. Such a SSW has to propagate downwards from the stratosphere to the troposphere. For instance, if the vortex is moved or breaks, the cold stored can be distributed over the different temperate zones at lower latitudes, and depending on different factors, leaving harsh winter weather in different countries. It can also alter the jet stream, causing it to undulate more than usual, creating a large area of blocking high pressure, typically over the North Atlantic and Scandinavia. In such scenario, northern Europe would have dry and cold weather, whereas southern Europe would be warmer, wet, and windy. For example, a record weakening of the polar vortex was seen in late autumn 2016. This can be seen looking at the pressure anomalies in the vertical over the polar regions for that time of the year. Figure A.1 displays the daily time series of the polar geopotential height anomalies from October 2016 to December 2016 as a function of the pressure level. First, a positive anomaly is present in both the troposphere and stratosphere at the beginning of October. This occurred due to thermal expansion of the polar troposphere as a result of a low sea ice extent anomaly. Second, a positive geopotential anomaly in the stratosphere is observed in November as a consequence of an anomalously warm polar stratosphere caused by strong planetary waves. Clearly, the pressure buildup that starts in mid-October was able to reach quite high, affecting the polar stratosphere. This SSW event was associated with the cold north European surface temperatures recorded from mid-November to early December [163].

Appendix B

Supplementary Results

Abstract: *This Appendix incorporates extra results obtained for some of the chapters and that have not been included in the main text to facilitate reading comprehension.*

B.1 Results for Chapter 2

B.1.1 PCA Analysis

In Section 2.4.2, the PCA approach is introduced in order to analyze the temperature effect of the measurements. Numerous tests were carried out to ensure the efficiency and quality of the technique. Mainly, this was required, on the one hand, to quantify the number of principal components needed and, on the other hand, to evaluate the peformance of the approach when noisy data is present. The objective of the tests is to guarantee that the temperature coefficients are reliably achieved.

For our purpose, we simulate a sample of cosmic-ray rates using the theoretical distribution of the temperature coefficients along with the temperature data retrieved from ERA-Interim. The data must include the variations from atmospheric origin, only the ones related to temperature effect for this case of study, and the variations related to statistical fluctuations (derived from the random nature of particle counting). The former is obtained from the following well-known relation:

$$\left.\frac{\Delta R}{R_0}\right|_T = \sum_{i=1}^{n} W_T(h_i)\Delta T_i \Delta h_i \tag{B.1}$$

The statistical fluctuations $\left.\frac{\Delta R}{R_0}\right|_{stat}$ are simulated getting random samples from a Gaussian distribution with its width being a certain percentage of the mean cosmic-ray rate and subsequently adding them to the sample. The degree of noise (low, medium or high) is modulated by increasing or droping this percentage. The expression that combines both types of variations to get the final sample is:

$$\left.\frac{\Delta R}{R_0}\right|_{obs} = \left.\frac{\Delta R}{R_0}\right|_T + \left.\frac{\Delta R}{R_0}\right|_{stat} \tag{B.2}$$

Figure B.1 depicts the results from the PCA regression implementation to simulated data

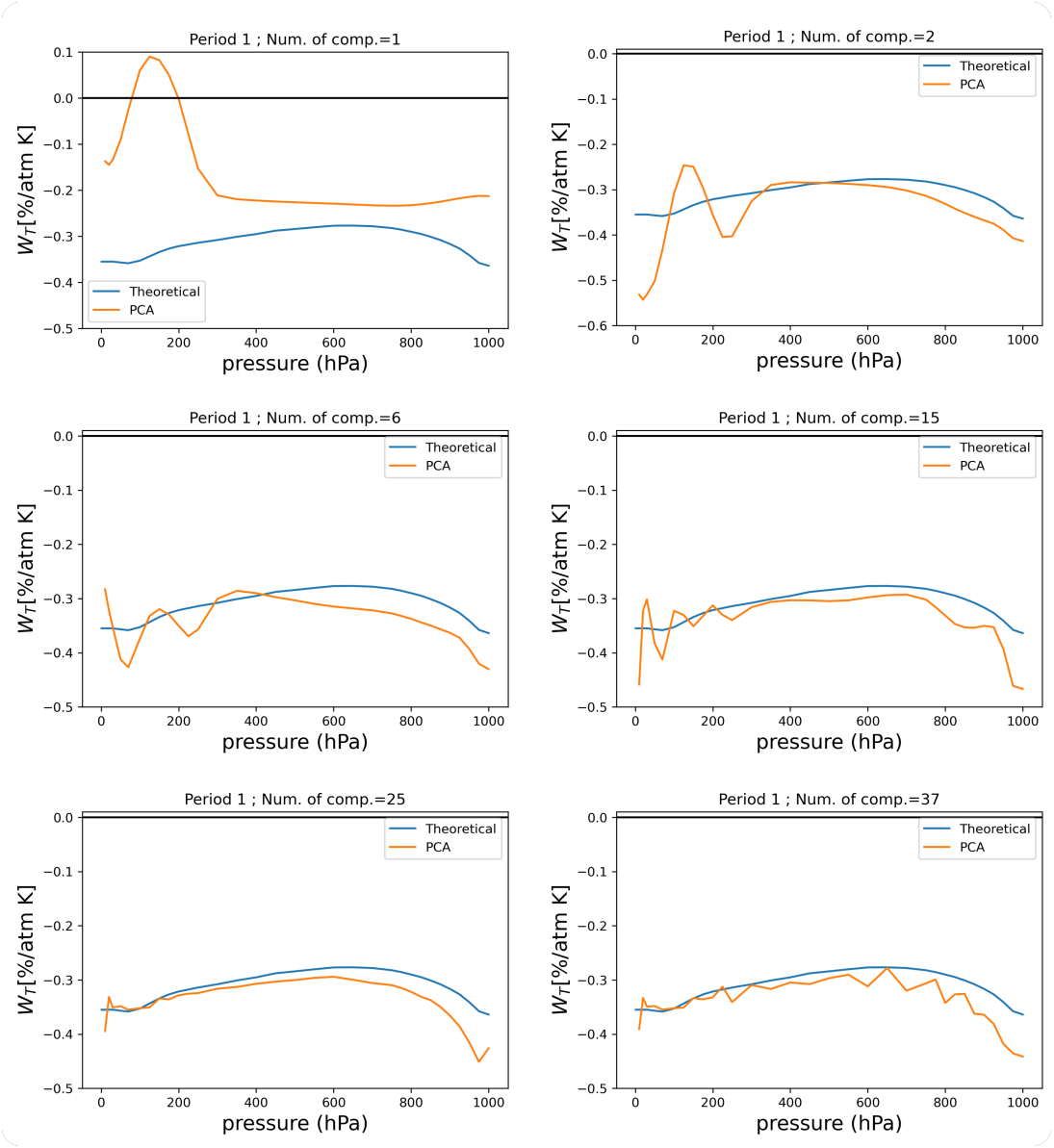

Figure B.1: Temperature coefficients obtained from PCA regression applied to simulated data of subperiod 1 (from October 2015 to December 2015) compared to the theoretical ones (blue lines). No statistical fluctuations have been added to the sample. The yellow lines represent the results obtained using a different number of principal components: 1, 2, 6, 15, 25, and 37.

for subperiod 1 (defined in the main text). This first test has been performed without adding statistical fluctuations to the data. Several features can be derived from the comparison between theoretical coefficients (blue lines) and those obtained by PCA (yellow lines). In the regression step, the multivariate regression on the selected principal components that is performed is equivalent to carry out p independent simple linear regressions (univariate regressions) separately on each of the components. When the PCA regression is solved with just one component, we observe that the distribution of coefficients obtained is the same as the ones obtained in Figure 2.10b. The reason is that the first component captures the largest variance in the data, which in this case corresponds to the seasonal variations of the troposphere. In fact, the first component can be seen as a sort of effective temperature of the atmosphere. When

the second component is included in the regression, information on the variance of the upper regions of the atmosphere is being incorporated. Thus, it can be seen in Figure B.1 (top right) that the values of the coefficients above 300 hPa obtained with 2 components are closer to the theoretical values. As more components are included in the regression, more information about the variations of the atmosphere is added and the estimation of coefficients can approximate more accurately to the real values.

The PCR performance is altered when the data includes noise. This means that some principal components will be identified with the corresponding noise variations, which, depending on their degree, will be more or less important. When the principal components are computed, they are ordered according to their eigenvalue in decreasing order, with the first component representing the most variance captured. If the level of noise in the data is not very high, the principal component representing its variance will be associated with a small eigenvalue. Hence, when we only consider some PCs with large eigenvalues, we are neglecting those components with little variance, which may correspond to noise. This is why PCA can be used as a method of noise reduction.

We have added extra noise to the original data in different levels (low, medium, and high)

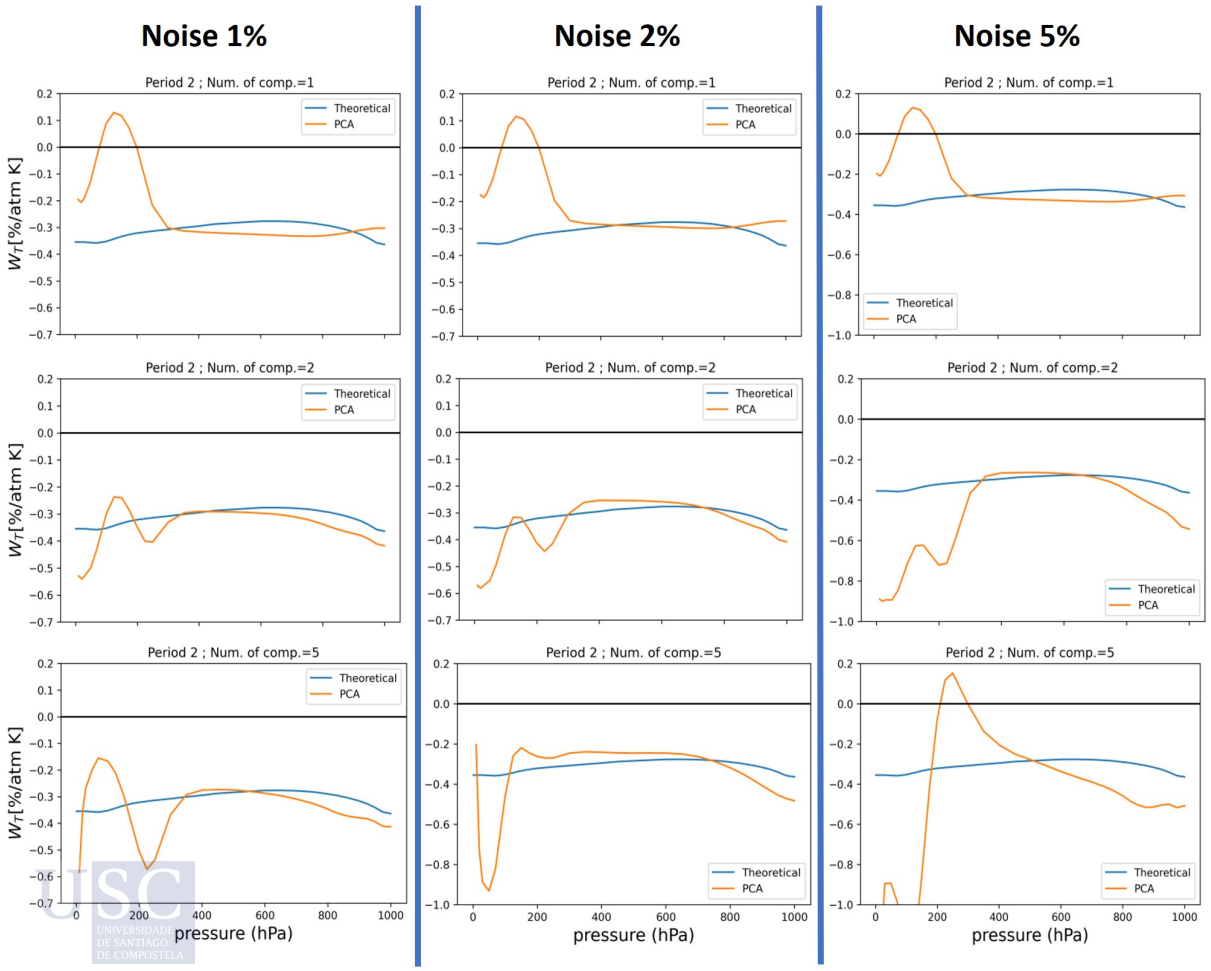

Figure B.2: Temperature coefficients obtained from PCA regression (yellow lines) applied to simulated data of subperiod 2 (from December 2015 to September 2016) compared to the theoretical ones (blue lines). From left to right, each column includes data with different levels of statistical fluctuations: 1%, 2% and 5%. The yellow lines of each row represent the results obtained using a different number of principal components: 1, 2, and 5.

to test the performance of the approach. For such case, we use gaussian noise with variance as a percentage of the average rate. The results are presented in Figure B.2 for subperiod 2. Each column represents the estimated coefficients using data with different levels of noise: 1%, 2%, and 5%. At the same time, each row includes the PCR results using a different number of components in the regression: 1, 2, and 5. The results with one component (first row) are similar to the ones analyzed in the previous paragraph and there are no significant differences among the different noise levels. However, the regression begins to destabilize when there is a high level of noise and two components are included (right figure in the middle row), especially for the values of the coefficients in the stratosphere. In contrast, the other two cases of noise maintain good accuracy. And finally, as more components are included and contrary to what happens when using noiseless data, the method becomes less and less accurate until it is completely destabilized. In the last row of Figure B.2, we are only using 5 components, but it can already be seen how the coefficients are far from the real values for a noise level of 5%.

B.2 Results for Chapter 3

B.2.1 Regression Model

A linear model is used to predict the temperatures on the basis of several predictor variables, $\Delta\mathbf{R}/\mathbf{R_0}$. The mathematical formula of the linear regression is presented in equation 3.11, where c_{jki} are known as the regression parameters which are obtained via the ordinary least squares method. In our case, we fit a multiple linear regression model, i.e., we assume that there exists a linear relationship between the input rates and the predicted temperature.

For illustration, we look at the fits for the multi-channel case (hard + soft + underground) analyzed at an optimal depth. Figure B.3 shows the best-fitting line obtained for the observed temperatures at several atmospheric levels. We also look at the model fit statistics using the R-squared (R^2) as a measure of the variability in the response explained by the chosen model. In the main text, we also analyze another important measure of the fitting, the RMSE.

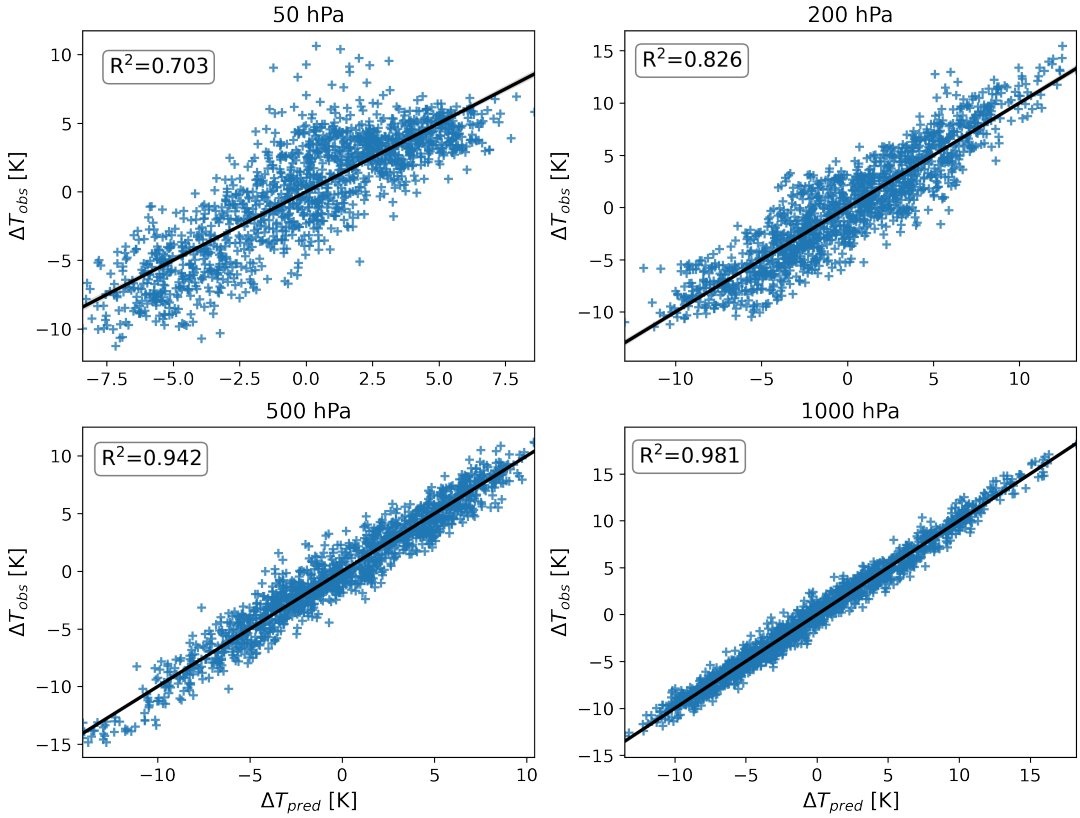

Figure B.3: Predicted temperatures obtained from the model in Equation 3.11 vs observed temperature for several atmospheric layers: 50, 200, 500, and 1000 hPa. The linear regression fit with the corresponding *R*-squared are also included. This results have been obtained for the multi-channel analysis at an optimal depth.

B.3 Results for Chapter 5

B.3.1 Correction Factors

The average correction factor is calculated following equation 5.15. The value of this factor indicates which electrostatic forces are predominant among aerosols: the repulsive or the attractive ones. Besides, this factor depends on several variables (see eq. 5.11): the size and concentrations of the particles involved, the temperature, and the number of elementary charges on each aerosol. At the same time, the latter is affected by the mobility ratio X. Figure B.4 shows the correction factors calculated for $X = 0.7$ and $X = 0.9$ between aerosol particles with size r_k and r_i. On the one hand, for $X = 0.7$ and particles with r_k of 0.3 μm, coagulation is inhibited with smaller particles ($r_i < 0.3\mu$m) and slightly enhanced with larger sizes. For aerosols with r_k values of 0.8 μm, coagulation is also inhibited with smaller particles but results to be enhanced with the larger ones. For larger particles with sizes of 1.5 μm, the situation is similar but the enhancement is even stronger with larger particles (see Fig. B.4a). On the other hand, for $X = 0.9$, the coagulation of particles with $r_k = 0.3$ μm tends to be unaffected for smaller sizes and enhanced for particles above 0.1 μm. For particles with r_k values of 0.8 and 1.5 μm, there is a general enhancement for all sizes (see Fig. B.4b).

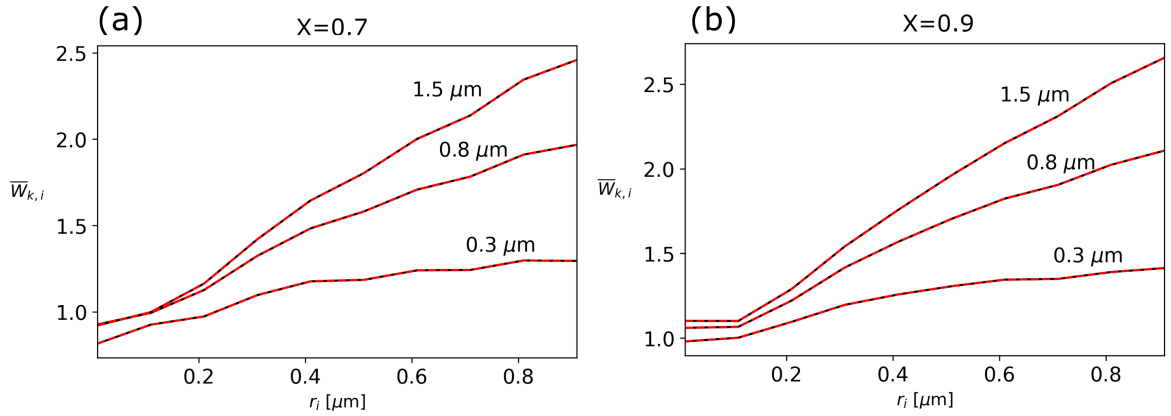

Figure B.4: Correction coefficients ($\overline{W}_{k,i}$) calculated with the exact summations (red solid lines) together with the optimized computation described in Vasilakos *et al.* (black dashed lines) between particles of size r_k and r_i. The r_k values are the ones indicated in the labels next to the curves: 0.3, 0.8 and 1.5 μm. The following values have been chosen for the calculations: $N_k = N_j = 6 \cdot 10^9$ m^{-3}, and $T = 270$ K. The values for the mobility ratios are (a) $X = 0.7$ and (b) $X = 0.9$.

B.3.2 Changes in Concentrations between Solar Minimum and Solar Maximum (X=0.9)

Figure B.5 shows the percent change in the zonal-mean CN values between the solar-minimum and the solar-maximum when $X = 0.9$. Changes for $X = 0.7$ are quite similar, therefore they are not displayed. In general, the changes in the concentrations for different particles sizes (CN3, CN10, CN80, and CCN) increase in the solar minimum at nearly all zonal regions. For CN3 and CN10, the biggest changes take place in the same mid-high latitude regions as in Figure 5.6b, where the nucleation rates are shown. However, CN80 and CCN display a zonal sensitivity less than 1 % on average.

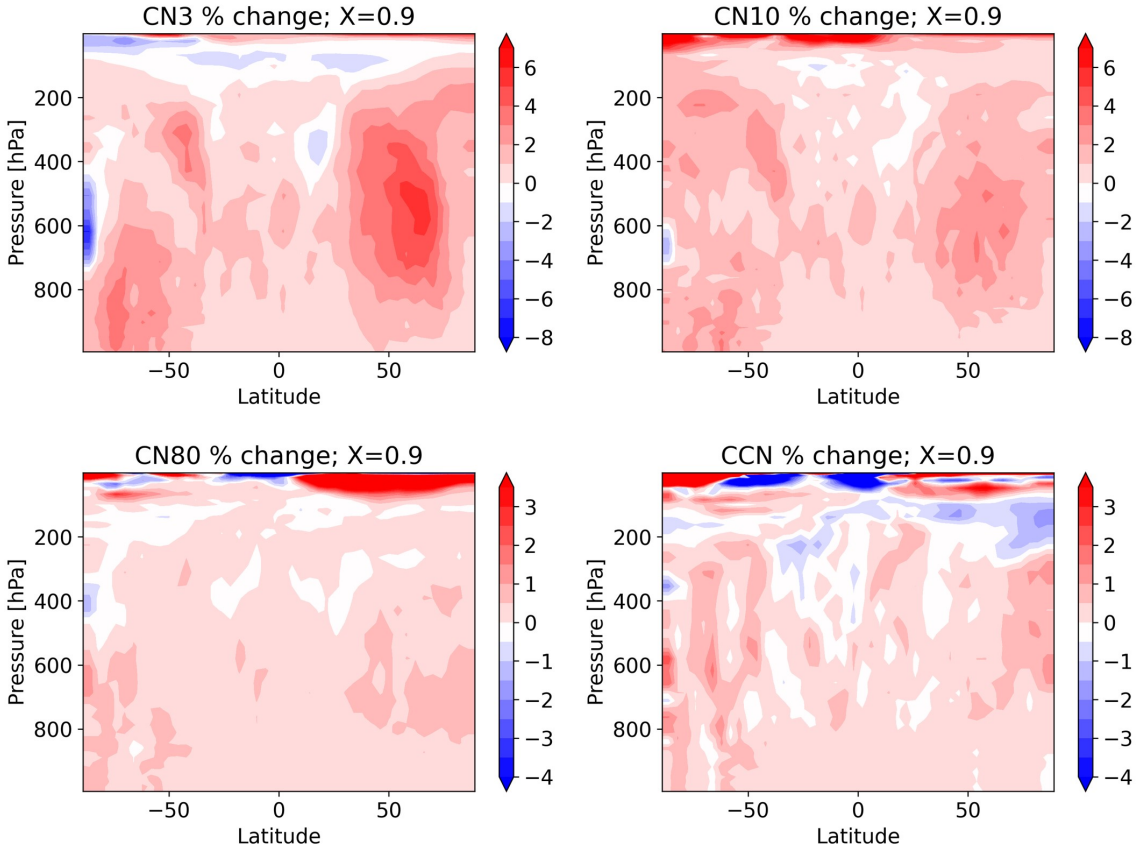

Figure B.5: Percentage change between the solar-minimum and the solar-maximum case of zonal-mean CN3, CN10, CN80, and CCN concentrations ($X = 0.9$)

Appendix C

Methods for the Air Shower Simulations

Abstract: *This Appendix includes some detailed mathematical descriptions for the simulation model of cosmic-ray cascades that have not been included in the main text.*

C.1 Inverse Transform Sampling

This method is used for the generation of pseudo-random numbers from the given probability distribution. Specifically, it is required to obtain the energy of the primary cosmic ray from the probability distribution derived from the energy spectrum.

The function that defines the primary energy spectrum is:

$$p(E) = E^{-(\gamma+1)} \quad with \;\; \gamma = 1.7 \tag{C.1}$$

To generate the random numbers according to a probability density function defined in the interval $[E_{min}, E_{max}]$, we calculate its cumulative probability distribution function integrating:

$$P(E) = \int_{E_{min}}^{E} p(E')dE' \tag{C.2}$$

this function has to be normalized so that $P(E_{max}) = 1$. Normalizing the function we obtain:

$$N \int_{E_{min}}^{E_{max}} E^{-(\gamma+1)} dE = 1 \rightarrow N = \frac{\gamma}{(E_{min}^{-\gamma} - E_{max}^{-\gamma})} \tag{C.3}$$

which gives

$$p(E) = NE^{-(\gamma+1)} \tag{C.4}$$

Calculating $P(E)$:

$$P(E) = N \int_{E_{min}}^{E} E'^{(-\gamma+1)} dE' = \frac{N}{\gamma}(E_{min}^{-\gamma} - E^{-\gamma}) \equiv r \tag{C.5}$$

where r is a random number such that $0 \leq r \leq 1$.

Finally, the inverse $E = P(r)^{-1}$ is obtained:

$$r = \frac{N}{\gamma}(E_{min}^{-\gamma} - E^{-\gamma}) \rightarrow E = (E_{min}^{-\gamma} - Kr)^{-1/\gamma} \tag{C.6}$$

with

$$K \equiv E_{min}^{-\gamma} - E_{max}^{-\gamma} \tag{C.7}$$

being equation C.6 with $E(r)$ the one that allows us to obtain the sampled energy.

Bibliography

[1] R. Abbasi, M. Abe, T. Abu-Zayyad, M. Allen, R. Azuma, E. Barcikowski, J. Belz, D. Bergman, S. Blake, R. Cady, et al. The energy spectrum of cosmic rays above 1017.2 eV measured by the fluorescence detectors of the Telescope Array experiment in seven years. *Astroparticle physics*, 80:131–140, 2016.

[2] M. Abbrescia, A. Agocs, S. Aiola, R. Antolini, C. Avanzini, R. B. Ferroli, G. Bencivenni, E. Bossini, E. Bressan, A. Chiavassa, et al. The EEE experiment project: status and first physics results. *The European Physical Journal Plus*, 128(6):62, 2013.

[3] P. Abreu, S. Andringa, P. Assis, A. Blanco, V. B. Martins, P. Brogueira, N. Carolino, L. Cazon, M. Cerda, G. Cernicchiaro, et al. MARTA: a high-energy cosmic-ray detector concept for high-accuracy muon measurement. *The European Physical Journal C*, 78(4):1–11, 2018.

[4] P. J. Adams and J. H. Seinfeld. Predicting global aerosol size distributions in general circulation models. *Journal of Geophysical Research: Atmospheres*, 107(D19):AAC–4, 2002.

[5] P. Adamson, T. Alexopoulos, W. Allison, G. Alner, K. Anderson, C. Andreopoulos, M. Andrews, R. Andrews, C. Arroyo, S. Avvakumov, et al. First observations of separated atmospheric ν_μ and $\bar{\nu}_\mu$ events in the MINOS detector. *Physical Review D*, 73(7):072002, 2006.

[6] P. Adamson, C. Andreopoulos, K. Arms, R. Armstrong, D. Auty, D. Ayres, C. Backhouse, J. Barnett, G. Barr, W. Barrett, et al. Observation of muon intensity variations by season with the MINOS far detector. *Physical Review D*, 81(1):012001, 2010.

[7] M. Aglietta, B. Alpat, E. Alyea, P. Antonioli, G. Badino, G. Bari, M. Basile, V. Berezinsky, F. Bersani, M. Bertaina, et al. Muon "depth-intensity" relation measured by the LVD underground experiment and cosmic-ray muon spectrum at sea level. *Physical Review D*, 58(9):092005, 1998.

[8] M. Ambrosio, R. Antolini, R. Assiro, G. Auriemma, D. Bakari, A. Baldini, G. Barbarino, E. Barbarito, B. Barish, G. Battistoni, et al. The MACRO detector at Gran Sasso. *Nuclear Instruments and Methods in Physics Research Section A: Accelerators, Spectrometers, Detectors and Associated Equipment*, 486(3):663–707, 2002.

[9] M. Ambrosio, R. Antolini, G. Auriemma, R. Baker, A. Baldini, G. Barbarino, B. Barish, G. Battistoni, R. Bellotti, C. Bemporad, et al. Vertical muon intensity measured with MACRO at the Gran Sasso laboratory. *Physical Review D*, 52(7):3793, 1995.

[10] M. Ambrosio, R. Antolini, G. Auriemma, R. Baker, A. Baldini, G. Barbarino, B. Barish, G. Battistoni, R. Bellotti, C. Bemporad, et al. Seasonal variations in the underground muon intensity as seen by MACRO. *Astroparticle Physics*, 7(1-2):109–124, 1997.

[11] S. An, R. Antolini, A. Badalà, R. B. Ferroli, G. Bencivenni, F. Blanco, E. Bressan, A. Chiavassa, L. Cifarelli, F. Cindolo, et al. Multigap resistive plate chambers for EAS study in the EEE Project. *Nuclear Instruments and Methods in Physics Research Section A: Accelerators, Spectrometers, Detectors and Associated Equipment*, 581(1-2):209–212, 2007.

[12] S. An, Y. Jo, J. Kim, M. Kim, D. Hatzifotiadou, M. Williams, A. Zichichi, and R. Zuyeuski. A 20 ps timing device—A Multigap Resistive Plate Chamber with 24 gas gaps. *Nuclear Instruments and Methods in Physics Research Section A: Accelerators, Spectrometers, Detectors and Associated Equipment*, 594(1):39–43, 2008.

[13] U. S. Atmosphere. *US standard atmosphere*. National Oceanic and Atmospheric Administration, 1976.

[14] S. Ayuso, J. J. Blanco, J. I. G. Tejedor, R. G. Herrero, I. Vrublevskyy, Ó. G. Población, and J. Medina. MITO: a new directional muon telescope. *Journal of Space Weather and Space Climate*, 11:13, 2021.

[15] P. Baesso, D. Cussans, C. Thomay, and J. Velthuis. Toward a RPC-based muon tomography system for cargo containers. *Journal of Instrumentation*, 9(10):C10041, 2014.

[16] N. Barbashina, R. Kokoulin, K. Kompaniets, G. Mannocchi, A. Petrukhin, O. Saavedra, D. Timashkov, G. Trinchero, D. Chernov, V. Shutenko, et al. The URAGAN wide-aperture large-area muon hodoscope. *Instruments and Experimental Techniques*, 51(2):180–186, 2008.

[17] P. H. Barrett, L. M. Bollinger, G. Cocconi, Y. Eisenberg, and K. Greisen. Interpretation of cosmic-ray measurements far underground. *Reviews of Modern Physics*, 24(3):133, 1952.

[18] G. Bazilevskaya and A. Svirzhevskaya. On the stratospheric measurements of cosmic rays. *Space Science Reviews*, 85(3):431–521, 1998.

[19] N. F. Beardsley. Correlation between cosmic-ray intensity and upper air pressures and temperatures. *Physical Review*, 57(4):336, 1940.

[20] D. Belver, A. Blanco, P. Cabanelas, J. Díaz, P. Fonte, J. Garzón, A. Gil, D. González-Díaz, W. Koenig, B. Kolb, et al. Analysis of the space-time microstructure of cosmic ray air showers using the HADES RPC TOF wall. *Journal of Instrumentation*, 7(10):P10007, 2012.

[21] D. Belver, P. Cabanelas, E. Castro, J. A. Garzon, A. Gil, D. Gonzalez-Diaz, K. Koenig, and M. Traxler. Performance of the low-jitter high-gain/bandwidth front-end electronics of the HADES tRPC wall. *IEEE Trans. Nucl. Sci.*, 57:2848–2856, 2010.

[22] V. Berezinsky, A. Gazizov, and S. Grigorieva. On astrophysical solution to ultrahigh energy cosmic rays. *Physical Review D*, 74(4):043005, 2006.

[23] M. Berkova, A. Belov, E. Eroshenko, and V. Yanke. Temperature effect of the muon component and practical questions for considering it in real time. *Bulletin of the Russian Academy of Sciences: Physics*, 75(6):820–824, 2011.

[24] P. M. Blackett. On the instability of the barytron and the temperature effect of cosmic rays. *Physical Review*, 54(11):973, 1938.

[25] A. Blanco, J. Adamczewski-Musch, K. Boretzky, P. Cabanelas, L. Cartegni, R. F. Marques, P. Fonte, J. Fruehauf, D. Galaviz, M. Heil, et al. Performance of timing resistive plate chambers with relativistic neutrons from 300 to 1500 MeV. *Journal of Instrumentation*, 10(02):C02034, 2015.

[26] A. Blanco, J. Blanco, J. Collazo, P. Fonte, J. Garzón, A. Gómez, G. Kornakov, T. Kurtukian, A. L. Agüera, J. López, et al. TRAGALDABAS: a new RPC based detector for the regular study of cosmic rays. *Journal of Instrumentation*, 9(09):C09027, 2014.

[27] A. Blanco, F. Clemencio, P. Fonte, C. Franco, N. Leonardo, L. Lopes, C. Loureiro, J. Saraiva, and G. Soares. The SHiP timing detector based on MRPC. *Journal of Instrumentation*, 15(10):C10017, 2020.

[28] J. Blümer, R. Engel, and J. R. Hörandel. Cosmic rays from the knee to the highest energies. *Progress in Particle and Nuclear Physics*, 63(2):293–338, 2009.

[29] L. Bogdanova, M. Gavrilov, V. Kornoukhov, and A. Starostin. Cosmic muon flux at shallow depths underground. *Physics of Atomic Nuclei*, 69(8):1293–1298, 2006.

[30] L. Bonechi, R. D'Alessandro, and A. Giammanco. Atmospheric muons as an imaging tool. *Reviews in Physics*, 5:100038, 2020.

[31] A. H. Butler, D. J. Seidel, S. C. Hardiman, N. Butchart, T. Birner, and A. Match. Defining sudden stratospheric warmings. *Bulletin of the American Meteorological Society*, 96(11):1913–1928, 2015.

[32] J. Calogovic, C. Albert, F. Arnold, J. Beer, L. Desorgher, and E. Flueckiger. Sudden cosmic ray decreases: No change of global cloud cover. *Geophysical Research Letters*, 37(3), 2010.

[33] H. Cane. Cosmic rays and earth, 2000.

[34] R. Cardarelli, R. Santonico, A. Di Biagio, and A. Lucci. Progress in resistive plate counters. *Nuclear Instruments and Methods in Physics Research Section A: Accelerators, Spectrometers, Detectors and Associated Equipment*, 263(1):20–25, 1988.

[35] K. Carslaw, R. Harrison, and J. Kirkby. Cosmic rays, clouds, and climate. *science*, 298(5599):1732–1737, 2002.

[36] H. Che, X. Zhang, L. Zhang, Y. Wang, Y. Zhang, X. Shen, Q. Ma, J. Sun, and J. Zhong. Prediction of size-resolved number concentration of cloud condensation nuclei and long-term measurements of their activation characteristics. *Scientific reports*, 7(1):1–12, 2017.

[37] C. Clement, R. Clement, and R. Harrison. Charge distributions and coagulation of radioactive aerosols. *Journal of Aerosol Science*, 26(8):1207–1225, 1995.

[38] M. Dayananda, X. Zhang, C. Butler, and X. He. Understanding the effect of atmospheric density on the cosmic ray flux variations at the earth surface. *arXiv preprint arXiv:1303.7191*, 2013.

[39] R. de Asmundis, P. Avella, and F. Toglia. Using RPC detectors as cosmic rays monitor. *IEEE Transactions on Nuclear Science*, 54(3):670–676, 2007.

[40] R. De Mendonça, C. Braga, E. Echer, A. Dal Lago, K. Munakata, T. Kuwabara, M. Kozai, C. Kato, M. Rockenbach, N. Schuch, et al. The temperature effect in secondary cosmic rays (muons) observed at the ground: analysis of the global muon detector network data. *The Astrophysical Journal*, 830(2):88, 2016.

[41] R. De Mendonca, J.-P. Raulin, E. Echer, V. Makhmutov, and G. Fernandez. Analysis of atmospheric pressure and temperature effects on cosmic ray measurements. *Journal of Geophysical Research: Space Physics*, 118(4):1403–1409, 2013.

[42] D. P. Dee, S. Uppala, A. Simmons, P. Berrisford, P. Poli, S. Kobayashi, U. Andrae, M. Balmaseda, G. Balsamo, d. P. Bauer, et al. The ERA-Interim reanalysis: Configuration and performance of the data assimilation system. *Quarterly Journal of the royal meteorological society*, 137(656):553–597, 2011.

[43] M. A. Del Rio Viera et al. Charge studies on multigap resistive plate chambers. Master's thesis, 2020.

[44] D. d'Enterria, R. Engel, T. Pierog, S. Ostapchenko, and K. Werner. Constraints from the first LHC data on hadronic event generators for ultra-high energy cosmic-ray physics. *Astroparticle Physics*, 35(2):98–113, 2011.

[45] D. Desilets, M. Zreda, and T. P. Ferré. Nature's neutron probe: Land surface hydrology at an elusive scale with cosmic rays. *Water Resources Research*, 46(11), 2010.

[46] A. Dmitrieva, I. Astapov, A. Kovylyaeva, and D. Pankova. Temperature effect correction for muon flux at the earth surface: estimation of the accuracy of different methods. In *Journal of physics: Conference series*, volume 409, page 012130. IOP Publishing, 2013.

[47] A. Dmitrieva, R. Kokoulin, A. Petrukhin, and D. Timashkov. Corrections for temperature effect for ground-based muon hodoscopes. *Astroparticle Physics*, 34(6):401–411, 2011.

[48] L. Dorman. To the theory of cosmic ray meteorological effects. *Doklady Academy of Sciences of USSR*, 94(3):433–36, 1954a.

[49] L. Dorman. *Cosmic-Ray Variations*. Moscow, 1957.

[50] L. Dorman. The meteorological effects of cosmic rays. *Nauka press, Russia*, 1972.

[51] L. I. Dorman. *Cosmic rays in the Earth's atmosphere and underground*, volume 303. Springer Science & Business Media, 2004.

[52] M. L. Duldig. Muon observations. *Cosmic Rays and Earth*, pages 207–226, 2000.

[53] E. Dunne, L. Lee, C. Reddington, and K. Carslaw. No statistically significant effect of a short-term decrease in the nucleation rate on atmospheric aerosols. *Atmospheric Chemistry and Physics*, 12(23):11573–11587, 2012.

[54] E. M. Dunne, H. Gordon, A. Kürten, J. Almeida, J. Duplissy, C. Williamson, I. K. Ortega, K. J. Pringle, A. Adamov, U. Baltensperger, et al. Global atmospheric particle formation from CERN CLOUD measurements. *Science*, 354(6316):1119–1124, 2016.

[55] A. Duperier. The seasonal variations of cosmic-ray intensity and temperature of the atmosphere. *Proceedings of the Royal Society of London. Series A. Mathematical and Physical Sciences*, 177(969):204–216, 1941.

[56] A. Duperier. The meson intensity at the surface of the earth and the temperature at the production level. *Proceedings of the Physical Society. Section A*, 62(11):684, 1949.

[57] R. Engel, D. Heck, T. Huege, T. Pierog, M. Reininghaus, F. Riehn, R. Ulrich, M. Unger, and D. Veberič. Towards a next generation of CORSIKA: a framework for the simulation of particle cascades in astroparticle physics. *Computing and Software for Big Science*, 3(1):1–12, 2019.

[58] H. Euler and W. Heisenberg. Theoretische gesichtspunkte zur deutung der kosmischen strahlung. In *Ergebnisse der exakten Naturwissenschaften*, pages 1–69. Springer, 1938.

[59] J. Eyre. Inversion of cloudy satellite sounding radiances by nonlinear optimal estimation. i: Theory and simulation for TOVS. *Quarterly Journal of the Royal Meteorological Society*, 115(489):1001–1026, 1989.

[60] J. Eyre. Inversion methods for satellite sounding data. *ECMWF Meteorological Training Course Lecture Series*, 1991.

[61] P. Fonte. Survey of physical modelling in Resistive Plate Chambers. *Journal of Instrumentation*, 8(11):P11001, 2013.

[62] P. Fonte, A. Smirnitski, and M. Williams. A new high-resolution TOF technology. *Nuclear Instruments and Methods in Physics Research Section A: Accelerators, Spectrometers, Detectors and Associated Equipment*, 443(1):201–204, 2000.

[63] N. Fuchs. The mechanics of aerosols, republication edition, edited by: Davies, CN. *Dover Publications, New York*, 5473:5, 1989.

[64] T. Gaisser and F. Halzen. IceCube. *Annual Review of Nuclear and Particle Science*, 64:101–123, 2014.

[65] T. K. Gaisser, R. Engel, and E. Resconi. *Cosmic rays and particle physics*. Cambridge University Press, 2016.

[66] F. Gensdarmes, D. Boulaud, and A. Renoux. Electrical charging of radioactive aerosols—comparison of the Clement–Harrison models with new experiments. *Journal of aerosol science*, 32(12):1437–1458, 2001.

[67] H. Gómez. Muon tomography using micromegas detectors: From archaeology to nuclear safety applications. *Nuclear Instruments and Methods in Physics Research Section A: Accelerators, Spectrometers, Detectors and Associated Equipment*, 936:14–17, 2019.

[68] N. Gopalswamy, S. Yashiro, G. Michalek, G. Stenborg, A. Vourlidas, S. Freeland, and R. Howard. The SOHO/LASCO CME Catalog. *Earth, Moon, and Planets*, 104(1-4):295–313, 2009.

[69] H. Gordon, J. Kirkby, U. Baltensperger, F. Bianchi, M. Breitenlechner, J. Curtius, A. Dias, J. Dommen, N. M. Donahue, E. M. Dunne, et al. Causes and importance of new particle formation in the present-day and preindustrial atmospheres. *Journal of Geophysical Research: Atmospheres*, 122(16):8739–8760, 2017.

[70] H. Gordon, K. Sengupta, A. Rap, J. Duplissy, C. Frege, C. Williamson, M. Heinritzi, M. Simon, C. Yan, J. Almeida, et al. Reduced anthropogenic aerosol radiative forcing caused by biogenic new particle formation. *Proceedings of the National Academy of Sciences*, 113(43):12053–12058, 2016.

[71] P. Grieder and R. A. E. COSMIC. Researcher's reference manual and data book. *Cosmic Rays at Earth. Elsevier, Amsterdam*, 2001.

[72] P. K. Grieder. *Cosmic rays at Earth*. Elsevier, 2001.

[73] J.-M. Grießmeier, F. Tabataba-Vakili, A. Stadelmann, J. Grenfell, and D. Atri. Galactic cosmic rays on extrasolar Earth-like planets-I. Cosmic ray flux. *Astronomy & Astrophysics*, 581:A44, 2015.

[74] J.-M. Grießmeier, F. Tabataba-Vakili, A. Stadelmann, J. Grenfell, and D. Atri. Galactic cosmic rays on extrasolar Earth-like planets-II. Atmospheric implications. *Astronomy & Astrophysics*, 587:A159, 2016.

[75] P. D. Group, P. Zyla, R. Barnett, J. Beringer, O. Dahl, D. Dwyer, D. Groom, C.-J. Lin, K. Lugovsky, E. Pianori, et al. Review of particle physics. *Progress of Theoretical and Experimental Physics*, 2020(8):083C01, 2020.

[76] S. Haino, T. Sanuki, K. Abe, K. Anraku, Y. Asaoka, H. Fuke, M. Imori, A. Itasaki, T. Maeno, Y. Makida, et al. Measurements of primary and atmospheric cosmic-ray spectra with the BESS-TeV spectrometer. *Physics Letters B*, 594(1-2):35–46, 2004.

[77] R. Harrison and K. Carslaw. Ion-aerosol-cloud processes in the lower atmosphere. *Reviews of Geophysics*, 41(3), 2003.

[78] R. G. Harrison and D. B. Stephenson. Empirical evidence for a nonlinear effect of galactic cosmic rays on clouds. *Proceedings of the Royal Society A: Mathematical, Physical and Engineering Sciences*, 462(2068):1221–1233, 2006.

[79] Y. Hayashi, Y. Aikawa, N. Gopalakrishnan, S. Gupta, N. Ikeda, N. Ito, A. Jain, A. John, S. Karthikeyan, S. Kawakami, et al. A large area muon tracking detector for ultra-high energy cosmic ray astrophysics—the GRAPES-3 experiment. *Nuclear Instruments and Methods in Physics Research Section A: Accelerators, Spectrometers, Detectors and Associated Equipment*, 545(3):643–657, 2005.

[80] B. Heber, H. Fichtner, and K. Scherer. Solar and heliospheric modulation of galactic cosmic rays. *Solar Variability and Planetary Climates*, pages 81–93, 2007.

[81] H. Hersbach, B. Bell, P. Berrisford, G. Biavati, A. Horányi, J. Muñoz Sabater, J. Nicolas, C. Peubey, R. Radu, I. Rozum, D. Schepers, A. Simmons, C. Soci, D. Dee, and J.-N. Thépaut. ERA5 hourly data on pressure levels from 1979 to preset, 2018. Accessed on 30-11-2020.

[82] A. Hillas. Shower simulation: Lessons from MOCCA. *Nuclear Physics B-Proceedings Supplements*, 52(3):29–42, 1997.

[83] R. Hippler, A. Mengel, F. Jansen, G. Bartling, W. Göhler, K. Kudela, K. Munakata, S. Yasue, C. Kato, M. Duldig, et al. First space weather observations at MuSTAnG–the muon space weather telescope for anisotropies at Greifswald. In *Proc. of 30th International Cosmic Ray Conference, Mexico*, volume 1, pages 347–350, 2008.

[84] A. Hirsikko, T. Bergman, L. Laakso, M. D. Maso, I. Riipinen, U. Horrak, and M. Kulmala. Identification and classification of the formation of intermediate ions measured in boreal forest. *Atmospheric Chemistry and Physics*, 7(1):201–210, 2007.

[85] W. A. Hoppel and G. M. Frick. Ion—aerosol attachment coefficients and the steady-state charge distribution on aerosols in a bipolar ion environment. *Aerosol Science and Technology*, 5(1):1–21, 1986.

[86] J. R. Hörandel. Models of the knee in the energy spectrum of cosmic rays. *Astroparticle Physics*, 21(3):241–265, 2004.

[87] D. D. Huang, J. H. Seinfeld, and W. H. Marlow. BGK equation solution of coagulation for large Knudsen number aerosols with a singular attractive contact potential. *Journal of colloid and interface science*, 140(1):258–276, 1990.

[88] G. Hubert, M. Pazianotto, and C. Federico. Modeling of ground albedo neutrons to investigate seasonal cosmic ray-induced neutron variations measured at high-altitude stations. *Journal of Geophysical Research: Space Physics*, 121(12):12–186, 2016.

[89] A. Ivanov, S. Knurenko, and I. Y. Sleptsov. Measuring extensive air showers with Cherenkov light detectors of the Yakutsk array: the energy spectrum of cosmic rays. *New Journal of Physics*, 11(6):065008, 2009.

[90] J. Jakobi, J. Huisman, H. Vereecken, B. Diekkrüger, and H. Bogena. Cosmic ray neutron sensing for simultaneous soil water content and biomass quantification in drought conditions. *Water resources research*, 54(10):7383–7402, 2018.

[91] I. T. Jolliffe. Principal components in regression analysis. *Principal component analysis*, pages 168–177, 2002.

[92] B. Keilhauer, J. Blümer, R. Engel, H. Klages, and M. Risse. Impact of varying atmospheric profiles on extensive air shower observation: atmospheric density and primary mass reconstruction. *Astroparticle Physics*, 22(3-4):249–261, 2004.

[93] Y.-h. Kim, S. Yiacoumi, A. Nenes, and C. Tsouris. Charging and coagulation of radioactive and nonradioactive particles in the atmosphere. *Atmospheric Chemistry and Physics*, 16(5):3449–3462, 2016.

[94] J. Kirkby, J. Duplissy, K. Sengupta, C. Frege, H. Gordon, C. Williamson, M. Heinritzi, M. Simon, C. Yan, J. Almeida, et al. Ion-induced nucleation of pure biogenic particles. *Nature*, 533(7604):521–526, 2016.

[95] M. Köhli, M. Schrön, M. Zreda, U. Schmidt, P. Dietrich, and S. Zacharias. Footprint characteristics revised for field-scale soil moisture monitoring with cosmic-ray neutrons. *Water Resources Research*, 51(7):5772–5790, 2015.

[96] T. Kohno, K. Imai, A. Inue, M. Kodama, and M. Wada. Estimation of the vertical profile of atmospheric temperature from cosmic-ray components. In *International Cosmic Ray Conference*, volume 10, page 289, 1981.

[97] G. Kopp and J. L. Lean. A new, lower value of total solar irradiance: Evidence and climate significance. *Geophysical Research Letters*, 38(1), 2011.

[98] G. Kornakov, O. Arnold, E. Atomssa, C. Behnke, A. Belyaev, J. Berger-Chen, J. Biernat, A. Blanco, C. Blume, M. Böhmer, et al. Time of flight measurement in heavy-ion collisions with the HADES RPC TOF wall. *Journal of Instrumentation*, 9(11):C11015, 2014.

[99] K. Kotera and A. V. Olinto. The astrophysics of ultrahigh-energy cosmic rays. *Annual Review of Astronomy and Astrophysics*, 49:119–153, 2011.

[100] J. Kristjánsson, J. Kristiansen, and E. Kaas. Solar activity, cosmic rays, clouds and climate–an update. *Advances in space research*, 34(2):407–415, 2004.

[101] P. Kuusiniemi, L. Bezrukov, I. Dzaparova, T. Enqvist, H. Fynbo, L. Inzhechik, J. Joutsenvaara, K. Loo, B. Lubsandorzhiev, V. Petkov, et al. Performance of tracking stations of the underground cosmic-ray detector array EMMA. *Astroparticle Physics*, 102:67–76, 2018.

[102] B. A. Laken, E. Pallé, J. Čalogović, and E. M. Dunne. A cosmic ray-climate link and cloud observations. *Journal of Space Weather and Space Climate*, 2:A18, 2012.

[103] Y. Lee and P. Adams. A fast and efficient version of the TwO-Moment Aerosol Sectional (TOMAS) global aerosol microphysics model. *Aerosol Science and Technology*, 46(6):678–689, 2012.

[104] A. Letessier-Selvon, P. A. Collaboration, et al. Highlights from the Pierre Auger Observatory. *Brazilian Journal of Physics*, 44(5):560–570, 2014.

[105] D. Li, M. Schrön, M. Kohli, H. Bogena, J. Weimar, M. A. Jiménez Bello, X. Han, M. A. Martínez-Gimeno, S. Zacharias, H. Vereecken, et al. Can drip irrigation be scheduled with cosmic-ray neutron sensing? *Vadose zone journal*, 18(1):1–13, 2019.

[106] P. Lipari and T. Stanev. Propagation of multi-TeV muons. *Physical Review D*, 44(11):3543, 1991.

[107] Y. Liu, T. Xu, and J. Liu. Characteristics of the seasonal variation of the global tropopause revealed by COSMIC/GPS data. *Advances in Space Research*, 54(11):2274–2285, 2014.

[108] L. Lopes, P. Assis, A. Blanco, N. Carolino, M. Cerda, R. Conceição, O. Cunha, M. Ferreira, P. Fonte, R. Luz, et al. Outdoor field experience with autonomous RPC based stations. *Journal of Instrumentation*, 11(09):C09011, 2016.

[109] I. Lázaro Roche. A compact muon tracker for dynamic tomography of density based on a thin time projection chamber with micromegas readout. *Particles*, 4(3):333–342, 2021.

[110] A. Maisels, F. E. Kruis, and H. Fissan. Determination of coagulation coefficients and aggregation kinetics for charged aerosols. *Journal of Colloid and Interface Science*, 255(2):332–340, 2002.

[111] L. Margato, A. Morozov, A. Blanco, P. Fonte, F. Fraga, B. Guerard, R. Hall-Wilton, C. Höglund, A. Mangiarotti, L. Robinson, et al. Boron-10 lined RPCs for sub-millimeter resolution thermal neutron detectors: Feasibility study in a thermal neutron beam. *Journal of Instrumentation*, 14(01):P01017, 2019.

[112] J. Matthews. A heitler model of extensive air showers. *Astroparticle Physics*, 22(5-6):387–397, 2005.

[113] R. Mendonça, C. Wang, C. Braga, E. Echer, A. Dal Lago, J. Costa, K. Munakata, H. Li, Z. Liu, J.-P. Raulin, et al. Analysis of cosmic rays' atmospheric effects and their relationships to cutoff rigidity and zenith angle using global muon detector network data. *Journal of Geophysical Research: Space Physics*, 124(12):9791–9813, 2019.

[114] Y. Miyazaki and M. Wada. Simulation of cosmic ray variation due to temperature effect. In *International Cosmic Ray Conference*, volume 2, page 591, 1970.

[115] H. Moraal and P. Stoker. Long-term neutron monitor observations and the 2009 cosmic ray maximum. *Journal of Geophysical Research: Space Physics*, 115(A12), 2010.

[116] K. Morishima, M. Kuno, A. Nishio, N. Kitagawa, Y. Manabe, M. Moto, F. Takasaki, H. Fujii, K. Satoh, H. Kodama, et al. Discovery of a big void in Khufu's Pyramid by observation of cosmic-ray muons. *Nature*, 552(7685):386–390, 2017.

[117] A. B. Nadykto and F. Yu. Uptake of neutral polar vapor molecules by charged clusters/particles: Enhancement due to dipole-charge interaction. *Journal of Geophysical Research: Atmospheres*, 108(D23), 2003.

[118] A. Osipenko, A. Abunin, M. Berkova, N. Barbashina, V. Grigoryev, S. Starodubtsev, V. Kuzmenko, V. Yanchukovsky, M. Titova, A. Belov, et al. Analyzing the temperature effect of high mountain cosmic ray detectors using the database of the global network of muon telescopes. *Bulletin of the Russian Academy of Sciences: Physics*, 79(5):662–666, 2015.

[119] S. Osprey, J. Barnett, J. Smith, P. Adamson, C. Andreopoulos, K. Arms, R. Armstrong, D. Auty, D. Ayres, B. Baller, et al. Sudden stratospheric warmings seen in MINOS deep underground muon data. *Geophysical Research Letters*, 36(5), 2009.

[120] V. Petkov, M. Kostyuk, R. Novoseltseva, Y. F. Novoseltsev, L. Volkova, P. Striganov, and M. Boliev. Temperature variations of high energy muon flux. In *32nd International Cosmic Ray Conference*, 2011.

[121] J. Pierce. Cosmic rays, aerosols, clouds, and climate: Recent findings from the cloud experiment. *Journal of Geophysical Research: Atmospheres*, 122(15):8051–8055, 2017.

[122] J. Pierce and P. Adams. Can cosmic rays affect cloud condensation nuclei by altering new particle formation rates? *Geophysical Research Letters*, 36(9), 2009.

[123] C. Pierre Auger Collaboration. The Pierre Auger cosmic ray observatory. *Nuclear Instruments and Methods in Physics Research Section A: Accelerators, Spectrometers, Detectors and Associated Equipment*, 798:172–213, 2015.

[124] A. Pla-Dalmau, A. D. Bross, and V. V. Rykalin. Extruding plastic scintillator at Fermilab. In *2003 IEEE Nuclear Science Symposium. Conference Record (IEEE Cat. No. 03CH37515)*, volume 1, pages 102–104. IEEE, 2003.

[125] H. A. Pol, R. Alves, A. Blanco, N. Carolino, J. Eschke, R. Ferreira-Marques, P. Fonte, J. Garzón, D. G. Díaz, A. Pereira, et al. A large area timing RPC prototype for ion collisions in the HADES spectrometer. *Nuclear Instruments and Methods in Physics Research Section A: Accelerators, Spectrometers, Detectors and Associated Equipment*, 535(1-2):277–282, 2004.

[126] S. Procureur. Muon imaging: Principles, technologies and applications. *Nuclear Instruments and Methods in Physics Research Section A: Accelerators, Spectrometers, Detectors and Associated Equipment*, 878:169–179, 2018.

[127] M. Pudovkin and S. Veretenenko. Cloudiness decreases associated with Forbush-decreases of galactic cosmic rays. *Journal of Atmospheric and Terrestrial Physics*, 57(11):1349–1355, 1995.

[128] M. Pudovkin and S. Veretenenko. Variations of the cosmic rays as one of the possible links between the solar activity and the lower atmosphere. *Advances in Space Research*, 17(11):161–164, 1996.

[129] A. Raghav, Z. Shaikh, A. Bhaskar, G. Datar, and G. Vichare. Forbush decrease: A new perspective with classification. *Solar Physics*, 292(8):1–14, 2017.

[130] J.-B. Renard, S. Tripathi, M. Michael, A. Rawal, G. Berthet, M. Fullekrug, R. Harrison, C. Robert, M. Tagger, and B. Gaubicher. In situ detection of electrified aerosols in the upper troposphere and stratosphere. *Atmospheric Chemistry and Physics*, 13(22):11187–11194, 2013.

[131] D. Reyna. A simple parameterization of the cosmic-ray muon momentum spectra at the surface as a function of zenith angle. *arXiv preprint hep-ph/0604145*, 2006.

[132] W. Riegler, C. Lippmann, and R. Veenhof. Detector physics and simulation of resistive plate chambers. *Nuclear Instruments and Methods in Physics Research Section A: Accelerators, Spectrometers, Detectors and Associated Equipment*, 500(1-3):144–162, 2003.

[133] M. Rockenbach, A. Dal Lago, N. Schuch, K. Munakata, T. Kuwabara, A. Oliveira, E. Echer, C. Braga, R. Mendonça, C. Kato, et al. Global muon detector network used for space weather applications. *Space Science Reviews*, 182(1-4):1–18, 2014.

[134] C. D. Rodgers. *Inverse methods for atmospheric sounding: theory and practice*, volume 2. World scientific, 2000.

[135] S. Sagisaka. Atmospheric effects on cosmic-ray muon intensities at deep underground depths. *Il Nuovo Cimento C*, 9(4):809–828, 1986.

[136] R. Santonico and R. Cardarelli. Development of resistive plate counters. *Nuclear Instruments and Methods in physics research*, 187(2-3):377–380, 1981.

[137] M. Savić, A. Dragić, D. Maletić, N. Veselinović, R. Banjanac, D. Joković, and V. Udovičić. A novel method for atmospheric correction of cosmic-ray data based on principal component analysis. *Astroparticle Physics*, 109:1–11, 2019.

[138] S. Sciutto. Aires: A system for air shower simulations. *arXiv preprint astro-ph/9911331*, 1999.

[139] D. J. Seidel and W. J. Randel. Variability and trends in the global tropopause estimated from radiosonde data. *Journal of Geophysical Research: Atmospheres*, 111(D21), 2006.

[140] J. Seinfeld and S. Pandis. Atmospheric chemistry and physics. 1997. *New York*, 2008.

[141] F. Sepúlveda and C. Dib. Simple hadronic cascade simulations. *Brazilian journal of physics*, 37(2B):633–636, 2007.

[142] P. Shukla and S. Sankrith. Energy and angular distributions of atmospheric muons at the Earth. *International Journal of Modern Physics A*, 33(30):1850175, 2018.

[143] E. Snow-Kropla, J. Pierce, D. Westervelt, and W. Trivitayanurak. Cosmic rays, aerosol formation and cloud-condensation nuclei: sensitivities to model uncertainties. *Atmospheric Chemistry and Physics*, 11(8):4001–4013, 2011.

[144] M. Sobotka. Solar activity ii: Sunspots and pores. *Astronomische Nachrichten: Astronomical Notes*, 324(4):369–373, 2003.

[145] P. H. Stoker, L. I. Dorman, and J. M. Clem. Neutron monitor design improvements. *Cosmic Rays and Earth*, pages 361–380, 2000.

[146] Y. I. Stozhkov. The role of cosmic rays in the atmospheric processes. *Journal of Physics G: Nuclear and Particle Physics*, 29(5):913, 2003.

[147] B. Sun and R. S. Bradley. Solar influences on cosmic rays and cloud formation: A reassessment. *Journal of Geophysical Research: Atmospheres*, 107(D14):AAC–5, 2002.

[148] H. Svensmark, T. Bondo, and J. Svensmark. Cosmic ray decreases affect atmospheric aerosols and clouds. *Geophysical Research Letters*, 36(15), 2009.

[149] H. Svensmark, M. Enghoff, N. Shaviv, and J. Svensmark. Increased ionization supports growth of aerosols into cloud condensation nuclei. *Nature communications*, 8(1):1–9, 2017.

[150] H. Svensmark, M. B. Enghoff, and J. O. P. Pedersen. Response of cloud condensation nuclei ($>$ 50 nm) to changes in ion-nucleation. *Physics Letters A*, 377(37):2343–2347, 2013.

[151] H. Svensmark and E. Friis-Christensen. Variation of cosmic ray flux and global cloud coverage—a missing link in solar-climate relationships. *Journal of atmospheric and solar-terrestrial physics*, 59(11):1225–1232, 1997.

[152] J. Svensmark, N. J. Shaviv, M. B. Enghoff, and H. Svensmark. The ION-CAGE code: A numerical model for the growth of charged and neutral aerosols. *Earth and Space Science*, 7(9):e2020EA001142, 2020.

[153] H. K. Tanaka, T. Uchida, M. Tanaka, M. Takeo, J. Oikawa, T. Ohminato, Y. Aoki, E. Koyama, and H. Tsuji. Detecting a mass change inside a volcano by cosmic-ray muon radiography (muography): First results from measurements at Asama volcano, Japan. *Geophysical Research Letters*, 36(17), 2009.

[154] S. Tilav, P. Desiati, T. Kuwabara, D. Rocco, F. Rothmaier, M. Simmons, and H. Wissing. Atmospheric variations as observed by IceCube. *arXiv preprint arXiv:1001.0776*, 2010.

[155] B. Tinsley. The global atmospheric electric circuit and its effects on cloud microphysics. *Reports on Progress in Physics*, 71(6):066801, 2008.

[156] B. A. Tinsley and R. A. Heelis. Correlations of atmospheric dynamics with solar activity evidence for a connection via the solar wind, atmospheric electricity, and cloud microphysics. *Journal of Geophysical Research: Atmospheres*, 98(D6):10375–10384, 1993.

[157] M. C. Todd and D. R. Kniveton. Changes in cloud cover associated with Forbush decreases of galactic cosmic rays. *Journal of Geophysical Research: Atmospheres*, 106(D23):32031–32041, 2001.

[158] M. C. Todd and D. R. Kniveton. Short-term variability in satellite-derived cloud cover and galactic cosmic rays: an update. *Journal of atmospheric and solar-terrestrial physics*, 66(13-14):1205–1211, 2004.

[159] S. C. Tognini and R. A. Gomes. Simulation of atmospheric temperature effects on cosmic ray muon flux. In *AIP Conference Proceedings*, volume 1663, page 120015. AIP Publishing LLC, 2015.

[160] W. Trivitayanurak, P. Adams, D. Spracklen, and K. Carslaw. Tropospheric aerosol microphysics simulation with assimilated meteorology: model description and intermodel comparison. *Atmospheric Chemistry and Physics*, 8(12):3149–3168, 2008.

[161] W. H. Trzaska, M. Slupecki, I. Bandac, A. Bayo, A. Bettini, L. Bezrukov, T. Enqvist, A. Fazliakhmetov, A. Ianni, L. Inzhechik, et al. Cosmic-ray muon flux at Canfranc Underground Laboratory. *The European Physical Journal C*, 79(8):1–5, 2019.

[162] N. Tsoulfanidis and S. Landsberger. *Measurement & detection of radiation*. CRC press, 2021.

[163] N. L. Tyrrell, A. Y. Karpechko, P. Uotila, and T. Vihma. Atmospheric circulation response to anomalous siberian forcing in October 2016 and its long-range predictability. *Geophysical Research Letters*, 46(5):2800–2810, 2019.

[164] S. Tzivion, G. Feingold, and Z. Levin. An efficient numerical solution to the stochastic collection equation. *Journal of Atmospheric Sciences*, 44(21):3139–3149, 1987.

[165] I. Usoskin, K. Alanko, K. Mursula, and G. Kovaltsov. Heliospheric modulation strength during the neutron monitor era. *Solar Physics*, 207(2):389–399, 2002.

[166] I. G. Usoskin. A history of solar activity over millennia. *Living Reviews in Solar Physics*, 14(1):1–97, 2017.

[167] I. G. Usoskin and G. A. Kovaltsov. Cosmic ray induced ionization in the atmosphere: Full modeling and practical applications. *Journal of Geophysical Research: Atmospheres*, 111(D21), 2006.

[168] P. Vasilakos, Y.-H. Kim, J. R. Pierce, S. Yiacoumi, C. Tsouris, and A. Nenes. Studying the impact of radioactive charging on the microphysical evolution and transport of radioactive aerosols with the TOMAS-RC v1 framework. *Journal of environmental radioactivity*, 192:150–159, 2018.

[169] P. I. Velinov, S. Asenovski, K. Kudela, J. Lastovicka, L. Mateev, A. Mishev, and P. Tonev. Impact of cosmic rays and solar energetic particles on the earth's ionosphere and atmosphere. *Journal of Space Weather and Space Climate*, 3:A14, 2013.

[170] K. Watanabe, S. Tanaka, W. Chang, H. Chen, M. Chu, J. Cuenca-García, T. Gogami, D. González-Díaz, M. Niiyama, Y. Ohashi, et al. A compensated multi-gap RPC with 2 m strips for the LEPS2 experiment. *Nuclear Instruments and Methods in Physics Research Section A: Accelerators, Spectrometers, Detectors and Associated Equipment*, 925:188–192, 2019.

[171] D. F. Webb and T. A. Howard. Coronal mass ejections: Observations. *Living Reviews in Solar Physics*, 9(1):1–83, 2012.

[172] R. C. Willson. Solar irradiance variations and solar activity. *Journal of Geophysical Research: Space Physics*, 87(A6):4319–4326, 1982.

[173] F. Xing-Ming, W. Yi, W. Xue-Wu, Z. Zhi, Z. Ming, Z. Zi-Ran, C. Jian-Ping, and D. Gonzalez-Diaz. A position resolution MRPC for muon tomography. *Chinese Physics C*, 38(4):046003, 2014.

[174] Y. Yair and Z. Levin. Charging of polydispersed aerosol particles by attachment of atmospheric ions. *Journal of Geophysical Research: Atmospheres*, 94(D11):13085–13091, 1989.

[175] V. Yanchukovsky. Muon intensity variations and atmospheric temperature. *Solar-Terrestrial Physics*, 6(1):108–115, 2020.

[176] V. Yanchukovsky, G. Y. Filimonov, and R. Hisamov. Atmospheric variations in muon intensity for different zenith angles. *Bulletin of the Russian Academy of Sciences: Physics*, 71(7):1038–1040, 2007.

[177] V. Yanchukovsky and V. Kuzmenko. Atmospheric effects of the cosmic-ray mu-meson component. *Solar-Terrestrial Physics*, 4(3):76–82, 2018.

[178] V. Yanchukovsky, S. Sunyakov, and V. Kuzmenko. Variations in temperature at different isobaric levels of the atmosphere, according to data on cosmic rays. *Bulletin of the Russian Academy of Sciences: Physics*, 79(5):667–669, 2015.

[179] F. Yu. Modified Kelvin–Thomson equation considering ion-dipole interaction: Comparison with observed ion-clustering enthalpies and entropies. *The Journal of chemical physics*, 122(8):084503, 2005.

[180] F. Yu. From molecular clusters to nanoparticles: second-generation ion-mediated nucleation model. *Atmospheric Chemistry and Physics*, 6(12):5193–5211, 2006.

[181] F. Yu. Ion-mediated nucleation in the atmosphere: Key controlling parameters, implications, and look-up table. *Journal of Geophysical Research: Atmospheres*, 115(D3), 2010.

[182] F. Yu, G. Luo, X. Liu, R. C. Easter, X. Ma, and S. J. Ghan. Indirect radiative forcing by ion-mediated nucleation of aerosol. *Atmospheric Chemistry and Physics*, 12(23):11451–11463, 2012.

[183] F. Yu and R. Turco. Case studies of particle formation events observed in boreal forests: implications for nucleation mechanisms. *Atmospheric Chemistry and Physics*, 8(20):6085–6102, 2008.

[184] M. Zazyan, M. Ganeva, M. Berkova, V. Yanke, and R. Hippler. Atmospheric effect corrections of mustang data. *Journal of space weather and space climate*, 5:A6, 2015.

[185] E. C. Zeballos, I. Crotty, D. Hatzifotiadou, J. L. Valverde, S. Neupane, M. Williams, and A. Zichichi. A new type of resistive plate chamber: The multigap RPC. *Nuclear Instruments and Methods in Physics Research Section A: Accelerators, Spectrometers, Detectors and Associated Equipment*, 374(1):132–135, 1996.

[186] Z. Zhu, L. Lu, W. Zhang, and W. Liu. AR6 Climate Change 2021: The Physical Science Basis. *IPCC: Geneva, Switzerland*, 2021.

"Cosmic Rays" is the name given to the radiation coming from outer space. They have their origin in some of the most violent and bizarre phenomena in the cosmos, such as supernovae or black holes. The study of cosmic rays is becoming a
research field of great interest in many areas, especially outside astrophysics and particle physics.

The objective of this thesis is to find innovative ways to investigate the everyday, bringing cosmic-ray research to a much
more mundane and practical purview. Thus, we will consider cosmic rays as a tool for atmospheric research, as well as an object of study concerning their interplay with the atmosphere. Some of the main topics include the retrieval of atmospheric temperature from cosmic-ray measurements and the study of the role of cosmic rays in cloud formation.